Numerical Simulations of Solar Eruptive Events

A thesis submitted in partial fulfillment of
the requirements for the degree of

Doctor of Philosophy

by

Satyam Agarwal

(Roll No. 19330016)

Under the guidance of

Dr. Ramitendranath Bhattacharyya

Professor

Udaipur Solar Observatory

Physical Research Laboratory, Udaipur, India.

DEPARTMENT OF PHYSICS

INDIAN INSTITUTE OF TECHNOLOGY GANDHINAGAR

2024

to

my mother

Declaration

I declare that this written submission represents my ideas in my own words and where others' ideas or words have been included, I have adequately cited and referenced the original sources. I also declare that I have adhered to all principles of academic honesty and integrity and have not misrepresented or fabricated or falsified any idea/data/fact/source in my submission. I understand that any violation of the above will be cause for disciplinary action by the Institute and can also evoke penal action from the sources which have thus not been properly cited or from whom proper permission has not been taken when needed.

(Signature)

(Name: Satyam Agarwal)

(Roll No: 19330016)

CERTIFICATE

It is certified that the work contained in the thesis titled **"Numerical Simulations of Solar Eruptive Events"** by **Mr. Satyam Agarwal** (Roll no: 19330016), has been carried out under my supervision and that this work has not been submitted elsewhere for degree.

I have read this dissertation and in my opinion, it is fully adequate in scope and quality as a dissertation for the degree of Doctor of Philosophy.

Dr. Ramitendranath Bhattacharyya

(Thesis Supervisor)

Professor

Udaipur Solar Observatory

Physical Research Laboratory

Badi Road, Udaipur 313001, India

Acknowledgements

It is always a great pleasure to express my deep gratitude toward people who have played an instrumental role during my academic journey and in my life. I know that my words will never be enough but I hope that they encapsulate the essence of my emotions.

I am grateful to my PhD supervisor Prof. Ramit Bhattacharyya for giving me the opportunity to work with him. I am thankful to him for giving the freedom of working on research problems of my interest and for guiding me in the right direction whenever required. His ability of piercing through the equations to reveal the underlying physics made our scientific discussions a very joyful and enriching experience for me. I hope to inculcate some of that ability into me as I progress along in field of research. I will always cherish our philosophical conversations over a cup of tea about life, society, love, politics, religion, and much more than I can recall at the moment.

I am grateful to Prof. Thomas Wiegelmann, Dr. Shangbin Yang, Dr. Sanjay Kumar, and Dr. Kamlesh Bora for collaborating with me. Their contributions to my scientific endeavors have been invaluable. I sincerely thank the members of my Doctoral Studies Committee, Prof. Shibu Mathew, Prof. Brajesh Kumar, and Dr. Arvind Singh for evaluating my work at regular intervals of time. Their comments and suggestions have been very helpful in gaining deeper insights into the research works carried out in this thesis. I am also grateful to SERB, India for funding my international travel to attend a training school on plasma physics in France.

I express my sincere thanks to the Physical Research Laboratory, Ahmedabad, where I became familiar with part and parcel of scientific research. I am thankful to Prof. Anil Bhardwaj, Director, PRL, Ahmedabad, for always being supportive and providing the necessary facilities to carry out my research. In particular, I express my thanks for the hostel, canteen, sports, computer center, library, contingency funds, and medical facilities, all of which allowed me to focus on my research work efficiently. I will remain indebted for the medical support because it helped me greatly with the financial expenses related to my autoimmune conditions of myositis and ILD, diagnosed during my PhD tenure.

I am also thankful to the Udaipur Solar Observatory, Udaipur, Rajasthan, where I was stationed to carry out my research in the domain of solar physics. I thank Prof. Shibu Mathew, Head, USO for always being supportive in academic affairs and other matters. I am grateful to all the faculty members of USO for the relevant scientific discussion and their help. I thank the administration department of both USO and PRL, Ahmedabad, for their active cooperation in various matters. In particular, I thank Abhishek Ji, Administrative Officer, USO, for always being understanding and trying his best to resolve student issues.

In my PhD tenure, I have been fortunate enough to cultivate some meaningful relationships including friends and some senior colleagues. I express my gratitude toward Dr. Ranadeep Sarkar, Dr. Prabir Kumar Mitra, Dr. Kamlesh Bora, and Ms. Binal Patel for being my friends, taking care of me in times of distress, for guiding me, and for the camaraderie we shared together. I express my thanks to Dr. Avijeet Prasad and Dr. Sanjay Kumar for helping me with my research when required. I thank Mr. Lovjeet Meena and Mr. Kushagra Upadhyay for sacrificing their sleep and taking me to hospital during my medical emergencies. I would also like to thank Ms. Bireddy Ramya and Mrs. Bharti Saradva for inviting me to their home and making me feel homely during my stay in USO. I thank Ashwini, Saurabh, Partha, who have been my friends since the post-graduation days, for their encouragement and support. I express my deepest possible gratitude to Dr. Kamlesh Bora for her unconditional support as a friend and mentorship as my senior colleague. I also thank Mrs. Anandi Devi for taking care of me like her son after my surgery for the removal of kidney stones.

Lastly, I thank my family for their love and lifelong support. I dedicate this thesis to my mother, who dreamt of nothing but for her children to receive a good education and become successful. With this thesis, I hope to bring her happiness and do some justice to her immeasurable sacrifices. I am thankful to my father for always working his hardest to earn money for the family and supporting us. I am grateful to my elder brother Mr. Shivam Agarwal for always having my back, understanding me, loving me, and taking care of me throughout my life.

(Satyam Agarwal)

Abstract

Solar eruptive events such as flares and Coronal Mass Ejections (CMEs) are the sudden explosive events on the Sun that release a tremendous amount of energy. These events are believed to be the manifestations of the magnetic reconnection process, which converts magnetic energy into heat, kinetic energy of the plasma, and fast acceleration of charged particles. Further, reconnection changes the connectivity of magnetic field lines, causing a rearrangement of the magnetic topology. Notably, the release of magnetic energy during such events is expected to relax the overall magnetic field configuration to a terminal state characterized by lesser magnetic energy. As a consequence, it is realized that these events merit interest from a fundamental perspective, namely self-organization in magnetized plasmas, also known as plasma relaxation.

Self-organization is the spontaneous and preferential evolution of a dynamical system toward states that exhibit some form of long-range ordering. Such kind of systems are governed by nonlinear partial differential equations with dissipation. Notably, the magnetized plasma in the solar corona is approximated to be governed by the equations of magnetohydrodynamics (MHD), which are nonlinear, implying that an investigation from the perspective of plasma relaxation is reasonable. The self-organized states are nearly independent of the system's initial configuration. Furthermore, the long-range order is always accompanied by short-range disorder, which is associated with the fact that in presence of dissipation, the ideal integrals of motion (e.g. magnetic energy, magnetic helicity) are not conserved and decay at different rates. This decay at different rates gives a way to formulate a variational problem, where a minimization of the fastest decaying quantity while treating slower decaying quantities as invariants determines a relaxed state. In the above background, the resulting lower magnetic energy state after eruptive events can be viewed in connection with the relaxed states that are obtained using variational method. In particular, the thesis explores the realization of force-free states that are analytically obtained by a constrained minimization of the magnetic energy with magnetic helicity as an invariant.

To achieve the above goals, data-based MHD simulations of various flares are carried out using the EULAG-MHD numerical model. The simulations employ a

magnetic field extrapolated using the measured photospheric magnetic field as an initial condition. Importantly, the extrapolation models are broadly classified into force-free and non-force-free, depending on whether the allowed Lorentz force is analytically zero or not at the bottom boundary. It is then imperative to study the influence of different extrapolation models on the simulated dynamics. Toward such an exploration, data-based MHD simulations of a GOES C6.6 flare in active region NOAA 11977 are carried out using three different initial conditions, each constituted by a suitable pair of initial magnetic and velocity fields. The relevant magnetic fields are constructed from non-force-free field (NFFF) and nonlinear force-free field (NLFFF) extrapolations. A morphological comparison on the global scale and particularly for selected topologies, such as a magnetic null point and a hyperbolic flux tube (HFT) suggests that similar magnetic field line structures are reproducible in both models, although the extent of agreement between the two varies. In all simulations, the dissipated magnetic energy and changes in field line connection for the null point and HFT configurations are found to be similar. In addition, a null point topology is found to appear spontaneously near the HFT in all the cases. The results suggest that the magnetofluid dynamics and the details of reconnection are nearly independent of the chosen initial conditions. Therefore, both the extrapolation techniques can be suitable for data-based simulations. The near-independence is a signature of self-organization, which further motivates an exploration of magnetic relaxation in eruptive events.

Consequently, data-based MHD simulation of a GOES M1.3 flare hosted by active region NOAA 12253 is carried out. The investigation of extrapolated NFFF in conjunction with the observed evolution of the flare reveals a HFT overlying the observed brightenings. The overall simulation shows signatures of relaxation. For a detailed analysis, three distinct sub-volumes are considered. The analysis focuses on the magnetic field line dynamics along with time evolution of physically relevant quantities like magnetic energy, current density, twist, and gradients in magnetic field. An approximate estimation of the Poynting flux and numerical diffusion is carried out to understand their role in governing the dynamics in sub-volumes. The force-free aspect of the magnetic field is explored numerically by analyzing the temporal evolution of angular alignment between the magnetic field and current density. In the terminal state, none of the sub-volumes is seen to reach a force-free state, thus remaining in non-equilibrium, suggesting the possibility of further relaxation. It is concluded that the extent of relaxation depends on the efficacy and duration of reconnection, and hence on the energetics and time span of the flare.

Toward such exploration, data-based MHD simulations of three energetically different flares, namely GOES B6.4, C4.0, and M1.1 are carried out. The NFFF extrapolation identifies magnetic null points for the B6.4 and C4.0 flares, and a HFT for the M1.1 flare as primary reconnection sites. The simulated evolution of the magnetofluid exhibits reconnection at these sites, which is exemplified by the slipping reconnection in the null point topology of the B6.4 flare. An estimation of the dissipated magnetic energy amounts to nearly 7%, 16.8%, and 33% of the available free magnetic energy in the simulation of B6.4, C4.0, and M1.1 flares. The angle between the current density and the magnetic field at the reconnection site decreases by 75.92° , 41.37°, and 40.13°, respectively, implying an increase in the alignment, indicating magnetic relaxation. The amount of dissipated magnetic energy in the simulated dynamics of each flare is in concurrence with the general energy relation between the classes of chosen flares. Furthermore, the increase in alignment at the reconnection sites suggests the occurrence of magnetic relaxation locally.

Overall, the thesis aims to explore eruptive events from the perspective of self-organization and magnetic relaxation using data-based MHD simulations of flares. It is found that solar transients exhibit signatures of self-organization and consequently of magnetic relaxation. However, the relaxation is not enough to reach a force-free state.

Keywords: Solar Flares, Solar magnetic fields, Magnetic reconnection, Magnetohydrodynamics, Self-organization, Plasma relaxation, Magnetic relaxation, and Numerical simulations.

List of Publications

Publications as First Author

1. **Satyam Agarwal**, Ramit Bhattacharyya, Study of magnetic relaxation in MHD simulations of energetically different flares, *Phys. Plasmas* **31** (2024), DOI:10.1063/5.0206697

2. **Satyam Agarwal**, Ramit Bhattacharyya, Shangbin Yang, Study of reconnection dynamics and plasma relaxation in MHD simulation of a solar flare, *Sol Phys* **299**, 15 (2024), DOI:10.1007/s11207-024-02255-5

3. **Satyam Agarwal**, Ramit Bhattacharyya, Thomas Wiegelmann, Effects of initial conditions on magnetic reconnection in a solar transient, *Sol Phys* **297**, 91 (2022), DOI:10.1007/s11207-022-02016-2

Publications as Co-author

1. Sanjay Kumar, Avijeet Prasad, Sushree S Nayak, **Satyam Agarwal**, Ramit Bhattacharyya, Magnetohydrodynamics simulation of magnetic flux rope formation in a quadrupolar magnetic field configuration, *Plasma Phys. Control. Fusion* **65** (2023), DOI:10.1088/1361-6587/acdd1d

2. K Bora, **Satyam Agarwal**, Sanjay Kumar, R Bhattacharyya, Hall effect on the magnetic reconnections during the evolution of a three-dimensional magnetic flux rope, *Phys. Scr.* **98** (2023), DOI:10.1088/1402-4896/acd3bb

Contents

List of Figures

List of Tables

Chapter 1

Solar Eruptive Events: Manifestations of Magnetic Reconnection

1.1 Introduction

The long-standing interest in studying the Sun originates from its fundamental role in sustaining life on the Earth and serving as an astrophysical laboratory for investigating many physical processes. In this regard, the magnetic field of the Sun, which threads its way from the interior of the Sun into the outer solar atmosphere (Solanki et al., 2006), plays an important role. To quote E. N. Parker, "If it were not for its variable magnetic field, the Sun would have been a rather uninteresting star"(Low, 1996). The solar magnetic field gives rise to various features and dynamical activities that vary over a wide range of spatial (e.g., a few hundred kilometers to several mega meters) and temporal (e.g., minutes to several years) scales. One example is a sudden and explosive release of magnetic energy in the form of transient events like solar flares and Coronal Mass Ejections (CMEs), which are casually referred to as eruptive phenomena (Priest, 2014).

Solar flares are the sudden and localized brightenings observed over a temporal scale of minutes to hours (Benz, 2017). The observed brightening exhibits emission in multiple wavelengths across the electromagnetic spectrum, broadly categorized into radio, visible, soft X-rays (SXR), hard X-rays (HXR), extreme ultraviolet (EUV), and gamma-rays. Solar flares vary in strength depending on the total amount of released energy, which typically ranges between $10^{23} - 10^{32}$ erg (Benz, 2017). The brightenings during a solar flare can be visualized using imaging observations of the Sun. As an example, observations of the last decade's strongest flare from some of the EUV wavelength channels of the Atmospheric Imaging Assembly (AIA) instrument (Lemen et al., 2012) onboard the Solar Dynamics Observatory (SDO; Pesnell et al., 2012) are analyzed to depict the corresponding brightening in figure 1.1. The constructed images correspond to the peak time of SXR emission. Notably, solar flares are often accompanied by an expulsion of magnetized plasma

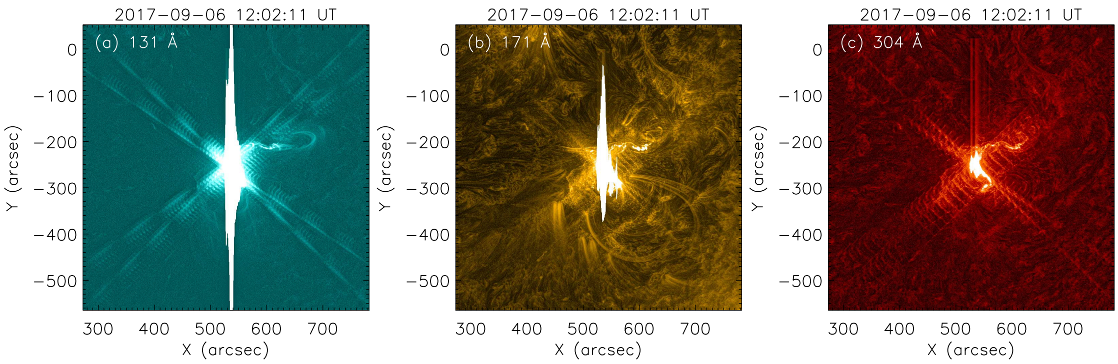

Figure 1.1: Imaging observations of a solar flare in 131 Å, 171 Å, and 304 Å by SDO/AIA on September 6, 2017.

in the form of coronal mass ejection, which is considered a major driver of space weather.

Coronal Mass Ejections are the sudden release of magnetized plasma into the heliosphere. Typically, CMEs have a mass of $10^{11} - 10^{12}$ kg and speed in the range of $400 - 1000$ km/s, resulting in a kinetic energy of up to 10^{25} Joules (Howard, 2011). The routine observations of CMEs are carried out in white light using a coronagraph, which artificially blocks the intense photospheric disk for imaging the solar corona (Stix, 2002). The photospheric light scattered off the free electrons in the plasma of CME highlights its morphological structure against the background of the low-density solar corona in the two-dimensional images. For example, the observations of a CME associated with the flare discussed in figure 1.1 are used to construct figure 1.2, which depicts the CME evolution with time. The red disk in the figure corresponds to the area blocked by the coronagraph, while the white ring represents the surface of the Sun. Importantly, CMEs are considered to be the eruptions of magnetic flux ropes (MFRs), where a MFR is defined as a bundle of helically twisted magnetic field lines (MFLs) that wind around a common axis (Priest, 2014; Vourlidas, 2014).

The release of magnetic energy in eruptive events leads to a basic expectation

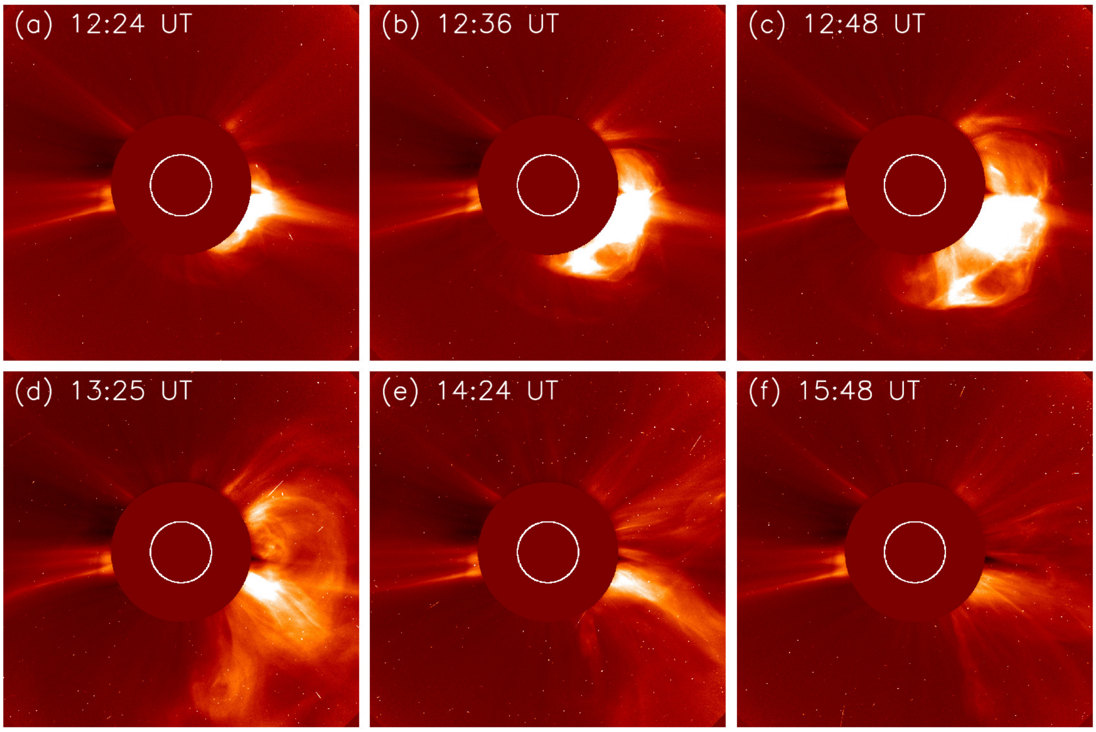

Figure 1.2: White light imaging observations of a Coronal Mass Ejection (CME) by the LASCO instrument onboard the SOHO satellite on September 6, 2017.

that the magnetic field should relax to a state having lesser magnetic energy. As a consequence, it is realized that solar transients merit interest from a fundamental perspective, namely self-organization in magnetized plasmas (Ortolani & Schnack, 1993), which is also known as plasma relaxation. The process of self-organization refers to the spontaneous and preferential evolution of a system toward states that exhibit some form of long-range ordering. Such systems are governed by nonlinear partial differential equations with dissipation. Relevantly, the magnetized plasma in the solar corona is governed by the equations of magnetohydrodynamics (MHD), which are nonlinear.

The properties of a self-organized state are nearly independent of the system's initial configuration (Hasegawa, 1985). Further, the long-range ordering is always accompanied by short-range disorder, which is associated with the fact that in the presence of dissipation, the ideal integrals of motion, like the magnetic energy and the magnetic helicity, are not conserved but decay at different rates. This gives a way to formulate a variational problem, where minimization of the fastest decaying quantity while treating slower decaying quantities as invariants determines a self-organized or relaxed state. In this background, the resulting lower magnetic energy state after solar transients can be viewed in connection with the relaxed states obtained using the variational method. In this regard, notable are the states obtained by Woltjer (1958) and Taylor (1974) where magnetic energy is minimized (more details in chapter 5), which directly relates to the lowering of magnetic energy during transients. Consequently, an investigation from the perspective of plasma relaxation is theoretically intriguing. Further, the abundance of solar observations and the inherent complexity of the solar magnetic field make transients a suitable testbed to explore relaxation in nature.

The release of magnetic energy during solar transients in the form of thermal and non-thermal emissions (Aschwanden, 2019) implies that a dissipative process is involved. In this regard, the general consensus is that transients are manifestations of magnetic reconnection, which changes the connectivity of magnetic field lines along with the conversion of magnetic energy into heat, bulk kinetic energy, and fast acceleration of charged particles (Li et al., 2021). Therefore, for studying relaxation in solar transients, it is imperative to understand the above-mentioned implications of reconnection in detail. Such an exploration provides insights into the underlying physics of eruptive events, which is not only of fundamental interest from the viewpoint of relaxation but also of practical significance considering the potential space-weather effects of these events. Since, the solar coronal plasma is generally approximated to be governed by the equations of MHD, the following section discusses the MHD theory of reconnection to introduce the relevant concepts.

1.2 MHD Theory of Magnetic Reconnection

In the magnetohydrodynamics description, plasma is treated as a single conducting fluid, hereafter referred to as a magnetofluid. The governing equations couple the Maxwell's equations of electromagnetism with those of hydrodynamics. The MHD description is valid at large length and time scales, i.e. when $l \gg R_i$ and $\tau \gg \Omega_i^{-1}$, where R_i and Ω_i denote the ion-gyroradius and ion-gyrofrequency (Goedbloed & Poedts, 2004).

1.2.1 MHD Equations

In a non-relativistic approximation, the standard MHD equations in MKS units are as follows

1. Conservation of momentum

$$\rho \frac{\mathrm{D}\mathbf{v}}{\mathrm{D}t} = -\nabla p + \frac{1}{\mu_0}(\nabla \times \mathbf{B}) \times \mathbf{B} - \rho \mathbf{g} \ , \tag{1.1}$$

   where $\rho \equiv$ density, $\mathrm{D}/\mathrm{D}t \equiv$ Lagrangian derivative, $\mathbf{v} \equiv$ velocity, $p \equiv$ kinetic pressure, $\mathbf{B} \equiv$ magnetic field, and $\mathbf{g} \equiv$ gravitational acceleration.

2. Conservation of mass

$$\frac{\partial \rho}{\partial t} + \nabla \cdot (\rho \mathbf{v}) = 0 \ , \tag{1.2}$$

   which for an incompressible fluid is equivalent to $\mathrm{D}\rho/\mathrm{D}t = 0$, meaning that in a frame co-moving with the magnetofluid, density is constant.

3. Magnetic induction equation

$$\frac{\partial \mathbf{B}}{\partial t} = \nabla \times (\mathbf{v} \times \mathbf{B}) + \eta \nabla^2 \mathbf{B} \ , \tag{1.3}$$

   where $\eta \equiv$ magnetic diffusivity and is assumed to be spatially constant for simplicity. The terms on the right represent the advection and diffusion of the magnetic field. An order of magnitude calculation for their ratio defines a dimensionless quantity, known as the magnetic Reynolds number, given by $R_m = V_0 L_0/\eta$, where L_0 denotes the length scale of magnetic field variability and V_0 is the typical speed of magnetofluid. Importantly, R_m measures the strength of the coupling between the magnetic field and plasma flow (Priest, 2014).

4. Energy equation

$$\frac{\mathrm{d}}{\mathrm{d}t}\left(\frac{p}{\rho^\gamma}\right) = 0 \ , \tag{1.4}$$

   where γ is the ratio of specific heats at constant pressure and volume. This equation assumes the plasma to be thermally isolated. Notably, other forms of energy equation are also possible (Priest, 2014).

The above equations constitute a set of eight nonlinear partial differential equations in the variables $\mathbf{v}(\mathbf{r},t)$, $\mathbf{B}(\mathbf{r},t)$, $\rho(\mathbf{r},t)$, and $p(\mathbf{r},t)$. In MHD, these are the primary variables, while $\mathbf{E}$ and $\mathbf{J}$ are secondary variables, determined from the following

1. Ampere's Law

$$\nabla \times \mathbf{B} = \mu_0 \mathbf{J} \ , \tag{1.5}$$

where $\mu_0 \equiv$ permeability of vacuum.

2. Ohm's Law

$$\mathbf{E} + \mathbf{v} \times \mathbf{B} = \sigma^{-1}\mathbf{J} \ . \tag{1.6}$$

where $\sigma \equiv$ electrical conductivity.

In addition, the solenoidality of the magnetic field ($\nabla \cdot \mathbf{B} = 0$) serves as a condition on the initial values, which, once satisfied, remains so for all times. In the following, two important limits of MHD, namely the ideal and resistive MHD are discussed, which will serve to lay down the background for discussing magnetic reconnection.

1.2.2 Background For Magnetic Reconnection

For an almost perfectly conducting fluid such as the solar corona (Aschwanden, 2005), the typical values $L_0 \simeq 10^6$ m, $V_0 \simeq 10^4\,\mathrm{m\,s^{-1}}$, and $\eta \simeq 1\,\mathrm{m^2\,s^{-1}}$ (Priest & Forbes, 2000; Priest, 2014) give $R_m = 10^{10} \gg 1$, which implies that the advection dominates over diffusion, also known as the ideal MHD limit. In ideal MHD, the magnetic flux remains conserved, also known as the Alfvén's flux-freezing theorem (Alfvén, 1942). This further leads to the magnetic field line conservation, meaning that the connectivity of plasma parcels with respect to the magnetic field lines is preserved. A way to envisage this is to write equation 1.3 in the ideal MHD limit and expand $\nabla \times (\mathbf{v} \times \mathbf{B})$, which gives

$$\frac{\partial \mathbf{B}}{\partial t} + (\mathbf{v} \cdot \nabla)\mathbf{B} = (\mathbf{B} \cdot \nabla)\mathbf{v} - \mathbf{B}(\nabla \cdot \mathbf{v}) \ , \tag{1.7}$$

where $\nabla \cdot \mathbf{B} = 0$. Then, using equation 1.2

$$\frac{\mathrm{D}}{\mathrm{D}t}\left(\frac{\mathbf{B}}{\rho}\right) = \left(\frac{\mathbf{B}}{\rho} \cdot \nabla\right)\mathbf{v} \ . \tag{1.8}$$

Further, for an infinitesimal length element $\mathrm{d}\mathbf{l}$ along any magnetic field line, the condition $\mathrm{d}\mathbf{l} \times \mathbf{B} = 0$ holds true, which leads to

$$\frac{\mathrm{D}}{\mathrm{D}t}\left(\mathrm{d}\mathbf{l} \times \frac{\mathbf{B}}{\rho}\right) = \frac{\mathrm{D}}{\mathrm{D}t}\mathrm{d}\mathbf{l} \times \left(\frac{\mathbf{B}}{\rho}\right) + \mathrm{d}\mathbf{l} \times \frac{\mathrm{D}}{\mathrm{D}t}\left(\frac{\mathbf{B}}{\rho}\right) = 0 \ . \tag{1.9}$$

Using equation 1.8 and vector algebraic manipulations

$$\left[\frac{\mathrm{D}}{\mathrm{D}t}\mathrm{d}\mathbf{l} - (\mathrm{d}\mathbf{l} \cdot \nabla)\mathbf{v}\right] \times \frac{\mathbf{B}}{\rho} = 0 \ , \tag{1.10}$$

which is true for any arbitrary displacement, if

$$\frac{\mathrm{D}}{\mathrm{D}t}\mathrm{d}\mathbf{l} - (\mathrm{d}\mathbf{l} \cdot \nabla)\mathbf{v} = 0 \ . \tag{1.11}$$

Since, the structure of equations 1.8 and 1.11 is identical, it follows that if $\mathrm{d}\mathbf{l}$ and $\mathbf{B}/\rho$ are initially parallel, they remain so for all subsequent times. In other words, the magnetofluid evolution is such that the plasma parcels remain stuck with the magnetic field lines and vice versa, as realized in figure 1.3.

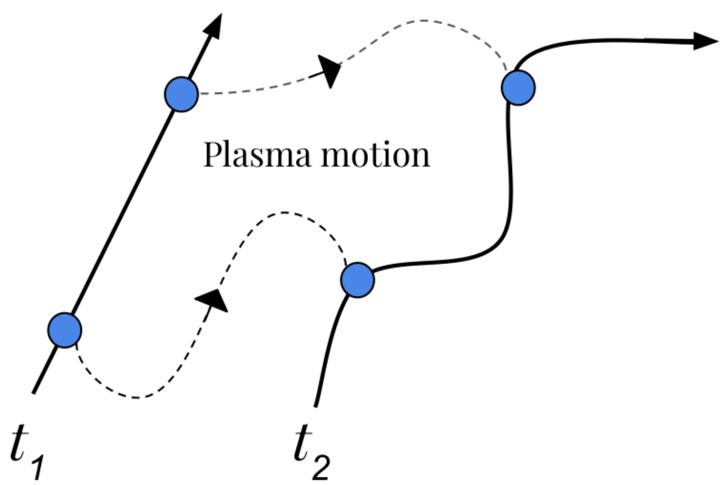

Figure 1.3: A schematic representation of magnetic field line conservation. The plasma parcels on magnetic field line at time t_1 will remain on the same magnetic field line at time t_2. The *blue* circles and the *solid black* arrows represent plasma parcels and magnetic field lines, respectively.

The resistive MHD limit is typically characterized by $R_m \lesssim 1$, which implies that diffusion dominates over advection. Notably, this can occur at small length scales in the system. An order of magnitude estimate of the diffusion term gives the time scale (τ_D) of magnetic field diffusion as $\tau_D = L_0^2/\eta$, which is equal to nearly 3×10^4 years for $L_0 \simeq 10^6$ m in the solar corona. This is to be expected because at large length scales, advection dominates diffusion. However, using a typical time scale of transients (say $\tau_D = 5$ minutes), the length scale $L_0 \simeq 20$ m, indicating that the occurrence of solar transients is associated with small length scales and hence the resistive MHD limit. In effect, both the limits are important for the occurrence of solar transients. The advection of magnetic field lines at large-scales results in the generation of small-scales. Consequently, the diffusion of field lines sets the stage for magnetic reconnection and hence, solar transients.

Further, from Ampere's law, it is apparent that $\mathcal{O}(\mathbf{J}) \propto L_0^{-1}$, suggesting that small-scales are characterized by an enhancement of current density. Therefore, the ohmic heating, given by $\sigma^{-1}|\mathbf{J}|^2$ is non-negligible, which plays an important role in converting some of the magnetic energy to heat during reconnection (Priest, 2016; Zweibel & Yamada, 2016). In resistive MHD limit, the conservation of magnetic flux breaks down. Further, the connectivity between plasma parcels and magnetic field lines can change, which forms the basis of magnetic reconnection (Schindler et al., 1988; Hesse & Schindler, 1988; Birn & Priest, 2007), as discussed in the next section.

1.2.3 Concepts of Magnetic Reconnection

The notion of magnetic reconnection originated during the mid-twentieth in the attempts to find a mechanism that explains the observed particle acceleration during flares and the structure of the magnetosphere (Giovanelli, 1946; Hoyle, 1949; Dungey, 1953, 1961). Since then, there has been much progress in reconnection research regarding its definition, conditions for occurrence, type of reconnection, preferential magnetic configurations associated with an enhancement of current density at small length scales, and conversion of magnetic energy to other forms (Yamada et al., 2010; Zweibel & Yamada, 2016; Hesse & Cassak, 2020; Li et al., 2021; Pontin & Priest, 2022).

The theory of general magnetic reconnection (GMR), proposed in the landmark paper by Schindler et al. (1988), defines a change in the connectivity of plasma parcels with the magnetic field lines due to a localized (at small length scales) breakdown of flux-freezing condition as reconnection. In other words, the connection between plasma parcels and field lines in the sense of magnetic field line conservation breaks down, as illustrated in figure 1.4. The plasma parcels A and B are considered to be connected to the same magnetic field line l at time t_1. If the magnetic field line l passes through a localized diffusion region at time t_2, the connectivity changes such that at time instant t_3, A and B are attached to magnetic field lines l_1 and l_2, respectively.

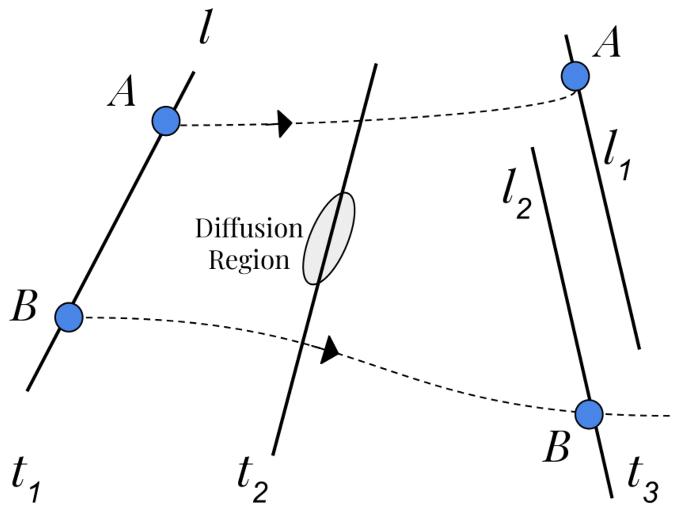

Figure 1.4: A schematic representation of change in connection of plasma parcels with respect to magnetic field lines. The magnetic field line l connected to plasma parcels A and B passes through a localized diffusion region, which changes the connectivity of A to l_1 and that of B to l_2, respectively.

Notably, the definition is independent of any particular magnetic topology, making it more general compared to earlier definitions by Vasyliunas (1975) and Sonnerup et al. (1984) that require an identification of topologies such as separatrices and separators, which may not always exist, or their identification might be non-trivial (Schindler et al., 1988; Birn et al., 1997). The definition proposed in the theory of

GMR is extremely helpful because a visualization of the changes in the connectivity of magnetic field lines serves as an indicator of magnetic reconnection. As a result, the works presented in this thesis identify the sudden changes in the connectivity of magnetic field lines to determine the occurrence of magnetic reconnection.

In GMR theory (Schindler et al., 1988; Hesse & Schindler, 1988), the condition for the breaking of magnetic connection between the plasma parcels and field lines is given by $\mathbf{B} \times (\nabla \times \mathbf{N}) = 0$ in the localized diffusion region, where $\mathbf{N}$ corresponds to any form of nonidealness or deviation from the ideal Ohms's law. In the case of resistive MHD, $\mathbf{N} = \sigma^{-1}\mathbf{J}$ or equivalently $\mathbf{E} + \mathbf{v} \times \mathbf{B} = \sigma^{-1}\mathbf{J}$, but other forms of $\mathbf{N}$, such as due to pressure tensor and Hall term may also be relevant (Schindler et al., 1988; Birn & Priest, 2007; Khomenko, 2020), particularly at small length scales. Nevertheless, resistive MHD suffices to capture the essence of reconnection process and model the large-scale macroscopic properties (Priest, 2014).

Further, GMR theory classifies reconnection into two broad categories, namely the (a) Zero-B and (b) Finite-B reconnection, depending on whether the magnetic field vanishes ($\mathbf{B} = 0$) at some point inside D_{R} or remains nonzero ($\mathbf{B} \neq 0$) in D_{R}, where D_{R} denotes the localized diffusion region. In Finite-B, there exist two cases, namely (a) local and (b) global, where local means that the plasma parcel changes its connectivity while passing through D_{R}, and global means that the plasma parcel changes its connectivity but always remains outside the diffusion region D_{R} during reconnection. Notably, figure 1.4 depicts global reconnection. In the GMR theory, if the integral $\int \mathbf{E}_{||}\mathrm{d}s \neq 0$, reconnection is global, otherwise it is local (Hesse & Schindler, 1988), where $\mathbf{E}_{||}$ is the electric field component parallel to the magnetic field line, $\mathrm{d}s$ is an infinitesimal length element along the field line, and the integral is carried out over D_{R}. The formal developments of GMR theory and the progress in understanding three-dimensional (3D) reconnection have established $\int \mathbf{E}_{||}\mathrm{d}s \neq 0$ over D_{R} as the necessary and sufficient condition for 3D reconnection (Priest, 2014; Pontin & Priest, 2022). It is worth mentioning that the notion of zero-B is relevant for only two-dimensional (2D) models of reconnection (Büchner, 1999) because in such a scenario, $\mathbf{E} \cdot \mathbf{B} = 0$ and hence, $\mathbf{E}_{||} = 0$, making the above described integral constraint inapplicable. Importantly, the process of magnetic reconnection in 2D and 3D are different in terms of preferential sites where localized diffusion regions occur and how field lines change connectivity. In the following, these aspects are discussed in the light of MHD theory and general magnetic reconnection. Further, the discussion naturally elaborates on the meaning of separatrices and separators mentioned earlier in the context of defining magnetic reconnection.

1.2.4 Two-Dimensional (2D) Magnetic Reconnection

In two-dimensions, reconnection occurs at a X-type magnetic null point or X-point. A magnetic null point is the location where magnetic field vanishes or $\mathbf{B} = 0$. The X-point has a hyperbolic magnetic field configuration, such as $\mathbf{B}_x = y$ and $\mathbf{B}_y = x$. The corresponding magnetic field lines can be obtained by integrating $\mathrm{d}\mathbf{l} \times \mathbf{B} = 0$, giving $y^2 - x^2 =$ constant, which represents a rectangular hyperbola (Priest & Forbes, 2000). The X-point geometry is shown in figure 1.5, where the *solid black*

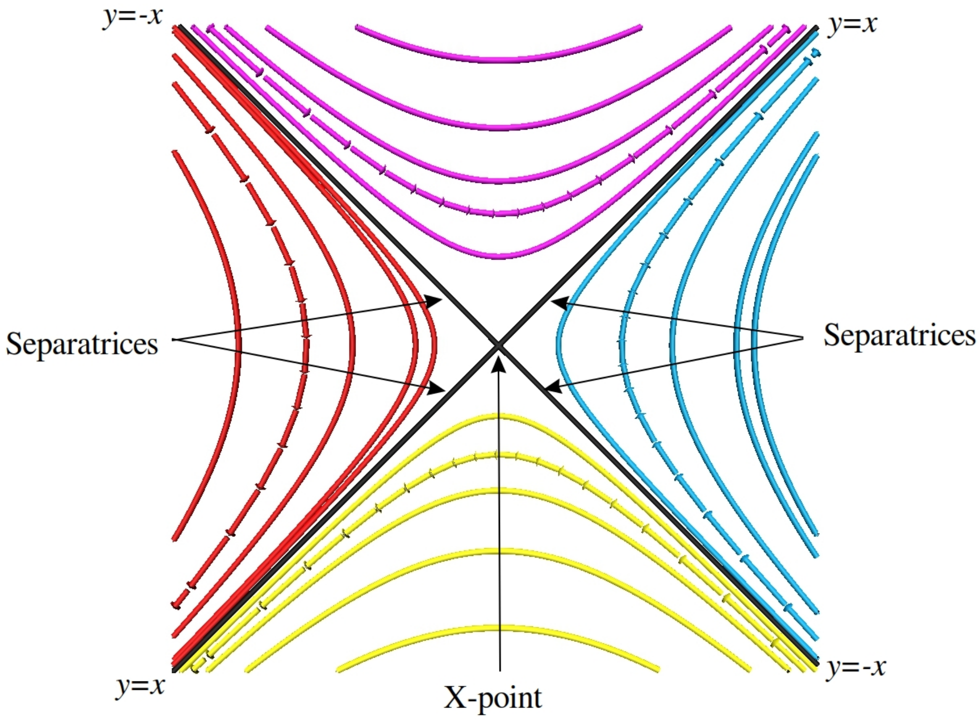

Figure 1.5: A schematic representation of X-type null point in hyperbolic magnetic configuration, constituted by the *blue*, *pink*, *red*, and *yellow* color magnetic field lines (MFLs). The *solid black* lines are asymptotes of hyperbola and are known as separatrices. The MFLs with arrows denote the direction of magnetic field lines in that connectivity domain.

lines are asymptotes ($y = \pm x$) of the hyperbola. These asymptotes are known as separatrix curves or separatrices for X-point geometry. In general, separatrices exist between topologically distinct connectivity domains or equivalently, when the mapping of magnetic field lines (MFLs) has a discontinuity (Priest & Forbes, 2000; Priest, 2014). In figure 1.5, each set of MFLs in the *blue*, *pink*, *red*, and *yellow* colors represents a connectivity domain because, in any given domain, all the field lines share a common source and sink (Pariat, 2020).

Notably, in the above example, $\mathbf{J} = 0$, giving Lorentz force $\mathbf{J} \times \mathbf{B} = 0$, which implies that the configuration is in equilibrium. However, there can be situations where $\mathbf{J} \neq 0$ and $\mathbf{J} \times \mathbf{B} \neq 0$, such as for $\mathbf{B}_x = y$ and $\mathbf{B}_y = 2x$, giving $\mathbf{J} = \hat{k}$ and $\mathbf{J} \times \mathbf{B} = -2x\hat{i} + y\hat{j}$. This implies that there exists a finite electric field perpendicular to the plane and that the X-point geometry is not in equilibrium. As a result, the X-point collapses to form a current sheet (Priest & Forbes, 2000), defined as the singular current layer along a surface across which there is a jump in the tangential component of the magnetic field (Priest & Forbes, 2000; Pontin & Hornig, 2020). In the context of current sheet formation, it is worthwhile mentioning that according to the Parker's magnetostatic theorem (Parker, 1994), current sheets can develop spontaneously when equilibrium magnetic fields are subjected to an arbitrary small perturbation, such as by boundary motion (e.g., photospheric driving). Therefore, there is a possibility of steep magnetic field gradient between topologically distinct domains, making separatrices favorable sites for current sheet formation (Lapenta et al., 2015; Pariat, 2020). Importantly, the current sheet serves the role of a localized diffusion region, which is necessary for reconnection.

The X-point gained importance as a reconnection site when Giovanelli (1946) and Hoyle (1949) suggested that particle acceleration and heating can occur at the X-point. Further, Dungey (1953) suggested that field lines can break and rejoin inside the current sheet, leading to the standard picture of magnetic reconnection at the X-point discussed below.

1.2.4.1 Magnetic Reconnection at X-type Null Point

The process of magnetic reconnection at the X-point can be understood from the previous example of $\mathbf{B}_x = y$ and $\mathbf{B}_y = 2x$. The corresponding X-point geometry is shown in figure 1.6. Since, $(\mathbf{J} \times \mathbf{B})_x = -2x\hat{i}$, an inward flow along the x-direction will bring the *red* and *blue* MFLs toward the X-point, as shown in panel (a) for field lines AB and CD, respectively. Consequently, a current sheet is formed and a part of these MFLs gets dragged into it. The part inside the current sheet diffuses out of the plasma parcels because its velocity differs from the rest of the magnetic field line lying outside the diffusion region. On reaching the X-point, the field lines AB and CD break, and the broken segment of each field line rejoins perfectly with that of other field line (Priest et al., 2003) to form new field lines AC and BD, as shown in panel (b) with *pink* and *yellow* colors. Subsequently,

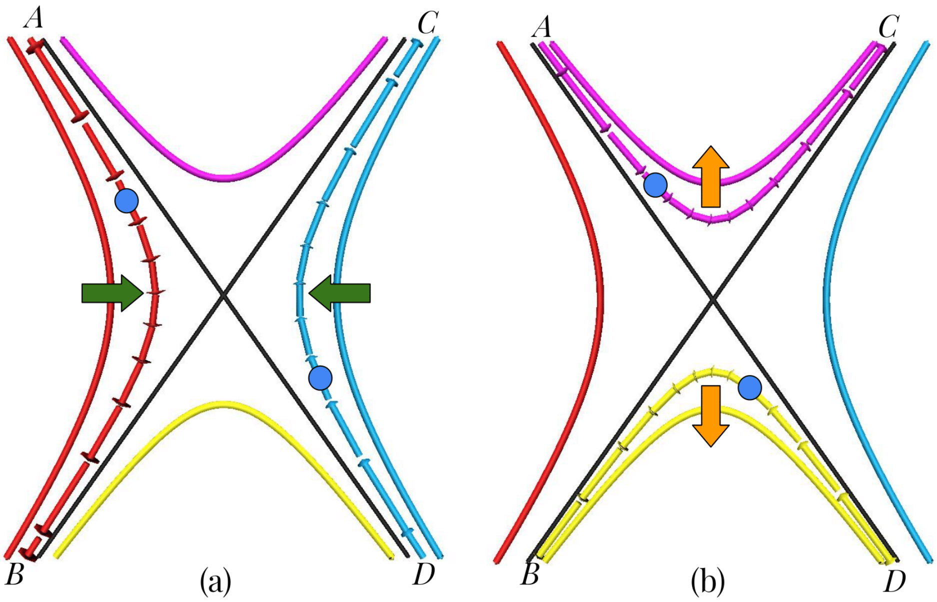

Figure 1.6: A schematic representation of reconnection at the X-type null point. Panels (a) and (b) show the magnetic configuration before and after reconnection. The *green* and *orange* arrows depict the direction of inward and outward flow. The circles in *blue* color represent plasma parcels. The *black* lines are the separatrices. In panel (a), field lines AB and CD, shown in *red* and *blue* color along with the direction of magnetic field, move toward the X-point. Similarly, panel (b) shows field lines AC and BD moving away from the X-point in *pink* and *yellow* colors.

the new MFLs are carried away from the X-point by an outward flow along the y-direction due to $(\mathbf{J} \times \mathbf{B})_y = y\hat{j}$. As a result, the plasma parcels, attached initially to AB and CD, move across the separatrices and get connected to AC and BD, respectively. Notably, the flow of plasma across separatrices was considered by Vasyliunas (1975) as the definition of reconnection. Further, since the magnetic field vanishes inside the current sheet at X-point, the reconnection at X-point is classified as zero-B. The above picture of reconnection at the X-point is only qualitative. The first quantitative model of 2D reconnection was given by Sweet (1958) and Parker (1957), popularly known as the Sweet-Parker model, which is discussed in the following.

1.2.4.2 The Sweet-Parker Model

The Sweet-Parker model is a steady state reconnection model, where the plasma is assumed to be incompressible and pressure gradient force is neglected. The model considers a current sheet of length $2L$ and width $2l$ between oppositely directed magnetic field lines, as shown in figure 1.7. The *blue* and *red* MFLs are pushed

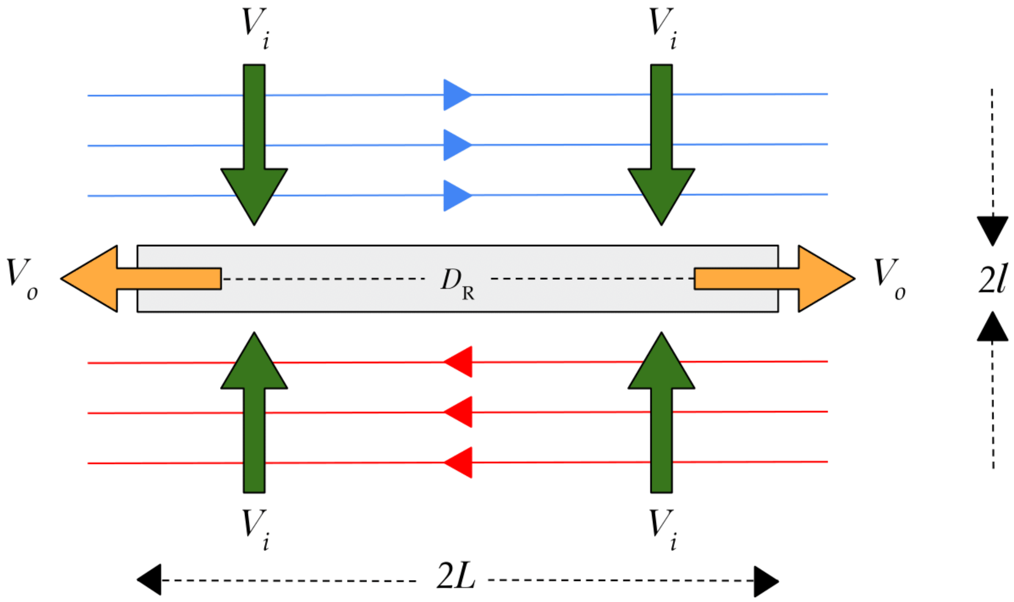

Figure 1.7: Sweet-Parker reconnection. The *grey* box shows the current sheet or the diffusion region D_R. The *blue* and *red* arrows show direction of magnetic field lines. The *green* and *orange* arrows depict direction of plasma inflow and outflow.

toward the diffusion region D_R with a speed V_i and after reconnection, they exit with speed V_o. Then, the problem statement is to estimate V_i and V_o, which is done using an order of magnitude analysis of the MHD equations. In the steady state, $\partial_t \mathbf{v} = \partial_t \rho = \partial_t \mathbf{B} = 0$ and under the assumption of incompressibility, equation 1.2 for mass conservation gives $\mathbf{v} \cdot \nabla \rho = 0$, implying uniform density. Then, since the rate at which mass enters and leaves D_R should be same, it implies that

$$2 \times (2L \times \rho \times V_i) = 2 \times (2l \times \rho \times V_o) \Rightarrow LV_i = lV_0 \ . \tag{1.12}$$

Subsequently, from magnetic induction equation, $\nabla \times (\mathbf{v} \times \mathbf{B}) = -\eta \nabla^2 \mathbf{B}$, which means that the diffusion is balanced by advection, giving

$$V_i B_i / l = \eta B_i / l^2 \Rightarrow V_i = \eta / l \ , \tag{1.13}$$

where B_i is the strength of the magnetic field entering D_{R}. Further, equation 1.1 for conservation of momentum becomes $\rho(\mathbf{v}\cdot\nabla)\mathbf{v} = \mathbf{J}\times\mathbf{B}$, giving

$$\rho V_0^2/L = B_i B_o/\mu_0 l \ , \tag{1.14}$$

where B_o is the strength of the magnetic field leaving D_{R}. Finally, $\nabla\cdot\mathbf{B} = 0$ implies that $B_i/L = B_o/l$, which gives V_0 from equation 1.14 as

$$V_0 = \frac{B_i}{\sqrt{\mu_0\rho}} = V_A \ , \tag{1.15}$$

where V_A is the Alfvén speed. Also, using equations 1.12 and 1.13, V_i is obtained as

$$V_i = \frac{V_A}{\sqrt{S}} \ , \tag{1.16}$$

where $S = LV_A/\eta$ is the Lundquist number (Priest, 2014). An important result of the Sweet-Parker model is the dimensionless reconnection rate, given by

$$M_i = \frac{V_i}{V_A} = \frac{1}{\sqrt{S}} \ , \tag{1.17}$$

where M_i is also known as the inflow Alfvén Mach number (Priest & Forbes, 2000). In solar corona, $L \simeq 10^6$ m, $V_A = 10^6\,\mathrm{m\,s^{-1}}$, and $\eta \simeq 1\,\mathrm{m^2\,s^{-1}}$, giving $M_i \simeq 10^{-6}$, which is way too small to explain the observed time scale of solar flares. Therefore, theories for fast reconnection emerged, such as the Petschek mechanism (Petschek, 1964), inclusion of the Hall effect (Bhattacharjee et al., 2003; Bora et al., 2021), and role of turbulence (Lazarian et al., 2012), but fast reconnection remains an active area of research.

The concepts of two-dimensional reconnection are invaluable, but the realistic magnetic geometries are inherently three-dimensional. Therefore, it is imperative to understand the 3D reconnection, which is the subject matter of the next section. The discussion is tailored according to the works carried out in this thesis.

1.2.5 Three-Dimensional (3D) Magnetic Reconnection

In three-dimensions, reconnection can occur at 3D null point ($\mathbf{B} = 0$) configuration and also at magnetic geometries where $\mathbf{B} \neq 0$, namely the quasi-separatrix layer

(QSL) and hyperbolic flux tube (HFT). Importantly, unlike the X-type null point, where change of connection occurs only when field lines reconnect at the X-point, 3D reconnection occurs in the whole diffusion region D_{R} and magnetic field lines change their connectivity continuously as long as they are passing through D_{R}. The localization of D_{R} around the above-mentioned 3D magnetic features satisfies $\mathbf{E}\cdot\mathbf{B}\neq 0$, implying that the three-dimensional reconnection is finite-B type even though $\mathbf{E}\cdot\mathbf{B}=0$ at the null point itself (Priest et al., 2003; Priest, 2014; Pontin & Priest, 2022). In particular, when a magnetic field line AB enters D_{R}, it splits into two field lines, both of which flip, as illustrated in figure 1.8. Before entering

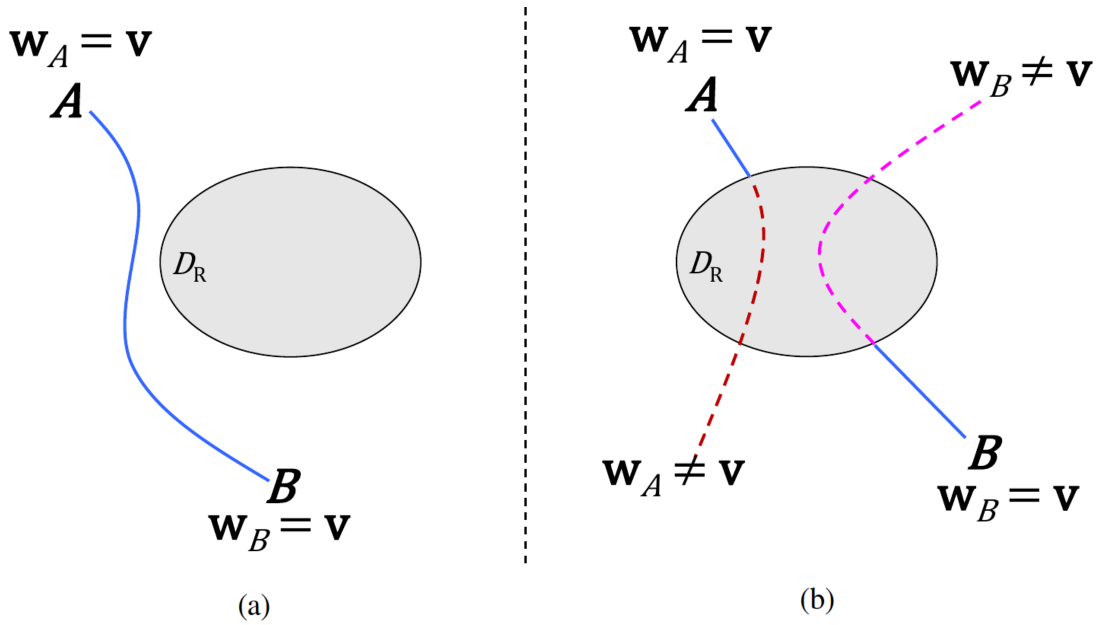

Figure 1.8: Schematic of magnetic flipping (a) The magnetic field line AB (*blue*) before entering into the diffusion region D_{R} (*grey*) (b) The splitting of AB after entering into D_{R}. The *red* and *pink* color *dashed* lines represent the segments of new field lines. On the side containing footpoints A or B, the velocity of field lines $\mathbf{w}_A=\mathbf{w}_B=\mathbf{v}$ (local plasma velocity), while inside D_{R} and outside of D_{R} on the other side, $\mathbf{w}_A\neq\mathbf{v}$ and $\mathbf{w}_B\neq\mathbf{v}$.

the diffusion region, both footpoints move with the local plasma velocity $\mathbf{v}$, as shown in the first panel. However, after entering into D_{R}, the field line AB splits into two field lines. The segment of each field line lying outside D_{R} on the side of A and B moves with velocity $\mathbf{v}$ but the remaining segments of each field line (both inside D_{R} and outside of D_{R} on the other side) do not move with plasma velocity, as depicted in the second panel. This is known as magnetic flipping (Priest et al., 2003) and was first proposed by Priest & Forbes (1992) as a mechanism of reconnection in the absence of magnetic null points. Further, flipping is referred to as slipping or slip-running reconnection (Aulanier et al., 2006; Pariat et al., 2006), particularly in the context of eruptive events on the Sun (Schmieder et al., 2009; Pontin et al., 2013; Dudík et al., 2016). Importantly, slip-running reconnection is a common feature of 3D reconnection and manifests at all the magnetic geometries, i.e., null points, QSL, and HFT. In view of $\mathbf{w}_A \neq \mathbf{v}$ as characteristic of flipping, the directions of plasma flow and footpoint movement of field lines are compared to identify slip-running reconnection in the works presented in this thesis. In the following, the details of magnetic configuration pertaining to 3D null points, QSL, and HFT are discussed.

1.2.5.1 3D Null Point

The simplest magnetic configuration of a 3D null point is $\mathbf{B}_x = \pm x$, $\mathbf{B}_y = \pm y$, and $\mathbf{B}_z = \mp 2z$, where the null point ($\mathbf{B} = 0$) is situated at the origin. Its field lines are depicted in figure 1.9 and are given by the intersection of $y = C_1 x$ and $z = C_2 x^2$ surfaces, where C_1, C_2 are constants. A linear analysis of the magnetic structure around a 3D null (Parnell et al., 1996) identifies a fan surface and spine in the geometry constituted by the field lines. Also, there are two distinct connectivity domains, each having its own spine and fan surface. These domains are separated by a separatrix surface, across which the mapping of field lines is discontinuous. In figure 1.9, the two connectivity domains are shown by the set of *red* and *yellow* MFLs, lying above and below the $z = 0$ plane.

In the above example, spine is along the z-direction and the fan surface is along the xy-plane at $z = 0$. Further, from $\mathbf{B}_z = \mp 2z$, it is seen that the spine field lines can either be directed toward null point or away from it, which leads to the notion of positive or negative null point, respectively (Pontin & Priest, 2022). In the near vicinity of null point, spine spreads to form a two-dimensional surface of field lines, namely the fan surface. The direction of field lines in the fan surface is governed by the components $\mathbf{B}_x = \pm x$ and $\mathbf{B}_y = \pm y$, respectively. Notably, a 3D null is not the generalization of X-type null because it has only two connectivity domains, as compared to four in the X-type (Pariat, 2020).

In solar corona, a common 3D null point configuration is the one with separatrix

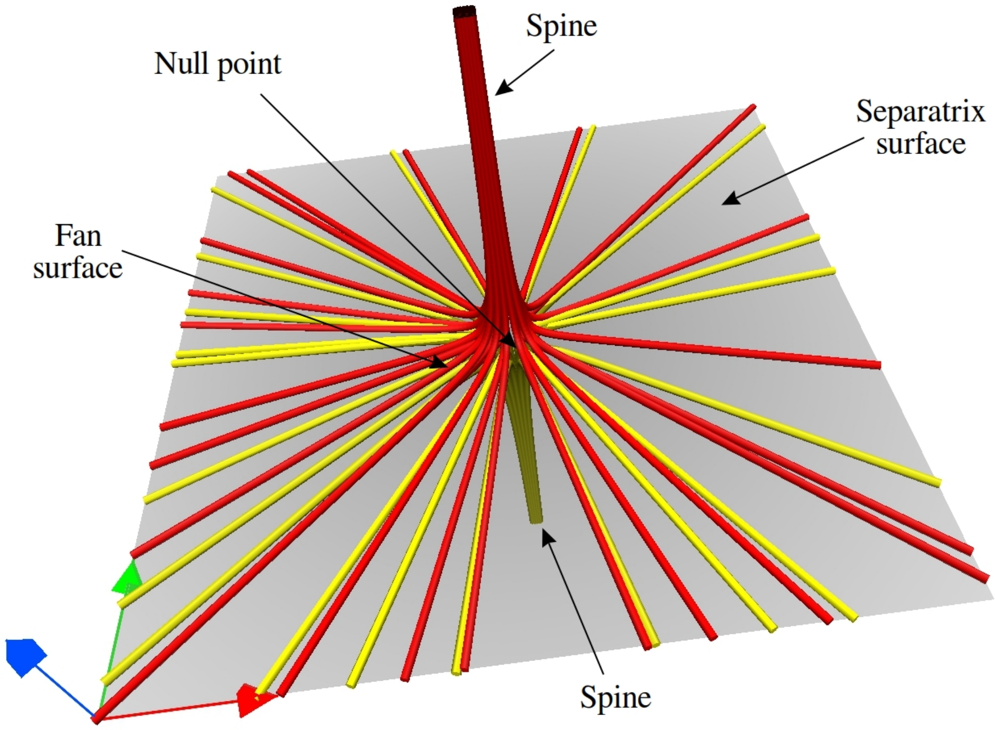

Figure 1.9: Magnetic configuration of a 3D null point. The set of *red* and *yellow* magnetic field lines represent two separate connectivity domains, each with its own spine and fan surface. The *grey* plane depicts the separatrix surface, and the *red*, *green*, and *blue* arrows denote the x-, y-, and z-directions.

dome in which the fan surface closes down on the photosphere (Priest, 2014; Pontin & Priest, 2022), as shown in figure 1.10. In general, this kind of geometry manifests when a magnetic polarity is surrounded by an opposite polarity (Mason et al., 2019) and are often associated with circular ribbon flares (Sun et al., 2013; Prasad et al., 2018; Joshi et al., 2021).

In 3D, an intersection of two separatrix surfaces results in a one-dimensional topological structure, namely the separator (Maurya et al., 2024). It may occur when the fan surfaces of two null points intersect, in which case, the separator joins one null point to another (Priest, 2014). Interestingly, if the X-point geometry is extended along the direction perpendicular to plane of X-point while maintaining invariance, the X-point transforms into the X-line. The obtained magnetic geometry is called 2.5-dimensional and the X-line denotes a separator (Birn & Priest, 2007). Notably, presence of an electric field along the separator was considered by Sonnerup et al. (1984) as a necessary condition for reconnection.

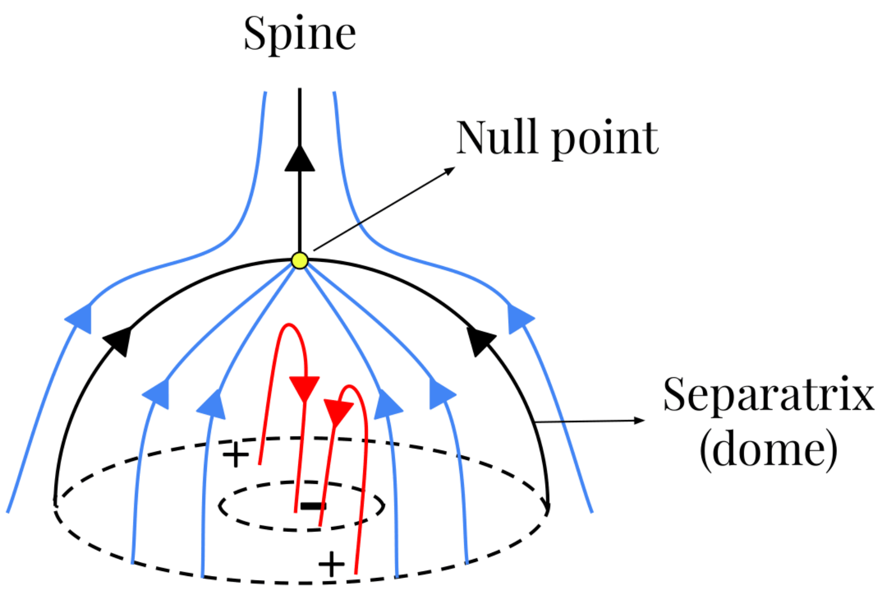

Figure 1.10: Magnetic configuration of 3D null point having separatrix dome. The *yellow* circle represents null point location. The + and − symbols represent positive and negative magnetic polarities. The field lines in *red* are inside the dome and closed, while those in *blue* are outside the dome and point upward.

1.2.5.2 QSL and HFT

The mapping of magnetic field lines is discontinuous across the separatrix surface in 3D nulls, as described earlier. However, in QSL and HFT, the stringent condition of discontinuity is weakened to very strong gradients in magnetic field line mapping such that it remains continuous (Priest, 2014; Pariat, 2020; Pontin & Priest, 2022). The concept of QSL was first introduced by Demoulin et al. (1996) and later, the formal definition was given by Titov et al. (2002) and further developed in Titov (2007) using a mathematical description of field line mapping. Further, Titov et al. (2002) showed that in a quadrupolar magnetic geometry, two QSLs can intersect to form a HFT. Importantly, magnetic flipping in QSL is believed to account for the observed displacement of EUV and SXR brightenings in the chromosphere and transition region (Démoulin, 2006; Pariat et al., 2006; Aulanier et al., 2006, 2011). In the following, important aspects and results of the formalism given by Titov et al. (2002) are discussed to arrive at the configuration of QSL and HFT.

Consider a positive (+) and negative (−) polarity on the photosphere, located at $\mathbf{r}_p\,(x_+, y_+)$ and $\mathbf{r}_n\,(x_-, y_-)$, respectively. The mapping of field line connecting these polarities is defined from $\mathbf{r}_p$ to $\mathbf{r}_n$, given by $X_-(\mathbf{r}_p) = x_-$ and $Y_-(\mathbf{r}_p) = y_-$, leading to a Jacobian matrix of the differential elements as

$$D = \begin{bmatrix} \partial X_-/\partial x_+ & \partial X_-/\partial y_+ \\ \partial Y_-/\partial x_+ & \partial Y_-/\partial y_+ \end{bmatrix} \equiv \begin{bmatrix} a & b \\ c & d \end{bmatrix}, \tag{1.18}$$

which describes the mapping locally. The geometrical implication of D is seen by mapping an orthonormal vector basis $(\hat{A}_+, \hat{B}_+)$, located in the region of positive polarity. The result is a non-orthonormal basis in general, given by $\vec{A}_- = D\hat{A}_+ = \lambda_1\hat{A}_-$ and $\vec{B}_- = D\hat{B}_+ = \lambda_2\hat{B}_-$, where $\lambda_1 = |\vec{A}_-|$ and $\lambda_2 = |\vec{B}_-|$, respectively. The ratio λ_1/λ_2 uniquely characterizes the mapping and is given by

$$\frac{\lambda_1}{\lambda_2} = \frac{Q}{2} + \sqrt{\frac{Q^2}{4} - 1}\,, \tag{1.19}$$

where $Q = (\lambda_1^2 + \lambda_2^2)/\lambda_1\lambda_2$ is equal to the ratio of diagonal length squared and area of the rectangle spanned by $\vec{A}_-$ and $\vec{B}_-$ vectors. The rectangle is shown in figure 1.11, comprised of *green* and *cyan* color regions. Notably, from equation 1.19, it

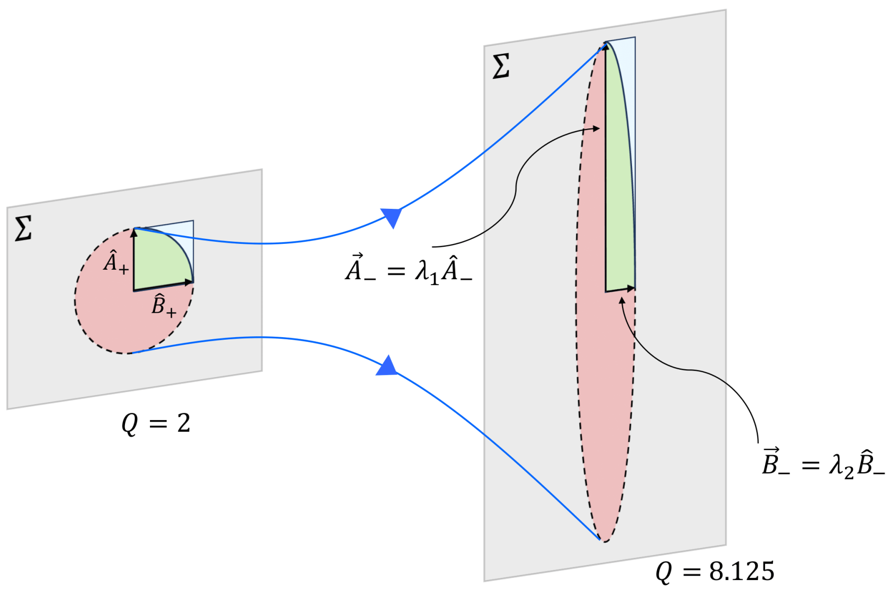

Figure 1.11: Schematic of magnetic connectivity. The field lines in *blue* connect the region of positive to negative polarity. The *black* arrows represent the vector basis $(\hat{A}_+, \hat{B}_+)$ and $(\vec{A}_-, \vec{B}_-)$ in these two regions. The polygons in *red*, *green*, and *cyan* together constitute the circle, ellipse, and rectangle spanned by the vector basis. The Σ plane represents the photosphere (see text for more details).

is seen that $\lambda_1/\lambda_2 \simeq Q$ for $Q \gg 1$, which suggests that the Q value measures the extent of gradient in magnetic field line mapping.

For example, the footpoints of *blue* MFLs at the diametric ends of the circle in figure 1.11 are 2 units apart, where $1\,\text{unit} = |\hat{A}| = |\hat{B}|$. The field lines get mapped to an ellipse, which changes the separation between footpoints to nearly 8 units. In the circle, $\lambda_1 = \lambda_2 = 1$ unit, giving $Q = 2$, while in the ellipse, $\lambda_1 = 4$ units, $\lambda_2 = 0.5$ units, which gives $Q = 8.125$. The circle gets squashed to an ellipse, hence Q is also called the squashing degree. Importantly, if a flux tube is envisaged between the circle and ellipse, the resulting layer-like flux tube is called a QSL when $Q \gg 2$ (Titov et al., 2002; Pontin & Priest, 2022). In the limit of $Q \to \infty$, the extent of squashing is such that the ellipse becomes a separatrix and in 3D, a separatrix surface, which is the regime of discontinuity in mapping. Using conservation of magnetic flux in a flux tube, it is readily seen that $\lambda_1\lambda_2 = B_{n,+}/B_{n,-}$, where $B_{n,+}$ and $B_{n,-}$ are the vertical components of magnetic field at the positive and negative polarity. Further, the elements of D matrix are related to λ_1 and λ_2 as $\lambda_1^2 + \lambda_2^2 = a^2 + b^2 + c^2 + d^2$, which results in

$$Q = \frac{a^2 + b^2 + c^2 + d^2}{B_{n,+}/B_{n,-}} \ , \tag{1.20}$$

which is used to estimate the squashing degree and typically, $Q \simeq 10^4 - 10^8$ (Titov et al., 2002; Aulanier et al., 2006; Liu et al., 2016b).

In the above, a region of positive polarity (circle) is mapped to another region of negative polarity (ellipse), defining a QSL. In more complex configurations, such as the quadrupolar geometry constituted by two bipolar groups of sunspots, there can be two intersecting QSL, which results in a hyperbolic flux tube. A HFT consists of four quasi-connectivity domains (Aulanier et al., 2006; Zhao et al., 2014), which are separated by a X-type cross section in the middle, as depicted in figure 1.12. This X-type region is favorable for the development of large current density and, hence, reconnection.

As mentioned earlier, the magnetic energy is converted to other forms during reconnection. It is then instructive to consider the temporal evolution of magnetic energy, as discussed in the following section.

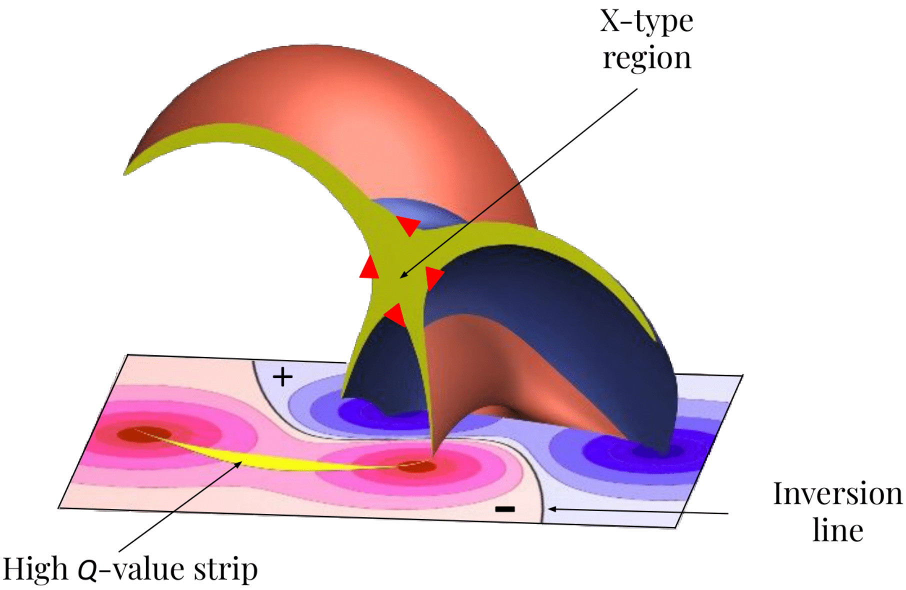

Figure 1.12: Schematic representation of a hyperbolic flux tube (HFT), showing its cross-section. The + and − symbols denote regions of positive (*blue*) and negative (*pink*) polarities at the photosphere, separated by the inversion line. The *yellow* strip corresponds to very high Q value, and *red* arrows depict the direction of magnetic field lines in the HFT (adapted from Titov et al., 2002).

1.2.6 Temporal Evolution of Magnetic Energy

In the framework of resistive MHD, the rate of change in the volume integrated magnetic energy W_{m} is given by (Yeates, 2020)

$$\frac{\mathrm{d}W_{\mathrm{m}}}{\mathrm{d}t} = -\int_V \mathbf{v}\cdot(\mathbf{J}\times\mathbf{B})\,\mathrm{d}^3x - \eta\int_V |\mathbf{J}|^2\,\mathrm{d}^3x - \frac{1}{\mu_0}\oint_S (\mathbf{E}\times\mathbf{B})\cdot\hat{n}\mathrm{d}^2x\ , \qquad (1.21)$$

where V is the volume of integration, S is the surface area bounded by V, and $\hat{n}$ denotes the direction of an infinitesimal area vector. The first term corresponds to the work done by the Lorentz force, which can increase or decrease W_{m}. The result is a conversion of magnetic energy to kinetic energy or vice-versa. The second term always decreases W_{m} by ohmic dissipation and the energy is irrecoverably lost from the system as heat. The third term represents Poynting flux, which is the amount of energy transported across the volume V per unit time. The energy either enters or leaves the volume, which depends on the direction of Poynting vector $\mathbf{S} = \mathbf{E}\times\mathbf{B}$. Interestingly, if only the ideal contribution of $\mathbf{E} + \mathbf{v}\times\mathbf{B} = \eta\mathbf{J}$ is considered, then

$\mathbf{E}_{\text{ideal}} = -\mathbf{v} \times \mathbf{B}$ and the corresponding surface integral can be written as

$$\frac{1}{\mu_0} \oint_S (\mathbf{E}_{\text{ideal}} \times \mathbf{B}) \cdot \hat{n} \mathrm{d}^2 x = \frac{1}{\mu_0} \oint_S |\mathbf{B}_t|^2 \mathbf{v}_n \cdot \hat{n} \mathrm{d}^2 x - \frac{1}{\mu_0} \oint_S (\mathbf{v}_t \cdot \mathbf{B}_t) \mathbf{B}_n \cdot \hat{n} \mathrm{d}^2 x \ , \quad (1.22)$$

where the subscripts t and n stand for tangential and normal components to the surface S. The first term in 1.22 measures to the advection of flux, meaning that field lines simply enter or leave V, while the second term is due to the transverse motion at the surface S, which can twist the field lines (Kusano et al., 2002). In summary, for any given volume of integration, magnetic energy can get converted into kinetic energy, dissipate in the form of heat, and change due to Poynting flux. Notably, the overall decrease of magnetic energy in solar transients is central to the relaxation of the magnetofluid. In order to realize such a decrease in magnetic energy from equation 1.21, it is essential to understand the interplay of the right-hand side terms at both local and global length scales. Here, local and global are used in the sense of smaller and larger volumes of integration only and do not refer to any characteristic length scales of the physical system.

For completeness, the following section describes the standard flare model to illustrate the association between magnetic reconnection and eruptive events. The model is two-dimensional but provides a reasonable explanation for the evolution of an erupting magnetic flux rope accompanied by a two-ribbon flare and CME.

1.3 Standard Reconnection Model of Flares

The origin of the standard flare model lies in the early works of Carmichael (1964), Sturrock (1966), Hirayama (1974), and Kopp & Pneuman (1976), thus earning the acronym CSHKP, which is derived from their initials. The CSHKP model assumes a pre-existing magnetic flux rope containing prominence material (Priest & Forbes, 2002; Priest, 2014), as shown by the MFR cross-section in panel (a) of figure 1.13. Initially, the flux rope begins to erupt (for details of flux-rope eruption mechanisms, see Chen, 2011; Howard, 2011) and rises upward, which decreases the magnetic pressure below the MFR. Consequently, the surrounding magnetic loop gets pinched and due to the magnetic pressure gradient force, a plasma flow is established along the horizontal direction (Benz, 2017), as shown in panel (b) of figure 1.13. The oppositely directed magnetic field lines of the loop move toward each other, forming a X-point geometry and thus, a current sheet. As a result, the reconnection process ensues, resulting in heating, plasma outflow, and acceleration of particles. The accelerated particles initially lose some of the energy by the thin-target bremsstrahlung mechanism, leading to the observed hard X-ray source in the solar corona (Masuda et al., 1994).

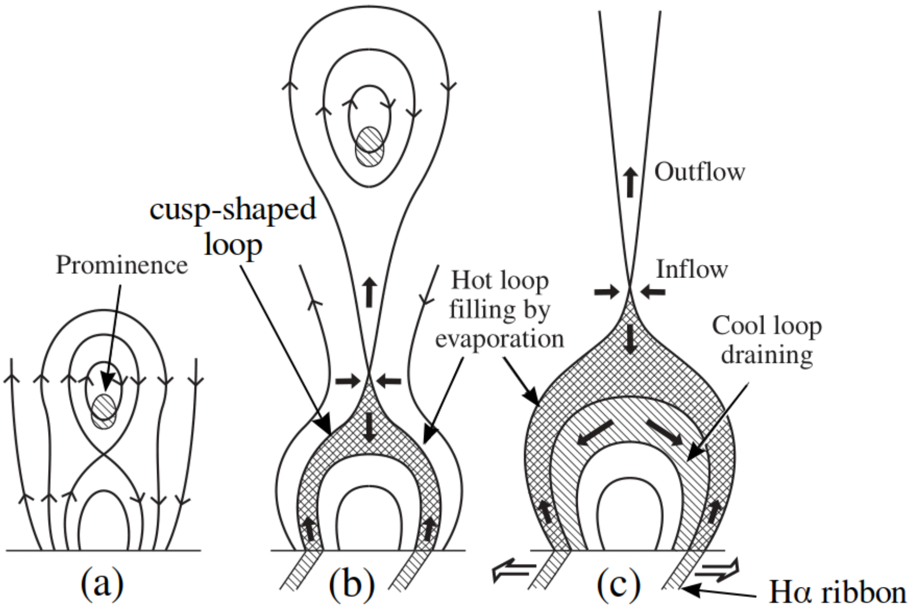

Figure 1.13: Schematic representation of the standard reconnection model of flares. Panel (a): Equilibrium magnetic configuration containing a magnetic flux rope with prominence material Panel (b): The eruption of MFR leads to reconnection below it and heated chromospheric plasma fills the magnetic loops Panel (c): The rising MFR causes repeated reconnection, which creates new hot loops, while the earlier loops begin to cool and drain (adapted from Priest, 2014).

Also, the particles gyrate along the magnetic field lines of the cusp-shaped loop formed after reconnection, and move toward the cool and denser chromosphere at nearly relativistic speeds. The gyration results in an enhancement of radio emission. On colliding with the chromosphere, thick-target bremsstrahlung occurs and emission in hard X-ray is observed at footpoints of the loop (Brown, 1971; Hudson, 1972). Further, footpoint emission is observed in Hα and EUV wavelengths in the form of elongated bright regions, known as flare ribbons or Hα ribbons, which trace the base of a magnetic arcade (Benz, 2017). In the process, chromospheric plasma is heated and an upflow of plasma fills the loop, making them visible in soft X-rays. This is also known as chromospheric evaporation. Notably, the rising

MFR causes the X-point to move upwards, leading to further reconnection in outer loops. As a result, new hot loops are created, while the old loops begin to cool, draining the plasma downwards (Priest, 2014), as shown in panel (c) figure 1.13. It also leads to an increase in the separation between Hα ribbons and transition of cusp-shaped loops to being rounded. Importantly, if the MFR erupts completely, it eventually leads to a coronal mass ejection.

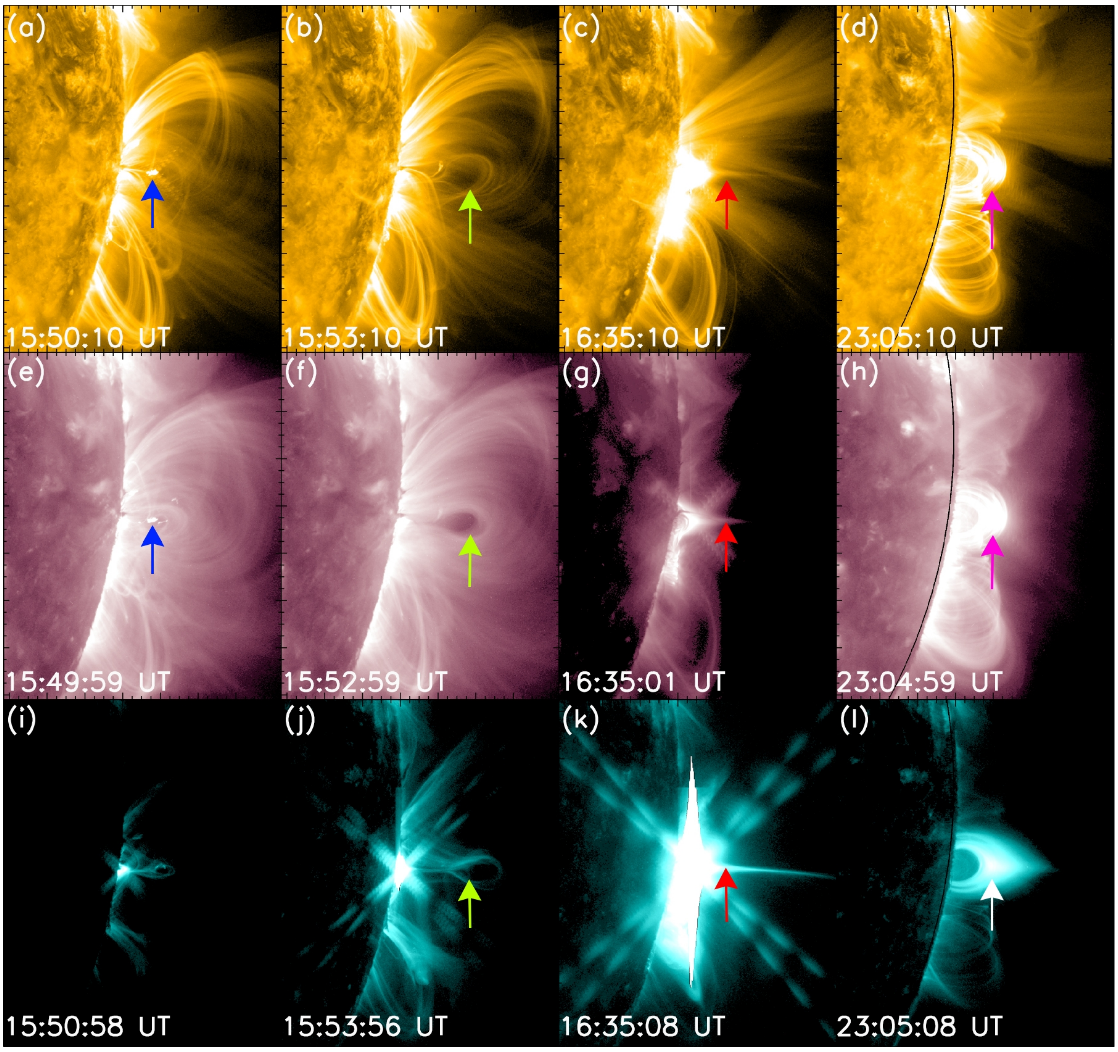

Figure 1.14: Imaging observations of a flare on September 10, 2017 by SDO/AIA in 171 Å (top), 211 Å (middle), and 131 Å (bottom). The arrows indicate prominence material (*blue*), the flux rope (*green*), current sheet (*red*), magnetic arcade (*pink*), and the cusp-shaped loop (white), respectively (adapted from Yan et al., 2018).

Contextually, a solar flare on September 10, 2017, investigated in Yan et al. (2018) is an apt example of the agreement between the model and observations. The imaging observations in 171 Å, 211 Å, and 131 Å by SDO/AIA (Lemen et al., 2012) are depicted in the top, middle, and bottom rows of figure 1.14, respectively. The arrows mark the prominence material (*blue*), the flux rope (*green*), current sheet (*red*), magnetic arcade (*pink*), and the cusp-shaped loop (white), respectively. It is important to keep in mind that the CSHKP model is only two-dimensional, while in a realistic scenario, the reconnection is inherently three-dimensional and much more complex.

1.4 Objective and Outline of the Thesis

Solar transients such as flares and CME are sudden explosive events in which the magnetic energy gets released as heat, bulk kinetic energy, and fast acceleration of charged particles by the magnetic reconnection process. The release of this energy is expected to relax the magnetic field to a state characterized by lesser magnetic energy. This lowering of the magnetic energy is only one of the various aspects of a transient activity. The other aspects may include their observational signatures, effect on space-weather, thermodynamics, morphological structure, and evolution. However, focusing on the decrease in magnetic energy allows the realization that solar transients merit exploration from the perspective of a general physical process known as self-organization. The occurrence of self-organization in various systems, such as economic, biological, robotic, chemical, and magnetized plasmas, reflects its inherent generality. Consequently, an investigation in the general framework of self-organization renders an impression of universality to the physics of transients, which is both tantalizing and theoretically interesting. Importantly, the systems that exhibit self-organization evolve toward certain preferred states. These states are nearly independent of the initial conditions and are often described by using a variational formulation. In the context of magnetized plasma as a system, such states are called relaxed states. Therefore, it is natural to consider the feasibility of analytically obtained relaxed states in the post-transient state of the magnetofluid. Furthermore, given that the amount of released magnetic energy depends on the strength of transient activity, the extent of relaxation is expected to vary, which naturally adds on as a next step in the course of the investigations described above. Notably, regarding such objectives, it is crucial to understand the implications of magnetic reconnection on the magnetofluid dynamics, with sudden changes in the connectivity of magnetic field lines and energetics of the system being of particular significance. To achieve the above goals, data-based simulations are executed for various solar flares. The simulations employ an extrapolated magnetic field as an initial condition, where extrapolation refers to the modeling of magnetic field in the solar atmosphere. Then, in combination with solar observations, such data-based simulations are a powerful tool to explore relaxation in solar transients, which is the subject matter of this thesis, organized into a total of nine chapters. A brief description of each chapter is given below.

Chapter 1: Solar Eruptive Events: Manifestations of Magnetic Reconnection

This chapter lays down the premise of the thesis, which is to investigate the eruptive events from the perspective of self-organization and plasma relaxation using data-based simulations. In this regard, the magnetohydrodynamics (MHD) description of the plasma and details of magnetic reconnection in 2D and 3D are presented. Further, to illustrate the application of reconnection, the standard model of flares is discussed.

Chapter 2: Solar Observations and Modeling of Magnetic Fields in the Solar Atmosphere

This chapter presents the details of solar observations from the GOES satellite, AIA and HMI instruments of the SDO satellite. This is followed by magnetic field extrapolation techniques, namely the potential field, linear force-free field (LFFF), nonlinear force-free field (NLFFF), and non-force-free field (NFFF) models. The thesis work uses only NLFFF and NFFF because they can quantitatively account for the amount of magnetic energy released during transients.

Chapter 3: Numerical Model for MHD Simulations: EULAG-MHD

The simulation of transients necessitates the preservation of flux-freezing condition to high fidelity, except at the sites where reconnection occurs. For this purpose, the EULAG-MHD numerical model is used. In the absence of any physical diffusion term, the ILES (Implicit Large Eddy Simulations) property of the EULAG-MHD model renders the magnetic reconnections to be numerically assisted but minimizes the computational cost. This chapter presents the theoretical background and the implementation aspects of the EULAG-MHD numerical model.

Chapter 4: Examples of MHD Simulations: Magnetic Flux Ropes

In this chapter, two MHD simulations initiated from analytical magnetic fields are discussed to illustrate the implications of reconnection and to exemplify the signatures of relaxation. The examples pertain to the formation and evolution of magnetic flux ropes (MFRs), which is crucial in understanding the dynamics of eruptive events like coronal mass ejections. Importantly, this chapter serves as a prelude to the exploration of relaxation in transients.

Chapter 5: Concepts of Plasma Relaxation

This chapter presents a detailed exposition on the subject of self-organization and plasma relaxation. In particular, relaxed states obtained by minimizing magnetic energy (referred to as magnetic relaxation) like Woltjer's state and Taylor's state are discussed. A review of earlier studies exploring relaxation in the solar plasma is presented. Since, these studies are based on theoretical arguments, observations, and numerical simulations employing analytical magnetic fields only, they fail to capture the field line complexity of an active region, which motivates an exploration of relaxation in data-based simulations.

Chapter 6: Effects of Initial Conditions on Magnetic Reconnection

This chapter explores three data-based simulations of a flare from the perspective that self-organized states are nearly independent of the initial configuration. For this purpose, three relevant initial conditions are generated using the NLFFF and NFFF extrapolations, followed by the corresponding simulations. A comprehensive analysis of the extrapolated magnetic fields is carried out. The three simulations are compared for global energetics, changes in the field line connectivity, and the spontaneous appearance and disappearance of a magnetic null to draw conclusions. The results are found to be in accordance with the expectation, suggesting a near independence with respect to the initial conditions, which further motivates an exploration of the magnetofluid dynamics and relaxation.

Chapter 7: Study of Reconnection Dynamics and Magnetic Relaxation

This chapter explores data-based simulation of a flare with particular focus on the magnetofluid dynamics and magnetic relaxation. For this purpose, the spatio-temporal evolution of magnetic energy, current density, twist, and gradients in magnetic field is analyzed for three different sub-volumes of integration within the computational box. The chapter focuses on understanding the energetics by investigating field line dynamics, numerical diffusion, and the Poynting flux. The angular alignment between current density and magnetic field is also explored to determine the extent of magnetic relaxation. The simulation is found to exhibit signatures of magnetic relaxation but does not reach a force-free state. The chapter concludes that flare energetics and its duration may have a bearing on the extent of relaxation, which motivates the work carried out in the next chapter.

Chapter 8: Study on the Extent of Magnetic Relaxation

This chapter explores data-based simulations of three energetically different solar flares, identified as B6.4, C4.0, and M1.1 in the GOES classification scheme. The NFFF extrapolation is carried out to identify the reconnection site in each case. The estimation of dissipated magnetic energy from simulations is found to be in concurrence with the general energy relation between the classes of chosen flares. Further, although the analysis of angular alignment between current density and magnetic field suggests a localized relaxation in each case, the result could not be understood from the perspective of extent of relaxation. An interesting finding of the work is a parameter based on the analysis of reconnection morphologies that may have applications in predicting the strength of solar flares.

Chapter 9: Thesis Summary and Future Prospects

This chapter presents the summary of the carried out work, focusing on the major findings of the thesis. Further scope for the future work is also discussed.

Chapter 2

Solar Observations and Modeling of Magnetic Fields in the Solar Atmosphere

2.1 Introduction

The electromagnetic radiations emitted from the Sun, particularly during the solar transients, prove to be an important means of investigating the physical processes occurring across different spatial and temporal scales on the Sun. In other words, photons carry a wealth of information regarding the dynamics of transients and magnetic field of the Sun, both of which are indispensable in understanding solar phenomena. In general, both ground-based and space-based observations are used. Notably, space-based observatories are not restricted by the Earth's atmosphere, which typically allows only the visible, infrared, and radio wavelengths to reach the Earth's surface (Aschwanden, 2005). Consequently, the Sun can be observed across the full range of emissions in different wavelengths almost uninterruptedly from space. In this thesis work, the solar observational data from the space-based Geostationary Operational Environmental Satellite (GOES) and Solar Dynamics Observatory (SDO) are used. In particular, the imaging observations are used to understand the spatio-temporal evolution of the transient activity and magnetic field measurements are utilized for the purpose of modeling the magnetic field in the solar atmosphere. Notably, only the photospheric magnetic field is measured routinely, giving all the magnetic field components in the form of a two-dimensional map known as vector magnetogram. Therefore, the modeling of the magnetic field is necessary to investigate and visualize the magnetic field structures in the solar atmosphere. The modeling procedure using measured photospheric magnetograms as boundary condition is referred to as the magnetic field extrapolation. The use of an extrapolated magnetic field allows a comparison of magnetic field configurations (e.g. magnetic loops) with the observed emission structures, such as the coronal loops. Further, it helps to determine an association, if any, between the preferential reconnection sites (e.g. 3D null point, QSL, HFT) and the solar transients.

The first method for magnetic field extrapolation was suggested by Schmidt (1964). Since then, the desire to model the solar magnetic field accurately has led to development of many other methods for extrapolation. The extrapolations can be used to model both the global magnetic field of the Sun and the localized active region magnetic fields. The two are typically carried out using the spherical and Cartesian coordinate systems, respectively. The models are broadly classified into force-free and non-force-free, depending on whether the associated Lorentz force is zero or not at the bottom boundary. In the following, starting with GOES and SDO observations, techniques for magnetic field extrapolation in localized regions are presented while briefly highlighting the global magnetic field models.

2.2 Geostationary Operational Environmental Satellite (GOES)

The GOES satellite (Donnelly et al., 1977; Reep & Knizhnik, 2019) whose data has been used in this thesis is only one of the many GOES satellites. These are built and launched by the National Aeronautics and Space Administration (NASA) but operated and managed by the National Oceanic and Atmospheric Administration (NOAA). Since 1975, there have been a total of 18 GOES satellites, many of which are now decommissioned. In this thesis, data from GOES-15 (also known as GOES-P) satellite is used, which was launched on 4 March, 2010. It recorded its first and last data in September, 2010, and March, 2020, respectively. Although the GOES satellites contain a suite of instruments, the X-ray sensor (XRS) is of particular importance because its measurements define the standard X-ray classification of solar flares. The incoming flux of soft X-rays is measured in two bandpasses by the XRS, namely the short channel ($0.5 - 4\,\text{Å}$) and the long channel ($1 - 8\,\text{Å}$), which approximately corresponds to the energy ranges of $3 - 25$ keV and $1.5 - 12$ keV, respectively. Subsequently, the X-ray irradiance is calculated and reported in the physical units of $\mathrm{W\,m^{-2}}$. The classification of the magnitude and duration of flares is defined by the NOAA's Space Weather Prediction Center (SWPC) by using the one minute average of X-ray operational irradiance in the $1-8$ Å channel at the peak time of a flare. The resulting scheme classifies flares into five categories, namely the A, B, C, M, and X, where each differs by an order of magnitude, ranging from $10^{-8}\,\mathrm{W\,m^{-2}}$ for A-class to $10^{-4}\,\mathrm{W\,m^{-2}}$ for X-class, respectively. The letters are further numbered, meaning that a M5 flare has the peak soft X-ray irradiance of $5 \times 10^{-5}\,\mathrm{W\,m^{-2}}$ and similarly for other classes (Chamberlin et al., 2009). The estimation of flare time duration is based on the following. The start time is the first minute of steep monotonic increase in $1-8$ Å flux while the end time is when the flux level decays to a point halfway between the maximum and pre-flare value. The GOES measurements serve to provide information about the intensity of flares, their start, peak, and end times, the duration of both impulsive and gradual phases of flares, and the temporal evolution of soft X-ray intensity. All of this information is valuable for conducting a preliminary investigation. For further analysis, imaging observations in multiple wavelengths and magnetic field measurements at the photosphere are acquired from the instruments of SDO, as discussed in the following.

2.3 Solar Dynamics Observatory (SDO)

The SDO (Pesnell et al., 2012) is the first space-weather mission under NASA's Living With a Star (LWS) program. It was launched on 11 February, 2010 and began its scientific operations on 1 May, 2010. It moves in a circular geosynchronous orbit of 36,000 km altitude and 28° inclination. The primary goal of SDO is to aid in understanding of the solar magnetic field and prediction of the solar activity. For this purpose, there are three instruments onboard SDO, namely the Atmospheric Imaging Assembly (AIA), Extreme Ultraviolet Variability Experiment (EVE), and Helioseismic and Magnetic Imager (HMI). It daily transmits approximately 1.5 TB of scientific data to the ground, showcasing the immense scale and capacity of the satellite. In this thesis, the data from only AIA and HMI instruments of SDO have been used, as discussed below.

Channel	Primary ion(s)	Region of atmosphere	Char. log(T)
4500 Å	continuum	photosphere	3.7
1700 Å	continuum	photosphere	3.7
304 Å	He II	chromosphere, transition region	4.7
1600 Å	C IV + continuum	transition region, upper photosphere	5.0
171 Å	Fe IX	quiet corona, upper transition region	5.8
193 Å	Fe XII, XXIV	corona and hot flare plasma	6.2, 7.3
211 Å	Fe XIV	active region corona	6.3
335 Å	Fe XVI	active region corona	6.4
94 Å	Fe XVIII	flaring corona	6.8
131 Å	Fe VIII, XXI	transition region, flaring corona	5.6,7.0

Table 2.1: Different channels of AIA centered on specific lines and corresponding regions of the solar atmosphere with different characteristic temperatures (Lemen et al., 2012)

2.3.1 Atmospheric Imaging Assembly (AIA)

The imaging observations of the Sun in different wavelengths reveal the structuring of solar atmosphere. Further, continual progress in development of high resolution imaging instruments paves the way to discovery of new solar features, such as the recently found campfires (Berghmans et al., 2021). Also, imaging observations at high temporal resolution allow for a detailed investigation of the dynamical processes occurring over small time scales, particularly transient phenomena such as solar flares. Contextually, the AIA (Lemen et al., 2012) instrument provides full-disk images of the Sun in multiple wavelength channels simultaneously. The 1.5-arcsec spatial resolution (0.6-arcsec pixel size) and 12-second temporal resolution of AIA allow it to capture a large number of concurrent high-resolution images of the solar corona and transition region up to 0.5 $R_\odot$ above the solar limb. It consists of four telescopes that are optimized to observe emissions from the transition region and solar corona. Each telescope has a 41-arcmin field-of-view (FOV) and 4096×4096 CCDs. In totality, AIA makes measurement in 10 wavelengths, of which seven are in extreme ultraviolet (EUV), two are in ultraviolet (UV), and one in optical. Table 2.1 summarizes the details of spectral lines, the corresponding ions, region of the solar atmosphere, and the characteristic temperature in log scale. In this thesis work, the wavelength channels used for the observational analysis of solar flares are (a) 1600 Å, which has a temporal cadence of 24 seconds and delineates flare ribbons (Liu et al., 2016a). It is also associated with plasma heating in the lower atmosphere during flares (b) 304 Å, which images filaments/prominences (Mierla et al., 2022) and prominence-corona transition region (c) 94 Å, and 131 Å, which measure emission from extremely hot plasma produced in flaring regions of solar corona. The imaging observations reveal the spatio-temporal evolution of solar transients, thus helping in gaining insights into the underlying physical processes. Since, the solar magnetic field plays a primary role in the manifestation of features like sunspots, flares, prominences, and CMEs, its measurement is essential for a comprehensive understanding of solar phenomena. Relevantly, the HMI instrument onboard SDO measures the photospheric magnetic field as discussed in the following.

2.3.2 Helioseismic and Magnetic Imager (HMI)

In principle, the entire solar atmosphere is magnetized but the measurements of magnetic field are made routinely for photosphere only (Solanki et al., 2006), using the principle of Zeeman effect (Zeeman, 1897). This is so because in comparison to chromosphere and solar corona, photospheric magnetic field is stronger, plasma density is higher (leading to stronger intensity of emission and hence better signal), and temperature is lower, which implies low thermal broadening (Cargill, 2009; Stenflo, 2013). The Zeeman effect refers to splitting of atomic energy levels in the presence of magnetic field. As a result, the atomic spectral line splits into different polarized components in accordance with the allowed transitions. The wavelength of the component lines is shifted ($\Delta\lambda$) from the central wavelength (λ_0), which is given by (Borrero et al., 2011)

$$\Delta\lambda = \pm 4.77 \times 10^{10} g_{\text{eff}} |\mathbf{B}|^2 \lambda_0 \ , \tag{2.1}$$

where g_{eff} is the Landé g-factor, $\Delta\lambda$ is in mÅ, λ_0 in Å, and $|\mathbf{B}|$ in Gauss. The HMI instrument (Schou et al., 2012; Scherrer et al., 2012) employs Fe I 6173.33 Å line ($g_{\text{eff}} = 2.5$), which is magnetically sensitive. The polarization state of the signals is measured in the form of Stokes vector (I, Q, U, and V), whose inversion using the VFISV (Very Fast Inversion of the Stokes Vector) code (Borrero et al., 2011) provides the required magnetic field vector.

The Helioseismic Magnetic Imager (HMI) onboard SDO began operations in May 2010 and since then, it has been continuously observing the entire visible disk of the Sun. It consists of two 4096^2-pixel CCD cameras, namely LoS/Doppler and vector cameras, which record full-disk images of the Sun at arcsecond-resolution (0.5-arcsec pixel size) every 3.75 seconds (Hoeksema et al., 2014). The LoS camera measures right and left circular polarization, each at six wavelengths within a 76 mÅ band centered around the Fe I 6173.33 Å line. It records a 12-filtergram set in 45 seconds. Similarly, the vector camera measures six polarization states (four linear and two circular), completing a 36-filtergram set in 135 seconds. The HMI data is categorized into (a) Level 0−raw HMI images (b) Level 1−data corrected for various instrumental effects (c) Level 1.5−HMI observables, computed using Level 1 data (Couvidat et al., 2016). The HMI employs two processing pipelines, namely LoS and Vector pipelines to produce the observables. Both of them compute the line-of-sight (LoS) Dopplergram, LoS magnetogram, and continuum intensity at a cadence of 45 and 720 seconds, respectively. The vector pipeline also computes the Stokes polarization vector (Couvidat et al., 2016). In addition to these observables, some higher-level data products such as vector magnetic field maps (Hoeksema et al., 2014) and active region patches (Bobra et al., 2014) are also produced.

In this thesis, the hmi.sharp_cea_720s (Bobra et al., 2014) data series from SDO/HMI is used, where CEA refers to the Cylindrical Equal Area (Calabretta & Greisen, 2002) projection to obtain the vector magnetic field corresponding to the photospheric surface. The magnetic field components on the photosphere are obtained as B_r, B_p, and B_t, which satisfy (a) B_z=B_r (r; radial), (b) B_x=B_p (p; poloidal), and (c) B_y=$-B_t$ (t; toroidal) in a Cartesian coordinate system. In the following, techniques of magnetic field extrapolation are presented, starting with force-free modeling.

2.4 Force-Free Modeling

The theoretical framework underlying the force-free modeling relies on the slow evolution of magnetic field structures in the solar corona (Sakurai, 1989, Priest, 2014). Relevantly, coronal features such as active region loops, arcades, sigmoids, and helmet streamers evolve slowly and are considered to be nearly stationary or quasi-stationary structures (Gary, 1989, Aschwanden, 2005, Priest, 2014). The formal analysis of this can be made by comparing the order of terms in the equation of motion

$$\rho \frac{\mathrm{d}\mathbf{v}}{\mathrm{d}t} = -\nabla p + \mathbf{J} \times \mathbf{B} - \rho \mathbf{g} \ , \tag{2.2}$$

where all the symbols have their usual meaning. The order comparison of left hand side term with the three forcing terms on the right hand side yields $|\mathbf{v}|^2 \big/ c_s^2$, $|\mathbf{v}|^2 \big/ V_A^2$, and $|\mathbf{v}| \big/ \sqrt{2gL_0}$, where c_s, V_A, and $\sqrt{2gL_0}$ denote the characteristic sound speed, Alfvén speed, and gravitational free-fall speed of the magnetized plasma system under consideration. The slow evolution of magnetic structures is encoded within the requirement that the plasma flow speed $|\mathbf{v}| \ll c_s$, V_A, and $\sqrt{2gL_0}$, implying that equation 2.2 can be approximated to be in an equilibrium, which satisfies the condition of magnetohydrostatic balance (Neukirch, 2005, Priest, 2014), given by

$$\nabla p - \mathbf{J} \times \mathbf{B} + \rho \mathbf{g} = \mathbf{0} \ . \tag{2.3}$$

Since, the magnetic field plays a key role in the structuring of the solar corona, it is informative to compare the order of Lorentz force with pressure gradient and gravitational forces. For this purpose, it is instructive to rewrite equation 2.3 in its dimensionless form. A substitution of the normalized variables, namely $p' \rightarrow \dfrac{p}{p_0}$, $\rho' \rightarrow \dfrac{\rho}{\rho_0}$, $\mathbf{r}' \rightarrow \dfrac{\mathbf{r}}{L_0}$, $\mathbf{g}' \rightarrow \dfrac{\mathbf{g}}{g_0}$, $\mathbf{B}' \rightarrow \dfrac{\mathbf{B}}{B_0}$, and $\mathbf{J}' \rightarrow \dfrac{\mathbf{J}}{J_0}$ in equation 2.3 gives

$$-\frac{\beta}{2} \nabla' p' + \mathbf{J}' \times \mathbf{B}' + \frac{\beta}{2} \frac{L_0}{H} \rho' \mathbf{g}' = 0 \ , \tag{2.4}$$

where $\beta = p_0 \left(\dfrac{B_0^2}{2\mu_0} \right)^{-1}$ denotes the plasma beta parameter, defined as the ratio of kinetic pressure to magnetic pressure, while $H = \dfrac{p_0}{\rho_0 g_0}$ refers to pressure scale-height, which is the distance over which the kinetic pressure decreases by a factor of e (Priest, 2014). In order to compare the relative magnitude of forcing terms in equation 2.4, an estimate of plasma β in the solar corona is crucial. Contextually, Gary (2001) took observational constraints into account and devised an empirical mathematical formulation to model the variation of magnetic field and kinetic pressure with height. The resulting plasma β plot is depicted in figure 2.1, which indicates the presence of a region in solar atmosphere for which $\beta \ll 1$. Within this region, magnetic force dominates over the hydrodynamic forces, which can be understood by realizing that β can be rewritten as $\beta \sim c_s^2/V_A^2 \approx 0.01 \ll 1$ for the typical values $c_s \approx 100\,\mathrm{km\,s^{-1}}$ and $V_A \approx 1000\,\mathrm{km\,s^{-1}}$ (Aschwanden, 2005, Priest, 2014) in the solar corona. The low-β value along with a typical $L_0 = 10$ Mm and $H = 100$ Mm for solar corona implies that the first and third terms of equation 2.4 can be dropped. This leads to a null Lorentz force or a force-free equilibrium, described by

$$\mathbf{J} \times \mathbf{B} = \mathbf{0} \;, \tag{2.5}$$

where the normalized variables have been replaced with dimensional dynamical variables for convenience. Equation 2.5 implies that the magnetic pressure force and the magnetic tension force balance each other, as following

$$\mathbf{J} \times \mathbf{B} = -\nabla\left(\frac{B^2}{2}\right) + (\mathbf{B}\cdot\nabla)\mathbf{B} = \mathbf{0} \;. \tag{2.6}$$

In the non-trivial case, current density is parallel to magnetic field. Consequently, equation 2.5 implies that

$$\nabla \times \mathbf{B} = \alpha(\mathbf{r})\,\mathbf{B} \;, \tag{2.7}$$

where the proportionality constant $\alpha(\mathbf{r})$ is a position dependent scalar function. Further, the divergence of equation 2.7 on both sides along with the solenoidaility of magnetic field leads to the condition

$$\nabla\alpha(\mathbf{r}) \cdot \mathbf{B} = 0 \;. \tag{2.8}$$

The mathematical structure of equations 2.7 and 2.8 withholds many interesting properties, some of which are mentioned below. Importantly, these are nonlinear partial differential equations and the force-free fields generally do not satisfy the superposition principle (Marsh, 1996). Equation 2.7 implies that $\alpha(\mathbf{r}) \sim \mathbf{J}\cdot\mathbf{B}/|\mathbf{B}|^2$, which suggests that $\alpha(\mathbf{r})$ is closely associated with field line topology (Parker, 2012) and representative of twist in magnetic field lines (Berger & Prior, 2006). Further,

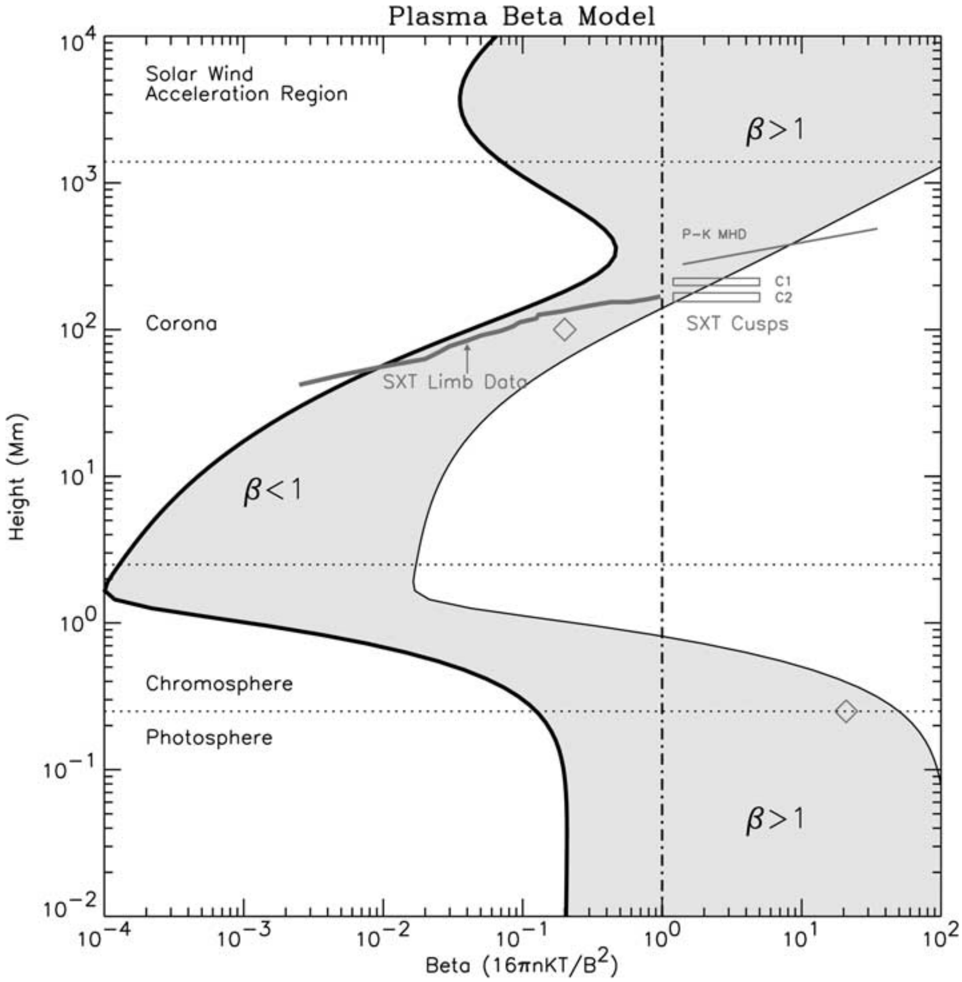

Figure 2.1: The variation of plasma β parameter with height; from Gary (2001). The left and right boundaries of the shaded region correspond to a sunspot and plage region having field strengths of 2500 G and 150 G, respectively. SXT refers to the observational data from the soft X-ray telescope mounted on the Yohkoh space-satellite.

from equation 2.8, it is readily seen that $\alpha(\mathbf{r})$ is constant along a magnetic field line (Marsh, 1996, Priest, 2014). The generic procedure to solve these equations is to construct a well defined boundary value problem (BVP) and an investigation regarding the existence and uniqueness of solutions (Molodenskii, 1969, Bineau, 1972, Molodensky, 1974, Aly, 1984, Aly, 1989, Boulmezaoud & Amari, 2000, Amari et al., 2006). However, owing to the nonlinearity, it is difficult to solve the equations analytically (Inoue, 2016, Wiegelmann & Sakurai, 2021). Nevertheless, simplified force-free solutions can be derived from equation 2.7 for $\alpha(\mathbf{r}) = 0$ and $\alpha(\mathbf{r}) = \alpha_0$, giving the so-called potential and linear force-free magnetic fields, respectively. In the following, the extrapolation models based on these solutions and the general nonlinear force-free magnetic field are discussed.

2.4.1 Potential Field Extrapolation

The earliest extrapolation model was developed by assuming current-free magnetic fields in the solar atmosphere (Schmidt, 1964, Semel, 1967), which is equivalent to untwisted field lines ($\alpha(\mathbf{r}) = 0$). The resulting model equations are given by

$$\mathbf{J} = \nabla \times \mathbf{B} = \mathbf{0} \Rightarrow \mathbf{B} = -\nabla\Phi \;, \tag{2.9}$$

$$\nabla \cdot \mathbf{B} = 0 \Rightarrow \nabla^2\Phi = 0 \;, \tag{2.10}$$

where Φ is a scalar function. Equation 2.10 represents a second-order linear partial differential equation, namely the Laplace equation and can be solved in Cartesian (spherical) geometry for local (global) magnetic field modeling. Importantly, it is well-known that any solution to Laplace equation is unique, provided it satisfies the boundary conditions. Relevantly, the line-of-sight magnetic field serves to impose a Neumann boundary condition on Φ at the photospheric surface ($z = 0$), given by

$$B_z(x,y)\big|_{z=0} = -\left.\frac{\partial\Phi(\mathbf{r})}{\partial z}\right|_{z=0} \;, \tag{2.11}$$

which along with the requirement that $|\mathbf{B}| \to 0$ as $z \to \infty$ leads to a well posed and straightforward boundary value problem with unique solution. Broadly, there are two approaches to solve the Laplace equation for potential field extrapolation, namely the Green's function method (Schmidt, 1964, Semel, 1967, Sakurai, 1982) and Fourier expansion (Hagyard & Teuber, 1978, Priest, 2014). Since, the gradient is a linear differential operator, the Green's function (Ohtaka, 2003) is obtained easily from the relations

$$\Phi(\mathbf{r}) = \int \mathrm{G}(\mathbf{r}, x', y') B_z(x', y') \mathrm{d}x', \mathrm{d}y' \;, \tag{2.12}$$

$$\nabla\, \mathrm{G}(\mathbf{r}, x', y') = \delta^3(\mathbf{r} - \mathbf{r}') \;, \tag{2.13}$$

where $\mathbf{r} = (x, y, z)$, $\mathbf{r}' = (x', y')$, $\delta^3(\mathbf{r}-\mathbf{r}')$ is the Dirac delta function, and $\mathrm{G}(\mathbf{r}, x', y')$ is the required Green's function. The solution of $\mathrm{G}(\mathbf{r}, x', y')$ from equation 2.13 is substituted into 2.12 to compute $\Phi(\mathbf{r})$, and hence the magnetic field. In the Fourier expansion method, the measured line-of-sight magnetic field is expressed in terms of Fourier components (Riley et al., 2002, Priest, 2014), which allows an estimation of the scalar potential Φ as follows

$$B_z(x,y)\big|_{z=0} = \sum_{\mathbf{k}} B_{\mathbf{k}} e^{\mathrm{i}\mathbf{k}\cdot\mathbf{r}} \ , \ \Phi = \sum_{\mathbf{k}} B_{\mathbf{k}} \frac{e^{\mathrm{i}\mathbf{k}\cdot\mathbf{r}}}{k} e^{-kz} \ , \tag{2.14}$$

where $\mathbf{k} = (k_x, k_y)$, $\mathbf{r} = (x, y)$, $k = \sqrt{k_x^2 + k_y^2}$, and $B_{\mathbf{k}}$ are the Fourier coefficients. The factor e^{-kz} accounts for the decaying magnetic field strength with height. An inverse Fourier transform of $B_z(x, y)$ allows to determine $B_{\mathbf{k}}$, and hence the scalar potential Φ and magnetic field. Notably, the counterparts of above methods in spherical coordinates for global modeling of the solar corona (Schatten, 1968, 1969, Altschuler & Newkirk, 1969, Sakurai, 1982) constitute the now well-known Potential Field Source Surface (PFSS) model (Mackay & Yeates, 2012). Basically, the boundary conditions are modified as

$$B_r(R_\odot, \theta, \phi) = -\frac{\partial \Phi(\mathbf{r})}{\partial r}\bigg|_{r=R_\odot} , \frac{\partial \Phi(\mathbf{r})}{\partial \theta}\bigg|_{r=R_s} = 0, \frac{\partial \Phi(\mathbf{r})}{\partial \phi}\bigg|_{r=R_s} = 0 \ , \tag{2.15}$$

where $B_r(R_\odot, \theta, \phi)$ is the photospheric line-of-sight magnetic field obtained from synoptic magnetograms (Nikolić, 2019; Li et al., 2021). The extrapolation is carried out in the region corresponding to $R_\odot \leq r \leq R_s$, where R_s (source surface) is the distance at which the magnetic field is assumed radial to account for the stretching of magnetic field lines by the solar wind. To illustrate, an extrapolation is carried out using the PFSS model and shown in figure 2.2. The potential field provides a first-order estimate of magnetic field in the solar corona. However, because of the current-free nature, it does not account for the free energy required to drive the transients. Consequently, potential fields are not suitable to model active regions, which may contain highly sheared and twisted magnetic field lines. Nevertheless, owing to the uniqueness of solution and ease of calculation, it is an indispensable tool for magnetic field modeling.

2.4.2 Linear Force-Free Field Extrapolation

In contrast to potential field, the linear force-free field (LFFF) extrapolation model incorporates finite currents in the system by considering a position independent

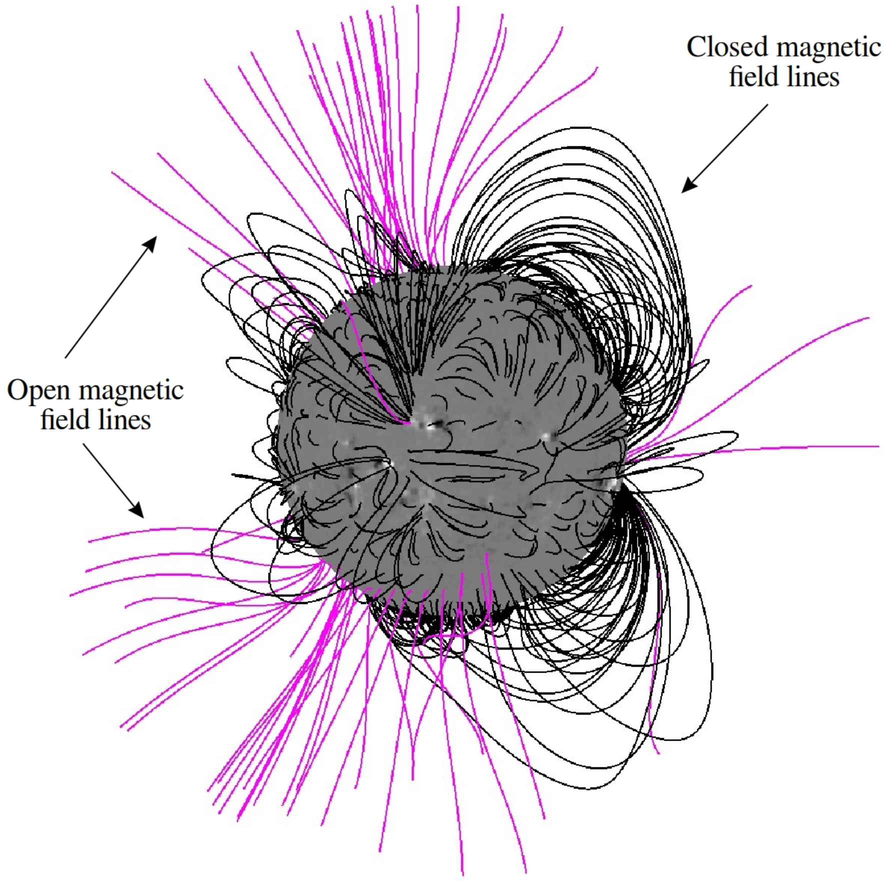

Figure 2.2: Global magnetic field of the Sun, extrapolated from PFSS model on October 1, 2014, 18:03 UT. The open (closed) magnetic field lines are shown by *pink* (*black*) colors.

$\alpha(\mathbf{r})$ in equation 2.7. Formally, this is described by

$$\nabla \times \mathbf{B} = \alpha_0 \mathbf{B} \ , \tag{2.16}$$

where α_0 is a constant, identical for every magnetic field line. The current density is field-aligned, thus complying with the force-free condition. LFFF is the simplest non-trivial ($\mathbf{J} \neq 0$) solution in the force-free modeling domain. The curl of equation 2.16 on both the sides along with the divergence-free condition on magnetic field gives the vector Helmholtz equation in magnetic field

$$\nabla^2 \mathbf{B} = -\alpha_0^2 \mathbf{B} \ , \tag{2.17}$$

whose general solution has been described in Chandrasekhar & Kendall (1957). It is solvable in both Cartesian (spherical) geometries for local (global) modeling. As in the case of potential field, there exists a Green's function approach (Chiu & Hilton, 1977, Seehafer, 1978) and a Fourier expansion based method (Nakagawa & Raadu, 1972, Alissandrakis, 1981) for linear force-free field extrapolation. Some of the aspects associated with the formulation of boundary value problem, the nature and uniqueness of solutions, can be understood easily in the framework of Fourier transforms (Alissandrakis, 1981, Gary, 1989). The Fourier transform of equation 2.16 leads to the following system of equations

$$\begin{pmatrix} \alpha_0 & -k & -i2\pi v \\ k & \alpha_0 & i2\pi u \\ i2\pi v & -i2\pi u & \alpha_0 \end{pmatrix} \begin{pmatrix} \widetilde{B}_x \\ \widetilde{B}_y \\ \widetilde{B}_z \end{pmatrix} = 0 \ , \tag{2.18}$$

where $\widetilde{\mathbf{B}}(u, v, z) = \mathcal{F}\{\mathbf{B}(x, y, z)\}$, satisfying the relation $\widetilde{\mathbf{B}}(u, v, z) = e^{-kz}\widetilde{\mathbf{B}}(u, v, 0)$. The solution exists if the determinant of coefficient matrix in equation 2.18 is zero, which gives the result

$$k^2 = 4\pi^2(u^2 + v^2) - \alpha_0^2 \Rightarrow k = \pm\sqrt{4\pi^2 q^2 - \alpha_0^2} \ , \tag{2.19}$$

where k is either real (imaginary) depending on $|\alpha_0| < \dfrac{2\pi}{L_0} \left(> \dfrac{2\pi}{L_0} \right)$ for a given $|\alpha_0|$, as shown in figure 2.3. For real k, only the positive root is considered, otherwise e^{-kz} blows up but for imaginary k, the general solution is a linear combination of the two roots. The two cases correspond to the so-called small-scale and large-scale solutions, respectively. Importantly, only small-scale solutions are physically meaningful because their energy content is finite. In contrast to this, the large-scale solutions are oscillatory in nature and the energy integral diverges (Alissandrakis, 1981, Gary, 1989). Further, the large-scale solutions cannot be specified uniquely unless the measurements of transverse magnetic field are available (Chiu & Hilton, 1977). Notably, the length scale L_0 being fixed by the size of magnetogram, the restrictions on α_0 are unphysical (Neukirch, 2005). Thus, for the purpose of application, while large-scale solutions may not be relevant, in case of small-scale, there is a range $|\alpha_0| < \dfrac{2\pi}{L_0}$, for which physical solutions can be found. In practice, the

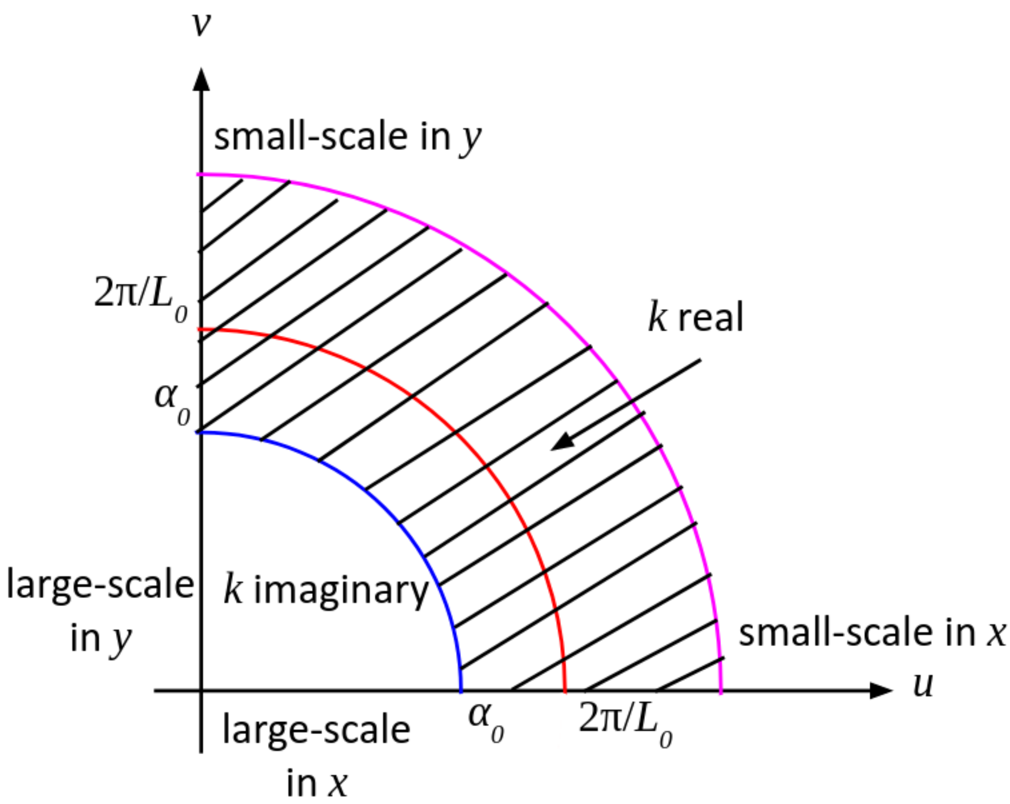

Figure 2.3: Illustration of real (imaginary) k regions in the Fourier space (u, v). In the *shaded* area enclosed by *blue* and *pink* curves, k is real, but imaginary for the area bounded by *blue* curve and origin of the plot. The *red* and *pink* curves represent the maximum α_0 and maximum frequency allowed in the Fourier space. This figure is adapted from Gary (1989).

value of α_0 can be fixed by using observations. The simplest method is to estimate the vertical current density component from measurements of transverse magnetic field, which is followed by computation of α_0 as follows

$$J_z = (\partial_x B_y - \partial_y B_x)/\mu_0 \ , \tag{2.20}$$

$$\alpha_0(x, y) = \mu_0 \frac{J_z}{B_z} \ . \tag{2.21}$$

Other methods derive the best fit for α_0 by comparing the projection of magnetic field configurations with chromospheric and coronal observations (Carcedo et al., 2003, Gosain et al., 2014). These calculations have revealed that a constant α_0 is not sufficient to model the magnetic field of an active region at different heights, thus limiting the usage of LFFF modeling. Consequently, nonlinear force-free field extrapolation is required, as discussed in the following.

2.4.3 Nonlinear Force-Free Field Extrapolation

In this case, the scalar function $\alpha(\mathbf{r})$ is position dependent and hence, need not to be identical for each magnetic field line. Therefore, the extrapolated magnetic field satisfies

$$\nabla \times \mathbf{B} = \alpha(\mathbf{r})\,\mathbf{B} \ , \tag{2.22}$$

$$\nabla \cdot \mathbf{B} = 0 \ . \tag{2.23}$$

Toward obtaining a solution, many numerical approaches (reviewed in Inoue, 2016, Wiegelmann et al., 2017) have been proposed. In this thesis, a NLFFF model based on an optimization procedure is used. The model was first proposed by Wheatland et al. (2000) and later developed in Wiegelmann & Neukirch (2002), 2004, 2006, 2010, 2012. In this method, an explicit estimation of $\alpha(\mathbf{r})$ on the bottom boundary is not required to specify the boundary condition. This is advantageous because the calculation of $\alpha(\mathbf{r})$ requires measurement of the transverse magnetic field, which contains more error than the line-of-sight magnetic field. Further, more errors are introduced for areas of low $|B_z|$ (e.g. PIL), as evident from equation 2.21. In the optimization scheme, a functional in minimized iteratively. Chronologically, Wiegelmann (2004) defined the functional (L) as

$$L = \int_V w(\mathbf{r}) \left[\frac{1}{|\mathbf{B}|^2} |(\nabla \times \mathbf{B}) \times \mathbf{B}|^2 + |\nabla \cdot \mathbf{B}|^2 \right] \mathrm{d}^3x \ , \tag{2.24}$$

where $w(\mathbf{r})$ is a weight function, while the first and second terms inside the brackets correspond to the Lorentz force and divergence of the magnetic field, respectively. Since, magnetic field measurements can be specified for bottom boundary alone, the influence of lateral and top boundaries should be minimal. This is accomplished by replacing these boundaries with boundary layers, where $w(\mathbf{r})$ changes smoothly from $w(\mathbf{r}) = 1$ at the beginning of layer to $w(\mathbf{r}) = 0$ at the edge of computational box (Wiegelmann, 2004). To initiate the iterative procedure, the initial magnetic field within the functional is chosen to be potential, which is also used to prescribe the side and top boundaries. For an iteration parameter t, minimization follows from

$$\frac{1}{2}\frac{\mathrm{d}L}{\mathrm{d}t} = -\int_V \frac{\partial \mathbf{B}}{\partial t} \cdot \widetilde{\mathbf{F}}\, \mathrm{d}^3x - \int_S \frac{\partial \mathbf{B}}{\partial t} \cdot \widetilde{\mathbf{G}}\, \mathrm{d}^2x \,, \tag{2.25}$$

$$\frac{\partial \mathbf{B}}{\partial t} = \mu \widetilde{\mathbf{F}} \,, \tag{2.26}$$

where $\widetilde{\mathbf{F}} = \widetilde{\mathbf{F}}(w, \mathbf{B})$ and $\widetilde{\mathbf{G}} = \widetilde{\mathbf{G}}(w, \mathbf{B})$, as derived in Wiegelmann (2004). Notably, the surface integral vanishes for the given magnetic field on boundaries, while 2.26 ensures that L decreases monotonically. Being a force-free model, the application of above formalism to the nonlinear force-free field (NLFFF) extrapolation would ideally require a vector magnetic field measured at the base of solar corona, where $\beta \ll 1$. However, the routine availability of only photospheric magnetograms makes the procedure slightly involved. Other than the challenges in measurement such as the 180° ambiguity (Metcalf, 1994), higher error in transverse component than the line-of-sight component (Wiegelmann & Sakurai, 2021), the magnetic field at the photosphere is not consistent with the force-free assumption. Consequently, by imposing the boundary integral relations obtained by Aly (1989) at the bottom boundary, Wiegelmann et al. (2006) defined some dimensionless quantities, namely the flux balance (ϵ_{flux}), the net force balance (ϵ_{force}), and the net torque balance (ϵ_{torque}) to quantify the suitability of a magnetogram with force-free modeling as follows

$$\epsilon_{\text{flux}} = \frac{\int_S B_z}{\int_S \left|B_z\right|},\ \epsilon_{\text{force}} = \frac{\left|\int_S B_x B_z\right| + \left|\int_S B_y B_z\right| + \left|\int_S \left[(B_x^2 + B_y^2) - B_z^2\right]\right|}{\int_S |\mathbf{B}|^2} \,,$$

$$\epsilon_{\text{torque}} = \frac{\left|\int_S x\left[(B_x^2 + B_y^2) - B_z^2\right]\right| + \left|\int_S y\left[(B_x^2 + B_y^2) - B_z^2\right]\right| + \left|\int_S yB_xB_z - xB_yB_z\right|}{\int_S |\mathbf{B}|^2\sqrt{x^2+y^2}} \,,$$

where the integral is over the magnetogram. In principle, these parameters should be zero but for measured magnetograms, it is not possible. However, if their value is low (< 0.1), the boundary conditions are considered sufficiently force-free and can be used directly, as done for SDO/HMI data in Wiegelmann et al. (2012). Unfortunately, many photospheric vector field measurements are not able to meet this criterion in the sense that ϵ_{force} and ϵ_{torque} are larger than about 0.1. The high plasma beta in photosphere naturally causes finite forces and torque, making direct use of the measured magnetogram as boundary condition unfeasible. Consequently, a preprocessing procedure (Wiegelmann et al., 2006) is employed to modify the lower boundary conditions as compared to observations. A 2D-functional L_p is defined as

$$L_p = \mu_1 L_1 + \mu_2 L_2 + \mu_3 L_3 + \mu_4 L_4 \ , \tag{2.27}$$

where the individual terms $L_{i=1,4}$ are

$$L_1 = \left[\left(\sum_p B_x B_z \right)^2 + \left(\sum_p B_y B_z \right)^2 + \left(\sum_p B_z^2 - B_x^2 - B_y^2 \right)^2 \right], \tag{2.28}$$

$$\begin{aligned} L_2 = &\left[\left(\sum_p x \left(B_z^2 - B_x^2 - B_y^2 \right) \right)^2 + \left(\sum_p y \left(B_z^2 - B_x^2 - B_y^2 \right) \right)^2 \right] \\ &+ \left[\left(\sum_p \left(y B_x B_z - x B_y B_z \right) \right)^2 \right], \end{aligned} \tag{2.29}$$

$$L_3 = \left[\sum_p (B_x - B_x^{\text{obs}})^2 + \sum_p (B_y - B_y^{\text{obs}})^2 + \sum_p (B_z - B_z^{\text{obs}})^2 \right], \tag{2.30}$$

$$L_4 = \left[\sum_p \left\{ (\nabla^2 B_x)^2 + (\nabla^2 B_y)^2 + (\nabla^2 B_z)^2 \right\} \right], \tag{2.31}$$

and μ_i are weight factors, $\mathbf{B}^{\text{obs}}$ is the observed magnetic field at the photosphere, and summation is over all the grid nodes of bottom boundary. The first two terms represent force balance and torque balance conditions, respectively. The L_3 term measures deviation between the preprocessed and observed magnetic field, while L_4 corresponds to smoothing, which aims to minimize the computational cost by averaging out small-scale features. Therefore, the goal is to minimize L_p such that all the individual terms are made small simultaneously, if possible. The resulting preprocessed magnetogram is relabeled as $\mathbf{B}^{\text{obs}}$ for convenience, and can be used as the boundary condition for extrapolation. The functional defined in Wiegelmann

(2004) was extended by Wiegelmann & Inhester (2010) to account for measurement errors and regions lacking observational data. The modified functional is given by

$$L = \int_V w_f \frac{|(\nabla \times \mathbf{B}) \times \mathbf{B}|^2}{B^2} \mathrm{d}^3x + \int_V w_d |\nabla \cdot \mathbf{B}|^2 \mathrm{d}^3x + \\ \nu \int_S (\mathbf{B} - \mathbf{B}^{\mathrm{obs}}) \cdot \mathbf{W}(x,y) \cdot (\mathbf{B} - \mathbf{B}^{\mathrm{obs}}) \mathrm{d}^2S \ , \tag{2.32}$$

where w_f and w_d are weight functions toward the lateral and top boundaries of the computational box. The newly added surface integral term is evaluated only over the bottom boundary. In this term, $\mathbf{W}(x, y)$ is a diagonal matrix, whose elements (w_{los}, w_{trans}, w_{trans}) are inversely proportional to local measurement error and ν is a Lagrange multiplier. Typically, $w_{\mathrm{los}} = 1$, while w_{trans} are small and positive, but in regions of poor signal-to-noise ratio, $w_{\mathrm{trans}} = 0$. In this definition, the bottom boundary is also allowed to relax during the iterative procedure, whose extent is determined by ν value. A smaller value implies slower injection of $\mathbf{B}^{\mathrm{obs}}$, which allows more time for relaxation toward a force-free state. This extrapolation procedure has also been extended to spherical coordinates for global modeling in the works of Wiegelmann (2007), Tadesse et al. (2009, 2011, 2014), Koumtzis & Wiegelmann (2023).

The extrapolated nonlinear force-free field effectively captures the twist of the magnetic structures and accounts for the magnetic energy released during solar transients. Notably, the existence of various methods for NLFFF modeling makes it necessary to compare their relative performance. The studies by Schrijver et al. (2006), 2008, De Rosa et al. (2009), 2015 present a comparison of models, highlighting the differences and similarities. Another way of extrapolating the coronal magnetic field is the non-force-free model, described in the following.

2.5 Non-Force-Free Field Extrapolation

In non-force-free field (NFFF) model, the Lorentz force $\mathbf{J} \times \mathbf{B} \neq 0$ at the bottom boundary. A rationale for the NFFF extrapolation can be given from dimensional analysis of the ratio of Lorentz force and rate of change of momentum (see 2.2), leading to

$$\frac{|\mathbf{J} \times \mathbf{B}|}{\left|\rho \dfrac{\mathrm{d}\mathbf{v}}{\mathrm{d}t}\right|} \sim \frac{\mathbf{B}^2}{\rho|\mathbf{v}|^2} \sim \frac{\mathbf{B}^2}{\rho|\mathbf{v}_{\mathrm{th}}|^2} \frac{|\mathbf{v}_{\mathrm{th}}|^2}{|\mathbf{v}|^2} \sim \frac{1}{\beta} \frac{|\mathbf{v}_{\mathrm{th}}|^2}{|\mathbf{v}|^2} \ , \tag{2.33}$$

where $\mathbf{v}_{\mathrm{th}}$ is the thermal velocity. Since, the typical flow speed and thermal velocity at the photosphere are of the order 1 km s^{-1} (Vekstein, 2016, Khlystova & Toriumi, 2017), the expression is simplified as

$$\frac{|\mathbf{J} \times \mathbf{B}|}{\left|\rho \dfrac{\mathrm{d}\mathbf{v}}{\mathrm{d}t}\right|} \sim \frac{1}{\beta} \ . \tag{2.34}$$

Since, $\beta \approx 1$ on the photosphere, equation 2.34 yields

$$|\mathbf{J} \times \mathbf{B}| \sim \left|\rho \frac{\mathrm{d}\mathbf{v}}{\mathrm{d}t}\right| \ , \tag{2.35}$$

which suggests that the non-zero Lorentz force at the photosphere can act as a driver for photospheric motions. Consequently, the modeling of this finite Lorentz force into an extrapolation model is relevant and necessary. Further, due to higher plasma beta in the lower atmosphere, the non-magnetic forces cannot be neglected in comparison to the Lorentz force. One way of doing so is to solve the equation 2.3 numerically, which is contextually referred to as the magnetohydrostatic (MHS) extrapolation (Wiegelmann et al., 2017, Miyoshi et al., 2020, Zhu et al., 2022, Yu et al., 2023). In this thesis work, the NFFF model developed by Bhattacharyya & Janaki (2004) has been employed. Its theoretical structure follows from an investigation of relaxed states in a driven system using the principle of Minimum Dissipation Rate (MDR) and two-fluid description of the plasma. The notion of relaxed states is discussed in chapter 5, while a detailed formalism of the model can be found in Bhattacharyya & Janaki (2004) and the references therein. For the purpose of this thesis, only the implementation aspects of the model are outlined here. Essentially, an inhomogeneous double curl Beltrami equation given by

$$\nabla \times (\nabla \times \mathbf{B}) + a\nabla \times \mathbf{B} + b\mathbf{B} = \nabla\phi \ , \tag{2.36}$$

is solved to obtain the magnetic field, where a, b are constants and ϕ is a scalar potential function. Bhattacharyya et al. (2007) derived an analytical solution from

2.36 to model the magnetic arcade structures in the solar corona.

Using the curl operator on both sides of equation 2.36 gives a homogenous equation

$$\nabla \times [\nabla \times (\nabla \times \mathbf{B})] + a\nabla \times (\nabla \times \mathbf{B}) + b\nabla \times \mathbf{B} = 0 \ . \tag{2.37}$$

The same can also be realized by writing the magnetic field vector as $\mathbf{B} = \mathbf{B}' + \dfrac{\nabla \phi}{b}$, which gives

$$\nabla \times (\nabla \times \mathbf{B}') + a\nabla \times \mathbf{B}' + b\mathbf{B}' = 0 \ . \tag{2.38}$$

Notably, equations 2.37 and 2.38 are equivalent, as discussed below. The solution of 2.37 is given by

$$\mathbf{B} = \sum_{i=1}^{3} \mathbf{B}_i \ , \tag{2.39}$$

where $\mathbf{B}_i$ are the Chandrasekhar-Kendall eigenfunctions (Chandrasekhar & Kendall, 1957), satisfying the eigenvalue equation

$$\nabla \times \mathbf{B}_i = \alpha_i \mathbf{B}_i \ , \tag{2.40}$$

where α_i are the real eigenvalues and $\mathbf{B}_i$ form a complete set of orthonormal vectors (Yoshida & Giga, 1990). Using equations 2.39 and 2.40 in equation 2.37, it is seen that $\sum_{i=1}^{3} \alpha_i \left(\alpha_i^2 + a\alpha_i + b\right) \mathbf{B}_i = 0$, which implies that one of the $\alpha_i = 0$, thus corresponding to a potential field. Since, $(\nabla\phi)/b$ is also a potential field, the proposed equivalency is established (Hu & Dasgupta, 2008). Thus, a superposition of two linear force-free fields with a potential magnetic field gives the required non-force-free solution. The numerical approach for non-force-free field extrapolation has been outlined in Hu et al. (2010). In the following, the stepwise methodology and procedure are described. From 2.39, the curl operations result in the following set of equations

$$\begin{aligned}
\mathbf{B} &= \mathbf{B}_1 + \mathbf{B}_2 + \mathbf{B}_3 \ , && (2.41)\\
\nabla \times \mathbf{B} &= \alpha_1\mathbf{B}_1 + \alpha_2\mathbf{B}_2 + \alpha_3\mathbf{B}_3 \ , && (2.42)\\
\nabla \times (\nabla \times \mathbf{B}) &= \alpha_1^2\mathbf{B}_1 + \alpha_2^2\mathbf{B}_2 + \alpha_3^2\mathbf{B}_3 \ , && (2.43)
\end{aligned}$$

which can be condensed into a matrix form, given by

$$\begin{pmatrix} \mathbf{B} \\ \nabla\times\mathbf{B} \\ \nabla\times(\nabla\times\mathbf{B}) \end{pmatrix} = \begin{pmatrix} 1 & 1 & 1 \\ \alpha_1 & \alpha_2 & \alpha_3 \\ \alpha_1^2 & \alpha_2^2 & \alpha_3^2 \end{pmatrix} \begin{pmatrix} \mathbf{B}_1 \\ \mathbf{B}_2 \\ \mathbf{B}_3 \end{pmatrix} = \mathcal{V} \begin{pmatrix} \mathbf{B}_1 \\ \mathbf{B}_2 \\ \mathbf{B}_3 \end{pmatrix} ,$$

where $\mathcal{V}$ is said to be the Vandermonde matrix having elements α_j^{i-1} for $i, j = 1, 2, 3$, and $\alpha_3 = 0$ (Hu & Dasgupta, 2008). Now, the constituent fields may be expressed as

$$\begin{pmatrix} \mathbf{B}_1 \\ \mathbf{B}_2 \\ \mathbf{B}_3 \end{pmatrix} = \mathcal{V}^{-1} \begin{pmatrix} \mathbf{B} \\ \nabla\times\mathbf{B} \\ \nabla\times(\nabla\times\mathbf{B}) \end{pmatrix} . \tag{2.44}$$

Now, as evident from the term $\nabla\times(\nabla\times\mathbf{B})$ in the right-hand column of equation 2.44, double derivatives are required for calculation. In the context of the solar corona, this translates into the requirement of two layers of magnetogram in the solar atmosphere. This criterion is not often met because routine observations of the magnetic field are available only for the photosphere and hence only one layer of magnetogram is possible. In order to get around this problem, the potential magnetic field is initially set to zero, thus leading to

$$\mathbf{B} = \mathbf{B}_1 + \mathbf{B}_2 , \tag{2.45}$$

where $\mathbf{B}_1$ and $\mathbf{B}_2$ are linear force-free fields. Then, the z components of $\mathbf{B}_1$ and $\mathbf{B}_2$ at the bottom boundary can be obtained by taking the curl of equation 2.45, as follows

$$\begin{aligned} (\nabla\times\mathbf{B}^{\text{obs}})_z &= \alpha_1\mathbf{B}_{1,z} + \alpha_2\mathbf{B}_{2,z} , \\ (\nabla\times\mathbf{B}^{\text{obs}})_z &= \alpha_1\mathbf{B}_{1,z} + \alpha_2(\mathbf{B}_z^{\text{obs}} - \mathbf{B}_{1,z}) , \\ \mathbf{B}_{1,z} &= \frac{1}{\alpha_1-\alpha_2}\left[(\nabla\times\mathbf{B}^{\text{obs}})_z - \alpha_2\mathbf{B}_z^{\text{obs}}\right] , \quad (2.46) \\ \mathbf{B}_{2,z} &= \frac{1}{\alpha_2-\alpha_1}\left[(\nabla\times\mathbf{B}^{\text{obs}})_z - \alpha_1\mathbf{B}_z^{\text{obs}}\right] , \quad (2.47) \end{aligned}$$

where $\mathbf{B}^{\text{obs}}$ refers to the magnetic field of vector magnetogram. Subsequently, for a given choice of α_1 and α_2, linear force-free field solver can be used to extrapolate the constituent fields, namely $\mathbf{B}_1$ and $\mathbf{B}_2$. The next step is to find an optimal pair of α_i by minimizing the average normalized deviation of the magnetogram transverse field ($\mathbf{B}_t^{\text{obs}}$) and extrapolated transverse field ($\mathbf{B}_t$), quantified as

$$E_n = \sum_{i=1}^{M} \left(|\mathbf{B}_{t,i}^{\text{obs}} - \mathbf{B}_{t,i}| \times |\mathbf{B}_{t,i}^{\text{obs}}| \right) / \sum_{i=1}^{M} |\mathbf{B}_{t,i}^{\text{obs}}| \ , \tag{2.48}$$

where $M = N^2$ is the total number of grid points on the bottom boundary plane. The state of minimum error corresponds to the optimized pair (α_1, α_2). Hu et al. (2010) introduced further improvements in the extrapolation procedure. The potential magnetic field $\mathbf{B}_3$ is decomposed as

$$\mathbf{B}_3 = \mathbf{B}_3^{(0)} + \mathbf{B}_3^{(1)} + \mathbf{B}_3^{(2)} + ... + \mathbf{B}_3^{(k)} \ , \tag{2.49}$$

where $\mathbf{B}_3^{(0)} = \mathbf{0}$ corresponds to the initial choice of no potential field. Now, using $\mathbf{B}_t = \mathbf{B}_{1t} + \mathbf{B}_{2t} + \mathbf{B}_{3t}^{(k)}$, the transverse difference $\triangle \mathbf{b}_t = \mathbf{B}_t^{\text{obs}} - \mathbf{B}_t$ is utilized to estimate the z-component of $\mathbf{B}_3^{(k+1)}$ (Venkatakrishnan & Gary, 1989), as follows

$$\mathbf{B}_{3z}^{(k+1)} = \mathcal{F}^{-1} \left[\frac{iv\mathcal{F}(\triangle \mathbf{b}_y) + iu\mathcal{F}(\triangle \mathbf{b}_x)}{\sqrt{(u^2 + v^2)}} \right] \ , \tag{2.50}$$

where $\mathcal{F}(\mathcal{F}^{-1})$ denote the Fourier(inverse Fourier) transforms with u and v as frequency domain variables. Subsequently, an estimation of transverse component $\mathbf{B}_{3t}^{(k+1)}$ is carried out by idealizing a periodic boundary condition. Afterwards, E_n is estimated, $\triangle \mathbf{b}_t$ is calculated, and the whole procedure is repeated until the value of E_n approximately saturates with the number of iterations, making the solution unique. Importantly, the procedure alters the bottom boundary and a correlation with the original magnetogram is necessary to check for the accuracy.

2.6 Summary

The chapter focuses on the importance of multi-wavelength observations, magnetic field measurements, and modeling of magnetic field in the solar atmosphere for the exploration of eruptive events. In this regard, measurements of the soft X-ray flux from the GOES satellite, imaging observations from SDO/AIA, and photospheric magnetic field measurements from SDO/HMI are presented. Further, for modeling of magnetic field, force-free field and non-force-free field extrapolation models are discussed. The extrapolation of magnetic field in the solar atmosphere is essential from the perspective of investigating the magnetic structures (e.g. coronal loops, magnetic flux ropes, sheared arcades) and reconnection sites such as the magnetic null points, quasi-separatrix layers, and hyperbolic flux tubes. However, in order to explore the dynamical evolution of magnetic field with time and to compare that with the spatio-temporal evolution of a transient activity in detail, numerical simulations are required. In this regard, the next chapter discusses the framework of the numerical model employed for carrying out the simulations presented in this thesis.

Chapter 3

Numerical Model for MHD Simulations: EULAG-MHD

3.1 Introduction

The implications of magnetic reconnection during a solar transient can be explored by solving the MHD equations with suitable initial conditions. Contextually, the process of solving the MHD equations numerically using an extrapolated magnetic field as the initial condition refers to a data-based MHD simulation. In this regard, the focus of this chapter is to outline the framework of the numerical model used for carrying out the data-based simulations presented in the thesis. Relevantly, it is informative to envisage the momentum balance and magnetic induction equations as transport equations. The form of a transport equation follows straightforwardly from the Navier-Stokes equation for a fluid parcel (Choudhuri, 1998), given by

$$\frac{\partial \mathbf{v}}{\partial t} + (\mathbf{v} \cdot \nabla)\mathbf{v} = \mathbf{R}^{\mathbf{v}} \ , \tag{3.1}$$

where $\mathbf{v}$ represents plasma flow and $\mathbf{R}^{\mathbf{v}}$ represents the forces acting on the plasma parcel. Similarly, the transport of any scalar field φ by the motion of the fluid is given by

$$\frac{\partial \varphi}{\partial t} + (\mathbf{v} \cdot \nabla)\varphi = \mathbf{R}^{\varphi} \ . \tag{3.2}$$

Notably, the transported quantity can also be a vector field, such as the magnetic field $\mathbf{B}$, transported by the plasma flow $\mathbf{v}$ in a magnetized plasma. It may be seen that the induction equation can also be written as

$$\frac{\partial \mathbf{B}}{\partial t} + (\mathbf{v} \cdot \nabla)\mathbf{B} = \mathbf{R}^{\mathbf{B}} , \tag{3.3}$$

which represents the transport of magnetic field. Since, plasma flow and magnetic field are the primary variables in MHD, the employed numerical model must solve the transport equations. Importantly, the physical variables and their derivatives need to be discretized on a grid for the numerical solution. To develop these ideas further, figure 3.1 shows a two-dimensional grid, which may be used to visualize the discretized form of derivatives appearing in the transport equation. The Taylor's expansion of the scalar field φ can be expressed as

$$\varphi_{i+1,j} = \varphi_{i,j} + \left.\frac{\partial \varphi}{\partial x}\right|_{i,j} \Delta x + \frac{1}{2!}\left.\frac{\partial^2 \varphi}{\partial x^2}\right|_{i,j} \Delta x^2 + \dots \text{ and} \tag{3.4}$$

$$\varphi_{i-1,j} = \varphi_{i,j} - \left.\frac{\partial \varphi}{\partial x}\right|_{i,j} \Delta x + \frac{1}{2!}\left.\frac{\partial^2 \varphi}{\partial x^2}\right|_{i,j} \Delta x^2 - \dots , \tag{3.5}$$

which can be used to obtain the first-order derivative of φ in the following forms

$$\left.\frac{\partial \varphi}{\partial x}\right|_{i,j} = \frac{\varphi_{i+1,j} - \varphi_{i,j}}{\Delta x} + \mathcal{O}(\Delta x) \text{ or} \tag{3.6}$$

$$\left.\frac{\partial \varphi}{\partial x}\right|_{i,j} = \frac{\varphi_{i+1,j} - \varphi_{i-1,j}}{2\Delta x} + \mathcal{O}(\Delta x^2) . \tag{3.7}$$

The distinction between equations 3.6 and 3.7 is important because the former is only first-order accurate while the latter is second-order accurate. The downside of this higher order accuracy is the presence of spurious oscillations in the solution, also known as dispersion error (Wendt, 1992). Furthermore, the absence of even derivatives in equation 3.7 on the right hand side amounts to lack of numerical diffusion, which is essential for the stability of solution (Wendt, 1992). These ideas are discussed later in greater detail.

Importantly, owing to the high electrical conductivity of coronal plasma, the flux-freezing condition is satisfied everywhere except at small length scales where

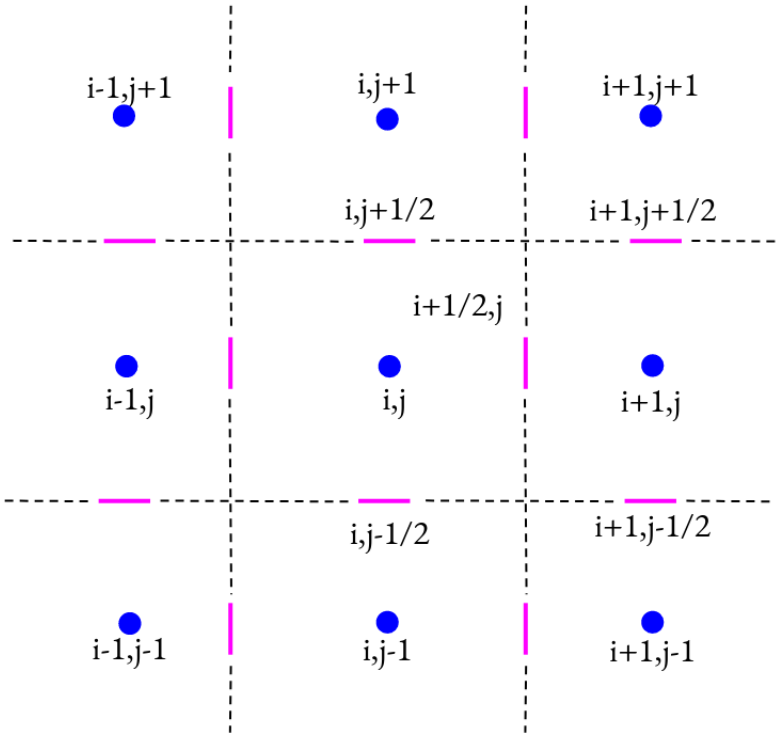

Figure 3.1: A two-dimensional numerical grid, where the i^{th} and j^{th} labels refer to the x and $y-$axis, respectively. The *blue* circles denote the centroid of grid cells, while the *pink* lines mark the edges of grid cells.

the diffusion of magnetic field dominates. Consequently, the numerical simulation of solar transients requires the model to account for the breakdown of flux-freezing condition at small length scales, but to maintain it when away from the localized diffusion region. The inclusion of such disparate physical conditions necessitates a minimization of numerical diffusion and dispersion errors away from the regions of high gradients in magnetic field. For this purpose, the solar MHD variant of the well-established EULAG (Eulerian/semi-Lagrangian fluid solver) model is used in this thesis. Notably, the Eulerian approach estimates changes in system variables at fixed points in space while in a Lagrangian scheme, the focus is on calculating particle trajectories (Smolarkiewicz & Charbonneau, 2013). A combination of the two methods results in a semi-Lagrangian fluid solver, where a Eulerian grid is employed but the equations come from a Lagrangian perspective (Smolarkiewicz & Pudykiewicz, 1992).

The EULAG model was developed to solve the fluid equations pertaining to the geophysical atmosphere and oceans (Prusa et al., 2008). Subsequently, solar MHD was incorporated (Smolarkiewicz & Charbonneau, 2013; Charbonneau &

Smolarkiewicz, 2013) into the model to simulate the solar convection process, thus earning the moniker EULAG-MHD. The operational core of EULAG-MHD is its advection scheme MPDATA (Smolarkiewicz, 1983, 1984; Smolarkiewicz & Clark, 1986) or the Multidimensional Positive Definite Advection Transport Algorithm (reviewed in Smolarkiewicz & Margolin, 1998; Smolarkiewicz & Margolin, 2001; Smolarkiewicz, 2006). Here, the meaning of positive definite is to preserve the sign of advected variable. The simplest example is density, which is a positive quantity by nature and hence, should not become negative during simulation. However, it does not mean that the algorithm is not applicable to negative definite variables (Smolarkiewicz & Clark, 1986). Importantly, the scheme achieves a second-order accuracy in space and time with low numerical diffusion. However, this does not mitigate the dispersion errors completely. To do so, Smolarkiewicz & Grabowski (1990) introduced a nonoscillatory scheme, which preserves the local monotone character of the transported field.

In the context of simulating reconnection, notable is the proven effectiveness of EULAG-MHD to model the effects of dissipative length scales. Basically, the turbulent flows contain eddies of varying sizes and for numerical simulation of such flows, it is usually not feasible to resolve all the eddies and hence their energy. In the conventional Large Eddy Simulation (LES) approach, this situation is tackled by scale-separation, wherein the dynamics of unresolved smallest eddies is taken into account by subgrid scale (SGS) closure models (Grinstein & Drikakis, 2007; Grinstein et al., 2007). In contrast to this, by virtue of being a nonoscillatory finite volume (NFV) scheme, EULAG-MHD can accommodate the effect of small-scales without resorting to the SGS modeling. This property of not requiring the subgrid scale models for simulation of turbulent flows is known as the implicit turbulence modeling (Margolin & Rider, 2002; Margolin et al., 2002; Margolin et al., 2006) and further as Implicit Large Eddy Simulations (ILES; Grinstein et al., 2007), as discussed in the following section.

The physical realizability of the simulations with EULAG-MHD has been well investigated and documented (Margolin et al., 2002, 2006; Smolarkiewicz et al., 2007). In the context of solar and stellar physics, global MHD simulations of turbulent stellar interiors and solar convection (Passos & Charbonneau, 2014; Strugarek et al., 2016; Beaudoin et al., 2018; Monteiro et al., 2023), simulations of current sheet formation (Bhattacharyya et al., 2010; Kumar et al., 2015, 2017), recent inclusion of the Hall magnetohydrodynamics within the EULAG-MHD model (Bora et al., 2021, 2022, 2023), and data-based simulations of solar transients (Prasad et al., 2017, 2018; Nayak et al., 2019; Kumar et al., 2022; Prasad et al., 2023) serve to highlight the applicability and relevancy of the numerical framework. In the following sections, starting with the MPDATA scheme, the details of EULAG-MHD model are discussed in detail.

3.2 The Advection Solver: MPDATA Scheme

As mentioned earlier, the central theme of the numerical model are the methods for solving the transport equations. In this regard, the notion of discretization was introduced (see figure 3.1). Earlier, the scalar function φ was expressed in discrete form (see equations 3.4 and 3.5) but to present the working principle of MPDATA scheme, discretization of the transport equation itself is required. Chronologically, the formulation of MPDATA was carried out in Smolarkiewicz (1983), followed by further developments in multiple notable works such as Smolarkiewicz (1984); Smolarkiewicz & Clark (1986); Smolarkiewicz & Grabowski (1990); Smolarkiewicz (1991); Smolarkiewicz & Margolin (1993); Smolarkiewicz & Charbonneau (2013). In the following, the simplest case of a one-dimensional transport equation for an incompressible fluid is considered (Smolarkiewicz, 1983) to fix the ideas.

3.2.1 Working Principle of MPDATA Scheme

In the absence of any external forcing and Euler equation limit (inviscid flow), the Navier-Stokes equation devolves into the advection equation of a nondiffusive quantity. Then, in an incompressible fluid, the resulting one-dimensional equation for a scalar function φ is given by

$$\partial_t \varphi + \partial_x (u\varphi) = 0 \ , \tag{3.8}$$

where u is the velocity component along $x-$axis. The discretization of the above equation involves an upwind differencing method, where the direction of fluid flow dictates further formulation. To understand this, consider figure 3.2, which shows a one-dimensional numerical grid along with the instances of fluid flow to the right ($\mathbf{u} > 0$) and left ($\mathbf{u} < 0$), respectively. For $\mathbf{u} > 0$, the preference is given to cell centroids on the left, while for $\mathbf{u} < 0$, the centroids on the right are given priority, i.e.

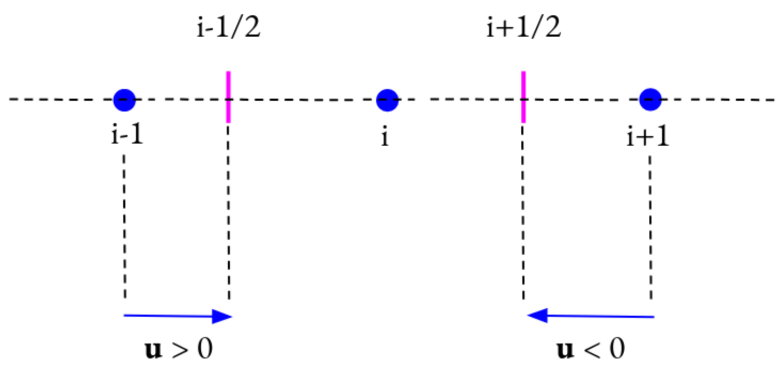

Figure 3.2: A one-dimensional numerical grid, where the i^{th} label refers to the $x-$axis. The *blue* circles denote the cell centroid, while the *pink* lines mark the cell edges. The labels $\mathbf{u} > 0$ and $\mathbf{u} < 0$ signify the direction of fluid flow toward right and left, respectively.

$$\varphi_{i+\frac{1}{2}} = \begin{cases} \varphi_i, & \mathbf{u} > 0 \ , \\ \varphi_{i+1}, & \mathbf{u} < 0 \ , \end{cases} \tag{3.9}$$

and

$$\varphi_{i-\frac{1}{2}} = \begin{cases} \varphi_{i-1}, & \mathbf{u} > 0 \ , \\ \varphi_i, & \mathbf{u} < 0 \ . \end{cases} \tag{3.10}$$

Since, the estimated φ at cell centroid and cell edge are same, accuracy is reduced in exchange for stability. We will return to this aspect later but for now, consider the discretized form of equation 3.8, given by

$$\frac{\varphi_i^{n+1} - \varphi_i^n}{\Delta t} + \frac{u_{i+\frac{1}{2}}\varphi_{i+\frac{1}{2}}^n - u_{i-\frac{1}{2}}\varphi_{i-\frac{1}{2}}^n}{\Delta x} = 0 \ , \tag{3.11}$$

where the label n corresponds to the temporal variable. In other words, φ_i^{n+1} refers to the solution at grid point (t^{n+1}, x_i) with $\Delta t = t^{n+1} - t^n$ and $\Delta x = x_{i+\frac{1}{2}} - x_{i-\frac{1}{2}}$ being the temporal and spatial increments, respectively. The two cases of opposing fluid flow directions can be condensed into a unified description as

$$\varphi_i^{n+1} = \varphi_i^n - \frac{\Delta t}{2\Delta x}\left[\varphi_i^n\left(u_{i+\frac{1}{2}} + \mid u_{i+\frac{1}{2}} \mid\right) + \varphi_{i+1}^n\left(u_{i+\frac{1}{2}} - \mid u_{i+\frac{1}{2}} \mid\right)\right]$$

$$+\frac{\Delta t}{2\Delta x}\left[\varphi_i^n\left(u_{i-\frac{1}{2}} - \mid u_{i-\frac{1}{2}} \mid\right) + \varphi_{i-1}^n\left(u_{i-\frac{1}{2}} + \mid u_{i-\frac{1}{2}} \mid\right)\right] . \tag{3.12}$$

Defining $U^{\pm}_{i+\frac{1}{2}} = \frac{\Delta t}{2\Delta x}\left(u_{i+\frac{1}{2}} \pm \mid u_{i+\frac{1}{2}} \mid\right)$ and $U^{\pm}_{i-\frac{1}{2}} = \frac{\Delta t}{2\Delta x}\left(u_{i-\frac{1}{2}} \pm \mid u_{i-\frac{1}{2}} \mid\right)$, φ_i^{n+1} may be expressed as

$$\varphi_i^{n+1} = \varphi_i^n - \left(\varphi_i^n U^+_{i+\frac{1}{2}} + \varphi_{i+1}^n U^-_{i+\frac{1}{2}}\right) + \left(\varphi_i^n U^-_{i-\frac{1}{2}} + \varphi_{i-1}^n U^+_{i-\frac{1}{2}}\right) , \tag{3.13}$$

which can be recasted into a flux form, given by

$$\varphi_i^{n+1} = \varphi_i^n - \left\{F\left(\varphi_i^n, \varphi_{i+1}^n, U_{i+\frac{1}{2}}\right) - F\left(\varphi_{i-1}^n, \varphi_i^n, U_{i-\frac{1}{2}}\right)\right\} . \tag{3.14}$$

The flux function F can be compactly written as

$$F(\varphi_l, \varphi_r, U) \equiv U^+\varphi_l + U^-\varphi_r , \tag{3.15}$$

where $(l, r) \equiv (i, i+1)$ or $(i-1, i)$ and for $u \equiv u_{i\pm\frac{1}{2}}$, $U = U^+ + U^- = \frac{u\Delta t}{\Delta x}$ is the local Courant number (Smolarkiewicz & Margolin, 1998). The estimate of φ given by equation 3.14 is also referred to as the donor cell approximation. The concept of positive definite in MPDATA can be understood now in more detail, as follows. Using a periodic solution of the form $\varphi \propto e^{ik(x-ut)}$ in equation 3.12 leads to

$$e^{-iku\Delta t} = 1 - \frac{\Delta t}{\Delta x}\left[|u| + e^{ik\Delta x}\left(\frac{u - |u|}{2}\right) - e^{-ik\Delta x}\left(\frac{u + |u|}{2}\right)\right] , \tag{3.16}$$

which can be written as

$$e^{-iku\Delta t} = 1 - \frac{\Delta t}{\Delta x}\left[|u| + u\left(\frac{e^{ik\Delta x} - e^{-ik\Delta x}}{2}\right) - |u|\left(\frac{e^{ik\Delta x} + e^{-ik\Delta x}}{2}\right)\right] , \tag{3.17}$$

$$e^{-iku\Delta t} = 1 - \frac{\Delta t}{\Delta x}\Big[|u| - |u|\cos(k\Delta x) + \mathrm{i}u\sin(k\Delta x)\Big] . \tag{3.18}$$

The stability of solution necessitates $|e^{-iku\Delta t}| \leq 1$, which may be seen to translate into the requirement

$$\left|\frac{\Delta t}{\Delta x} u\sin(k\Delta x)\right| \leq 1 \Rightarrow \frac{\Delta t}{\Delta x}|u| \cdot |\sin(k\Delta x)| \leq 1 \ . \tag{3.19}$$

Therefore, the criterion $\max|\sin(k\Delta x)| = 1$ implies that the stability condition in donor cell scheme for every time step has the form

$$\max\left(\frac{\Delta t|u|}{\Delta x}\right) \leq 1 \ , \tag{3.20}$$

which ensures the positive definite behavior of the advected variable (see equation 3.12). The preceding analysis completes the stability aspect of the upwind scheme, as described earlier. However, being only first-order accurate (both in space and time), the amount of numerical diffusion is large. The properties associated with diffusion are brought to the surface by what is known as the modified equation analysis (MEA; Margolin et al., 2006). It utilizes the Taylor's expansion to identify the partial differential equation whose solution closely approximates the solution of numerical algorithm. The Taylor's expansion of φ upto second-order about (n, i) are given by

$$\varphi_i^{n+1} = \varphi_i^n + \left.\frac{\partial \varphi_i}{\partial t}\right|_n \Delta t + \frac{1}{2!}\left.\frac{\partial^2 \varphi_i}{\partial t^2}\right|_n (\Delta t)^2 + ... \ , \tag{3.21}$$

$$\varphi_{i\pm1}^n = \varphi_i^n \pm \left.\frac{\partial \varphi^n}{\partial x}\right|_i \Delta x + \frac{1}{2!}\left.\frac{\partial^2 \varphi^n}{\partial x^2}\right|_i (\Delta x)^2 + ... \ . \tag{3.22}$$

Further, for the simpler case of $u =$ const., the second-order derivative of φ with respect to time can be represented as

$$\frac{\partial^2 \varphi}{\partial t^2} = \frac{\partial}{\partial t}\left(\frac{\partial \varphi}{\partial t}\right) = \frac{\partial}{\partial x}\frac{\partial x}{\partial t}\left[-\frac{\partial}{\partial x}(u\varphi)\right] = \frac{\partial}{\partial x}\left(u^2 \frac{\partial \phi}{\partial x}\right) \ . \tag{3.23}$$

The substitution of these equations in 3.12 leads to

$$\left.\frac{\partial \varphi_i}{\partial t}\right|_n = -\left.\frac{\partial}{\partial x}(u\varphi^n)\right|_i + \left.\frac{\partial}{\partial x}\left[\frac{1}{2}\left(|u|\Delta x - u^2 \Delta t\right)\frac{\partial \varphi^n}{\partial x}\right]\right|_i \ , \tag{3.24}$$

which approximates an advection-diffusion equation (Wendt, 1992) given by

$$\frac{\partial \varphi}{\partial t} + \frac{\partial (u\varphi)}{\partial x} = \frac{\partial}{\partial x}\left(D\frac{\partial \varphi}{\partial x}\right) , \tag{3.25}$$

where, the diffusion coefficient $D = 0.5\,(|u|\Delta x - u^2\Delta t)$ is guaranteed to be positive from the stability condition, which ensures the well-posedness of equation 3.24 in terms of an advection-diffusion problem. On closer inspection, it may be realized that the foundation of diffusion in the numerical algorithm is contained within the second-order (even derivative) truncation term. Further, while diffusion is crucial for stability, too much of it runs the risk of underestimating the solution. Hence, it needs to be minimized. For this purpose, Smolarkiewicz (1983) developed an ingenious numerical trick based on the idea that solutions of the diffusion equation are reversible in time. Its formulation emphasizes on the diffusive component as

$$\frac{\partial \varphi^\star}{\partial t} = \frac{\partial}{\partial x}\left(D\frac{\partial \varphi^\star}{\partial x}\right) = -\frac{\partial}{\partial x}(u_d\varphi^\star) , \tag{3.26}$$

where, $\varphi^\star$ is the solution corresponding to advection, $u_d = -\dfrac{D}{\varphi^\star}\dfrac{\partial \varphi^\star}{\partial x}$ is termed as the diffusion velocity. Subsequently, an anti-diffusion velocity defined as $\tilde{u} = -u_d$, results in the advection equation

$$\partial_t\varphi^\star - \partial_x(\tilde{u}\varphi^\star) = 0 , \tag{3.27}$$

which can be dealt with using a donor cell scheme. The modified scheme is then a two-step process, given by

$$\varphi_i^\star = \varphi_i^n - \left\{F\left(\varphi_i^n, \varphi_{i+1}^n, U_{i+\frac{1}{2}}\right) - F\left(\varphi_{i-1}^n, \varphi_i^n, U_{i-\frac{1}{2}}\right)\right\} , \tag{3.28}$$

$$\varphi_i^{n+1} = \varphi_i^\star - \left\{F\left(\varphi_i^\star, \varphi_{i+1}^\star, \tilde{U}_{i+\frac{1}{2}}\right) - F\left(\varphi_{i-1}^\star, \varphi_i^\star, \tilde{U}_{i-\frac{1}{2}}\right)\right\} , \tag{3.29}$$

where, as earlier, $\tilde{U}^\pm_{i+\frac{1}{2}} = \dfrac{\Delta t}{2\Delta x}\left(\tilde{u}_{i+\frac{1}{2}} \pm \mid \tilde{u}_{i+\frac{1}{2}} \mid\right)$ and $\tilde{U}^\pm_{i-\frac{1}{2}} = \dfrac{\Delta t}{2\Delta x}\left(\tilde{u}_{i-\frac{1}{2}} \pm \mid \tilde{u}_{i-\frac{1}{2}} \mid\right)$, $\tilde{U} = \tilde{U}^+ + \tilde{U}^-$. Further, using the fact that $\tilde{u} = -u_d = \dfrac{D}{\varphi^\star}\partial_x\varphi^\star$ and the relations

$$\partial_x\varphi^\star = \frac{\varphi^\star_{i+1} - \varphi^\star_i}{\Delta x},\ \varphi^\star = \frac{\varphi^\star_{i+1} + \varphi^\star_i}{2}$$

$$\tilde{u}_{i\pm\frac{1}{2}} = \frac{\varphi^\star_{i+1} - \varphi^\star_i}{\varphi^\star_{i+1} + \varphi^\star_i}\left[\frac{\Delta x\left|u_{i\pm\frac{1}{2}}\right| - \Delta t u^2_{i\pm\frac{1}{2}}}{\Delta x}\right] . \tag{3.30}$$

The estimate of φ_i^{n+1} given by 3.29 preserves the sign and is second-order accurate in space and time, as evident by the consideration of second-order derivatives in equations 3.21 and 3.22. Now, in the following, extensions of MPDATA to cases of more than one dimension and $u \neq$ const. are discussed.

3.2.2 Multidimensional MPDATA Scheme

The development of multidimensional MPDATA scheme is quite straightforward. In order to highlight the essential features, a two-dimensional case is considered in the following. Then, the advection equation is given by

$$\partial_t\varphi + \partial_x(u\varphi) + \partial_y(v\varphi) = 0 \ , \tag{3.31}$$

where u and v are the velocities in x and $y-$directions. The corresponding donor cell approximation is then

$$\varphi^{n+1}_{i,j} = \varphi^n_{i,j} - \left\{F\left(\varphi^n_{i,j}, \varphi^n_{i+1,j}, U_{i+\frac{1}{2},j}\right) - F\left(\varphi^n_{i-1,j}, \varphi^n_{i,j}, U_{i-\frac{1}{2},j}\right)\right\}$$

$$- \left\{F\left(\varphi^n_{i,j}, \varphi^n_{i,j+1}, V_{i,j+\frac{1}{2}}\right) - F\left(\varphi^n_{i,j-1}, \varphi^n_{i,j}, V_{i,j-\frac{1}{2}}\right)\right\} . \tag{3.32}$$

Importantly, the modified equation analysis in this case introduces an additional term as follows

$$\frac{\partial^2\varphi}{\partial t^2} = \frac{\partial}{\partial t}\left(\frac{\partial\varphi}{\partial t}\right) = -\frac{\partial}{\partial t}\left[u\frac{\partial\varphi}{\partial x} + v\frac{\partial\varphi}{\partial y}\right] = \left[u\frac{\partial}{\partial x} + v\frac{\partial}{\partial y}\right]\left[u\frac{\partial\varphi}{\partial x} + v\frac{\partial\varphi}{\partial y}\right] ,$$

$$= \frac{\partial}{\partial x}\left(u^2\frac{\partial\varphi}{\partial x}\right) + \frac{\partial}{\partial y}\left(v^2\frac{\partial\varphi}{\partial y}\right) + 2uv\frac{\partial^2\varphi}{\partial x\partial y} . \tag{3.33}$$

The last term in eq. 3.33 corresponds to a cross term, which arises as a consequence of more than one dimension. It ultimately leads to the following

$$\begin{aligned}\left.\frac{\partial \varphi_{i,j}}{\partial t}\right|_n = &-\left.\frac{\partial}{\partial x}(u\varphi^n)\right|_{i,j} - \left.\frac{\partial}{\partial y}(v\varphi^n)\right|_{i,j} + \left.\frac{\partial}{\partial x}\left[\frac{1}{2}\left(|u|\Delta x - u^2\Delta t\right)\frac{\partial \varphi^n}{\partial x}\right]\right|_{i,j} \\ &+\left.\frac{\partial}{\partial y}\left[\frac{1}{2}\left(|v|\Delta y - v^2\Delta t\right)\frac{\partial \varphi^n}{\partial y}\right]\right|_{i,j} - uv\left.\frac{\partial^2 \varphi}{\partial x \partial y}\right|_{i,j}\Delta t \ ,\end{aligned} \tag{3.34}$$

which can be easily seen to approximate

$$\frac{\partial \varphi}{\partial t} + \frac{\partial (u\varphi)}{\partial x} + \frac{\partial (v\varphi)}{\partial y} = \frac{\partial}{\partial x}\left(D_x\frac{\partial \varphi}{\partial x}\right) + \frac{\partial}{\partial y}\left(D_y\frac{\partial \varphi}{\partial y}\right) - uv\frac{\partial^2 \varphi}{\partial x \partial y}\Delta t \ , \tag{3.35}$$

where D_x and D_y are the diffusion coefficients. Notably, the right hand side of eq. 3.35 can be written as

$$\frac{\partial}{\partial x}\left[\frac{1}{\varphi}\left(D_x\frac{\partial \varphi}{\partial x} - \frac{uv}{2}\frac{\partial \varphi}{\partial y}\Delta t\right)\varphi\right] + \frac{\partial}{\partial y}\left[\frac{1}{\varphi}\left(D_y\frac{\partial \varphi}{\partial y} - \frac{uv}{2}\frac{\partial \varphi}{\partial x}\Delta t\right)\varphi\right] \ , \tag{3.36}$$

thus yielding a formulation in terms of diffusion velocity, given by

$$\frac{\partial \varphi^\star}{\partial t} = -\frac{\partial}{\partial x}(u_d^x\varphi^\star) - \frac{\partial}{\partial y}(u_d^y\varphi^\star) \ , \tag{3.37}$$

with anti-diffusion velocities being $\tilde{u}^x = -u_d^x = \frac{1}{\varphi^\star}\left[D_x\frac{\partial \varphi^\star}{\partial x} - \frac{uv}{2}\frac{\partial \varphi^\star}{\partial y}\Delta t\right]$ and $\tilde{u}^y = -u_d^y = \frac{1}{\varphi^\star}\left[D_y\frac{\partial \varphi^\star}{\partial y} - \frac{uv}{2}\frac{\partial \varphi^\star}{\partial x}\Delta t\right]$. The evaluation of the first component of $\tilde{u}^x$, i.e., $\tilde{u}^x_{1} = \frac{1}{\varphi^\star}\left[D_x\frac{\partial \varphi^\star}{\partial x}\right]$ has been discussed earlier in equation 3.30 and now for the second component (denoted by $\tilde{u}^x_{2}$), note that

$$\tilde{u}^x_{2} = -0.5\Delta t\frac{uv}{\varphi^\star}\left.\frac{\partial \varphi^\star}{\partial y}\right|_{i+\frac{1}{2},j} \ , \tag{3.38}$$

which utilizes the following Taylor's expansions for simplification

$$\varphi^\star_{i,j+1} = \varphi^\star_{i+\frac{1}{2},j} - \left.\frac{\partial \varphi^\star}{\partial x}\right|_{i+\frac{1}{2},j}\frac{\Delta x}{2} + \left.\frac{\partial \varphi^\star}{\partial y}\right|_{i+\frac{1}{2},j}\Delta y + ... \ , \tag{3.39}$$

$$\varphi^{\star}_{i,j-1} = \varphi^{\star}_{i+\frac{1}{2},j} - \left.\frac{\partial \varphi^{\star}}{\partial x}\right|_{i+\frac{1}{2},j} \frac{\Delta x}{2} - \left.\frac{\partial \varphi^{\star}}{\partial y}\right|_{i+\frac{1}{2},j} \Delta y + ... \ , \tag{3.40}$$

$$\varphi^{\star}_{i+1,j+1} = \varphi^{\star}_{i+\frac{1}{2},j} + \left.\frac{\partial \varphi^{\star}}{\partial x}\right|_{i+\frac{1}{2},j} \frac{\Delta x}{2} + \left.\frac{\partial \varphi^{\star}}{\partial y}\right|_{i+\frac{1}{2},j} \Delta y + ... \ , \tag{3.41}$$

$$\varphi^{\star}_{i+1,j-1} = \varphi^{\star}_{i+\frac{1}{2},j} + \left.\frac{\partial \varphi^{\star}}{\partial x}\right|_{i+\frac{1}{2},j} \frac{\Delta x}{2} - \left.\frac{\partial \varphi^{\star}}{\partial y}\right|_{i+\frac{1}{2},j} \Delta y + ... \ . \tag{3.42}$$

The addition of equations 3.39 to 3.42 and the algebraic operation [3.39-3.40]+[3.41-3.42] give

$$\varphi^{\star}_{i+\frac{1}{2},j} = \frac{1}{4}\left[\varphi^{\star}_{i,j+1} + \varphi^{\star}_{i,j-1} + \varphi^{\star}_{i+1,j+1} + \varphi^{\star}_{i+1,j-1}\right] \ , \tag{3.43}$$

$$\left.\frac{\partial \varphi^{\star}}{\partial y}\right|_{i+\frac{1}{2},j} = \frac{1}{4\Delta y}\left[\varphi^{\star}_{i,j+1} - \varphi^{\star}_{i,j-1} + \varphi^{\star}_{i+1,j+1} - \varphi^{\star}_{i+1,j-1}\right] \ , \tag{3.44}$$

which when substituted back in equation 3.38 gives

$$\tilde{u}^{x}_{2} = -0.5\Delta t \frac{u_{i+\frac{1}{2},j} v_{i+\frac{1}{2},j}}{\Delta y} \left[\frac{\varphi^{\star}_{i,j+1} - \varphi^{\star}_{i,j-1} + \varphi^{\star}_{i+1,j+1} - \varphi^{\star}_{i+1,j-1}}{\varphi^{\star}_{i,j+1} + \varphi^{\star}_{i,j-1} + \varphi^{\star}_{i+1,j+1} + \varphi^{\star}_{i+1,j-1}}\right] \ . \tag{3.45}$$

Now, the results can be generalized to any number of dimensions. The advection equation for M-dimensional space can be written as

$$\frac{\partial \varphi}{\partial t} + \sum_{k=1}^{M} \frac{\partial}{\partial x^{k}} (u^{k} \varphi) = 0 \ , \tag{3.46}$$

where x^k and u^k refer to the coordinate and velocity along the dimension k, which gives the donor cell scheme as

$$\varphi^{n+1}_{\underset{\sim}{i}} = \varphi^{n}_{\underset{\sim}{i}} - \sum_{k=1}^{M} \left\{ F\left(\varphi^{n}_{\underset{\sim}{i}}, \varphi^{n}_{\underset{\sim}{i}+\underset{\sim}{k}}, U_{\underset{\sim}{i}+\frac{1}{2}\underset{\sim}{k}}\right) - F\left(\varphi^{n}_{\underset{\sim}{i}-\underset{\sim}{k}}, \varphi^{n}_{\underset{\sim}{i}}, U_{\underset{\sim}{i}-\frac{1}{2}\underset{\sim}{k}}\right) \right\} \ , \tag{3.47}$$

where $\underset{\sim}{i}$ is an M-dimensional vector and defines the point on numerical grid where the solution of advected variable is desired. Similarly, $\underset{\sim}{k}$ refers to the unity vector along the k^{th} direction. The MEA analysis of this leads to the following generalized result

$$\left.\frac{\partial \varphi_{\underset{\sim}{i}}}{\partial t}\right|_n = -\sum_{k=1}^{M} \frac{\partial}{\partial x^k}(u^k \varphi^n)\Bigg|_{\underset{\sim}{i}} + \sum_{k=1}^{M} \frac{\partial}{\partial x^k}\left[\frac{1}{2}\left(|u^k|\Delta x^k - (u^k)^2 \Delta t\right)\frac{\partial \varphi^n}{\partial x^k}\right]\Bigg|_{\underset{\sim}{i}}$$
$$-\sum_{k=1}^{M} \frac{\partial}{\partial x^k}\left[\sum_{k'=1, k\neq k'}^{M} 0.5 \Delta t u^k u^{k'} \frac{\partial \varphi^n}{\partial x^{k'}}\right]\Bigg|_{\underset{\sim}{i}} , \tag{3.48}$$

where the 0.5 in last term is to avoid double counting (see equations 3.24 and 3.34 for reference). In a similar manner, it is easy to generalize the expression of the anti-diffusion velocity (see equations 3.30 and 3.45 for reference) as

$$\tilde{u}^k_{\underset{\sim}{i}+\frac{1}{2}\underset{\sim}{k}} = \frac{\varphi^\star_{\underset{\sim}{i}+\underset{\sim}{k}} - \varphi^\star_{\underset{\sim}{i}}}{\varphi^\star_{\underset{\sim}{i}+\underset{\sim}{k}} + \varphi^\star_{\underset{\sim}{i}}}\left[\frac{\Delta x^k |u^k_{\underset{\sim}{i}\pm\frac{1}{2}\underset{\sim}{k}}| - \Delta t (u^k)^2_{\underset{\sim}{i}\pm\frac{1}{2}\underset{\sim}{k}}}{\Delta x^k}\right] - 0.5\Delta t \sum_{k'=1, k\neq k'}^{M} \frac{u^k_{\underset{\sim}{i}\pm\frac{1}{2}\underset{\sim}{k}} u^{k'}_{\underset{\sim}{i}\pm\frac{1}{2}\underset{\sim}{k}'}}{\Delta x^{k'}}$$
$$\times \left[\frac{\varphi^\star_{\underset{\sim}{i}+\underset{\sim}{k}'} - \varphi^\star_{\underset{\sim}{i}-\underset{\sim}{k}'} + \varphi^\star_{\underset{\sim}{i}+\underset{\sim}{k}+\underset{\sim}{k}'} - \varphi^\star_{\underset{\sim}{i}+\underset{\sim}{k}-\underset{\sim}{k}'}}{\varphi^\star_{\underset{\sim}{i}+\underset{\sim}{k}'} + \varphi^\star_{\underset{\sim}{i}-\underset{\sim}{k}'} + \varphi^\star_{\underset{\sim}{i}+\underset{\sim}{k}+\underset{\sim}{k}'} + \varphi^\star_{\underset{\sim}{i}+\underset{\sim}{k}-\underset{\sim}{k}'}}\right] . \tag{3.49}$$

So far, the case of constant u^k has been considered for analysis. In the following, the cases of space and time dependent velocity fields are discussed. Using the case of one-dimensional advection equation, the second-order time derivative of φ is

$$\frac{\partial^2 \varphi}{\partial t^2} = \frac{\partial}{\partial t}\left(\frac{\partial \varphi}{\partial t}\right) = \frac{\partial}{\partial x}\frac{\partial x}{\partial t}\left[-\frac{\partial}{\partial x}(u\varphi)\right] = \frac{\partial}{\partial x}\left[u\frac{\partial}{\partial x}(u\varphi)\right]$$
$$= \frac{\partial}{\partial x}\left[u\frac{\partial u}{\partial x}\varphi\right] + \frac{\partial}{\partial x}\left[u^2\frac{\partial \varphi}{\partial x}\right] , \tag{3.50}$$

where the first term appears due to space dependence of velocity. Similarly, in the case of time dependence

$$\frac{\partial^2 \varphi}{\partial t^2} = \frac{\partial}{\partial t}\left(\frac{\partial \varphi}{\partial t}\right) = \frac{\partial}{\partial t}\left[-\frac{\partial}{\partial x}(u\varphi)\right] = -\frac{\partial}{\partial x}\left[\frac{\partial}{\partial t}(u\varphi)\right] = -\frac{\partial}{\partial x}\left[\frac{\partial u}{\partial t}\varphi\right] + \frac{\partial}{\partial x}\left[u\frac{\partial}{\partial x}(u\varphi)\right]$$
$$-\frac{\partial}{\partial x}\left[\frac{\partial u}{\partial t}\varphi\right] + \frac{\partial}{\partial x}\left[u\frac{\partial}{\partial x}(u\varphi)\right] = -\frac{\partial}{\partial x}\left[\frac{\partial u}{\partial t}\varphi\right] + \frac{\partial}{\partial x}\left[u^2\frac{\partial \varphi}{\partial x}\right] , \tag{3.51}$$

where the first term arises due to time dependence. Consequently, in the case of more than one dimension, the modified equation analysis includes additional terms of the form

$$\left.\frac{\partial \varphi_{\underset{\sim}{i}}}{\partial t}\right|_n = ... - \sum_{k=1}^{M} \frac{\partial}{\partial x^k}\left[0.5\Delta t\left(u^k \sum_{k'=1}^{M}\frac{\partial u^{k'}}{\partial x^{k'}}\right)\varphi^n\right]\Bigg|_{\tilde{i}} + \sum_{k=1}^{M}\frac{\partial}{\partial x^k}\left[0.5\Delta t\frac{\partial u^k}{\partial t}\varphi^n\right]\Bigg|_{\tilde{i}} , \tag{3.52}$$

where the ... refers to equation 3.48. These functional dependencies of the velocity field alter the expression of anti-diffusion velocity also. Importantly, for the case of time dependence, the expression for anti-diffusion velocity is as follows

$$\tilde{u}^k_{\underset{\sim}{i}+\frac{1}{2}\underset{\sim}{k}} = ... + \sum_{k=1}^{M} 0.5\Delta t \left.\frac{\partial u^k}{\partial t}\right|_{\underset{\sim}{i}+\frac{1}{2}\underset{\sim}{k}} , \tag{3.53}$$

where the ... refers to equation 3.49. The use of equation 3.53 to minimize temporal truncation error introduces higher order numerical diffusion, which is contradictory to the objective of improving the accuracy (Smolarkiewicz & Clark, 1986). Hence, to resolve this, the temporal positioning of u and φ (see equation 3.46) are decoupled as

$$\frac{\varphi^{n+1}-\varphi^n}{\Delta t} = -\sum_{k=1}^{M}\frac{\partial}{\partial x^k}\left[{}^{n+\frac{1}{2}}u^k\varphi^{n}\right] , \tag{3.54}$$

where the circles highlight the decoupling of temporal labels. Then, using Taylor's series expansions up to second-order given by

$$\varphi^{n+1} = \varphi^n + \Delta t\left.\frac{\partial \varphi}{\partial t}\right|_n - 0.5\nabla\cdot\left[\frac{\partial \mathbf{u}}{\partial t}\varphi\right]\Delta t^2 + 0.5\nabla\cdot\left[\mathbf{u}\nabla\cdot(\mathbf{u}\varphi)\right]\Delta t^2 , \tag{3.55}$$

$$\mathbf{u}^{n+\frac{1}{2}} = \mathbf{u}^n + \frac{1}{2}\Delta t\left.\frac{\partial \mathbf{u}}{\partial t}\right|_n + \mathcal{O}(\Delta t^2) , \tag{3.56}$$

where both $\mathbf{u}$ and ∇ are M-dimensional, the modified equation analysis results in the following generalized equation

$$\frac{\partial \varphi}{\partial t} + \nabla\cdot(\mathbf{u}\varphi) = -0.5\Delta t\nabla\cdot\left[(\mathbf{u}.\nabla\varphi)\mathbf{u} + \mathbf{u}\varphi(\nabla\cdot\mathbf{u})\right] + \mathcal{O}(\Delta t^2) , \tag{3.57}$$

where the $\mathcal{O}(\Delta t)$ truncation error is eliminated. In the generalized case of a forcing term R, the Taylor's expansion given by

$$R^{n+\frac{1}{2}} = R^n + 0.5\Delta t\nabla\cdot(\mathbf{u}R)\big|_n + \mathcal{O}(\Delta t^2) , \tag{3.58}$$

can be used to obtain

$$\frac{\partial\varphi}{\partial t} + \nabla\cdot(\mathbf{u}\varphi) = R - 0.5\Delta t\nabla\cdot\left[(\mathbf{u}.\nabla\varphi)\mathbf{u} + \mathbf{u}\varphi(\nabla\cdot\mathbf{u})\right] + 0.5\Delta t\nabla\cdot(\mathbf{u}R) + \mathcal{O}(\Delta t^2)\ . \tag{3.59}$$

Notably, in equation 3.59, the first-order truncation error associated with R is not compensated. Smolarkiewicz (1991) suggested to subtract the donor cell scheme approximation of the term $0.5\Delta t\nabla\cdot(\mathbf{u}R)$ from the right hand side of equation 3.59 to achieve second-order accuracy, represented by

$$\varphi_{\underset{\sim}{i}}^{n+1} = \varphi_{\underset{\sim}{i}}^{n} + R_{\underset{\sim}{i}}^{n+\frac{1}{2}}\Delta t - \mathcal{A}\mathrm{II}_{\underset{\sim}{i}}\left[\varphi^n, \mathbf{U}^{n+\frac{1}{2}}\right] - \mathcal{A}\mathrm{I}_{\underset{\sim}{i}}\left[0.5\Delta t R_{\underset{\sim}{i}}^{n}, \mathbf{U}^{n}\right]\ , \tag{3.60}$$

where $\mathcal{A}\mathrm{II}_{\underset{\sim}{i}}$ and $\mathcal{A}\mathrm{I}_{\underset{\sim}{i}}$ are advective flux-divergence operators from second and first-order accurate dissipative advection schemes (Smolarkiewicz, 1991; Smolarkiewicz & Margolin, 1993). Also, $\mathbf{U}$ refers to the M-dimensional vector of the local Courant numbers. Furthermore, the assumption $R_{\underset{\sim}{i}}^{n+\frac{1}{2}} = \dfrac{1}{2}\left[R_{\underset{\sim}{i}}^{n} + R_{\underset{\sim}{i}}^{n+1}\right]$ and the freedom to take Courant number at $n+\frac{1}{2}$ than n (Smolarkiewicz & Margolin, 1993) gives

$$\varphi_{\underset{\sim}{i}}^{n+1} = \mathcal{D}\mathrm{II}_{\underset{\sim}{i}}\left[\varphi_{\underset{\sim}{i}}^{n}, \mathbf{U}^{n+\frac{1}{2}}\right] + \mathcal{D}\mathrm{I}_{\underset{\sim}{i}}\left[0.5\Delta t R_{\underset{\sim}{i}}^{n}, \mathbf{U}^{n+\frac{1}{2}}\right] + R_{\underset{\sim}{i}}^{n+1}\frac{\Delta t}{2}\ , \tag{3.61}$$

where, $\mathcal{D}\mathrm{II}_{\underset{\sim}{i}}$ and $\mathcal{D}\mathrm{I}_{\underset{\sim}{i}}$ denote the second-order and first-order accurate advection schemes (Smolarkiewicz & Margolin, 1993). Lastly, benefiting from the MPDATA scheme, both $\mathcal{D}\mathrm{II}_{\underset{\sim}{i}}$ and $\mathcal{D}\mathrm{I}_{\underset{\sim}{i}}$ can be placed under the same roof, giving

$$\varphi_{\underset{\sim}{i}}^{n+1} = \mathrm{MPDATA}\left[\varphi_{\underset{\sim}{i}}^{n} + 0.5\Delta t R_{\underset{\sim}{i}}^{n}, \mathbf{U}^{n+\frac{1}{2}},\right] + R_{\underset{\sim}{i}}^{n+1}\frac{\Delta t}{2}\ . \tag{3.62}$$

Notably, the estimation of velocities at the time stamp $n+\frac{1}{2}$ utilizes interpolation or extrapolation (not to be confused with magnetic field extrapolation) schemes such that the second-order accuracy is maintained. Some examples are

$${}^{n+\frac{1}{2}}u^k_{\underset{\sim}{i}+\frac{1}{2}\underset{\sim}{k}} = 0.5\left[{}^{n}u^k_{\underset{\sim}{i}+\frac{1}{2}\underset{\sim}{k}} + {}^{n+1}u^k_{\underset{\sim}{i}+\frac{1}{2}\underset{\sim}{k}}\right]\ , \tag{3.63}$$

$${}^{n+\frac{1}{2}}u^k_{\underset{\sim}{i}+\frac{1}{2}\underset{\sim}{k}} = 0.5\left[3({}^{n}u^k_{\underset{\sim}{i}+\frac{1}{2}\underset{\sim}{k}}) - {}^{n-1}u^k_{\underset{\sim}{i}+\frac{1}{2}\underset{\sim}{k}}\right]\ . \tag{3.64}$$

For the subtleties involved in a particular choice of $\mathbf{u}^{n+\frac{1}{2}}$, readers are referred to (Smolarkiewicz & Clark, 1986). In the following, details of the nonoscillatory option are presented to complete the description of MPDATA scheme.

3.2.3 Nonoscillatory Feature of MPDATA Scheme

The nonoscillatory feature of MPDATA scheme works to control the unphysical oscillations in the solution, which might appear due to an overestimation of flux terms. This is also referred to as the preservation of monotonicity of the advected variable. In MPDATA scheme, this is achieved by implementing the flux-corrected transport (FCT) methodology (Boris & Book, 1973; Book et al., 1975; Boris & Book, 1976). The basic principle of this can be understood by writing the advection algorithm for φ as

$$\varphi_{\underset{\sim}{i}}^{n+1} = \varphi_{\underset{\sim}{i}}^{n} - \sum_{k=1}^{M}\left[FH^{k}_{\underset{\sim}{i}+\frac{1}{2}\underset{\sim}{k}} - FH^{k}_{\underset{\sim}{i}-\frac{1}{2}\underset{\sim}{k}}\right] , \tag{3.65}$$

where $FH^{k}_{\underset{\sim}{i}\pm\frac{1}{2}\underset{\sim}{k}}$ refers to any high order flux term (Smolarkiewicz & Grabowski, 1990). Importantly, this can be decomposed as $FH^{k}_{\underset{\sim}{i}\pm\frac{1}{2}\underset{\sim}{k}} = FL^{k}_{\underset{\sim}{i}\pm\frac{1}{2}\underset{\sim}{k}} + A^{k}_{\underset{\sim}{i}\pm\frac{1}{2}\underset{\sim}{k}}$, where $FL^{k}_{\underset{\sim}{i}\pm\frac{1}{2}\underset{\sim}{k}}$ and $A^{k}_{\underset{\sim}{i}\pm\frac{1}{2}\underset{\sim}{k}}$ have the sense of a low order flux term and residual flux which serves to correct at least the first-order truncation error. This leads to the result

$$\varphi_{\underset{\sim}{i}}^{n+1} = \Phi_{\underset{\sim}{i}}^{n+1} - \sum_{k=1}^{M}\left[A^{k}_{\underset{\sim}{i}+\frac{1}{2}\underset{\sim}{k}} - A^{k}_{\underset{\sim}{i}-\frac{1}{2}\underset{\sim}{k}}\right] , \tag{3.66}$$

where $\Phi_{\underset{\sim}{i}}^{n+1}$ is the solution from lower order scheme. The monotonicity of φ, given by $\varphi_{\underset{\sim}{i}}^{\max} \geq \Phi_{\underset{\sim}{i}}^{n+1} \geq \varphi_{\underset{\sim}{i}}^{\min}$ is then obtained by limiting the residual flux as

$$\tilde{A}^{k}_{\underset{\sim}{i}+\frac{1}{2}\underset{\sim}{k}} = C^{k}_{\underset{\sim}{i}+\frac{1}{2}\underset{\sim}{k}} A^{k}_{\underset{\sim}{i}+\frac{1}{2}\underset{\sim}{k}} , \tag{3.67}$$

where the coefficients $C^{k}_{\underset{\sim}{i}+\frac{1}{2}\underset{\sim}{k}}$ satisfy $0 \leq C^{k}_{\underset{\sim}{i}+\frac{1}{2}\underset{\sim}{k}} \leq 1$. Further, the determination of the limiting values $\varphi_{\underset{\sim}{i}}^{\max}$ and $\varphi_{\underset{\sim}{i}}^{\min}$ allows the estimation of maximum possible residual flux so that there is no overestimation. In order to conclude the discussion of MPDATA scheme, the aspects of its application in the context of Implicit Large Eddy Simulations (ILES) are described in the following section.

3.2.4 ILES using MPDATA Scheme

As mentioned earlier, the implication of ILES is the modeling of small-scale effects by the inherent dissipative character of the numerical model. Further, the foregoing discussion of the MPDATA scheme has revealed the association between truncation errors and diffusion of the advected variable. Consequently, the question pertaining to the physical justification of numerical diffusion in modeling of turbulent flows is natural. It turns out that the rationale for using the nonoscillatory finite volume (NFV) algorithms such as MPDATA emerges from their accurate approximation of the equations that govern the dynamics of finite fluid volumes (Margolin et al., 2002, 2006; Margolin et al., 2006). Contextually, note that the equations governing the dynamics of an infinitesimal point and a finite volume are not same (Margolin & Rider, 2002). However, the latter may be derived from spatial (Δx) and temporal (Δt) averaging of the point equations. This leads to nonlinear dispersion terms in finite volume equations (Margolin & Rider, 2002). The resemblance of these terms with truncation terms obtained during the MEA analysis of the MPDATA scheme or any other NFV algorithm in general, provides the required physical justification. The dissipation in ILES approach is adaptive, meaning that it does not simply add in to the physical dissipation (Margolin et al., 2006). Importantly, the length scales involved in averaging reflect the length scale of observer in the sense of numerical resolution allowed by the computational grid. Therefore, the finite volume equations and hence the NFV algorithms are practical and realistic descriptions (Margolin et al., 2006). In the context of simulating solar transients with ILES approach, note that the small length scales or the under-resolved scales are recognized as the locations of magnetic reconnection. The controlled numerical dissipation of the MPDATA scheme relates to the diffusion term ($\eta\nabla^2\mathbf{B}$) of the magnetic induction equation. This leads to the onset of magnetic reconnections that are consistent and collocated with the reconnection sites. In a nutshell, the MPDATA scheme and it's ILES property are central to the numerical simulation of solar transients, which are manifestations of magnetic reconnection. In the following, the algorithm of EULAG-MHD is described, which gives more insight into the step-wise procedure used to solve the MHD equations.

3.3 Algorithm of the EULAG-MHD

As discussed earlier, it is important to visualize the MHD equations as transport equations. In this regard, equations 3.1 and 3.3 were only indicative and now, the required formalism is presented in more detail. The EULAG-MHD framework solves[†] the MHD equations in a non-rotating Cartesian coordinate system for an incompressible magnetofluid with zero physical resistivity. The momentum balance equation, given by

$$\rho_0 \left[\frac{\partial \mathbf{v}}{\partial t} + (\mathbf{v} \cdot \nabla)\mathbf{v} \right] = \mathbf{J} \times \mathbf{B} - \nabla p + \mu \nabla^2 \mathbf{v} \ , \tag{3.68}$$

where ρ_0 and μ denote a constant mass density and the dynamic viscosity, can be written as

$$\begin{aligned} \frac{\partial \mathbf{v}}{\partial t} + (\mathbf{v} \cdot \nabla)\mathbf{v} &= \frac{1}{\rho_0} \left[(\mathbf{B} \cdot \nabla)\mathbf{B} - \nabla \left(\frac{B^2}{2} + p \right) + \mu \nabla^2 \mathbf{v} \right] \ , \\ \frac{\partial \mathbf{v}}{\partial t} + \nabla \cdot (\mathbf{v}\mathbf{v}) &= \frac{1}{\rho_0} (\mathbf{B} \cdot \nabla)\mathbf{B} - \nabla \phi + \nu \nabla^2 \mathbf{v} \ , \\ \frac{\partial \mathbf{v}}{\partial t} + \nabla \cdot (\mathbf{v}\mathbf{v}) &= \mathbf{R}^{\mathbf{v}} \ , \end{aligned} \tag{3.69}$$

where $\mathbf{R}^{\mathbf{v}} = -\nabla \phi + \dfrac{1}{\rho_0}(\mathbf{B} \cdot \nabla)\mathbf{B} + \mathbf{F}_\nu$ with ϕ as density normalized total pressure and $\mathbf{F}_\nu$ as the viscous drag force. All the other symbols have their usual meaning. Consequently, equations 3.3 and 3.69, along with the conditions of incompressible plasma flow and solenoidality of magnetic field, give

$$\partial_t \mathbf{v} + \nabla \cdot (\mathbf{v}\mathbf{v}) = \mathbf{R}^{\mathbf{v}} \ , \tag{3.70}$$

$$\partial_t \mathbf{B} + \nabla \cdot (\mathbf{v}\mathbf{B}) = \mathbf{R}^{\mathbf{B}} \ , \tag{3.71}$$

$$\nabla \cdot \mathbf{v} = 0 \ , \tag{3.72}$$

$$\nabla \cdot \mathbf{B} = 0 \ , \tag{3.73}$$

which represent the set of equations solved by the EULAG-MHD for simulation of solar transients. Importantly, to reduce the extent of nonlinearities posed by the MHD equations and to simplify the model problem, the EULAG-MHD framework

[†]EULAG-MHD code can use either CGS, MKS, or dimensionless units

utilizes the anelastic approximation (Lantz & Fan, 1999; Prusa & Smolarkiewicz, 2003; Smolarkiewicz & Charbonneau, 2013). In this, the perturbations of density appear in the buoyancy term ($\propto \rho\mathbf{g}$) only, which serves to remove the sound waves from physical description. Consequently, the requirement of high time resolution to track the sound waves is relaxed. Thus, the computational effort is minimized. Notably, the approximation allows density to have spatial dependence, which helps to include stratification without resorting to compressibility. There exists another important facet of EULAG, namely the formulation of governing equations in a transformed time-dependent generalized curvilinear coordinates, given by

$$(\bar{t}, \bar{\mathbf{x}}) \equiv (t, F(t, \mathbf{x})) \ , \tag{3.74}$$

where the domain of physical problem, i.e. $(t, \mathbf{x})$, is assumed to be stationary and orthogonal, but it does not need to be Cartesian. Since, the extrapolation of magnetic field is done for localized regions in Cartesian geometry, the physical domain is Cartesian and it remains so for all times, i.e., $(\bar{t}, \bar{\mathbf{x}}) \equiv (t, \mathbf{x})$. Note that the formulation of EULAG-MHD in generalized coordinates requires an extensive tensorial exposition of the MHD equations (Smolarkiewicz & Charbonneau, 2013). In the following, the details of EULAG-MHD are presented in Cartesian domain. The discussion utilizes original notations of Smolarkiewicz & Charbonneau (2013) to maintain homogeneity with the contemporary literature. It is easy to see that equations 3.70 and 3.71 can be jointly written as

$$\frac{\partial \mathbf{\Psi}}{\partial t} + \nabla \cdot (\mathbf{v}\mathbf{\Psi}) = \mathbf{R}, \tag{3.75}$$

where $\mathbf{\Psi} = \{\mathbf{v}, \mathbf{B}\}^T$ and $\mathbf{R} = \{\mathbf{R}^{\mathbf{v}}, \mathbf{R}^{\mathbf{B}}\}^T$. Consequently, the numerical solutions of $\mathbf{\Psi}$ (see equation 3.62) have the form (Smolarkiewicz & Charbonneau, 2013)

$$\mathbf{\Psi}_{\underset{\sim}{i}}^{n+1} = \text{MPDATA}\left[\mathbf{\Psi}_{\underset{\sim}{i}}^{n} + 0.5\Delta t \mathbf{R}_{\underset{\sim}{i}}^{n}, \mathbf{U}^{n+\frac{1}{2}}\right] + 0.5\Delta t \mathbf{R}_{\underset{\sim}{i}}^{n+1} \equiv \hat{\mathbf{\Psi}}_{\underset{\sim}{i}} + 0.5\Delta t \mathbf{R}_{\underset{\sim}{i}}^{n+1} \ . \tag{3.76}$$

From a numerical standpoint, an auxiliary term $-\nabla\phi^{\star}$ is added to right hand side of equation 3.71 to enforce the solenoidality of magnetic field. Similarly, the pressure ϕ is utilized to keep plasma flow solenoidal. Notably, under the anelastic approximation, the algorithm given by 3.76 is implicit for $\mathbf{\Psi} = \{\mathbf{v}, \mathbf{B}\}^T$, $\phi^\star$, ϕ. Here, the connotation of implicit differs from the one used in Implicit LES. It refers to implicit finite-difference scheme of discretization (Wendt, 1992). Importantly, to incorporate the nonlinearities posed by the set of MHD equations while preserving the structure EULAG template, Smolarkiewicz & Charbonneau (2013) anticipated

$$\mathbf{\Psi}_{\underset{\sim}{i}}^{n+1,q} = \hat{\mathbf{\Psi}}_{\underset{\sim}{i}} + 0.5\delta t \mathbf{L}\mathbf{\Psi}\Big|_{\underset{\sim}{i}}^{n+1,q} + 0.5\delta t \mathbf{N}(\mathbf{\Psi})\Big|_{\underset{\sim}{i}}^{n+1,q-1} - 0.5\delta t \nabla\mathbf{\Phi}\Big|_{\underset{\sim}{i}}^{n+1,q} , \tag{3.77}$$

where the forcing $\mathbf{R}$ is sum of a linear term $\mathbf{L\Psi}$, a nonlinear part of forcing, i.e., $\mathbf{N}(\mathbf{\Psi})$, and a potential term $-\nabla\mathbf{\Phi}$ with $\mathbf{\Phi} \equiv (\phi, \phi, \phi, \phi^\star, \phi^\star, \phi^\star)$. The index $q = 1, 2, .., m$ numbers the fixed point iterations. The expression in 3.77 is implicit with respect to the forcing terms $\mathbf{L\Psi}$ and $-\nabla\mathbf{\Phi}$. To obtain a closed-form expression for ${\mathbf{\Psi}_{\underset{\sim}{i}}}^{n+1,q}$, algebraic manipulation leads to

$$\left[\mathbf{I} - 0.5\delta t \mathbf{L}\right] \mathbf{\Psi}_{\underset{\sim}{i}}^{n+1,q} = \left(\hat{\mathbf{\Psi}} + 0.5\delta t \mathbf{N}(\mathbf{\Psi})\Big|^{n+1,q-1} - 0.5\delta t \nabla\mathbf{\Phi}\Big|^{n+1,q}\right)_{\underset{\sim}{i}} , \tag{3.78}$$

which gives

$$\mathbf{\Psi}_{\underset{\sim}{i}}^{n+1,q} = \left[\mathbf{I} - 0.5\delta t \mathbf{L}\right]^{-1} \left(\hat{\hat{\mathbf{\Psi}}} - 0.5\delta t \nabla\mathbf{\Phi}\Big|^{n+1,q}\right)_{\underset{\sim}{i}} , \tag{3.79}$$

where the explicit element is modified to

$$\hat{\hat{\mathbf{\Psi}}}_{\underset{\sim}{i}} \equiv \hat{\mathbf{\Psi}}_{\underset{\sim}{i}} + 0.5\delta t \mathbf{N}(\mathbf{\Psi})\Big|_{\underset{\sim}{i}}^{n+1,q-1} , \tag{3.80}$$

with explicit referring to the explicit finite-difference scheme (Wendt, 1992). The divergence of equation 3.79 along with $\nabla \cdot \mathbf{v} = \nabla \cdot \mathbf{B} = 0$ generates elliptic Poisson equations for ϕ and $\phi^\star$, which are solved by generalized conjugate residual (GCR) algorithm (Eisenstat et al., 1983; Eisenstat, 1983; Smolarkiewicz & Margolin, 1994; Smolarkiewicz et al., 1997). Subsequently, the time updated $\mathbf{\Psi}$ can be obtained. In EULAG-MHD, the iterations corresponding to the GCR algorithm and those in equation 3.77 are called “inner” and “outer”, respectively. The convergence of outer iterations is controlled by the model time step, while being monitored by the convergence of inner iterations in the GCR solver (Smolarkiewicz & Szmelter, 2009, 2011). The solution is updated upon the completion of outer iterations. For the next time step, implicit forcing becomes $\mathbf{RI}_{\underset{\sim}{i}}^{n+1} = \dfrac{2}{\delta t}(\mathbf{\Psi}_{\underset{\sim}{i}}^{n+1} - \hat{\hat{\mathbf{\Psi}}}_{\underset{\sim}{i}})$. The explicit forcing denoted by $\mathbf{N}(\mathbf{\Psi})$ is evaluated from updated solution as $\mathbf{RE}_{\underset{\sim}{i}}^{n+1} = \mathbf{RE}_{\underset{\sim}{i}}(\mathbf{\Psi}^{n+1})$. The total forcing $\mathbf{R}_{\underset{\sim}{i}}^{n+1} = \mathbf{RI}_{\underset{\sim}{i}}^{n+1} + \mathbf{RE}_{\underset{\sim}{i}}^{n+1}$ is then used in argument of the MPDATA operator in equation 3.76. This completes the description of EULAG-MHD algorithm and now, the implementation of algorithm in the context of magnetohydrodynamics is presented.

3.3.1 Implementation of EULAG-MHD Algorithm

As mentioned earlier, there are two types of iterations, namely the "inner" and "outer'. An outer iteration consists of a "hydrodynamic" and a "magnetic" block. In essence, the hydrodynamic block emulates the standard EULAG solution of hydrodynamical equations (Prusa et al., 2008). In this block, the magnetic field is treated as supplementary input and the elliptic equation for ϕ is solved to return the final updated velocity. This is then used in the magnetic block, where induction equation is solved to obtain the final magnetic field through the solution of elliptic equation for ϕ^*. The sequence of steps executed at each outer iteration for integration of equations 3.70 to 3.73 are discussed below in detail. In order to keep the expressions uncluttered, **the superscript** $n+1$ is dropped. In the first step, magnetic field $\mathbf{B}^{q-1/2}$ is estimated implicitly through inversion of the induction equation

$$\mathbf{B}_{\underset{\sim}{i}}^{q-1/2} = \hat{\mathbf{B}}_{\underset{\sim}{i}} + 0.5\delta t\Big[\mathbf{B}^{q-1/2}\cdot\nabla\mathbf{v}^{q-1} - \mathbf{B}^{q-1/2} tr\{\nabla\mathbf{v}^{q-1}\}\Big]_{\underset{\sim}{i}} , \tag{3.81}$$

which is subsequently utilized to obtain

$$\mathbf{v}_{\underset{\sim}{i}}^{q} = \hat{\mathbf{v}}_{\underset{\sim}{i}} + \frac{0.5\delta t}{\rho_0\mu_0}\nabla\cdot\mathbf{BB}\Big|_{\underset{\sim}{i}}^{q-1/2} - 0.5\delta t\nabla\phi\Big|_{\underset{\sim}{i}}^{q} . \tag{3.82}$$

Notably, this can be expressed in a closed form

$$\mathbf{v}_{\underset{\sim}{i}}^{q} = \hat{\hat{\mathbf{v}}}_{\underset{\sim}{i}} - 0.5\delta t\nabla\phi\Big|_{\underset{\sim}{i}}^{q} , \tag{3.83}$$

which, on imposing the condition of incompressible plasma flow, leads to

$$\nabla\cdot\Big[\hat{\hat{\mathbf{v}}}_{\underset{\sim}{i}} - 0.5\delta t\nabla\phi\Big|_{\underset{\sim}{i}}^{q}\Big] = 0 , \tag{3.84}$$

thus yielding the elliptic equation for total pressure ϕ. Thereafter, the solution of equation 3.84 is used to calculate the required solenoidal velocity (Smolarkiewicz & Margolin, 1997). Using this velocity, the magnetic block calculates

$$\mathbf{B}_{\underset{\sim}{i}}^{q-1/4} = \hat{\mathbf{B}}_{\underset{\sim}{i}} + 0.5\delta t \Big[\mathbf{B}^{q-1/4} \cdot \nabla \mathbf{v}^{q} - \mathbf{B}^{q-1/4} tr\{\nabla \mathbf{v}^{q}\}\Big]_{\underset{\sim}{i}} , \tag{3.85}$$

where $q-1/4$ stands for the calculation at a quarter of iteration. Then, the solution of induction equation is given by

$$\mathbf{B}_{\underset{\sim}{i}}^{q} = \hat{\mathbf{B}}_{\underset{\sim}{i}} + 0.5\delta t \nabla \cdot \mathbf{B}^{q-1/4}\mathbf{v}^{q}\Big|_{\underset{\sim}{i}} - 0.5\delta t \nabla \phi^{\star}\Big|_{\underset{\sim}{i}}^{q} . \tag{3.86}$$

The final updated magnetic field $\mathbf{B}$ is estimated from equation 3.86 by imposing the solenoidality condition and solving the elliptic equation for $\phi^{\star}$. In the following, the practical implementation of the EULAG-MHD model for numerical simulation of solar transients is described.

3.4 MHD Simulation of Solar Transients

The numerical simulation of solar transients requires magnetic reconnection to be localized at the plausible sites, while allowing for the condition of flux-freezing to hold good elsewhere. For the simulations presented in this thesis, the coronal plasma is idealized to be thermodynamically inactive, incompressible magnetofluid. The governing dimensionless MHD equations are

$$\frac{\partial \mathbf{v}}{\partial t} + (\mathbf{v} \cdot \nabla)\mathbf{v} = -\nabla p + (\nabla \times \mathbf{B}) \times \mathbf{B} + \frac{1}{R_F^A} \nabla^2 \mathbf{v}, \tag{3.87}$$

$$\frac{\partial \mathbf{B}}{\partial t} = \nabla \times (\mathbf{v} \times \mathbf{B}), \tag{3.88}$$

$$\nabla \cdot \mathbf{v} = 0, \tag{3.89}$$

$$\nabla \cdot \mathbf{B} = 0, \tag{3.90}$$

where $R_F^A = (V_A L)/\nu$ is an effective fluid Reynolds number with V_A as the Alfvén speed and ν as the kinematic viscosity. Hereafter, R_F^A is referred as fluid Reynolds number to keep the terminology uncluttered. The normalization used to obtain the dimensionless equations are listed below

$$\mathbf{B} \to \frac{\mathbf{B}}{B_0}, \mathbf{v} \to \frac{\mathbf{v}}{V_A}, L \to \frac{L}{L_0}, t \to \frac{t}{\tau_a}, p \to \frac{p}{\rho_0 V_A^2} \ . \tag{3.91}$$

In general, B_0 and L_0 are characteristic values of the system under consideration. The factor $\tau_a = L_0/V_A$ represents the Alfvénic transit time and the Alfvén speed is given by $V_A = B_0/\sqrt{4\pi\rho_0}$, where ρ_0 denotes the constant mass density. Further, the boundary conditions are set to keep the vertical components of magnetic field and velocity field constant at each of the boundaries of computational box. The incompressibility condition is applied on the integral form of momentum equation to generate an elliptic boundary value problem for the pressure, as described in section 3.3.1. Similarly, to keep $\mathbf{B}$ solenoidal, an auxiliary potential is added to the induction equation and an identical procedure is invoked. As discussed earlier, the presented simulations are executed by delegating magnetic diffusion entirely to the dissipative property of MPDATA, rendering magnetic reconnections to be solely numerical. Therefore, the effective numerical implementation of the induction equation by EULAG-MHD is

$$\frac{\partial \mathbf{B}}{\partial t} = \nabla \times (\mathbf{v} \times \mathbf{B}) + \mathbf{D_B} \ , \tag{3.92}$$

where, $\mathbf{D_B}$ represents the numerical magnetic diffusion, rendering reconnections to be solely numerically assisted. Although this turns out to be advantageous, a cautious approach is required in analyzing and extracting results from the simulated dynamics. Being localized and intermittent, the magnetic reconnection in the spirit of ILES minimizes the computational effort, while tending to maximize the effective Reynolds number of simulations (Waite & Smolarkiewicz, 2008). However, the absence of physical diffusivity makes it impossible to accurately identify the relation between electric field and current density——rendering a precise estimation of magnetic Reynolds number unfeasible. Being intermittent in space and time, quantification of this numerical dissipation is strictly meaningful only in the spectral space where, analogous to the eddy viscosity of explicit subgrid-scale models for turbulent flows, it only acts on the shortest modes admissible on the grid (Domaradzki et al., 2003), particularly near steep gradients in simulated fields.

3.5 Summary

The data-based numerical simulations of the solar transients should account for the breakdown of flux-freezing condition at small-length scales but should maintain it when away from the reconnection region. The EULAG-MHD model meets these criterion to high fidelity and owing to the ILES property, computational cost is also minimized. The model utilizes a MPDATA scheme, which essentially relies on iterative application of the upwind differencing to reduce numerical diffusion and to make the solution second-order accurate in space and time. Further, the nonoscillatory option of MPDATA serves to ensure that there are no unphysical oscillations. In regard with the MPDATA scheme, its mathematical formalism has been presented and physicality of numerical dissipation inherent to MPDATA or any other NFV algorithm is discussed. Lastly, the algorithm of EULAG-MHD and its implementation in the context of data-based simulations is presented.

To illustrate the application of EULAG-MHD model, the following chapter presents examples of MHD simulations that are initiated from analytical magnetic field configurations rather than an extrapolated magnetic field. Such simulations are comparatively easier to analyze and investigate because the magnetic geometry is well-organized and can be tailored as required. However, it should be kept in mind that these are idealized scenarios and may not reflect the realistic magnetic configurations, which are generally much more complex. The simulations focus on the formation of magnetic flux rope and their evolution, an investigation of which is important for a comprehensive understanding of eruptive events.

Chapter 4

Examples of MHD Simulations: Magnetic Flux Ropes

4.1 Introduction

As discussed in chapter 1, magnetic flux rope is a bundle of helically twisted magnetic field lines (MFLs) that wind around a common axis. The twisted MFLs represent regions of strong currents and facilitate the storage of magnetic energy. According to the standard model of flares (see section 1.3), their upward ascension triggers reconnection and hence, MFRs play an important role in eruptive events. Consequently, the formation mechanism and evolution of MFRs is an active area of research. Broadly, MFRs can appear in the solar atmosphere in two ways. In the first mechanism, a pre-existing MFR below the photospheric surface emerges into the atmosphere due to magnetic buoyancy (Fan, 2001; Fan & Gibson, 2003; Manchester et al., 2004; Fan, 2010, 2021). In the other method, a MFR forms in the solar atmosphere by magnetic reconnection in sheared magnetic arcades (Van Ballegooijen & Martens, 1989; Moore et al., 2001; Amari et al., 2003; Aulanier et al., 2010; Amari et al., 2014). The examples of MHD simulations discussed in this chapter pertain to the second mechanism, exploring MFR formation and evolution due to reconnection in a bipolar sheared arcade and a quadrupolar magnetic geometry. The two cases are discussed separately in the following.

4.2 Example-I: Bipolar Sheared Arcade

The magnetic configuration of a three-dimensional bipolar sheared arcade (K Bora, Satyam Agarwal, Sanjay Kumar, & R Bhattacharyya, 2023) can be constructed as $\mathbf{B}^* = \mathbf{B} + a_0\mathbf{B}^{'}$, where the components of $\mathbf{B}$ are

$$\mathrm{B}_x = a_z \sin(a_x x) \exp\left(-a_z z/s_0\right) \ , \tag{4.1}$$

$$\mathrm{B}_y = a_y \sin\left(a_x x\right) \exp\left(-a_z z/s_0\right) \ , \tag{4.2}$$

$$\mathrm{B}_z = s_0 a_x \cos\left(a_x x\right) \exp\left(-a_z z/s_0\right) \ , \tag{4.3}$$

and the components of the $\mathbf{B}^{'}$ are

$$\mathrm{B}'_x = \left(\sin x \cos y - \cos x \sin y\right) \exp\left(-z/s_0\right) \ , \tag{4.4}$$

$$\mathrm{B}'_y = -\left(\cos x \sin y + \sin x \cos y\right) \exp\left(-z/s_0\right) \ , \tag{4.5}$$

$$\mathrm{B}'_z = 2s_0 \sin x \sin y \exp\left(-z/s_0\right) \ . \tag{4.6}$$

The initial magnetic configuration along with the direction of resulting Lorentz force is shown in figure 4.1, where the value of constants are $a_x = 1$, $a_z = 0.9$, $a_y = \sqrt{a_x^2 - a_z^2}$, $a_0 = 0.5$, and $s_0 = 6$. Importantly, the Lorentz force decreases sharply with height, tending toward zero at the top of computational box. Therefore, the magnetic configuration is relevant to solar magnetic fields, where the solar corona is believed to be in nearly force-free state, as discussed in chapter 2.

The simulation is carried out using the EULAG-MHD model with a physical domain of extent $\{0, 2\pi\}$, $\{0, 2\pi\}$, $\{0, 8\pi\}$, which is mapped on a numerical grid of $64\times64\times128$ voxels along the x, y, and z directions, where a voxel represents a value on a regular grid in the 3D space. The normal component of velocity is set to be zero at the bottom boundary while the horizontal components evolve in accordance with the MHD equations. As a result, the used boundary conditions mimic the line-tying effect (Jiang et al., 2021). The time duration of the simulation is $7000 \times \Delta t \times \tau_A = 11.2\tau_A$, where $\Delta t = 16\times10^{-4}$ (see paper for more details on simulation setup). Notably, there are two polarity inversion lines (PILs) and the arcade configuration is symmetric about each of the PILs, implying that it is sufficient to investigate the magnetofluid dynamics in only half of the computational box. In the absence

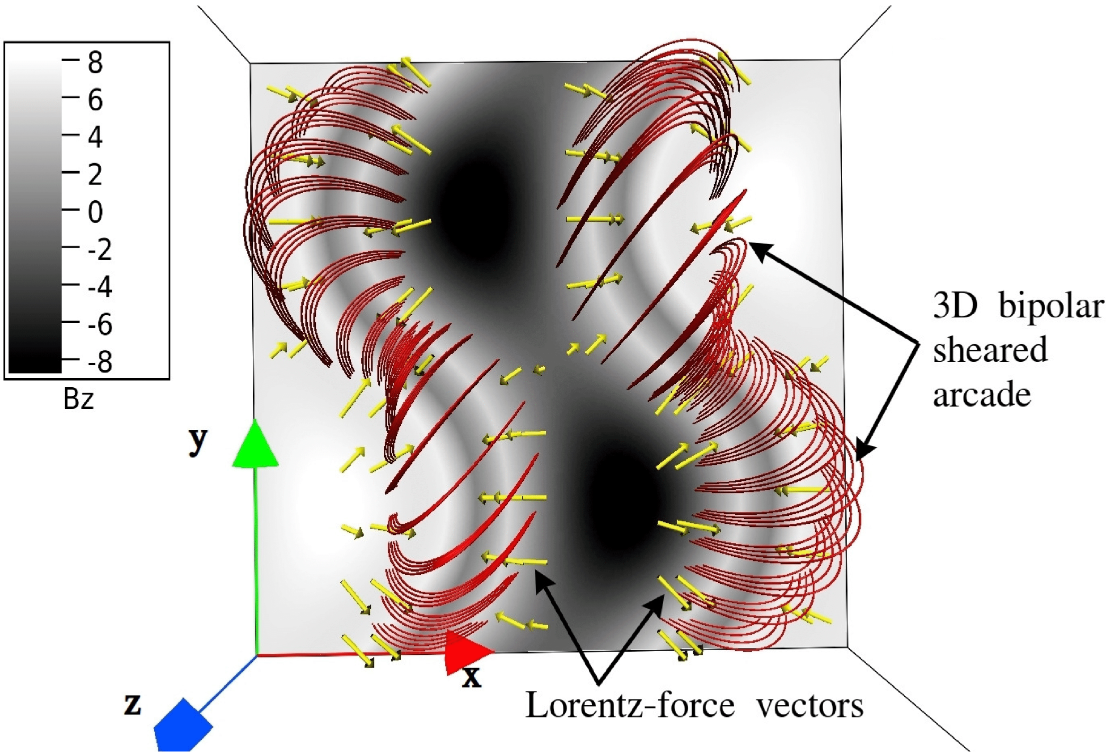

Figure 4.1: Initial 3D sheared magnetic field lines (*red*) and Lorentz force vectors (*yellow*) around the sigmoid-shaped polarity inversion line (PIL). The bottom boundary shows the B_z map in grayscale. The *red*, *green*, and *blue* arrows in each panel represent the x, y, and z-axis of the Cartesian system.

of any initial plasma flow ($\mathbf{v} = 0$), the Lorentz force corresponding to $\mathbf{B}^*$ triggers the evolution of magnetofluid, causing shearing motion and reconnection between field lines of the arcade configuration. Consequently, the field lines change their connectivity and form a magnetic flux rope, as depicted in figure 4.2†. The twisted MFLs of the rope are most evident in panel (d) at $t = 1.60\tau_A$. Importantly, this example of flux rope formation serves to illustrate the implication of reconnection pertaining to changes in the connection of magnetic field lines. Similarly, from the perspective of energetics, $|\mathbf{B}|^2$ is decreases monotonically as shown in panel (a) of figure 4.3, implying lowering of the magnetic energy and hence, relaxation of the magnetofluid. Notably, the initial Lorentz force that triggers the system dynamics is due to the arcade geometry. Therefore, the evolution of the arcade configuration while undergoing magnetic reconnections will modify the Lorentz force. In order to quantify the changes in the Lorentz force, the temporal variation of alignment

†The magnetic field line plots throughout the thesis are visualized using the VAPOR software, discussed in appendix A with all the relevant details, including other functionalities like DVR, barb, isosurface and slice rendering.

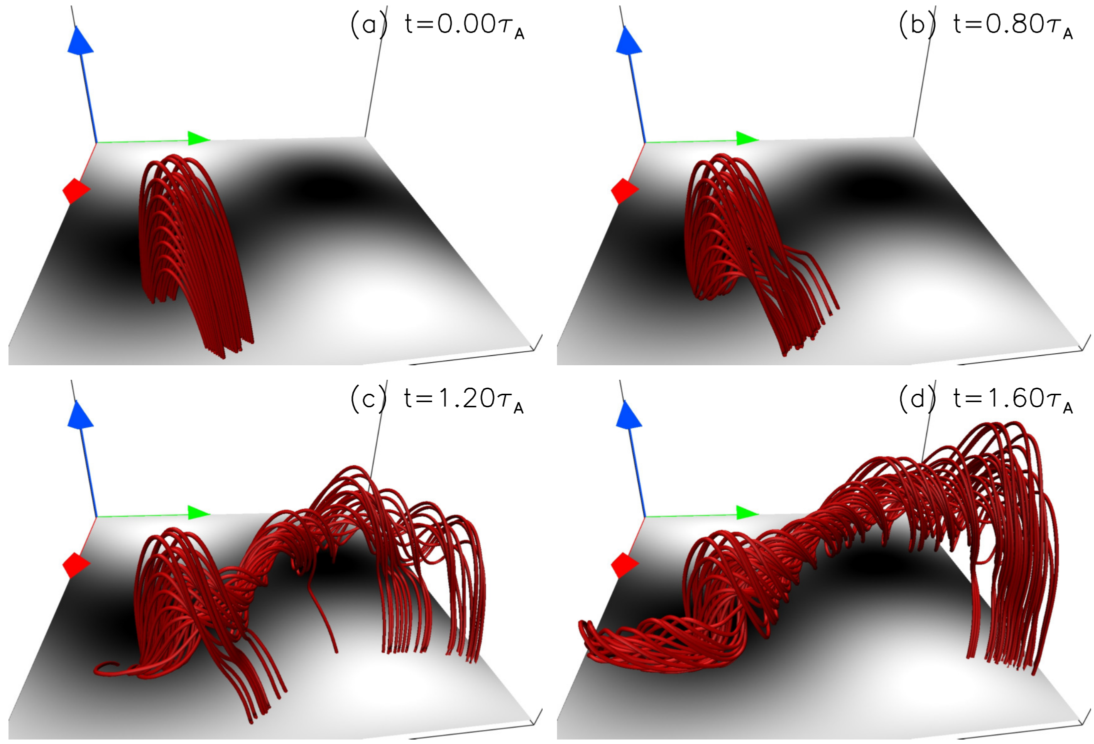

Figure 4.2: Magnetic flux rope formation due to reconnection between field lines of sheared magnetic arcade. The bottom boundary shows the B_z map in grayscale. The *red*, *green*, and *blue* arrows in each panel represent the x, y, and z-axis of the Cartesian system.

between **J** and **B** is computed. The alignment (θ) is defined (Wheatland et al., 2000) as

$$\theta = \sin^{-1}\sigma_j, \quad \sigma_j = \frac{\sum_i |\mathbf{J}|_i \sigma_i}{\sum_i |\mathbf{J}|_i}, \quad \sigma_i = \frac{|\mathbf{J}\times\mathbf{B}|_i}{|\mathbf{J}|_i \times |\mathbf{B}|_i}\ , \tag{4.7}$$

where i runs over all the voxels in the computational box. The θ value decreases by approximately 15° as shown in panel (b) of figure 4.3, which implies that the magnetic configuration tends toward a force-free equilibrium.

4.3 Example-II: Quadrupolar Magnetic Configuration

The observations of solar flares suggest an association of some flaring events with a quadrupolar magnetic configuration (Nishio et al., 1997; Sun et al., 2012; Kawabata et al., 2017; Chintzoglou et al., 2017; Mitra et al., 2022). Therefore, investigations of the quadrupolar geomtry regarding magnetic topology, energy storage and flux rope formation (Hudson & Wheatland, 1999; Régnier, 2012; Fang & Fan, 2015; Syntelis et al., 2019) have been carried out. However, not many studies have been

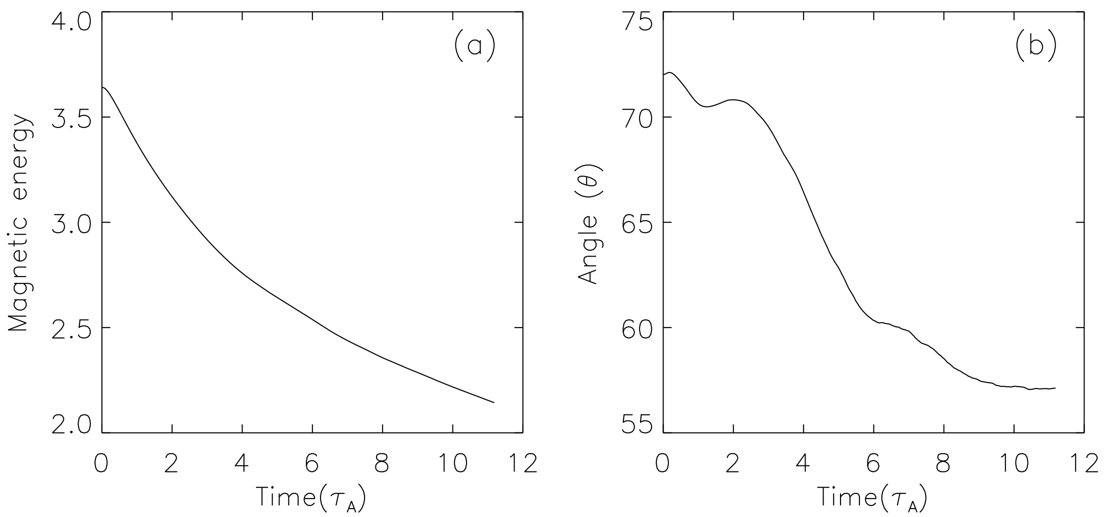

Figure 4.3: Temporal evolution of the (a) volume integrated magnetic energy (b) angular alignment (θ).

conducted to explore the formation and evolution of flux ropes in a quadrupolar geometry. The following example describes such a study (Sanjay Kumar, Avijeet Prasad, Sushree S Nayak, Satyam Agarwal, & R Bhattacharyya, 2023), where the initial magnetic field is given by

$$\mathrm{B}_x = 0.5\left[\alpha_0 \sin(x)\cos(y) - k_0\cos(x)\sin(y)\right]\exp\left(-\frac{k_0 z}{s_0}\right), \quad (4.8)$$

$$\mathrm{B}_y = -0.5\left[\alpha_0 \cos(x)\sin(y) + k_0\sin(x)\cos(y)\right]\exp\left(-\frac{k_0 z}{s_0}\right), \quad (4.9)$$

$$\mathrm{B}_z = s_0\sin(x)\sin(y)\exp\left(-\frac{k_0 z}{s_0}\right), \quad (4.10)$$

where α_0, k_0 and s_0 are constants, with $k_0 = \sqrt{2-\alpha_0{}^2}$. The field $\mathbf{B}$ is specified in the positive half-space ($z \geq 0$) of a Cartesian domain, periodic along the lateral directions (ranging from 0 to 2π in x and y) and open along the vertical direction (ranging from 0 to 6π in z). Notably, the field $\mathbf{B}$ supports a non-zero Lorentz force (if $s_0 \neq 1$), which triggers the simulation from a motionless state ($\mathbf{v} = 0$). To have an optimal Lorentz force, s_0 is chosen to be $s_0 = 6$. Notably, $\mathbf{B}$ satisfies the linear force-free equation $\nabla \times \mathbf{B} = \alpha_0 \mathbf{B}$ (see equation 2.16) for $s_0 = 1$, where α_0 is related to the twist of field lines. The choice $\alpha_0 = 1$ gives sufficiently twisted initial MFLs and implies high k_0, which leads to a steep exponential decay of the initial Lorentz force with height, as depicted in figure 4.4. Panel (a) shows a DVR (see appendix A) of the Lorentz force density inside the computational domain, while panel (b)

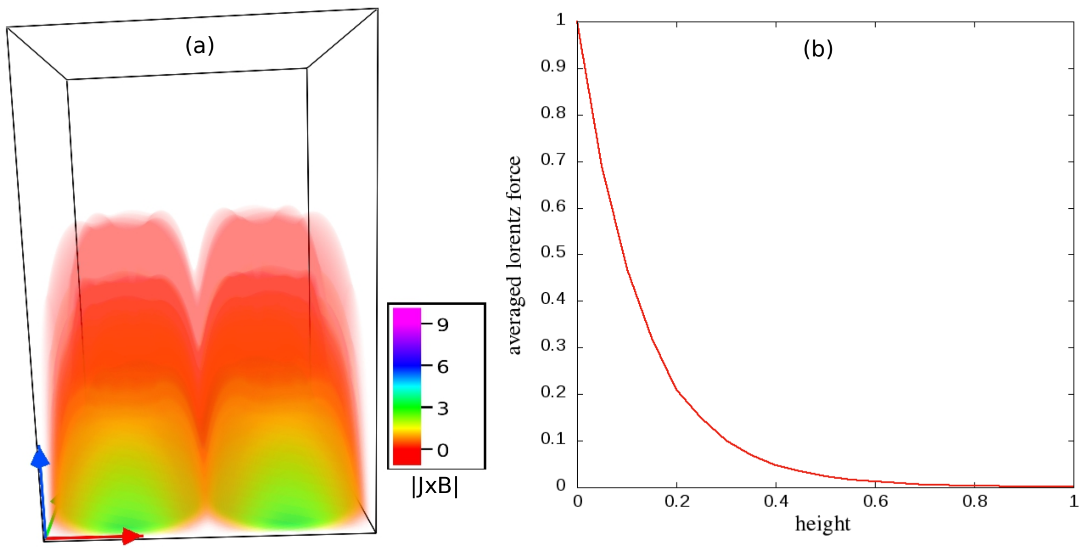

Figure 4.4: Panel (a): DVR plot showing distribution of the initial Lorentz force in the computational box. Panel (b): Magnitude variation of horizontally averaged Lorentz force with height in normalized units.

plots the variation of horizontally averaged Lorentz force with height, exhibiting a sharp decrease. Therefore, as in the example of sheared arcade discussed earlier, the quadrupolar geometry is also relevant to solar corona, which is considered to be force-free under low plasma-β approximation, while the photosphere ($\beta \sim 1$) is expected to be non-force-free due to the convective driving (Gary, 2001). The initial magnetic geometry is shown in figure 4.5, where the bottom boundary is overlaid with the map of B_z. Panel (a) depicts the magnetic field lines connecting the regions of positive (P1, P2) to negative (N1, N2) polarity. The polarities are marked in panel (b) along with the polarity inversion lines (PILs) corresponding to the different opposite polarities (P1, N1), (P1, N2), (P2, N1), and (P2, N2) in *white* lines. Noticeably, the opposite polarities satisfy mirror symmetry across the PILs. Because of the mirror symmetry, the initial magnetic field supports an X-line (see section 1.2.5.1) located at (x, y)=(π, π) along $z-$axis, shown in panel (c) with *pink* color. Panel (d) shows the top view of initial field, which reveals the quadrupolar configuration immediately. Since, the computational box is periodic along x and y, additional X-lines exist at boundaries (not shown) at (x, y)=$(0, 0)$, $(0, \pi)$, $(0, 2\pi)$, $(\pi, 0)$, $(2\pi, 0)$, $(\pi, 2\pi)$, $(2\pi, \pi)$, and $(2\pi, 2\pi)$ along the $z-$axis. The initial magnetic geometry with two positive and negative polarities resembles the observed quadrupolar configurations at the solar surface (Kawabata

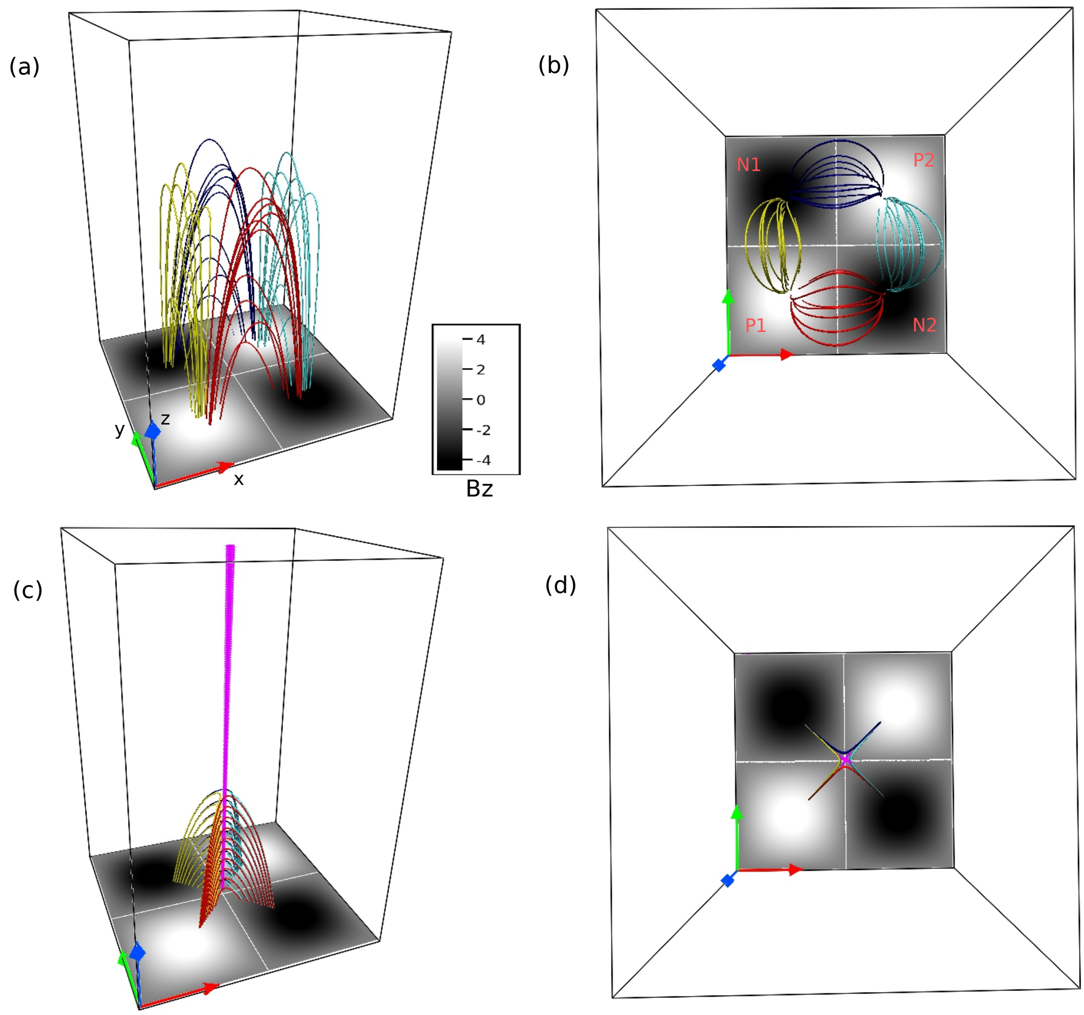

Figure 4.5: Quadrupolar magnetic configuration overlaid with B_z contours at the bottom boundary. Panel (a) plots the MFLs connecting the positive (P1, P2) to negative (N1, N2) polarities, which are marked in panel (b) and are separated by the PILs shown as *white* lines. Panel (c) shows the existence of a X-line (*pink*) at $(x, y) = (\pi, \pi)$ along the $z-$axis inside the domain, while panel (d) depicts the top view of the configuration.

et al., 2017; Mitra et al., 2022). However, in the absence of mirror symmetry and periodicity, the observed configurations exhibit a more complex magnetic field line topology. The EULAG-MHD model is employed for the simulation, where the grid size corresponds to $128 \times 128 \times 384$ along the x, y, and $z-$axis. The simulations are carried out for $R_F^A = 200$ and $R_F^A = 100$ with time duration of $4000 \times \Delta t \times \tau_A = 128\tau_A$ (equivalent to writing 128 seconds), where $\Delta t = 32 \times 10^{-3}$. The process of flux rope formation is depicted for $R_F^A = 200$ in figure 4.6, showing two bipolar magnetic loops at $t = 0$ along the PIL separating P1 and N2. The Lorentz force, shown by *grey* arrows, pushes the two complementary anti-parallel field lines of

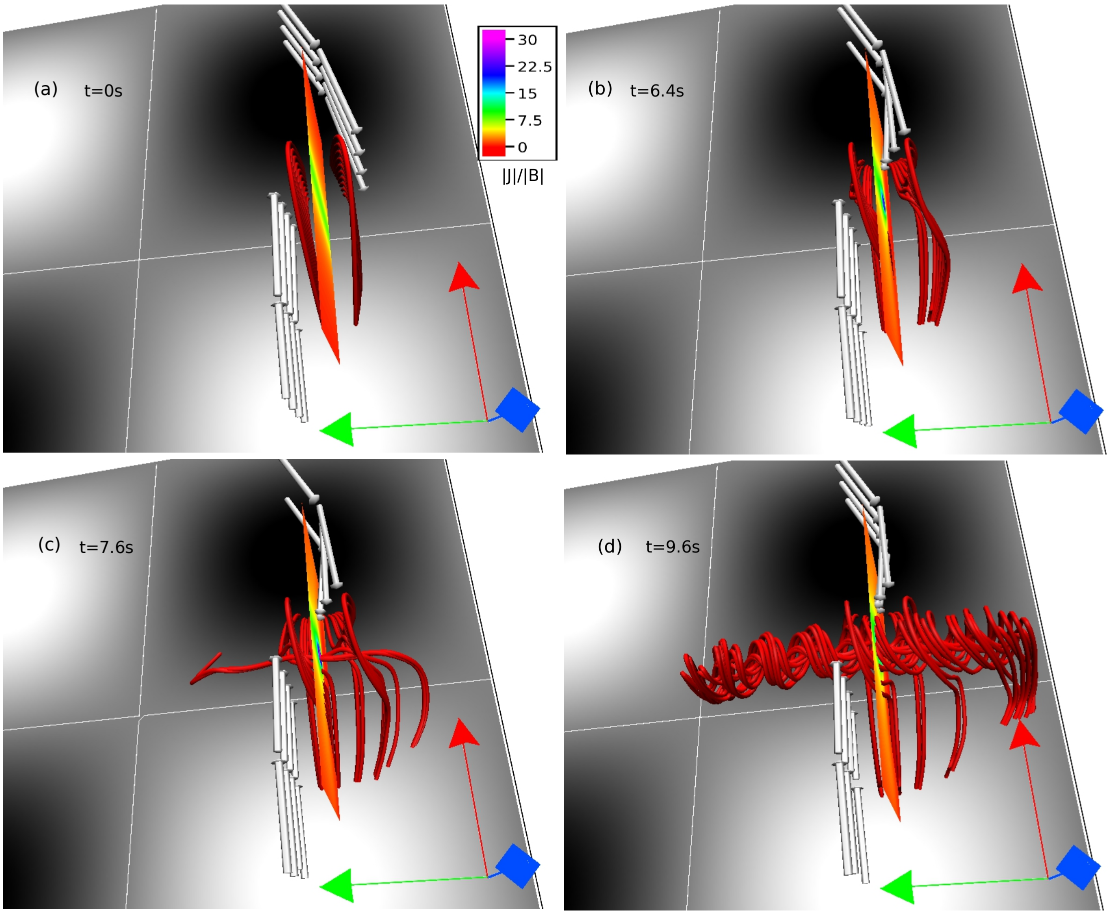

Figure 4.6: Early phase of the MFL dynamics for two sets of bipolar loops situated over the PIL between polarities P1 and N2. The Lorentz force is shown in *grey* arrows and $|\mathbf{J}|/|\mathbf{B}|$ is plotted on y-constant planes. The Lorentz force brings oppositely directed MFLs in proximity, evident by increase in $|\mathbf{J}|/|\mathbf{B}|$ values. The evolution leads to repeated reconnections and formation of a flux rope over the PIL.

loops toward each other. Consequently, small-scales are generated (quantified by an increase in $|\mathbf{J}|/|\mathbf{B}| \propto L^{-1}$)[†], which onsets reconnection, leading to formation of flux rope. A similar process along all the four PILs generates four MFRs. The legs of these flux ropes approach the X-line and MFRs start to reconnect, developing complex magnetic structure around the X-line, notable at $(x, y) = (\pi, \pi)$. As the reconnections repeat, more and more flux is sucked into the central region, which shapes the resulting magnetic structure and finally leads to a non-uniform ascension of the magnetic flux ropes. The above-described dynamics is visualized in figure 4.7, showing the top view of all the four MFRs and complex structuring of field lines around the X-line due to reconnection between them. Importantly,

[†]The slice rendering of $|\mathbf{J}|/|\mathbf{B}|$ is plotted on $y-$constant planes.

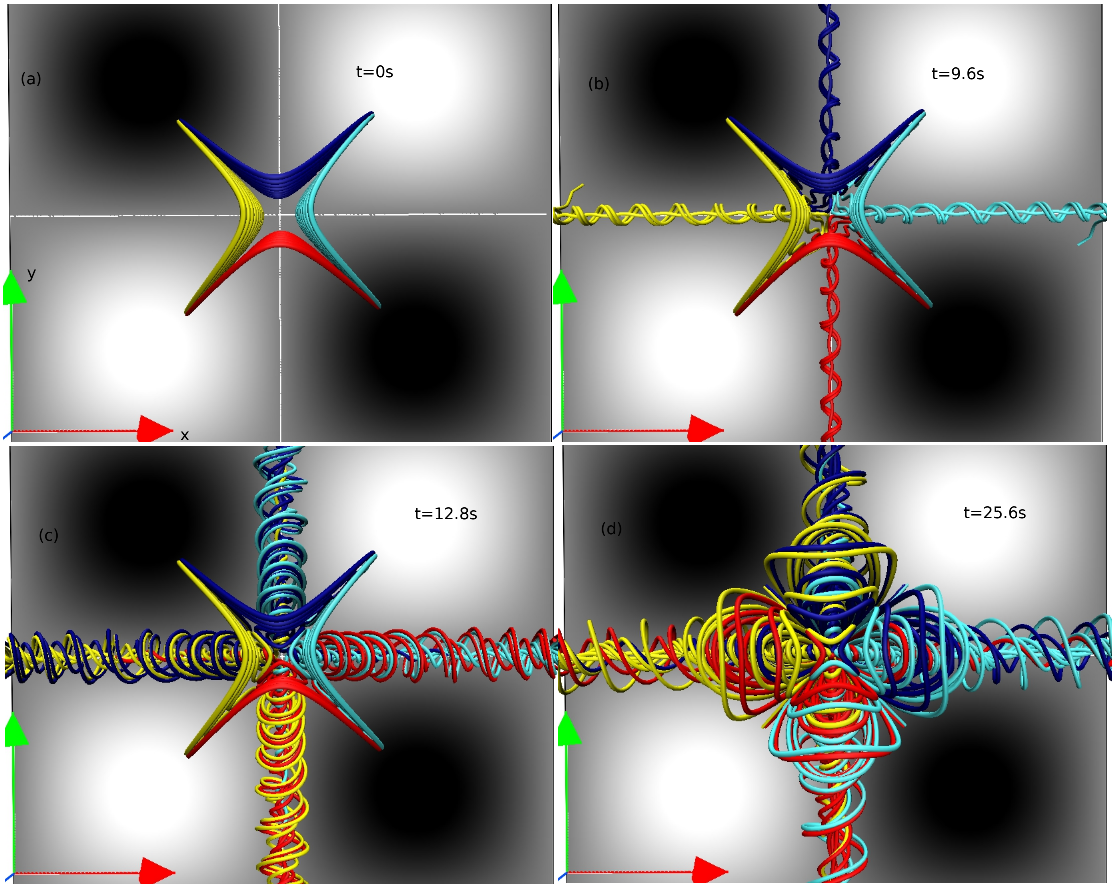

Figure 4.7: The zoomed-in top view of the MHD evolution of the magnetic field lines near the X-line inside the computational domain. Reconnections of the flux ropes at the X-line are evident—leading to the formation of complex magnetic structures.

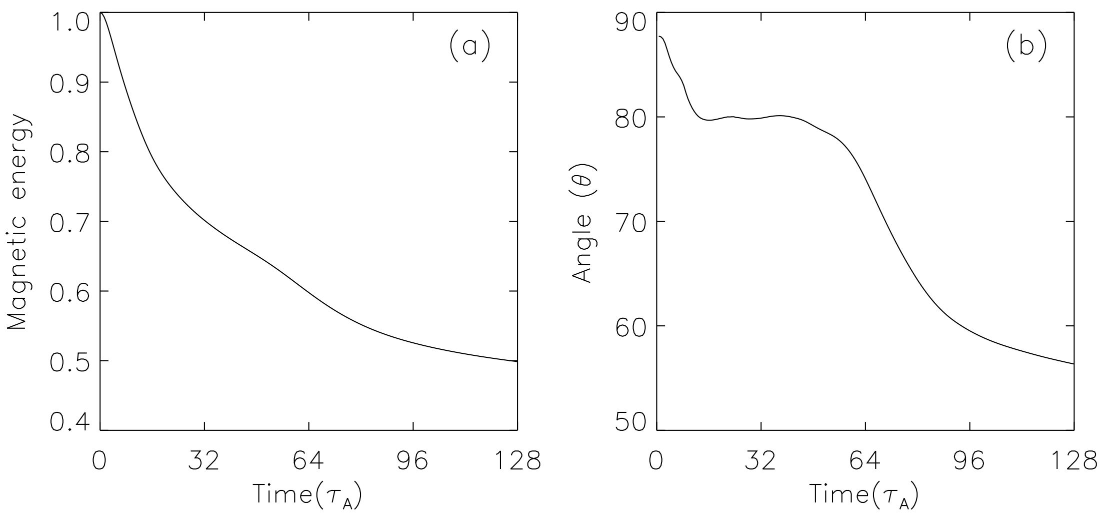

Figure 4.8: Temporal evolution of the (a) volume integrated magnetic energy in normalized units (b) angular alignment (θ).

as in the case of sheared arcade, the temporal variation of magnetic energy for $R_F^A = 100$ in figure 4.8 shows an overall decrease in magnetic energy. Further, the

θ value decreases by approximately 31°, implying that the magnetic configuration tends toward a force-free equilibrium.

4.4 Summary

The chapter presents two examples of MHD simulations initiated from idealized analytical magnetic fields using the EULAG-MHD numerical model. The examples pertain to the formation and evolution of magnetic flux ropes in 3D bipolar sheared arcade and quadrupolar magnetic configurations.

In both the cases, the variation of the Lorentz force with height is in accordance with the typical plasma-β value in the photosphere and force-free region of the solar corona. This suggests that the considered analytical configurations are of relevance in the context of solar magnetic fields, even though the realistic magnetic fields can be much more complex.

Importantly, even though the primary focus of the presented MHD simulations is to explore flux rope formation and its evolution, an unrelated but interesting aspect of these simulations is noteworthy, as discussed in the following. Despite the differences in the initial magnetic topology and the nitty-gritty of the magnetofluid dynamics, there exist certain commonalities. For instance, reconnection between the set of bipolar loops leads to change in connection of field lines and hence, formation of a magnetic flux rope. Further, the volume integrated magnetic energy decreases, indicating relaxation of the magnetofluid in the sense of reaching toward a lower magnetic energy state. Lastly, the increase in angular alignment between current density and magnetic field suggests that the magnetic configurations tend to evolve toward a force-free equilibrium.

The above-described commonalities are tell-tale signatures of self-organization and plasma relaxation. In particular, the lowering of magnetic energy and increase in the angular alignment point toward magnetic relaxation (Woltjer, 1958; Taylor, 1974), which associates directly with the release of magnetic energy during solar transients. Consequently, the discussed examples of MHD simulations serve as a pivotal point in motivating an exploration of relaxation in solar transients using data-based simulations, which corresponds to a more realistic scenario. With this objective in mind, the following chapter discusses the concept of self-organization and plasma relaxation, particularly the Woltjer (1958) and Taylor (1974) states.

Chapter 5

Concepts of Plasma Relaxation

"I owe my interest in the subject of plasma relaxation to the thesis of my supervisor Prof. Ramit Bhattacharyya"

Satyam Agarwal

5.1 Introduction

It is observed that many dynamical systems whose time evolution is governed by nonlinear partial differential equations with dissipation, evolve spontaneously and preferentially to a state that shows some form of long-range ordering, also known as self-organization (Ortolani & Schnack, 1993). In all cases, long-range ordering in one physical variable is accompanied by short-range disorder in other variables, which ensures that the overall entropy increases and therefore, the second law of thermodynamics is not violated. The short-range disorder is associated with the formation of complex coherent structures, characterized by an increased efficiency of dissipation around them (Veltri et al., 2009). Importantly, this autonomously achieved or self-organized state is independent of the way the system was prepared and is predominantly insensitive to any local perturbations (Hasegawa, 1985). In systems exhibiting self-organization, ideal integrals of motion are conserved in the absence of dissipation but decay at different rates when dissipation is taken into account. This is believed to be essential for self-organization and is known as the selective decay principle (Matthaeus & Montgomery, 1980), which compares the decay rates of two or more variables in the presence of dissipation. Consequently, the self-organized state can be determined by a constrained minimization of the fastest decaying variable, while treating the slower decaying variables as invariants. Contextually, the ordering in one or more parameters (invariants) is maintained at the cost of disorder in another parameter (minimizer) so that the overall entropy of the system increases. Notably, in magnetized plasmas, self-organization is also referred to as plasma relaxation, wherein the magnetofluid relaxes toward a state of minimum energy, while preserving appropriate physical variables. Contextually, the self-organized states are also known as relaxed states. The early application of constrained minimization to magnetized plasma considered magnetic energy as the minimizer (Woltjer, 1958; Taylor, 1974) and magnetic helicity as an invariant. The resulting relaxed states are distinguished as outcomes of magnetic relaxation, as discussed in the following.

5.2 Magnetic Helicity and Woltjer's Relaxed State

Consider the infinite set of integrals, first defined by Woltjer (1958) as

$$H_l = \int_{V_l} \mathbf{A}\cdot\mathbf{B}\,\mathrm{d}^3x \ \ , \, l = 0, 1, 2, ..., \infty \tag{5.1}$$

where V_l is the volume of the l^{th} flux tube and H_l is called the magnetic helicity of the flux tube. It is a measure of magnetic topology and arises from the internal structuring of flux tube (i.e. twist and kink) as well as external relations between flux tubes, such as linking and knotting (Berger & Field, 1984). Importantly, for a perfectly conducting plasma, Woltjer (1958) showed that $\mathrm{d}H_l/\mathrm{d}t = 0$, implying that the magnetic helicity H_l is an invariant. Further, Woltjer (1958) carried out minimization of the magnetic energy of a flux tube keeping its magnetic helicity invariant to look for a relaxed state. The resulting functional F_l and its first order variation are given by

$$F_l = \frac{1}{2\mu_0}\int_{V_l} |\mathbf{B}|^2\,\mathrm{d}^3x - \alpha_l \int_{V_l} \mathbf{A}\cdot\mathbf{B}\,\mathrm{d}^3x \tag{5.2}$$

$$\delta F_l = \frac{1}{\mu_0}\int_{V_l} \mathbf{B}\cdot\delta\mathbf{B}\,\mathrm{d}^3x - \alpha_l \int_{V_l} (\delta\mathbf{A}\cdot\mathbf{B} + \mathbf{A}\cdot\delta\mathbf{B})\,\mathrm{d}^3x \ , \tag{5.3}$$

where α_l is the Lagrange multiplier for l^{th} flux tube. Using simple vector algebra and $\delta F_l = 0$ for minimum energy configuration, the following can be written

$$0 = \int_V \delta\mathbf{A} \cdot (\mathbf{J} - 2\alpha_l \mathbf{B})\, \mathrm{d}^3x + \frac{1}{\mu_0} \oint_S \delta\mathbf{A} \cdot [(\mathbf{B} - \alpha_l \mathbf{A}) \times \hat{n}]\, \mathrm{d}^2x \ , \qquad (5.4)$$

which gives $\mathbf{J} = 2\alpha_l \mathbf{B}$ for arbitrary variation of $\delta\mathbf{A}$ within the volume if $\delta\mathbf{A}|_S = 0$ or $\delta\mathbf{A} \times \hat{n}|_S = 0$ is set as the boundary condition. Further, the constants can be absorbed within the multiplier α_l, giving

$$\nabla \times \mathbf{B} = \alpha_l \mathbf{B} \ , \qquad (5.5)$$

which describes the Woltjer's relaxed state (Woltjer, 1958). Since, the number of flux tubes are infinite, there will be infinite number of Lagrange multipliers, one for each flux tube. Consequently, α becomes space-dependent and a generalized version of equation 5.5 can be written as

$$\nabla \times \mathbf{B} = \alpha(\mathbf{r})\mathbf{B} \ . \qquad (5.6)$$

The solenoidality of magnetic field leads to the result

$$\nabla \alpha(\mathbf{r}) \cdot \mathbf{B} = 0 \ , \qquad (5.7)$$

which implies that α is constant along a flux tube. Together, these two equations represents a nonlinear force-free field (see section 2.4.3) and are used to describe various physical systems including the solar corona. Notably, during the relaxation process, α_l remains constant for a flux tube, which implies that the relaxed state depends on initial conditions or how the system was prepared. However, this is in contradiction with the properties of a self-organized state. Therefore, ideal MHD over-determines the evolution of a magnetofluid system and a smaller number of invariants is desirable. A way to do so was proposed by Taylor (1974), as discussed in the following.

5.3 Taylor's Theory of Relaxation

In the presence of resistivity, $\mathrm{d}H_l/\mathrm{d}t \neq 0$ and is given by

$$\frac{\mathrm{d}H_l}{\mathrm{d}t} = -2\sigma^{-1}\int_V \mathbf{J}\cdot\mathbf{B}\,\mathrm{d}^3x\ , \tag{5.8}$$

where σ^{-1} is assumed spatially constant and $\mathbf{A}\times\hat{n}|_S = 0$ is the boundary condition. The implication is that H_l are no longer invariants and decay at a rate proportional to the resistivity (Ortolani & Schnack, 1993). The primary effect of this resistivity is to allow reconnection between flux tubes, as discussed in the first chapter. The field lines lose their identities and hence, α_l does not remain a constant anymore. Based on this result, Taylor (1974) conjectured that in a slightly resistive plasma bounded by perfectly conducting walls, the global magnetic helicity defined by

$$H = \int_V \mathbf{A}\cdot\mathbf{B}\,\mathrm{d}^3x \tag{5.9}$$

will remain approximately invariant (Taylor, 1974, 1986, 2000), where the integral is carried out over the entire plasma volume. The rationale put forward by Taylor (1974) was that the changes in $\mathbf{B}$ due to reconnection are very small and therefore, the sum of H_l over all flux tubes will be nearly constant. Moreover, the integrand $\mathbf{A}\cdot\mathbf{B}$ will get redistributed among field lines but not destroyed. The reconnection between flux tubes is believed to homogenize $\alpha(\mathbf{r})$ and plasma pressure, implying that the Taylor's state is characterized by uniform pressure. The approximate invariance of H is meaningful in the context of relaxed state when its decay rate is much smaller as compared to that of magnetic energy (W_m). For this purpose, note that $|\mathbf{J}| \propto |\mathbf{B}|/L$, implying that at small-scales, $|\mathbf{J}\cdot\mathbf{B}| \ll |\mathbf{J}|^2$, which gives (Browning, 1988)

$$\left|\frac{\mathrm{d}H}{\mathrm{d}t}\right| \propto |\mathbf{J}\cdot\mathbf{B}| \ll \left|\frac{\mathrm{d}W_\mathrm{m}}{\mathrm{d}t}\right| \propto |\mathbf{J}|^2\ , \tag{5.10}$$

which suggests that the selective decay principle is applicable. Consequently, the constrained minimization of magnetic energy while treating the global magnetic helicity as invariant leads to a relaxed state. Then, for a static zero-beta plasma having no internal energy, the relaxed state is given by

$$\nabla \times \mathbf{B} = \alpha_0 \mathbf{B} \ , \tag{5.11}$$

where α_0 is the Lagrange's undetermined multiplier. This represents a linear force-free field (see section 2.4.2) configuration. It is worth mentioning that while dissipation is central in obtaining the Taylor's state, resistivity does not enter explicitly into variational formulation (Ortolani & Schnack, 1993). Further, the theory is appropriate for isolated systems only. A general proof of the Taylor's conjecture can be found in Faraco & Lindberg (2020) and Faraco et al. (2022).

5.4 Additional Remarks on Relaxed States

In the post-Taylor period, studies on relaxation focused on various minimizers, invariants, and new principles to obtain the relaxed states. The Woltjer and Taylor states focus only on the magnetic properties of plasma and do not include other variables like the plasma flow, kinetic pressure, or dissipation rates. Inclusions of these variables are possible within the framework of two-fluid description of the plasma. Further, due to its inherent generality over MHD and natural flow-field coupling, the two-fluid formalism is preferable. The two-fluid approach generally includes plasma flow in the minimizer, while the invariants are either generalized helicities (Steinhauer & Ishida, 1997), their derivatives (Bhattacharyya & Janaki, 2004), and can even include total (magnetic+kinetic) energy (Yoshida & Mahajan, 2002). The relaxed states are always flow-coupled, i.e the magnetic field and flow are interrelated.

It is also of interest to note that Yeates et al. (2010) proposed the existence of an additional constraint along with magnetic helicity, namely the topological degree of field line mapping (also see Yeates et al., 2015, Yeates et al., 2021) to obtain relaxed states. The relaxed states turned out to be either linear force-free field or nonlinear force-free field depending on the topological degree. Lastly, as mentioned in chapter 2, the principle of minimum dissipate rate (MDR) is used in a two-fluid formalism to obtain the non-force-free field as relaxed state. The fundamental idea behind the MDR principle is that during an irreversible process, a system evolves naturally to those states (or relaxed states) in which the energy dissipation rate is minimum. A simple example is that of ohmic conductors, where $\mathbf{E} = \rho\mathbf{J}$ and the steady state is given by $\partial_t\mathbf{B} = 0 \Rightarrow \nabla \times \mathbf{E} = \nabla \times (\rho\mathbf{J}) = 0$, which can be obtained from MDR principle also. The energy dissipation rate is given by

$$R = \int_V \rho|\mathbf{J}|^2 \, \mathrm{d}^3x \; . \tag{5.12}$$

where $\rho = \sigma^{-1}$ denotes resistivity. Using $\nabla \times \mathbf{B} = \mu_0\mathbf{J}$ and some vector algebra, the first-order variation in R can be written as

$$\delta R = 2\int_V \delta\mathbf{B} \cdot (\nabla \times \rho\mathbf{J}) \, \mathrm{d}^3x + 2\oint_S \delta\mathbf{B} \cdot (\rho\mathbf{J} \times \hat{n}) \, \mathrm{d}^2x \; . \tag{5.13}$$

which gives the required result $\nabla \times (\rho\mathbf{J}) = 0$ for arbitrary variation of $\delta\mathbf{B}$ within the volume if $\delta\mathbf{B}|_S = 0$ or $\mathbf{J} \times \hat{n}|_S = 0$ is set as the boundary condition. Relevantly, in accordance with the selective decay principle, Bhattacharyya & Janaki (2004) chose total dissipation rate (ohmic and viscous) as the minimizer and generalized helicity dissipation rates (for ion and electron fluid) as invariants to obtain a non-force-free field as the MDR relaxed state.

5.5 Brief Survey of Studies on Relaxation in Solar Plasma

One of the essential characteristics of magnetic relaxation process is the decrease of magnetic energy through reconnection. Consequently, the concepts of magnetic relaxation can be carried over and applied to the solar plasma, where reconnection manifests in the form of eruptive events. Importantly, when viewed in conjunction with the extrapolated magnetic fields described in chapter 2, the relaxed states discussed in this chapter seem to be relevant in the context of solar magnetic field. Such a connection further encourages the exploration of relaxation in the solar plasma.

In the following, a brief survey of studies on relaxation in the solar plasma is presented. Norman & Heyvaerts (1983) carried out an order of magnitude analysis to compare the rate of helicity decay with that of the magnetic energy. They argued that the final state of a solar flare is a linear force-free field, where the constant α is determined by the boundary conditions. Importantly, they assumed the effect of slow photospheric driving and conversion of magnetic energy to bulk kinetic energy as negligible. Heyvaerts & Priest (1984) applied Taylor's theory to arrive at a theory of coronal heating via dissipation of DC currents and to conclude that reconnection is a viable mechanism for it. In a 3D MHD simulation, Kusano et al. (1994) investigated the reconnection between magnetic loops and found that the decay of energy is faster than helicity. Further, they found spontaneous generation of magnetic dips, which are favorable sites for prominence condensation (Gibson, 2018). The formation of such structures due to reconnection is essentially similar to that of MFR formation discussed in chapter 5, and illustrates the occurrence of long-range ordering. The simulation by Amari & Luciani (2000) employed bipolar potential fields driven by a 2D velocity field imposed at the bottom boundary. The terminal state was found to be far from a constant-α field. Contrarily, Browning et al. (2008) and Hood et al. (2009) investigated the nanoflare heating model by following the development of kink instability in coronal loops and the relaxed state was found to be consistent with a linear force-free configuration. Pontin et al. (2011) found the terminal state of relaxation to be nearly nonlinear force-free in 3D resistive MHD simulation of braided magnetic fields. In resistive MHD simulation of a solar coronal jet, Pariat et al. (2015) analyzed the evolution of helicity for several gauge choices and found it to be nearly conserved. Robinson et al. (2023) explored the formation of a magnetic flux rope in MHD simulation of the Quiet Sun, where disordered low-lying coronal field lines undergo multiple small-scale reconnections. The authors recognized the process as self-organization, where an inverse cascade of helicity occurs and the system tends toward Taylor relaxation. Along with the theoretical studies and numerical simulations employing analytical magnetic fields, investigations using observations have also been carried out. For example, Nandy et al. (2003) analyzed several flare-productive active regions and found their time evolution to be tending toward a linear force-free state. Murray et al. (2013) investigated the pre-flare and post-flare coronal magnetic fields in active region NOAA 10953 and determined the post-flare configuration to be closer to linear force-free field. Recently, Liu et al. (2023) found some evidence for Taylor relaxation in increased homogenization of $\alpha(\mathbf{r})$ for multiple X-class flares.

5.6 Summary

This chapter presents the concept of self-organization and plasma relaxation. The self-organized or relaxed state is nearly independent of how the system is configured initially. A relaxed state can be determined by a variational formulation based on the selective decay principle. In particular, the chapter focuses on the Woltjer and Taylor states, which represent force-free magnetic field configurations.

Notably, the variational principle determines a relaxed state but fails to provide any understanding of the involved physical process or dynamics of the system. In other words, the details of the relaxation mechanism are not known. For example, Taylor's theory conjectures occurrence of reconnection for relaxation to the linear force-free field state but does not give information on aspects such as the type of reconnection, how it occurs, quantitative estimate on decrease in magnetic energy, and energetics of the magnetofluid system at local and global scales.

Consequently, investigating the system dynamics is of paramount importance in understanding the relaxation process. In the context of solar plasma, exploration of relaxation has been carried out earlier using theoretical arguments, observations, and numerical simulations employing analytical magnetic fields. However, they do not account for the actual field line complexity of an actual active region. For this purpose, data-based MHD simulations in combination with the multi-wavelength observations are required to explore the implications of 3D magnetic reconnection on the magnetofluid dynamics and relaxation. As a first step in this direction, the aspect pertaining to independence of relaxed state with respect to initial conditions is explored in the next chapter using data-based MHD simulations of a solar flare.

Chapter 6

Effects of Initial Conditions on Magnetic Reconnection

6.1 Introduction

The data-based MHD simulations of solar transients use an extrapolated magnetic field as initial condition. Since, it is possible to construct the solar magnetic field using different extrapolation models (see chapter 2), suitable combinations of the extrapolated magnetic fields with velocity fields can be made to generate relevant initial conditions for the data-based simulations. Consequently, the independence aspect of a self-organized state with respect to the initial configuration of system can be investigated. For this purpose, it is crucial to explore the effects of initial conditions on the implications of reconnection such as changes in the connectivity of magnetic field lines and energetics. Notably, reconnection dissipates magnetic energy as heat, which is lost irrecoverably from the system. As a result, a parallel can be drawn with the dissipative dynamics of a system governed by classical mechanics. Conceptually, the analogy infers the post-reconnection dynamics to be relatively insensitive to the initial condition as, presumably, dissipation erases the memory of a system. The inference can have strong implications in the data-based simulation of transients because it raises the expectation that simulations having analogous initial MFL morphologies can yield similar reconnection. The problem statement is then to explore the effect of different initial conditions on reconnection in data-based MHD simulations. Noticeably, this may also complement the studies that compare the relative performance of various extrapolation models to address their credibility in reproducing the observed solar magnetic field (Schrijver et al., 2008, Duan et al., 2017, Warren et al., 2018).

Toward such an exploration, the two most widely used approaches for modeling of active region magnetic fields are considered, namely the nonlinear force-free field (NLFFF) and the non-force-free field (NFFF) extrapolation. The rationale behind employing these models is as following. The NLFFF model based on the principle of weighted optimization (see chapter 2) is widely accepted in the contemporary research. The choice seems to be appropriate because NLFFF can account for the amount of released free magnetic energy during eruptive events (Wiegelmann & Sakurai, 2021). Further, previous works have shown the capability of this NLFFF scheme to adequately reproduce coronal loops (Warren et al., 2018), magnetic flux rope structures (Mitra et al., 2020), and complex magnetic topologies like magnetic null points and QSLs (Zhao et al., 2014, Joshi et al., 2021). Importantly, being force-free, the numerical implementation allows for residual Lorentz force because of the unavoidable numerical errors. Therefore, following Inoue et al. (2016), this residual force is used as a perturbation to initiate one of the simulations.

The NFFF extrapolation model based on Minimum Dissipation Rate principle (see chapter 2), gains its importance from an implicit presence of non-zero Lorentz force at the bottom boundary which can drive the plasma dynamics. Some of the earlier works that have confirmed the efficacy of NFFF model in exploring several scenarios of observational interest include magnetic field lines evolution leading to solar flares and blowout jets (Prasad et al., 2018, Nayak et al., 2019, Nayak et al., 2021) along with the development of current sheets around null points (Kumar & Bhattacharyya, 2016) and QSLs (Kumar et al., 2021).

The overall workflow selects an active region hosting a flare, extrapolates the magnetic field using the two approaches, and uses them as input for simulations. The simulation results are then compared to draw conclusions. In the following, the details of active region and the chosen solar flare for this study are presented.

6.2 Active Region and Flare Event

For the purpose of this study, the choice of flare is guided only to the extent that the associated active region is in accordance with the requirements of magnetic field extrapolation and boundary conditions employed in the MHD simulation. Consequently, a C6.6 class flare on 2014 February 17 from active region NOAA 11977 with heliographic coordinates S13W05 is selected. The reason for this choice follows from (a) nearly disk-centered positioning of the active region, which pertains to low measurement error in photospheric vector magnetic field and also minimizes the projection effects due to finite curvature of the photospheric surface (Venkatakrishnan et al., 1988). Both the effects combinedly reduce error during magnetic field extrapolation (b) minimal changes during the course of the flare in the photospheric magnetic flux integrated over the active region, which complies with the condition B_z=const. at the bottom boundary, used in the MHD simulation. The panel (a) in figure 6.1 depicts the GOES soft X-ray flux during the

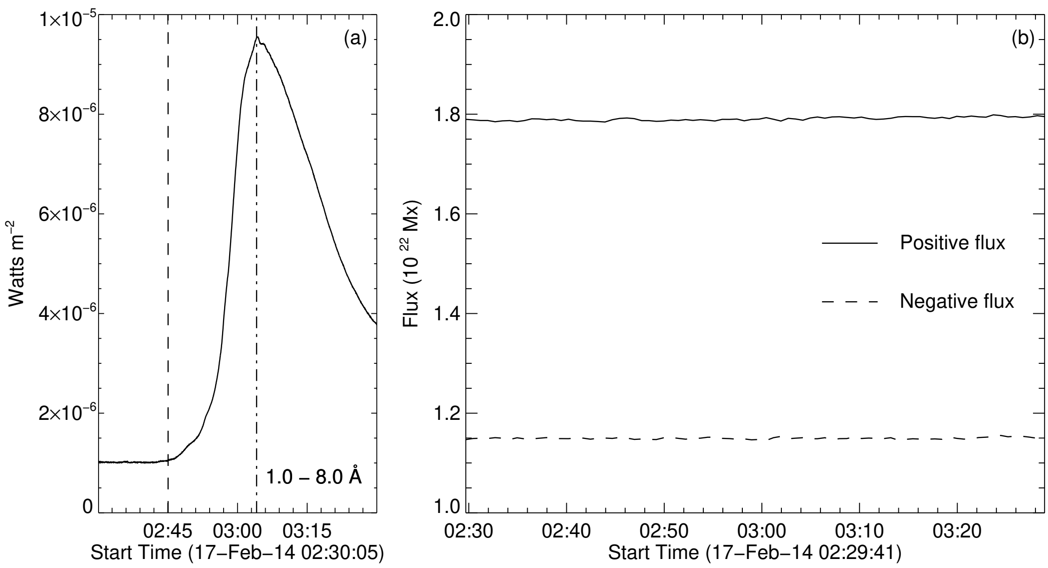

Figure 6.1: (a) GOES soft X-ray flux for one hour period starting at 02:30 UT in 1-8 Å channel. The *dashed black line* marks the rising phase at ∼ 02:45 UT and the *dashed-dot line* marks the peak time of the flare. (b) Photospheric flux during one hour period starting from 02:30 UT where the *solid line* denotes positive flux and the *dashed line* denotes negative flux.

course of the flare in the 1-8 Å channel, revealing a gradual rise in intensity around ∼ 02:45 UT, peaking at 03:04 UT. The panel (b) in figure 6.1 shows the evolution of horizontally averaged positive (*solid*) and negative (*dashed*) photospheric magnetic flux obtained from hmi.M_45 series of HMI for a duration of ∼ 1 hr, starting around 02:30 UT. The magnetic flux is reasonably constant during the flare, the relative changes for both positive and negative fluxes being well within 1 %. In figure 6.2 the temporal evolution of the flaring event in 131 Å channel of

AIA for a duration of $\sim$ 35 m, starting around 02:45 UT is illustrated. Panels (b), (c), and (f) mark the approximate spatial locations of brightenings identified at different instances during the flare as b_1, b_2, b_3, and b_4, respectively. Notably, a

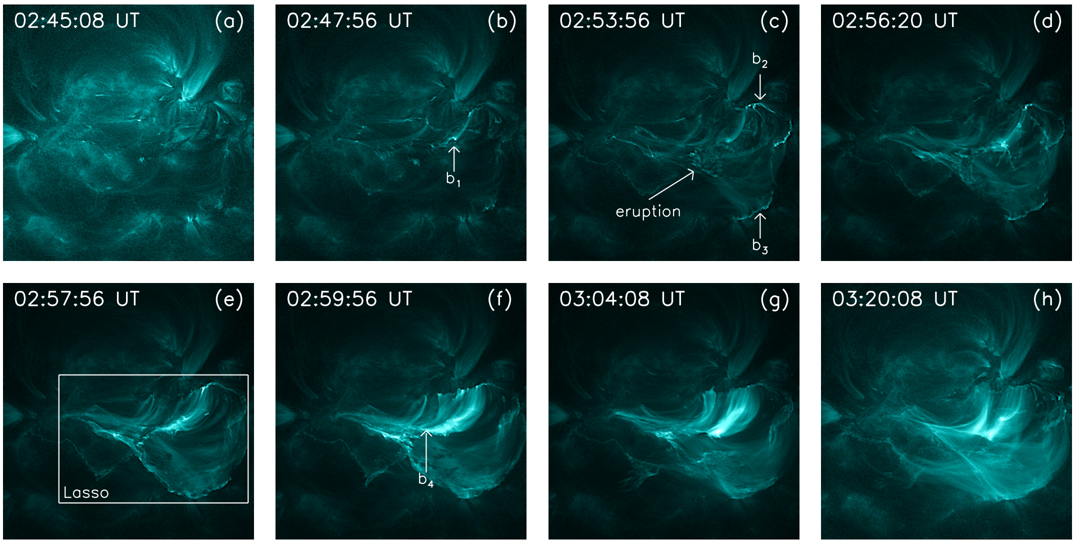

Figure 6.2: Snapshots from the temporal evolution of active region NOAA 11977 in Extreme Ultraviolet (131 Å) channel of SDO/AIA, starting around 02:45 UT. Panels (b), (c), and (f) mark the brightenings b_1, b_2, b_3, and b_4 identified during the course of flare. Panel (e) highlights the *lasso* structure that describes the overall flaring configuration. Panel (g) and panel (h) correspond to the peak time and termination time of the flare.

lasso structure is recognized, visible in panel (e), which prominently displays the overall geometry of the flaring region. After identifying the spatial locations of the observed brightenings, measurements of the photospheric magnetic field (vector magnetograms) are employed in order to extrapolate the magnetic field. The details of extrapolation are presented below.

6.3 Details of Magnetic Field Extrapolation

The magnetic field is extrapolated at 02:48:00 UT, using the hmi.sharp_cea_720s data series of HMI, which offers the advantage that the measured magnetic field is corrected for projection and foreshortening effects. The dimensions of the SHARP series data for active region NOAA 11977 is 906×540 pixels, which is equivalent to $328.4\,\mathrm{Mm} \times 195.7\,\mathrm{Mm}$. In the context of force-free modeling or nonlinear force-free extrapolation model, recall that the photospheric vector field measurements are generally not force-free because of high plasma-β. A quantification of this is made by the parameters ϵ_{flux}, ϵ_{force}, and ϵ_{torque} (see section 2.4.3). If their values are low (below about 0.1) the boundary conditions are considered sufficiently force-free. However, the used SHARP data amounts to $\epsilon_{\text{flux}} \sim 0.2326$, $\epsilon_{\text{force}} \sim 0.1590$, and $\epsilon_{\text{torque}} \sim 0.1690$, respectively. Consequently, the preprocessing procedure is applied, giving $\epsilon_{\text{flux}} \sim 0.2466$, $\epsilon_{\text{force}} \sim 0.0005$, and $\epsilon_{\text{torque}} \sim 0.0015$, respectively. This preprocessed magnetogram is used as the boundary condition for 3D NLFFF modeling. The values of the parameters used in the extrapolation are specified in table 6.1. The extrapolation is carried out with a bottom boundary grid of 896 $\times$ 528 voxels and the vertical extent of 272 voxels. In physical lengths the size is $\sim$ 324.8 Mm $\times$ 191.4 Mm $\times$ 98.6 Mm. For the purpose of quantitative and

μ_1	μ_2	μ_3	μ_4	w_f	w_d	ν	w_{los}	w_{trans}
1	1	0.01	0.01	1	1	0.001	1	$\text{B}_\text{T}/\max(\text{B}_\text{T})$

Table 6.1: Summary of the parameters used in the NLFFF extrapolation.

morphological comparison, the non-force-free extrapolation is also carried out on the same computational grid of 896 $\times$ 528 $\times$ 272 voxels as in the NLFFF case. Importantly, the Lorentz force at the photosphere is non-zero for the NFFF but decays sharply with height. In the present case, the values are $\in [5.8\%, 0.04\%]$ of its photospheric value for height $\in [3.2, 98.6]$ Mm, thus making it approximately force-free at the coronal heights. The variation of E_n (see equation 2.48) along with the number of iterations is depicted in figure 6.3, documenting a difference of 34.5% between the extrapolated and measured transverse magnetic fields. Since, two extrapolation models are being used, it is important to evaluate the goodness of respective extrapolated magnetic fields and also to analyze the differences between the nonlinear and non-force-free magnetic fields, as discussed in the following.

6.4 Analysis of Extrapolated Magnetic Fields

Following Wheatland et al. (2000), the quality or the goodness of the extrapolated fields is determined by evaluating the averaged fractional flux error, given by

$$\langle f_i \rangle = \left\langle \frac{(\nabla.\mathbf{B})_i \triangle V_i}{B_i A_i} \right\rangle, \tag{6.1}$$

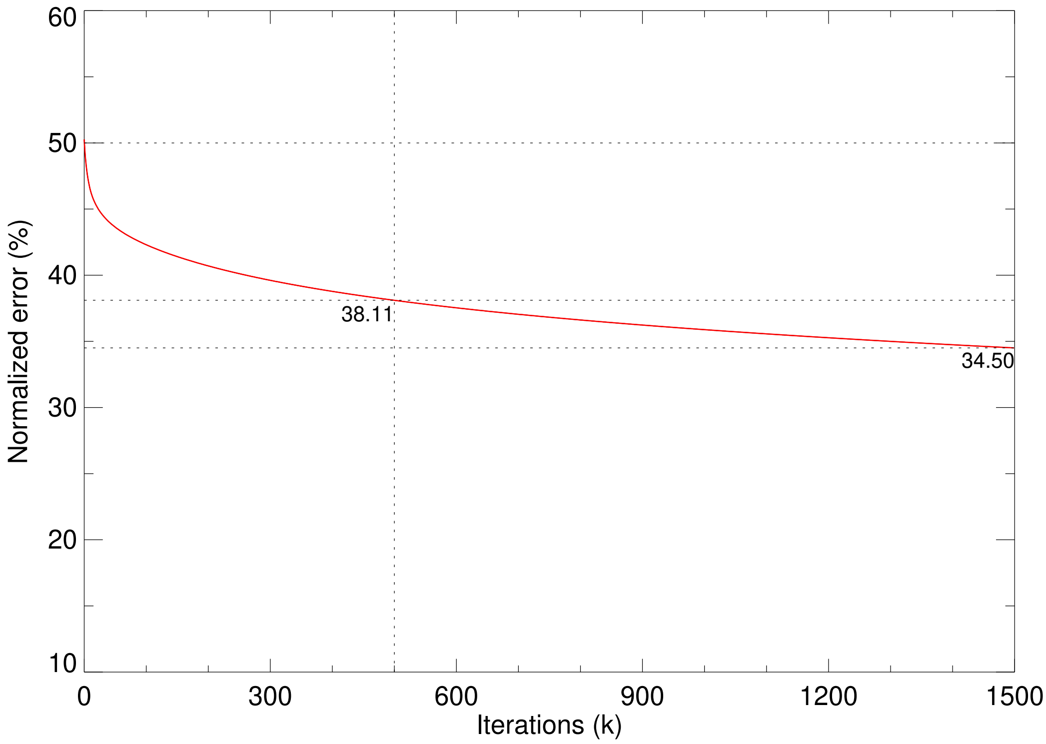

Figure 6.3: Minimized deviation (E_n) vs. number of iterations for NFFF extrapolation, which decreases monotonically and saturates approximately at $\sim 34.5\%$ for 1500 iterations.

where A_i is the surface area of the volume element $\triangle V_i$, and by computing the alignment $\theta = \sin^{-1}\sigma_j$ (see equation 4.7). The values are listed in table 6.2. The

Model	$\langle f_i \rangle$	σ_j	$\sin^{-1}\sigma_j$
NFFF	$1.11 \times 10{-}5$	0.9123	65.83°
NLFFF	2.89×10^{-4}	0.1491	8.58°

Table 6.2: Averaged fractional flux error ($\langle f_i \rangle$) and current weighted average of the sine of the angle between the current density and the magnetic field (σ_j) for NFFF and NLFFF extrapolations.

order of $\langle f_i \rangle$ in NFFF ($\sim 10^{-5}$) and NLFFF ($\sim 10^{-4}$) suggests that the extrapolated fields satisfy the divergence-free condition to an acceptable extent. The θ values which measure the departure from force-free condition turn out to be $\sim 65.83°$ for NFFF and $\sim 8.58°$ for NLFFF, respectively. In the case of force-free modeling, a numerical value of $\theta < 10°$ is usually considered acceptable. Relevantly, panels (a) and (b) in figure 6.4 plot the variation of horizontally averaged θ (denoted by $\theta_{\rm av}^{\rm H}$) for NFFF and NLFFF. At lower heights, the large ($> 50°$) values of $\theta_{\rm av}^{\rm H}$ in NFFF and small ($< 20°$) values in NLFFF seem to be in accordance with the model

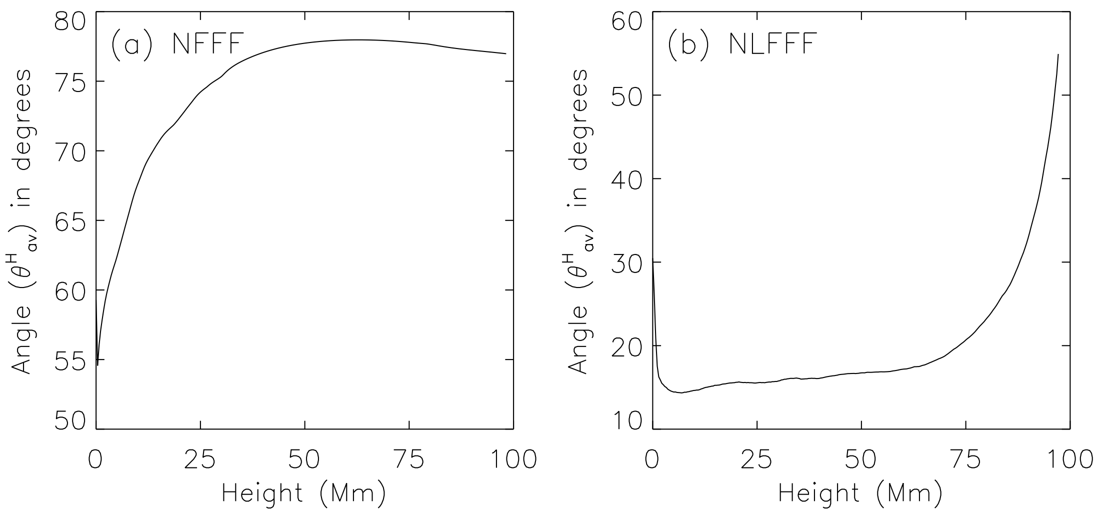

Figure 6.4: The variation of horizontally averaged θ (denoted by $\theta^{\mathrm{H}}_{\mathrm{av}}$) with height for (a) NFFF and (b) NLFFF

definitions. However, the increase in $\theta^{\mathrm{H}}_{\mathrm{av}}$ with height suggests that in the higher layers of solar atmosphere, the models are not force-free ($\mathbf{J} \times \mathbf{B} = 0$) from the viewpoint of alignment between current density and magnetic field. Therefore, to gain more insight, panels (a) and (b) in figure 6.5 plot the logarithmic variation of horizontally averaged $|\mathbf{B}|$, $|\mathbf{J}|$, and $|\mathbf{J} \times \mathbf{B}|$ with height in normalized units. As expected, all the variables decrease monotonically with height, albeit the curves are steeper for the NLFFF extrapolation. Therefore, the decrease in Lorentz force with height is presumably governed by the decay in magnitude of current density and magnetic field. On the other hand, the increase of $\theta^{\mathrm{H}}_{\mathrm{av}}$ with height could be due to field lines becoming more potential, which are characterized analytically by zero current density and low twist. Further, in a numerical implementation, there are always residual numerical currents which are randomly oriented (particularly for the potential field where $\mathbf{J} = 0$) and can lead to high values of $\theta^{\mathrm{H}}_{\mathrm{av}}$. In the next section, the quantitative and morphological differences between the nonlinear and non-force-free extrapolated magnetic fields are presented.

6.4.1 Quantitative Differences

To explore the deviation of $\mathbf{B}_{\mathrm{NFFF}}$ from $\mathbf{B}_{\mathrm{NLFFF}}$, the angle ($\Theta$) between the two magnetic fields is evaluated in each voxel of the computational domain. Panel (a) of figure 6.6 shows that the histogram plot of Θ peaks in the range $25^\circ \leq \Theta \leq 30^\circ$.

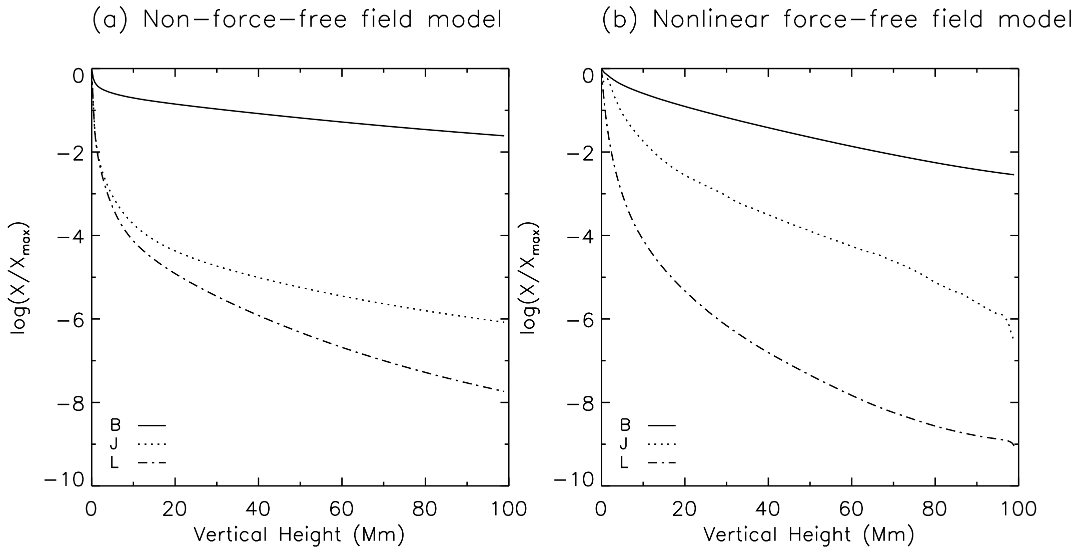

Figure 6.5: Panels (a) and (b) show the variation of horizontally averaged magnetic field ($X = B$), current density ($X = J$), and Lorentz force ($X = L$) with height on log scale for NFFF and NLFFF models. The normalization is done using the maximum value.

Also, it is found that $\Theta \leq 40°$ for $\sim 80\,\%$ of the voxels. The difference between the two extrapolated fields is further investigated by computing the following metric in every voxel

$$d = \frac{\sum_{i=1}^{3} \left(\mathbf{B}^{\mathrm{i}}_{\mathrm{NLFFF}} - \mathbf{B}^{\mathrm{i}}_{\mathrm{NFFF}}\right)^2}{|\mathbf{B}_{\mathrm{NLFFF}}| \times |\mathbf{B}_{\mathrm{NFFF}}|}, \tag{6.2}$$

where $\mathbf{B}^{\mathrm{i}}_{\mathrm{NLFFF}}(i = x, y, z)$ and $\mathbf{B}^{\mathrm{i}}_{\mathrm{NFFF}}(i = x, y, z)$ denote the i^{th} component of nonlinear force-free field and non-force-free field, respectively. The corresponding histogram plot is shown in panel (b) of figure 6.6 and the maximum value of d is found to be $d_{\mathrm{max}} \sim 500$ but $d \leq 10$ for $\sim 99.9\,\%$ of the voxels in the computational volume. For further exploration, vector magnetograms are used to compute the difference between the measured ($|\mathbf{B}^{\mathrm{O}}_{\mathrm{T}}|$, $|\mathbf{B}^{\mathrm{O}}_{\mathrm{LOS}}|$) and extrapolated ($|\mathbf{B}^{\mathrm{M}}_{\mathrm{T}}|$, $|\mathbf{B}^{\mathrm{M}}_{\mathrm{LOS}}|$) magnetic fields at the bottom boundary. The subscripts "T" and "LOS" refer to the transverse and line-of-sight components of the magnetic field. Panels (c) and (d) in figure 6.6 plot the histogram distribution of $|\mathbf{B}^{\mathrm{O}}_{\mathrm{T}}| - |\mathbf{B}^{\mathrm{M}}_{\mathrm{T}}|$ and $|\mathbf{B}^{\mathrm{O}}_{\mathrm{LOS}}| - |\mathbf{B}^{\mathrm{M}}_{\mathrm{LOS}}|$, respectively. It is seen that for the transverse component, the representative curves are almost overlapping, implying nearly identical distribution for the two models. However, NFFF (*red*) shows a relatively higher peak as compared to NLFFF (*blue*), suggesting that a greater fraction of voxels satisfy the condition $|\mathbf{B}^{\mathrm{O}}_{\mathrm{T}}| - |\mathbf{B}^{\mathrm{M}}_{\mathrm{T}}| \approx 0$

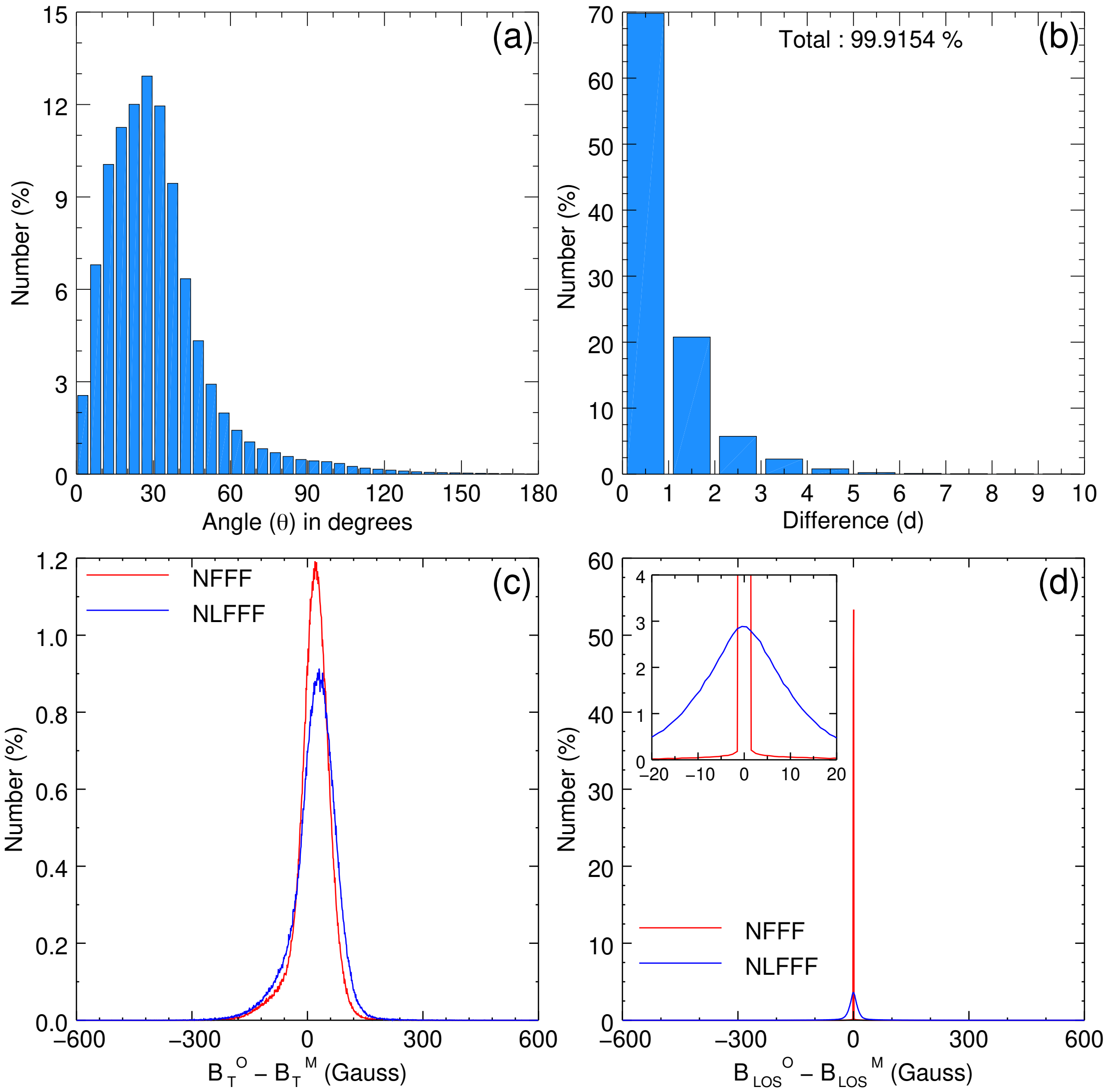

Figure 6.6: Panels (a) and (b) Histogram plot for the distribution of angle (Θ) and difference metric (d) inside the computational domain with bin size of 5° and one unit, respectively Panels (c) and (d) Distribution of difference between measured and extrapolated transverse ($|\mathbf{B}^{\mathrm{O}}_{\mathrm{T}}| - |\mathbf{B}^{\mathrm{M}}_{\mathrm{T}}|$) and line-of-sight ($|\mathbf{B}^{\mathrm{O}}_{\mathrm{LOS}}| - |\mathbf{B}^{\mathrm{M}}_{\mathrm{LOS}}|$) fields on the bottom boundary for NFFF (*red*) and NLFFF (*blue*). The sub-panel in (d) shows the zoomed-in view of distribution for $-20 \leq |\mathbf{B}^{\mathrm{O}}_{\mathrm{LOS}}| - |\mathbf{B}^{\mathrm{M}}_{\mathrm{LOS}}| \leq 20$, highlighting the central peak in NLFFF in comparison to NFFF. Total refers to the fraction of voxels that lie within the range of values defined along x-axis.

in NFFF extrapolation. For the line-of-sight magnetic field, the distribution for NLFFF is broad, peaking at $\sim 3\,\%$ (sub-panel in (d)) while for NFFF, it is narrow, peaking at $\sim 50\,\%$, centered at $|\mathbf{B}^{\mathrm{O}}_{\mathrm{LOS}}| - |\mathbf{B}^{\mathrm{M}}_{\mathrm{LOS}}| \approx 0$. This suggests that the NFFF performs better than NLFFF for line-of-sight field. The differences in the above distributions can also be understood in terms of a scatter plot where the Pearson correlation coefficient (R) is estimated, as shown in panels (a) to (d) of

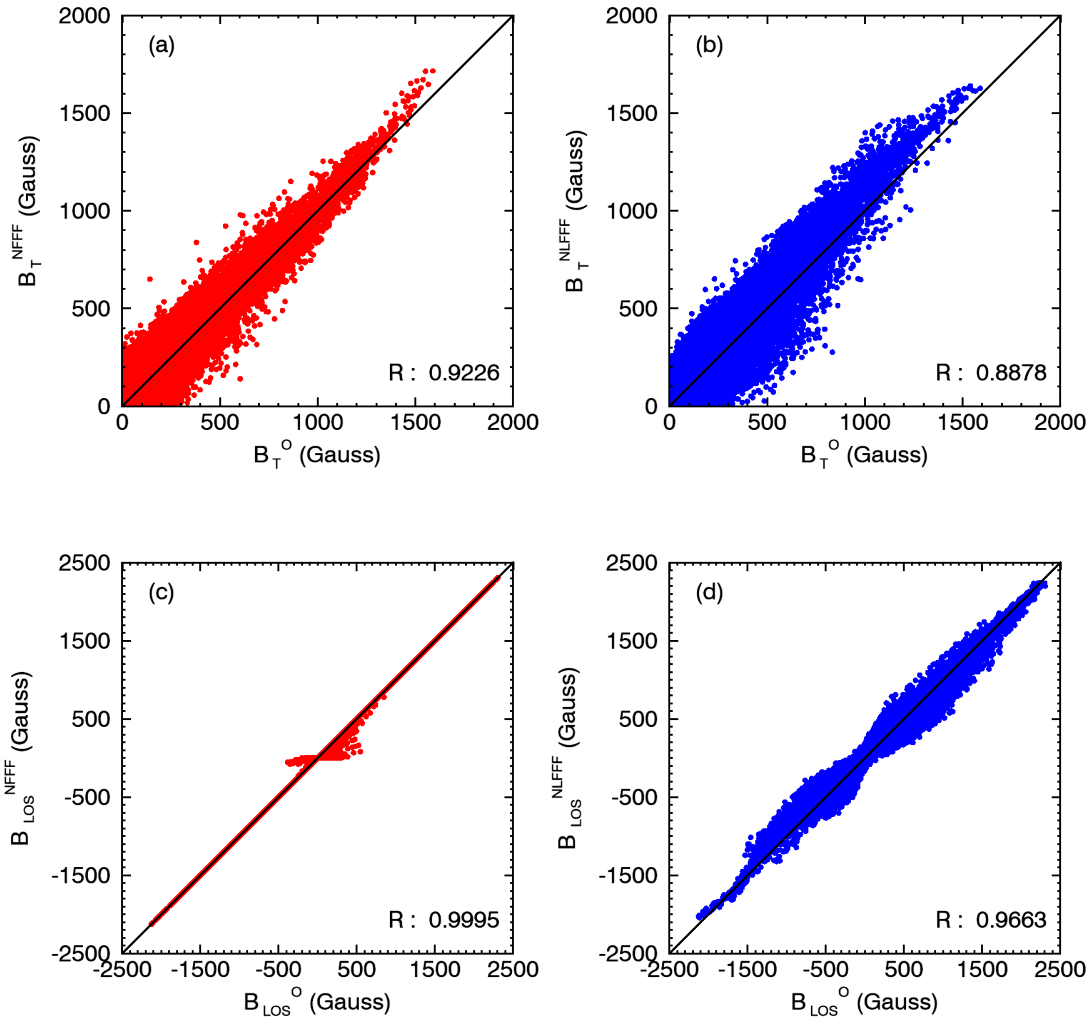

Figure 6.7: The correlation between extrapolated and measured magnetic fields on the bottom boundary using scatter plot for (a) Transverse component of NFFF field, (b) Transverse component of NLFFF field, (c) line-of-sight component of NFFF field, (d) line-of-sight component of NLFFF field.

figure 6.7. The values $\mathrm{R_{NFFF}} = \{0.9226, 0.9995\}$ and $\mathrm{R_{NLFFF}} = \{0.8878, 0.9663\}$ indicate that NFFF has a better correlation to the measured line-of-sight and transverse magnetic fields. Notably, the correlation between $\mathbf{B}^{\mathrm{NFFF}}_{\mathrm{LOS}}$ and $\mathbf{B}^{\mathrm{O}}_{\mathrm{LOS}}$ is not exactly identical because a Hanning window is employed in the NFFF model, which smoothens the magnetic field values near the edges of the magnetogram to zero via a cosine function to ensure periodic boundaries. Consequently, the two data sets do not match perfectly, leading to a deviation of data points from the straight line. In order to explore the differences between the two extrapolated fields further, the variations of Θ and d as a function of distance from the location of magnetic null points is investigated. The null points in both the extrapolated

fields are detected by using the trilinear method (Haynes & Parnell, 2007), which is discussed briefly in Appendix B. For a particular null point, the results are depicted in figure 6.8 and it is seen that both the parameters decrease with distance. This

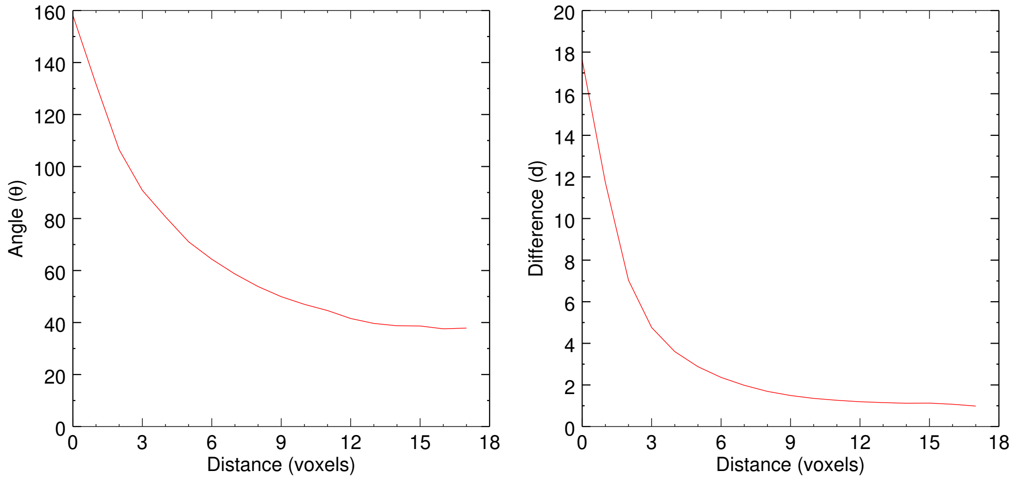

Figure 6.8: Example of the variation of averaged angular deviation, Θ (*left*) and the averaged difference metric d (*right*) as a function of distance from the location of detected magnetic null point in NFFF.

result points toward the possibility that regions of maximal difference between the extrapolated fields could be in the near neighborhood of magnetic nulls. In order to confirm this, a detailed statistical analysis involving multiple active regions is required. Since the source of energy release during eruptive events is the stored free magnetic energy, it is noted that the extrapolated magnetic field configuration in the NFFF model has more free magnetic energy compared to the extrapolated NLFFF i.e., $\mathrm{E_F(NFFF)} \sim 1.94 \times 10^{32}$ erg and $\mathrm{E_F(NLFFF)} \sim 4.34 \times 10^{31}$ erg, where $\mathrm{E_F}$ denotes the total free magnetic energy inside the computational domain. This implies that $\mathrm{E_F(NFFF)} \sim 5 \times \mathrm{E_F(NLFFF)}$. Presumably, the difference is due to a combined effect of the faster decay of magnetic field with height in the NLFFF and higher average twist in the NFFF, where the volume averaged twist amounts to 0.56 and 7.87 for nonlinear and non-force-free models, respectively.

6.4.2 Morphological Differences

To explore the morphological differences between the two extrapolation models, the overall *lasso* geometry is considered first. The magnetic field lines (MFLs) at the large length scales, overlying the *lasso* geometry are considered to be the indicator of magnetic field configuration on the global scales, as shown in panels (a) and (b) of figure 6.9 for the NFFF and NLFFF models, respectively. There are two sets of magnetic field lines, namely the high-lying (*yellow*) and low-lying (*red*) MFLs. One of the footpoints of these MFLs trace the *lasso* boundary while the other end of these MFLs are rooted within the area enclosed by the boundary. The overall magnetic configuration in both models is aptly described by the description that MFLs emerging from the noose of *lasso* are directed toward the knot and further extend to the handle of the *lasso*. Following Liu et al. (2016b), squashing degree is calculated[†] and it is found that in the near vicinity of b_2 and b_4, the footpoints of red and yellow MFLs map the region of high $\ln Q \sim 10$, thus indicating the possibility of slipping reconnections at large length scales. Notably, the squashing degree map for NLFFF appears to be smudged as compared to the NFFF, which is presumably due to the pre-processing procedure adopted in the NLFFF model. To explore the flare dynamics in more detail, an investigation for the reconnection sites at smaller length scales is carried out. From preliminary MHD simulations, it is found that multiple reconnection events spread over the spatial extent of the *lasso*. Understandably, it is a non-trivial task to categorize all the reconnection sites in terms of their importance with respect to the observations. Consequently, further analysis is narrowed down to topological structures which are cospatial with the observed brightenings. The structures of interest are a hyperbolic flux tube (HFT) in the vicinity of b_2, characterized by large squashing degree, and a magnetic null point in the near neighborhood of b_3. Using trilinear method, the null point in NFFF extrapolation is found to be at x = 588, y = 147 and z = 18 while the same null point is detected at x = 579, y = 153 and z = 13 in NLFFF extrapolation; in voxel units. In order to illustrate various features of the null point geometry, three positive and a negative polarity are defined as shown in panels (a) and (b) of figure 6.10 for NFFF and NLFFF models, respectively. The polarities are labeled as P_1, P_2, P_3, and N_1 in NFFF while in NLFFF by the corresponding primed variables. Notice that P_1' is highlighted in red, the significance of which will be explained shortly. As shown in panel (a) of figure 6.11

[†]The used code is available at http://staff.ustc.edu.cn/~rliu/qfactor.html

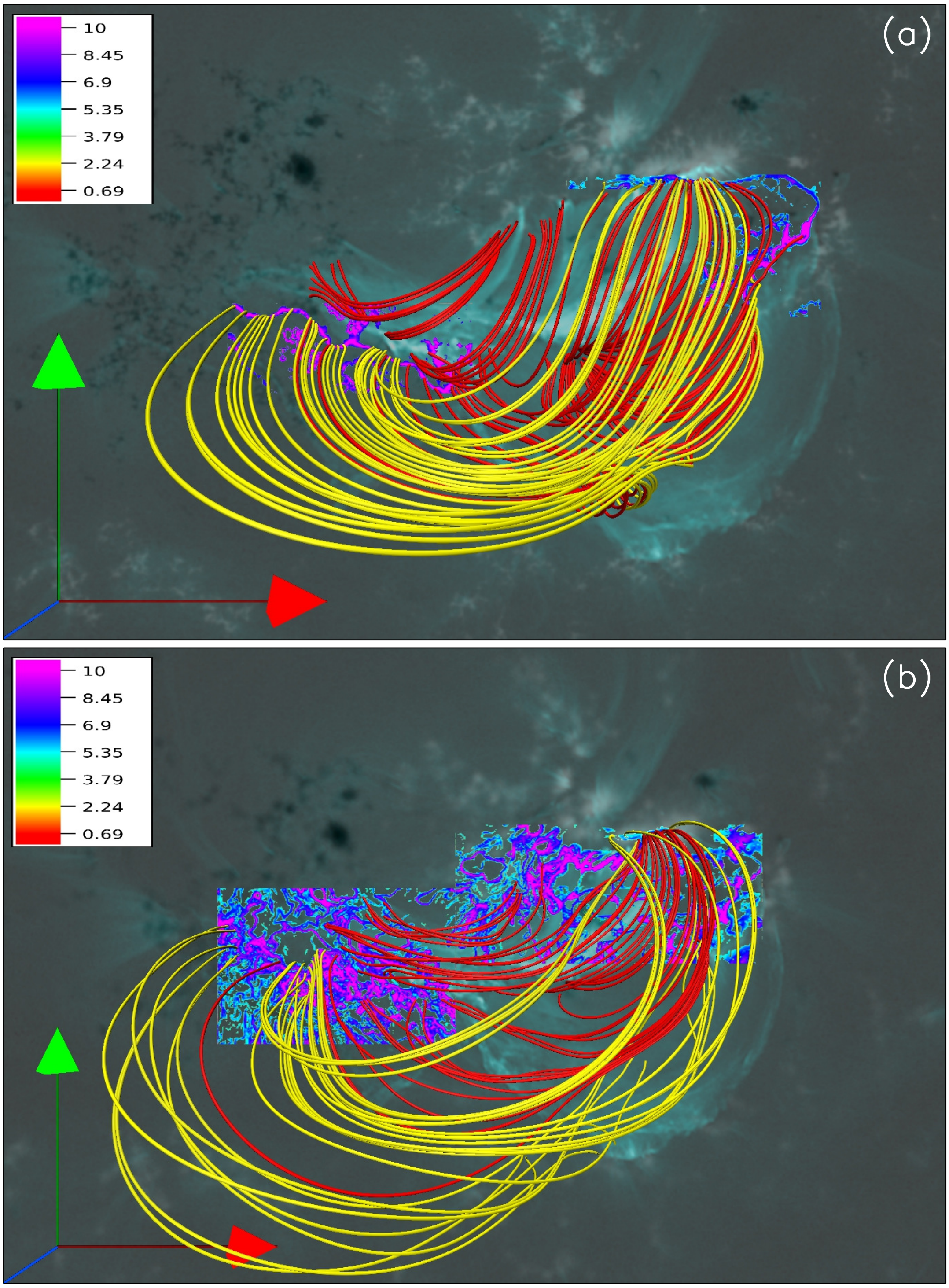

Figure 6.9: Panels (a) and (b): Top side view of the global MFL morphology in NFFF and NLFFF modeling. Two sets (*red* and *yellow*) of magnetic field lines are overlaid on the line-of-sight magnetogram along with the *lasso* structure identified in the 131 Å channel of SDO/AIA at 02:59:56 UT (figure 6.2). The regions of high gradient in magnetic field line connectivity are shown using the map of calculated squashing degree ($\ln Q$) distribution on the bottom boundary, with the coded color table. The *red*, *green* and *blue arrows* mark the x, y and z-axis, respectively.

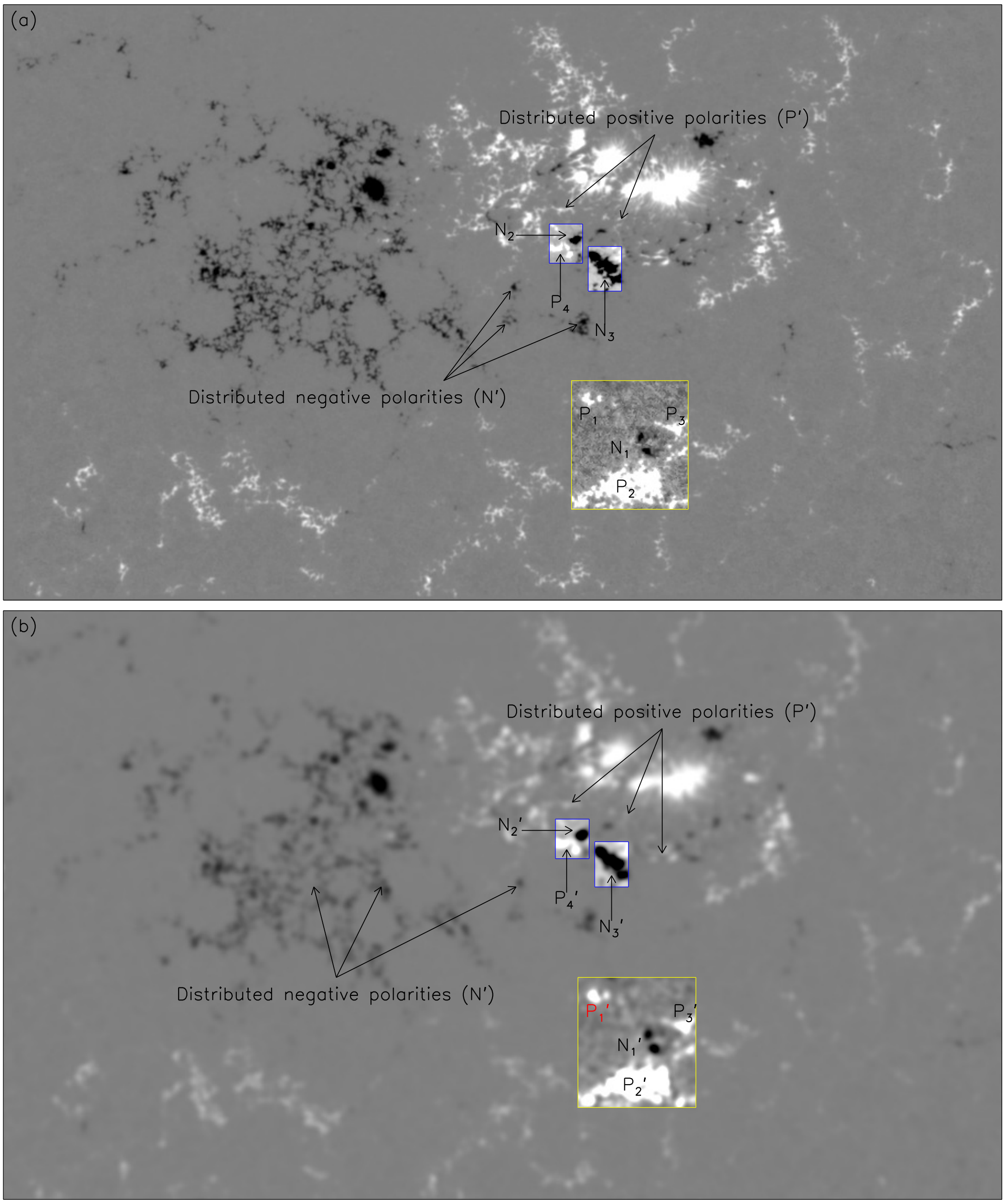

Figure 6.10: Panels (a) and (b) Distribution of $|\mathbf{B}^{\mathrm{M}}_{\mathrm{LOS}}|$ over the photospheric boundary in non-force-free and nonlinear force-free modeling. The images are scaled for $|\mathbf{B}^{\mathrm{M}}_{\mathrm{LOS}}| \leq 1000$ G in (a) $|\mathbf{B}^{\mathrm{M}}_{\mathrm{LOS}}| \leq 1500$ G in (b). The *yellow box* enclosing polarities $\mathrm{P}_1, \mathrm{P}_2, \mathrm{P}_3$, and N_1 in (a) and the corresponding primed polarities in (b) constitute the null point topology. The magnetic polarities P_4 and N_2 within the *blue* box along with distributed polarities (P and N) in (a) and the corresponding primed polarities in (b) comprise the HFT geometry. The additional polarity $\mathrm{N}_3(\mathrm{N}_3')$ in (a) and (b) will be used to describe the field-line dynamics at HFT during the simulated evolution. The regions within the *yellow* and *blue boxes* are scaled further for enhanced visibility.

for the non-force-free field, the magnetic field lines originating from $\mathrm{P}_1, \mathrm{P}_2$, and P_3 terminate at N_1, thus constituting the dome-shaped fan surface (*red* MFLs) and the lower spine (S_1) of the null while the *white* MFLs, originating from P_1, P_2, and P_3, extend into the corona forming the upper spine (S_2) of null. For nonlinear

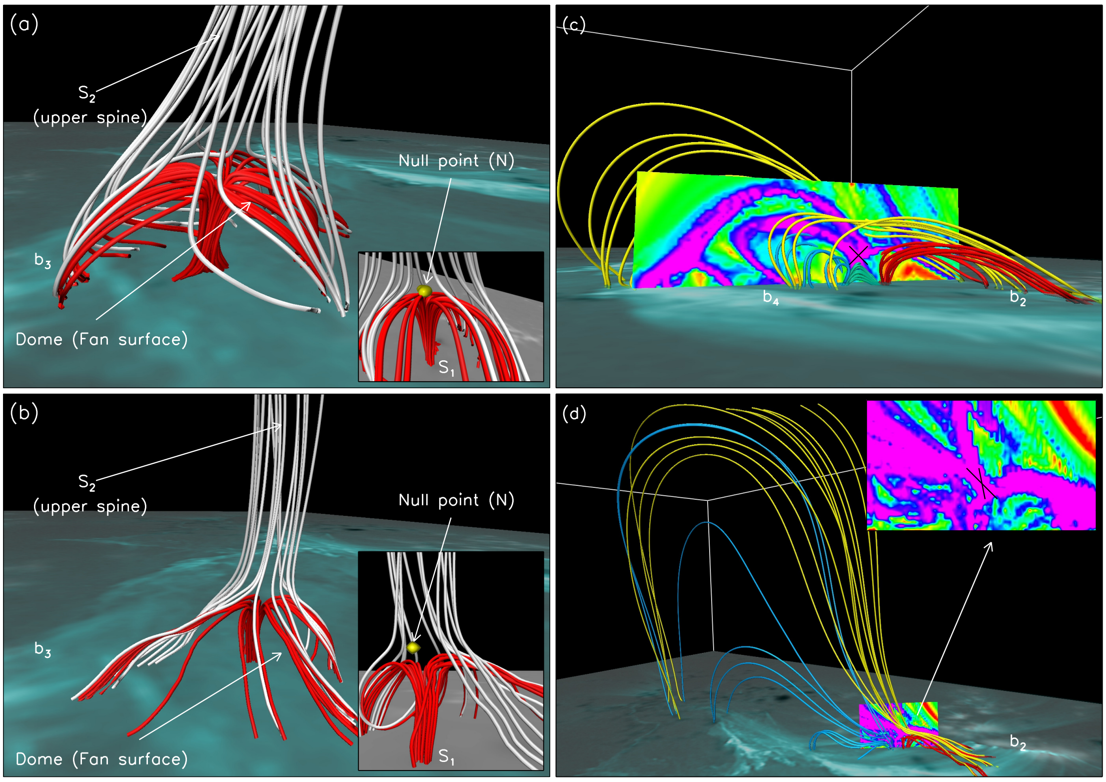

Figure 6.11: Panels (a) and (b): Magnetic null point topology in non-force-free and nonlinear force-free extrapolation models, depicting the dome-shaped fan surface (*red*), lower spine (*red*; S_1) and upper spine (*white*; S_2). The sub-panels in (a) and (b) highlight the null point location (*yellow*). Panels (c) and (d): Hyperbolic flux tube morphology in NFFF and NLFFF extrapolation models along with $\ln Q$ distribution in plane perpendicular to bottom boundary.

force-free field, panel (b) depicts a similar magnetic null point morphology with an identifiable fan surface, upper and lower spines. Despite the apparent similarity of null point topology as obtained in the two models, a crucial difference regarding the relevance of P'_1 is noted. It is seen that there is no recognizable magnetic field line connectivity between the polarities P'_1 and N'_1. This particular difference could be due to the preprocessing adopted in NLFFF modeling, thus effectively destroying the connectivity of P'_1 with respect to N'_1.

The magnetic field lines constituting the hyperbolic flux tube can be categorically separated into four distinct quasi-connectivity domains such that the field lines inside each domain share similar field line connectivity. To specify the domains, magnetic polarities are defined manually as $P_4(P'_4)$, $N_2(N'_2)$, and two extended regions of distributed positive and negative polarities - P(P′) and N(N′) as shown in panels (a) and (b) of figure 6.10 for NFFF and NLFFF, respectively. Four different sets of magnetic field lines (*green, yellow, blue* and *red*) comprising the HFT morphology in NFFF are depicted in panel (c) of figure 6.11, where each set of MFL represents a quasi-connectivity domain. The HFT configuration contains two intersecting QSLs, as follows. The *green* and *blue* MFLs originating from P_4 constitute a QSL whose footpoints terminate at N_2 and N, respectively. Another QSL is defined by the set of *red* and *yellow* MFLs, which originate from P and terminating at N_2 and N. Similarly, for the nonlinear force-free field, a similar morphology is obtained, as shown in panel (d) of figure 6.11 but with two subtle differences. Comparison of panels (c) and (d) reveals that the counterpart of *green* MFLs (in NFFF) is not found in NLFFF, which could be due to the weaker correlation of the nonlinear force-free field with observed line-of-sight magnetic field. Further, it is seen that the terminating footpoints of *yellow* and *blue* MFLs are more scattered in NLFFF, extending more towards the handle of *lasso*. The map of calculated squashing degree in the plane perpendicular to the bottom boundary reveals a characteristic X-shape for the distributed $\ln Q$ (~ 10) values in both the models, thus supporting our interpretation of the MFL morphology. Importantly, an additional negative polarity $N_3(N_3')$ is marked, whose significance will be explained later in the context of simulated evolution. For the chosen null point and HFT, the effect of such similarities and differences on the process of magnetic reconnection is explored with simulated evolution of the magnetofluid, as described in the following sections.

6.5 The MHD Simulation and its Analysis

The EULAG-MHD model is employed to execute the simulation. The boundaries are kept open, meaning that the net flux through the boundaries is constant. In order to optimize the computational cost, the active region cutout is remapped on a coarser grid having $448 \times 256 \times 192$ voxels, resolved on a computational grid of $x \in [-0.875, 0.875]$, $y \in [-0.5, 0.5]$ and $z \in [-0.375, 0.375]$ in a Cartesian coordinate system. The spatial step sizes are $\Delta x = \Delta y = \Delta z \approx 0.0039$ (or, ≈ 725 km), while the time step is $\Delta t = 2 \times 10^{-3}$. Further, the fluid Reynolds number is set to 5000, which is five times smaller than the coronal value of ≈ 25000. The coronal value is calculated using kinematic viscosity, $\nu = 4 \times 10^9$ m^{2}s^{-1} (Aschwanden, 2005, p.791) in the solar corona. The reduced R_F^A can be interpreted as a smaller computed Alfvén speed where $V_A|_{\text{sim.}} \approx 0.14 \times V_A|_{\text{corona}}$. The Alfvén speeds are estimated with 139.2 Mm (the active region scale) as the characteristic scale for the computational domain and 100 Mm for the typical corona. The simulation time is $1000\Delta t$, which approximately equals to an observation time of 33 minutes. Importantly, although the coronal plasma with a reduced fluid Reynolds number is not realistic, the choice does not affect the changes in field line connectivity because of reconnection, but only the rate of evolution. Additionally, it saves computational cost, as demonstrated by Jiang et al. (2016).

Three distinct simulations (hereafter referred as S_1, S_2 and S_3), starting from different choices of initial configuration have been carried out. All the simulations are initiated by utilizing the vector magnetogram measured at 02:48:00 UT. The reduction in resolution is checked to have no effects on the identified topological structures. Simulation S_1 takes NFFF as the input magnetic field with non zero Lorentz force in the computational volume, initialized from a motionless state or with zero external flow. Initially, the Lorentz force pushes the plasma to generate dynamics. In simulation S_2, the NLFFF is driven only by the residual Lorentz force due to numerical deviation from its analytical value of exact zero. For the simulation S_3, a perturbative flow is imposed to S_2, derived from the 100^{th} timestep of S_1. For brevity, hereafter the three initial conditions are referred to as $S_1 \equiv \{\mathbf{B}_{\text{NFFF}}, \mathbf{0}\}$, $S_2 \equiv \{\mathbf{B}_{\text{NLFFF}}, \mathbf{0}\}$ and $S_3 \equiv \{\mathbf{B}_{\text{NLFFF}}, \mathbf{v}_{\text{pert}}\}$.

With these simulations, the underlying magnetic reconnection at the magnetic null point and at the hyperbolic flux tube (HFT) is explored. Importantly, in all the simulations, magnetic null point generation and annihilation (the null is named as transient null or TN) is found in near neighborhood of the HFT. The presence of this magnetic null point (TN) is confirmed by using the trilinear method of null point detection. The null point coordinates (voxel units) are shown in table 6.3. The next section details the simulation results.

	S_1	S_2	S_3
x	247	259	259
y	144	155	157
z	1	4	6

Table 6.3: Coordinates of the transient magnetic null point as detected in S_1, S_2 and S_3 by the trilinear method of null point detection.

6.5.1 Global Energetics

The global-scale dynamics is investigated in the simulations by exploring the time evolution of volume integrated magnetic, free magnetic, kinetic and total (magnetic + kinetic) energies; depicted in panels (a), (b), (c), and (d) of figure 6.12. The *solid*, *dotted* and *dashed* lines correspond to simulations S_1, S_2, and S_3. Panels (a) and (b) establish a similar behavior of magnetic and free magnetic energies in all the three simulations—exhibiting continuous decrease with time and plots being parallel to each other; albeit starting from different initial values. Noticeably, the plots for simulations S_2 and S_3 overlap, being almost indistinguishable. The free energies at the initial states are 2.65×10^{32} ergs in S_1 and 8.8×10^{31} ergs in S_2 and S_3. The changes in free energies over the simulation, covering the flare duration, are of the order 4.46×10^{31} in S_1 and 3.33×10^{31} ergs in the other two—presumably consistent with the range of upper C-class to M-class flares (Rempel et al., 2021). Interestingly, the decrease in total magnetic energy (panel (a)) in all three simulations are approximately equal. For S_1 the decrease is 5.76% while 5.58% in S_2 and S_3, agreeing with the idea put forward in the beginning of this chapter. Moreover, the residual magnetic energy after relaxation is still much higher than the potential energy ($\sim 5.09 \times 10^{32}$ ergs), hence the active region, in principle, can still produce additional flares. Contrary to the free magnetic energy, the variation of the kinetic energy with time shows different behavior for S_1 when compared to S_2 or S_3. For the simulation initiated with NFFF, the Lorentz force is not balanced entirely over the simulation period and the kinetic energy exhibits an increasing profile throughout the simulation time. Furthermore, notable is the change in slope of the kinetic energy plot for S_1 at two distinct points (marked by *dashed blue* lines) in panel (c)—first at 4 min. (≡02:52:00 UT) and the second one at nearly 12 min (≡03:00:00 UT), which agrees approximately with instances of the observed brightenings, depicted in panels (b) and (c) of figure 6.2. For the

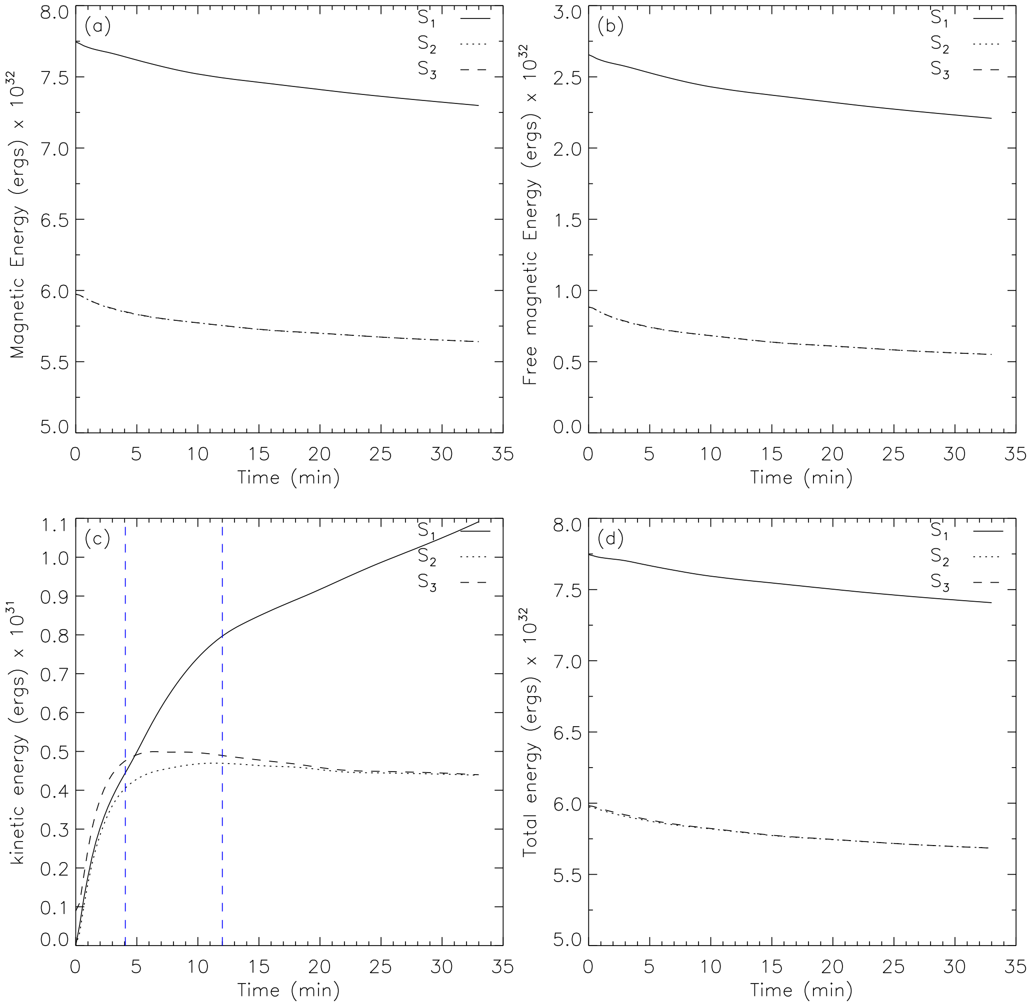

Figure 6.12: Panels (a), (b), (c), and (d) depict the time evolution of magnetic energy, free magnetic energy, kinetic energy and total energy (magnetic + kinetic) for simulations S_1 (*solid line*), S_2 (*dotted line*) and S_3 (*dashed line*) respectively. The x and y axis represent time (minutes) and energy (ergs) in physical units. The dashed blue lines correspond to instances of change in slope of kinetic energy profile for S_1.

simulations S_2 and S_3 which are initiated with NLFFF, the magnetofluid relaxes to an approximate steady state (in kinetic energy), as evident from panel (c). In the initial phase, kinetic energy in S_3 is higher than S_2, which is due to the imposed perturbative flow. The sum of magnetic and kinetic energies in all the simulations behave similarly and decreases monotonously with time, as shown in panel (d). In the following, investigation of changes in field line connectivity due to reconnection at the null point and HFT are discussed.

6.5.2 Magnetic Null Point

In the left column of figure 6.13, the evolution of various MFLs constituting the

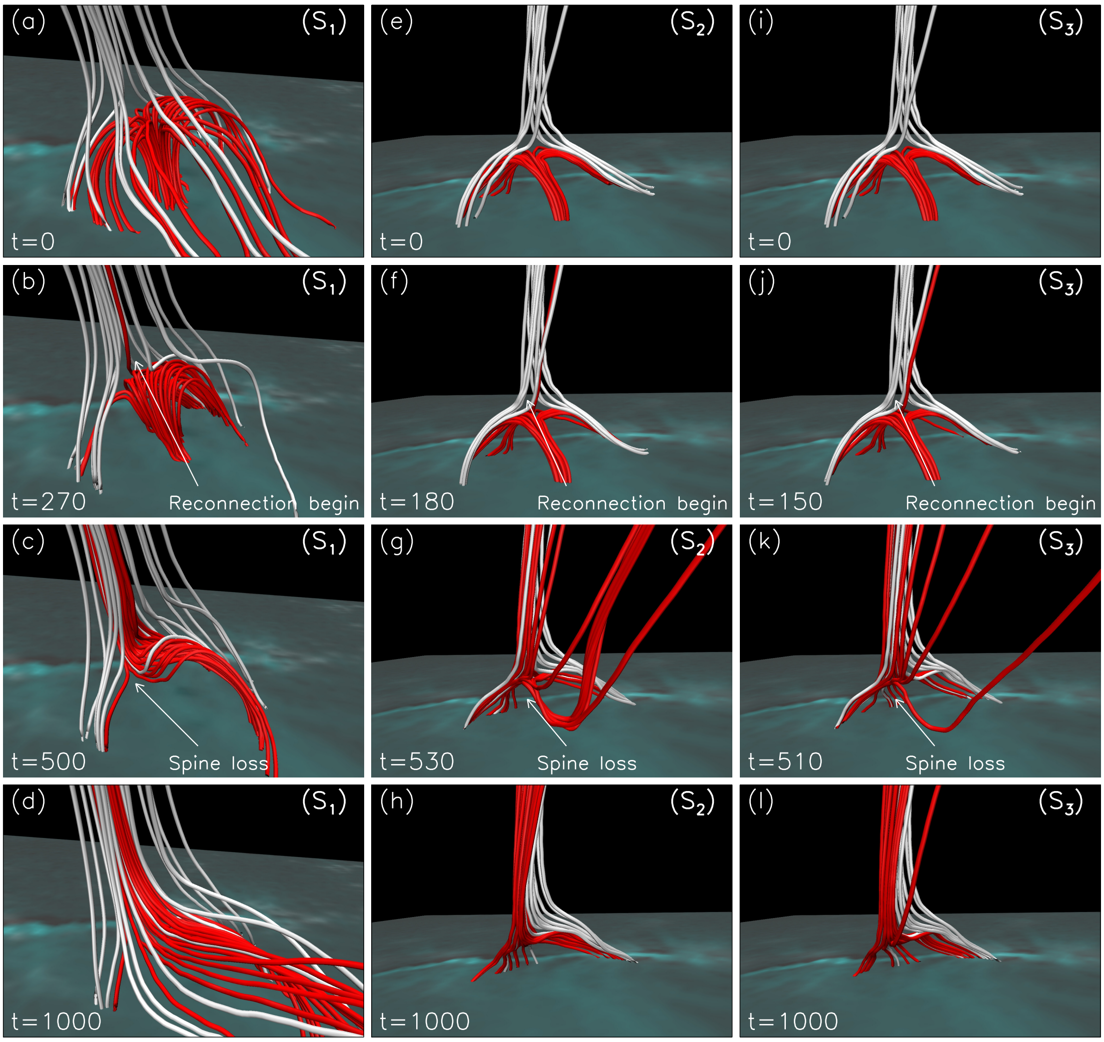

Figure 6.13: Snapshots from the simulated evolution of magnetic field lines in null point topology for S_1 (*left column*), S_2 (*middle column*) and S_3 (*right column*). The *second row* depicts the first instance of magnetic reconnection at the null point location while the *third row* corresponds to the loss of lower spine. The cospatiality of the observed brightening b_3 and the null point topology can be seen from the overlaid line-of-sight magnetogram from SDO/HMI at 02:48 UT along with an image of flaring region from SDO/AIA in 131 Å channel at 02:59:56 UT on the bottom boundary.

fan surface (*red*) and spine structures (*white*) for S_1 is depicted. From the selected field lines, the first instance of magnetic reconnection at null point location is found to occur at $t = 270$ ($\sim$8m54s$\equiv$02:56:54 UT), as shown in panel (b), where one of the red MFL constituting the lower spine (S_1) changes its connectivity from photospheric boundary to that of an open field line. During this time window, the fan plane is seen to exhibit slipping reconnection, which traces the brightening b_3, thus correlating well with the observed temporal sequence of b_3 (panels (c) and (d) in figure 6.2). The reconnection at the null point and slipping reconnections continue until about $t = 500$ ($\sim$16m30s$\equiv$03:04:30 UT), where the lower spine (S_1) is missing. This suggests that all the red magnetic field lines forming the lower spine have reconnected at the null point. Coincidentally, the corresponding time agrees precisely with the peak time of flare$\equiv$03:04:08 UT. Toward the end of simulation S_1, small circular motions along the footpoints of *red* and *white* MFLs constituting the fan plane relax the overall magnetic field configuration in local neighborhood of the null point. Panel (d) in figure 6.13 depicts the final state of simulated null point topology at $t = 1000$ ($\sim$33m$\equiv$03:21:00 UT), characterized by open magnetic field lines emerging from P_1, P_2, and P_3. Simulations utilizing the nonlinear force-free field as input magnetic field, S_2 and S_3 are analyzed and selective instances from the field line evolution in null point topology are presented in the middle (S_2) and right (S_3) columns of figure 6.13. As seen in panels (f) and (j), the first instance of magnetic reconnection at the null point location occurs at $t = 180$ in S_2, while in S_3, the same occurs at $t = 150$, presumably due to presence of finite perturbative flow. Notably, the reconnection in S_2 occurs earlier than in S_1, which may be accredited to the fact that the null point topology in the two extrapolation models are similar and not identical. As more and more magnetic field lines reconnect at the null point, the lower spine is lost at $t = 530$ in S_2 and at $t = 510$ in S_3, as shown in Panels (g) and (k), respectively. Interestingly, the lower spine is seen to disappear in all the simulations, nearly around the same time instance. In close correspondence with simulation S_1, the final state in S_2 and S_3, at $t = 1000$ is also identified by open magnetic field lines emerging from P'_2 and P'_3, as shown in Panels (h) and (l), respectively. For all the simulations, various changes in the magnetic field line connectivity due to reconnection at the null point topology, are summarized in table 6.4.

6.5.3 Hyperbolic Flux Tube

The magnetic field line dynamics at the location of hyperbolic flux tube (HFT) is complex, exhibiting multiple reconnection events for each set of magnetic field

	Before reconnection	After reconnection
S_1	P_1, P_2, $\mathrm{P}_3 \rightarrow \mathrm{N}_1$	P_1, P_2, $\mathrm{P}_3 \rightarrow$ open
S_2	P'_2, $\mathrm{P}'_3 \rightarrow \mathrm{N}'_1$	P'_2, $\mathrm{P}'_3 \rightarrow$ open
S_3	P'_2, $\mathrm{P}'_3 \rightarrow \mathrm{N}'_1$	P'_2, $\mathrm{P}'_3 \rightarrow$ open

Table 6.4: Summary of the footpoint mapping, before and after reconnection, corresponding to the magnetic null point topology for simulations S_1, S_2 and S_3.

lines. To simplify the analysis, rather than considering the overall dynamics at the HFT, each MFL set is considered separately. Further, due to absence of *green* field lines in the nonlinear force-free field extrapolation, only *yellow*, *red* and *blue* MFLs are considered for comparison across the three simulations. Also, due to the frequent changes associated with field line connectivity during reconnection, the analysis is limited to the peak time of flare, which corresponds to $t = 500$ in the simulated evolution. The relation between simulated time and peak time of flare is estimated by calculating the time in seconds corresponding to one unit time step in the numerical simulations ($\sim$ 19.8s). The reconnection assisted changes in connectivity of *yellow* MFLs during the simulated evolution are depicted in figure 6.14 for S_1 (*left column*), S_2 (*middle column*), and S_3 (*right column*) simulations. Panels (a), (d), and (g) show the initial geometrical configuration, characterized by field line mapping between the polarity pairs (P, N) for S_1 and $(\mathrm{P}', \mathrm{N}')$ for the other two simulations. The MHD evolution of plasma leads to magnetic reconnection. The resulting sequence of changes in field line connectivity are divided into three distinct parts. First, a few of the selected field lines change their mapping from N to N_3 in S_1, as shown by panel (b) at $t = 310$ and from N' to N'_3 in S_2 and S_3, as shown by panels (e) and (h) at $t = 230$ and $t = 180$ respectively (table 6.5). Interestingly, reconnection in S_2 occurs earlier than in S_1, similar to what was found in the null point topology also. Second, the connectivity changes in reverse order, i.e. from N_3 to N for S_1 and from N'_3 to N' for simulations S_2 and S_3, as depicted by panels (c), (f), and (i) at $t = 500$. The aforementioned changes can be summarized to follow $\mathrm{N}(\mathrm{N}') \rightarrow \mathrm{N}_3(\mathrm{N}'_3) \rightarrow \mathrm{N}(\mathrm{N}')$ (table 6.5) for all the initial conditions. Third, some field lines, rooted in the $\mathrm{N}(\mathrm{N}')$ polarities exhibit slipping reconnection in all the three simulations, which leads to a small shift in the footpoints across regions (pink patches at bottom boundary) of high squashing degree ($\ln Q{\sim}10$). The slipping motions partially map the brightenings b_2 and b_4,

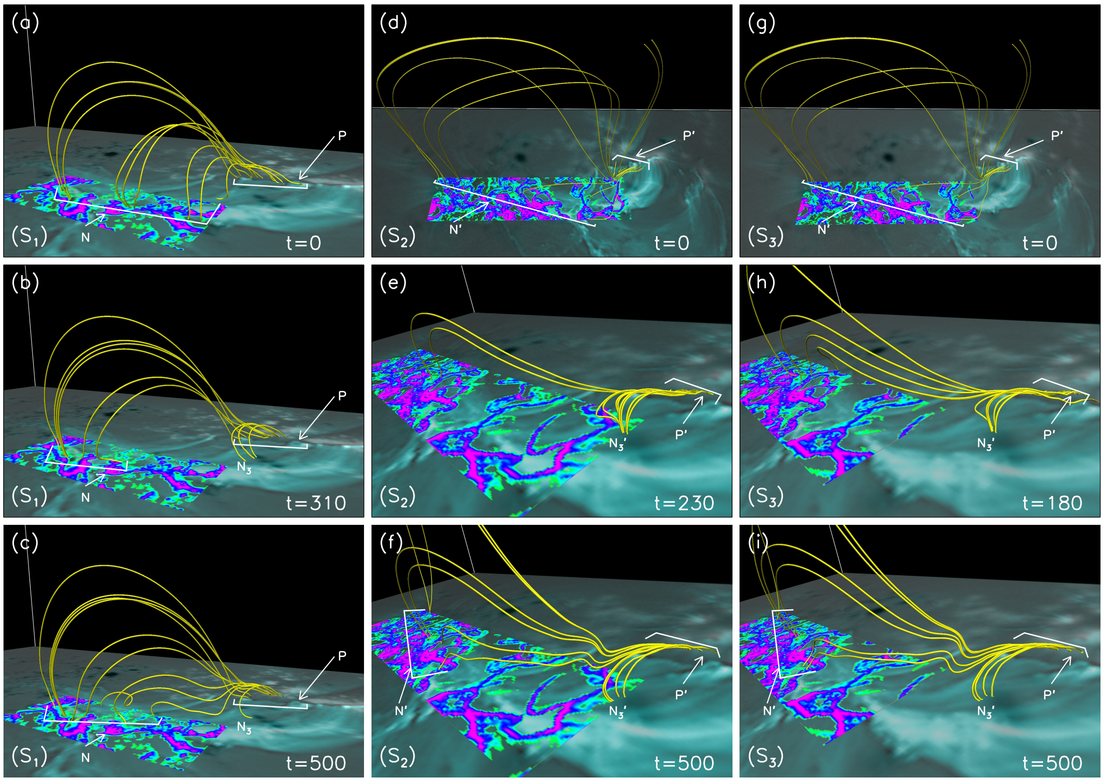

Figure 6.14: Snapshots from the simulated evolution of *yellow* magnetic field lines in hyperbolic flux tube (HFT) morphology for S_1 (*left column*), S_2 (*middle column*) and S_3 (*right column*). The *first row* depicts initial field line configuration, *second row* shows the change in footpoint mapping from $\mathrm{N}(\mathrm{N}') \to \mathrm{N}_3(\mathrm{N}_3')$ while the *third row* corresponds to the change $\mathrm{N}_3(\mathrm{N}_3') \to \mathrm{N}(\mathrm{N}')$. To analyze the associated slipping reconnection, the distribution of $\ln Q$ is shown on the bottom boundary with the same color coding as in figure 6.9. The cospatiality of observed brightening b_2 with the HFT can be seen from the overlaid line-of-sight magnetogram from SDO/HMI at 02:48 UT along with an image of AR11977 from SDO/AIA in 131 Å channel at 02:59:56 UT on the bottom boundary.

thus contributing toward the observed transient activity.

Next, the dynamics of the *red* colored MFL set is explored, as illustrated in figure 6.15. The MFLs follow a sequence of complex changes owing to a combined effect of reconnection and advection. The initial morphology for the three initial fields are shown in panels (a), (d), and (g) of the same figure. The morphologies are characterized by field line connectivity between the polarity pairs $(\mathrm{P}, \mathrm{N}_2)$ for S_1 and $(\mathrm{P}', \mathrm{N}_2')$ for the other two initial fields. As the reconnection ensues, some of the field line change their footpoint mapping from N_2 to N in S_1, as shown in panel (b) at $t = 10$ and from N_2' to N' in S_2 and S_3, as depicted in panels (e) and (h) at $t = 50$ and $t = 40$, respectively (table 6.5). Following this, small changes facilitated by advection occur, causing some minor but identifiable shift in

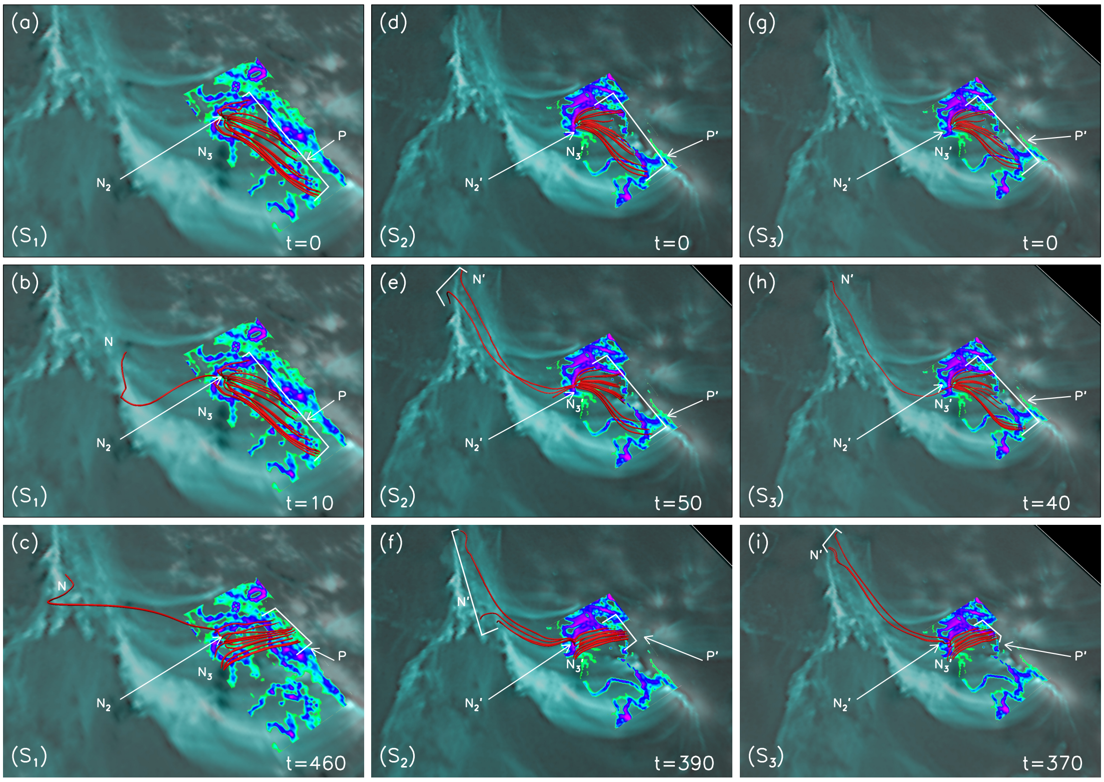

Figure 6.15: Snapshots from the simulated evolution of *red* magnetic field lines in hyperbolic flux tube (HFT) morphology for S_1 (*left column*), S_2 (*middle column*) and S_3 (*right column*). The *first row* depicts initial field line configuration, *second row* shows the change in footpoint mapping from $\mathrm{N_2(N_2')} \rightarrow \mathrm{N(N')}$ while the *third row* corresponds to the final morphological arrangement, post advection. To analyze the associated slipping reconnection, the distribution of $\ln Q$ is shown at the bottom boundary with the same color coding as in figure 6.9. The cospatiality of observed brightening $\mathrm{b_2}$ with the HFT can be seen from the overlaid line-of-sight magnetogram from SDO/HMI at 02:48 UT along with an image of AR11977 from SDO/AIA in 131 Å channel at 02:59:56 UT on the bottom boundary.

footpoint connectivity from $\mathrm{N_2(N_2')}$ toward $\mathrm{N_3(N_3')}$, across all the simulations. The advection is distinguished from slipping reconnection based on the continuity of field line movement over the photospheric boundary and low value of the squashing degree in that region. Subsequently, another occurrence of reconnection produces a change in connectivity toward the polarity N in S_1, as shown in panel (c) at $t = 460$ and toward N′ in simulations S_2 and S_3, as shown in panels (f) and (i) at $t = 390$ and $t = 370$ respectively. The changes in connectivity of the red MFLs because of reconnection can be summarized into the sequence $\mathrm{N_2(N_2')} \rightarrow \mathrm{N(N')} \rightarrow$ advection $\rightarrow \mathrm{N(N')}$, which is preserved in all the simulations. Further, slipping reconnection in the P(P′) region during the course of evolution is found to contribute in the observed brightening $\mathrm{b_2}$.

Finally, the field line dynamics in the set of *blue* magnetic field lines is explored. Particularly, for this set of MFLs, slipping reconnections dominate the simulated evolution. The initial magnetic field line configuration at $t = 0$ is depicted in figure 6.16, identified by field line connectivity between the polarity pairs $(\mathrm{P}_4, \mathrm{N})$ for S_1 and $(\mathrm{P}'_4, \mathrm{N}')$ for the other two simulations, as shown in panels (a), (d), and (g) respectively. As the slipping reconnection sets in, the initial configuration is

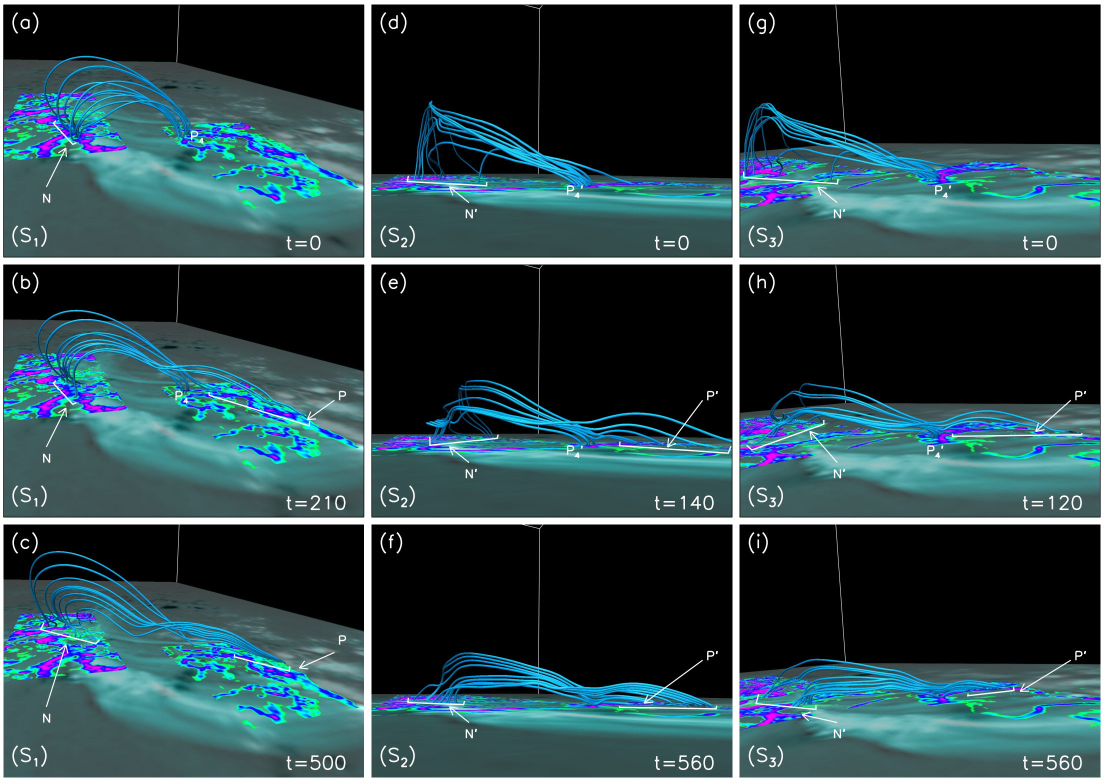

Figure 6.16: Snapshots from the simulated evolution of *blue* magnetic field lines in hyperbolic flux tube (HFT) morphology for S_1 (*left column*), S_2 (*middle column*) and S_3 (*right column*). The *first row* depicts initial field line configuration, *second row* shows the change in footpoint mapping from $\mathrm{P}_4(\mathrm{P}'_4) \rightarrow \mathrm{P}(\mathrm{P}')$ due to slipping reconnection while the *third row* represents the final morphological structure. To analyze the associated slipping reconnection, the distribution of $\ln Q$ is shown on the bottom boundary with the same color coding as in figure 6.9. The cospatiality of observed brightening b_2 with the HFT can be seen from the overlaid line-of-sight magnetogram from SDO/HMI at 02:48 UT along with an image of AR11977 from SDO/AIA in 131 Å channel at 02:59:56 UT on the bottom boundary.

transformed. The first significant change is noted where the footpoint mapping of a few magnetic field lines change from P_4 to P in S_1, as shown in panel (b) at $t = 210$ and from P'_4 to P' in simulations S_2 and S_3, as depicted in the corresponding panels (e) and (h) at $t = 140$ and $t = 120$ (table 6.5). The final morphological organization of the *blue* MFLs at $t = 500$ is characterized by the field line connectivity between the polarity pair (P, N) in simulation S_1, as shown in panel (c) while the same mapping between polarity pair (P′, N′) is found in simulations S_2 and S_3 at $t = 560$, as shown in panels (f) and (i). Additionally, *blue* MFLs exhibit slipping reconnection in the P(P′) region, thus tracing the region of observed brightening b_2. Importantly, the sequence of change $P_4(P'_4) \rightarrow P(P')$ remains identical across all the simulations.

	$t = 0$	$t = t_1$		$t = t_2$	
Yellow					
S_1	$P \rightarrow N$ (10)	$P \rightarrow N$ (6)	$t = 310$	$P \rightarrow N$ (9)	
		$P \rightarrow N_3$ (4)	$t = 310$	$P \rightarrow N_3$ (1)	
S_2	$P' \rightarrow N'$ (10)	$P' \rightarrow N'$ (2)	$t = 230$	$P' \rightarrow N'$ (6)	
		$P' \rightarrow N'_3$ (8)	$t = 230$	$P' \rightarrow N'_3$ (4)	
S_3	$P' \rightarrow N'$ (10)	$P' \rightarrow N'$ (5)	$t = 180$	$P' \rightarrow N'$ (6)	
		$P' \rightarrow N'_3$ (5)	$t = 180$	$P' \rightarrow N'_3$ (4)	
Red					
S_1	$P \rightarrow N_2$ (15)	$P \rightarrow N$ (1)	$t = 10$	$P \rightarrow N$ (1)	$t = 470$
		$P \rightarrow N_2$ (14)	$t = 10$	$P \rightarrow N_2$ (7)	$t = 470$
				$P \rightarrow N_3$ (6)	$t = 470$
				$P_4 \rightarrow N_3$ (1)	$t = 470$
S_2	$P' \rightarrow N'_2$ (15)	$P' \rightarrow N'$ (2)	$t = 50$	$P' \rightarrow N'$ (3)	$t = 390$
		$P' \rightarrow N'_2$ (13)	$t = 50$	$P' \rightarrow N'_2$ (6)	$t = 390$
				$P' \rightarrow N'_3$ (6)	$t = 390$
S_3	$P' \rightarrow N'_2$ (15)	$P' \rightarrow N'$ (1)	$t = 40$	$P' \rightarrow N'$ (3)	$t = 370$
		$P' \rightarrow N'_2$ (14)	$t = 40$	$P' \rightarrow N'_2$ (6)	$t = 370$
				$P' \rightarrow N'_3$ (6)	$t = 370$
Blue					
S_1	$P_4 \rightarrow N$ (10)	$P_4 \rightarrow N$ (6)	$t = 210$	$P \rightarrow N$ (10)	$t = 500$
		$P \rightarrow N$ (4)	$t = 210$		
S_2	$P'_4 \rightarrow N'$ (10)	$P'_4 \rightarrow N'$ (5)	$t = 140$	$P' \rightarrow N'$ (10)	$t = 560$
		$P' \rightarrow N'$ (5)	$t = 140$		
S_3	$P'_4 \rightarrow N'$ (10)	$P'_4 \rightarrow N'$ (5)	$t = 120$	$P' \rightarrow N'$ (10)	$t = 560$
		$P' \rightarrow N'$ (5)	$t = 120$		

Table 6.5: Summary of the footpoint mapping corresponding to *yellow*, *red* and *blue* magnetic field lines in the hyperbolic flux tube morphology for simulations S_1, S_2, and S_3. The round brackets denote the precise number of selected magnetic field lines between the specified polarities while the *arrows* indicate direction of field line. The *left* ($t = 0$), *middle* ($t = t_1$) and *right* ($t = t_2$) columns represent the initial state, first and second instances of significant changes in the connectivity of field lines. Note that t_1 and t_2 are variable depending on the set of magnetic field line under consideration.

6.5.4 Transient Magnetic Null

Astoundingly, all the three simulations show generation of a magnetic null point in the near neighborhood of the HFT. The analysis of null point generation is carried out by following two different sets of *green* and *purple* MFLs during their evolution. The evolution for simulations S_1, S_2, and S_3 is shown in the *left*, *middle* and *right* columns of figure 6.17. At $t = 0$, there is no identifiable magnetic null point, as

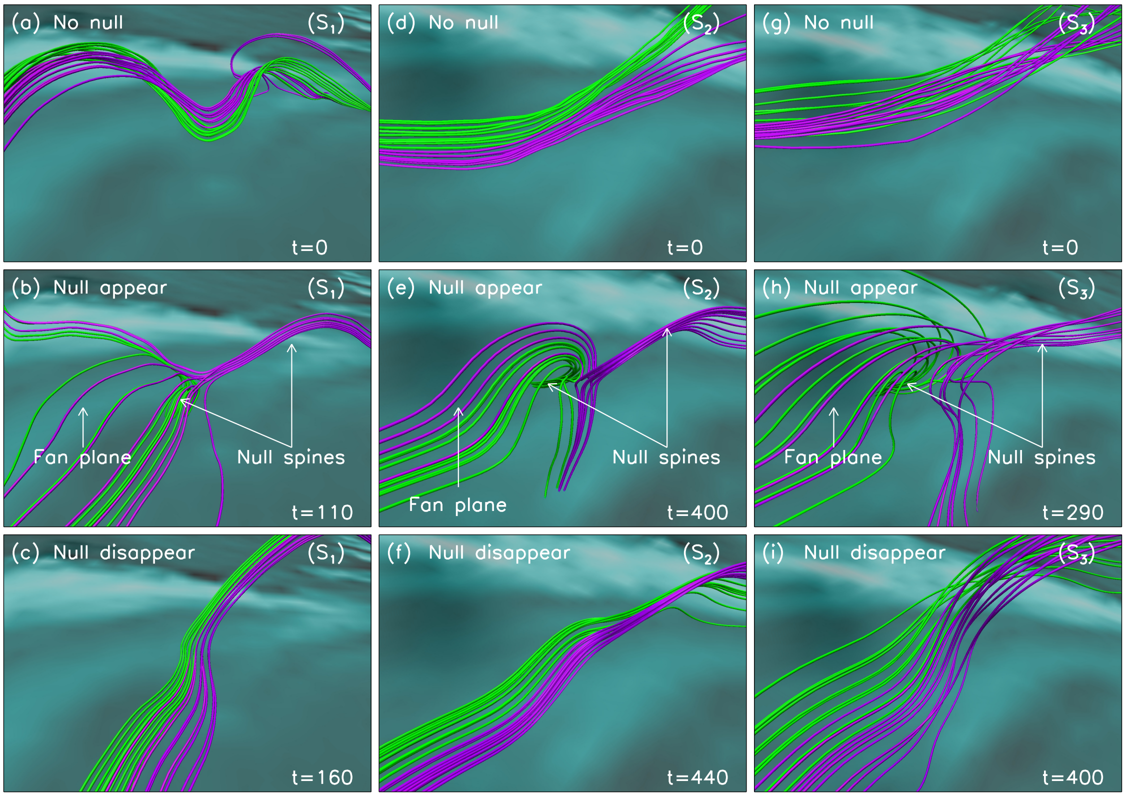

Figure 6.17: Snapshots from the simulated evolution of selected *green* and *purple* magnetic field lines to capture the generation of magnetic null in time for S_1 (*left column*), S_2 (*middle column*) and S_3 (*right column*). The *first row* depicts the initial field line configuration when there is no magnetic null point, *second row* corresponds to the instance of null point appearance while the *last row* captures the disappearance of null point. The bottom boundary is overlaid with line-of-sight magnetogram from SDO/HMI at 02:48 UT along with an image of AR11977 from SDO/AIA in 131 Å channel at 02:59:56 UT.

shown in panels (a), (d), and (g). The null appears at $t = 110$ in S_1 as shown in panel (b), while in the other two simulations, null point generates at $t = 400$ and $t = 300$, as depicted in panels (e) and (h) respectively. The null is detected with the same trilinear method as used earlier. Interestingly, the null point is located in close proximity of the HFT (near b_2) across all the simulations. Subsequently, all the three nulls corresponding to the three simulations disappear, as shown in panels (c), (f), and (i), thus prompting the terminology of a transient null. Interestingly, the MFLs constituting the fan plane of the transient nulls contribute toward the observed brightening b_2. To capture the associated reconnection process, which occurs in a small time window due to the transient property of the null point, the field line configuration is analyzed slightly before the instance of the null point appearance (panels (a), (d), and (g) of figure 6.18) for the three simulations. The

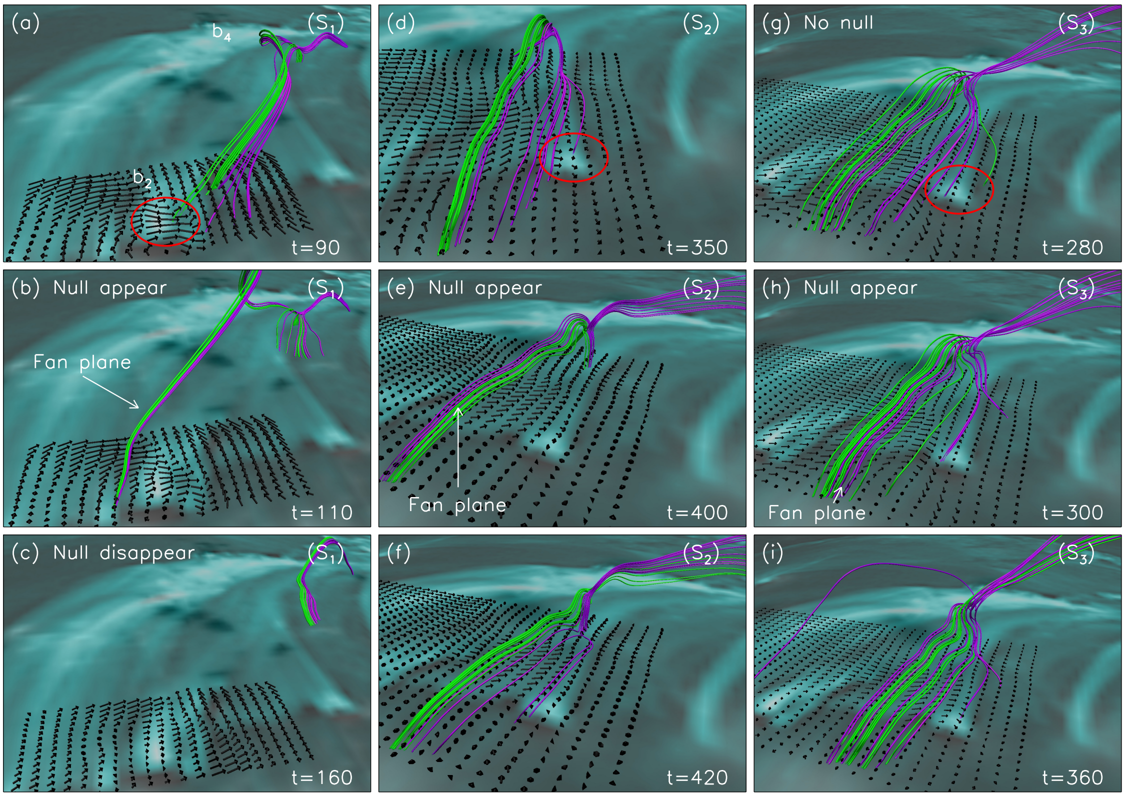

Figure 6.18: Snapshots from the simulated evolution of selected *green* and *purple* magnetic field lines to illustrate the contribution of transient magnetic null in the observed brightening b_2, as shown in panel (a), for S_1 (*left column*), S_2 (*middle column*) and S_3 (*right column*). The first row shows initial field line configuration, just before the instance of null point generation. The *red circle* indicates the region of interest in terms of observed brightening while the *black arrows* represent the flow velocity vectors. *Second row* highlights the footpoint movement of fan plane, which does not follow the direction of plasma flow (*black arrows*). The third row depicts the instance where null point is lost in time. The bottom boundary is overlaid with line-of-sight magnetogram from SDO/HMI at 02:48 UT along with an image of AR11977 from SDO/AIA in 131 Å channel at 02:59:56 UT.

emphasis here is on the field lines whose footpoints are enclosed by the *red circle* that has been overlaid on a section of the observed brightening b_2. During a very small time span, centered at the instance of null point generation, the footpoints of the fan planes break the flux freezing condition and do not move in the direction of the plasma flow (shown in *black arrows*). The footpoints of the fan plane move in the leftward direction while the plasma flow vectors are in the rightward direction, as evident in panel (b) at $t = 110$ for S_1, and in panels (e) and (h) at $t = 400$ and $t = 300$ for the other two simulations. Such slippage of MFLs from the plasma flow are indicative of slipping reconnection, thus contributing toward the brightening b_2. Further along the simulated evolution, the null point disappears, as shown in panels (c), (f), and (i) for the three simulations.

6.6 Summary

The chapter explores the independence aspect of self-organized states with respect to the initial conditions in data-based MHD simulations of a solar flare. For this purpose, three different initial conditions are generated using the non-force-free field (NFFF) and nonlinear force-free field (NLFFF) extrapolations. The analysis of quantitative and morphological differences between the extrapolated magnetic field indicates that the two are nearly similar. The investigation reveals complex magnetic structures having plausible reconnection topologies to be co-spatial with the observed flare brightenings. In particular, QSLs constitute the magnetic field configuration at large-scale while at relatively smaller-scales, a magnetic null point and hyperbolic flux tube are found to be the primary reconnection sites. Notably, these structures are reproduced in both the extrapolated fields, although the extent of agreement between the two varies.

The comparison of the three simulations for changes in the magnetic field line connectivity due to reconnection at the magnetic null point and HFT morphologies indicate a near similarity, except for the differences in time scale of these changes. The differences in timing are expected because the initial Lorentz force and the initial plasma flow vary across the three simulations. Further, from the perspective of energetics, the temporal evolution of volume integrated magnetic, free magnetic, and total energy suggests near independence of the MHD evolution with respect to the initial conditions in presence of reconnection. The order of dissipated free magnetic energy ($\sim 10^{31}$ ergs) and percentage decrement in total magnetic energy ($\sim 5.5\,\%$) are also nearly similar across all the simulations. Notably, the order is presumably consistent with the range of upper C-class to M-class solar flares, thus providing credence to the carried out data-based simulations.

In addition to the near similarity of energetics and changes in connectivity of magnetic field lines, a magnetic null (referred to as the transient null) is found to appear and disappear spontaneously near the HFT in all simulations. Moreover, the footpoints of the field lines constituting the fan plane of this transient null are co-spatial with brightening b_2 and exhibit slipping reconnection in all simulations, suggesting that the transient null contributes to the flare brightening and has an observable signature. Such generation of null point configuration indicates that the field line evolution is nearly independent of the initial conditions. Further, the results suggest that transient structures should be accounted for a comprehensive analysis of the observed brightenings in the solar corona.

The similarity of results across the three simulations suggests the magnetofluid dynamics to be nearly independent of the initial conditions, which is in accordance with the principle of self-organization. Further, the appearance and disappearance of the transient null and its contribution to the observed brightening b_2 indicate formation of a complex coherent structure at small-scale having increased efficiency of dissipation, which is also representative of self-organization. From a pragmatic viewpoint, the results lead to the conclusion that both the extrapolations can be used as valid initial conditions in data-based simulations. Since, the inference is based on the study of a single active region using idealized numerical simulations, more such numerical experiments are required to arrive at a statistically significant conclusion. Nevertheless, the results on signatures of self-organization in this study are encouraging enough to explore relaxation further using data-based simulations. Consequently, the following chapter presents a detailed study of the magnetofluid dynamics, energetics at local and global scales, and extent of magnetic relaxation in data-based MHD simulation of a solar flare.

Chapter 7

Study of Reconnection Dynamics and Magnetic Relaxation

7.1 Introduction

The release of magnetic energy in solar transients is expected to relax the magnetic configuration to a lower energy state. As a result, from the perspective of exploring relaxation in transients, the relaxed states obtained by minimizing magnetic energy draw immediate attention. Relevantly, the Woltjer and Taylor states representing force-free magnetic field are of interest. Toward exploring the realization of these states and understanding the magnetofluid dynamics for a transient, the following subtleties need to be considered. In Taylor's theory, the magnetized plasma system is assumed to be isolated and bounded by perfectly conducting walls. However, the solar corona is an open system and driven continuously by the photospheric motion. Therefore, there are no conducting walls to define the volume in which relaxation occurs (Browning & Lazarian, 2013). Further, since the reconnection is localized, even if a volume with open boundaries is defined, not all the field lines within the volume will reconnect, which might affect the homogenization of $\alpha(\mathbf{r})$ and plasma pressure. Notably, the generation of small-scales (quantified by $|\mathbf{J}|/|\mathbf{B}|$) is necessary to onset the magnetic reconnection and hence, the observed transient activity. Consequently, it is reasonable to expect that the end state of the transient will be characterized by a lower $|\mathbf{J}|/|\mathbf{B}|$, implying its decrease over the course of event. From the viewpoint of relaxation also, the magnetofluid will tend toward an equilibrium having lower magnetic energy, presumably simplifying the field line complexity and minimizing the magnetic field gradient. In the above backdrop, data-based MHD simulation of a solar flare is carried out to understand the dynamics in presence of reconnection and to investigate magnetic relaxation. The following section presents the details of active region and the solar flare chosen for this study.

7.2 Active Region and Flare

In principle, any flare may be chosen to study relaxation, but to identify a flare that is favorable for such exploration; two additional criteria are employed along with those in the previous chapter. First, since the decay of magnetic energy is a prime signature of relaxation, the flare should be GOES M-class or higher because they are considered to release significantly large amounts of magnetic energy. Second, the post-flare phase should not be associated with any other major flaring activity so that the magnetic energy buildup and decay phases are sharp and clear. With these constraints in mind, the AR NOAA 12253 with heliographic coordinates S05E01 on January 4, 2015 is selected. It hosts a GOES M1.3 class flare of net duration 35 minutes (min.), having start, peak, and end time as 15:18 UT, 15:36 UT, and 15:53 UT, respectively. Importantly, in the post-flare phase, there is no flaring activity for the next six hours. Along with the above-mentioned criterion, the selected AR is checked to comply with the condition $\mathrm{B_z} = \mathrm{const.}$ at the bottom boundary, used in the MHD simulation. This translates into the requirement that during the course of flaring activity, the total relative change in magnetic flux (integrated over the bottom boundary) is minimal. To evaluate this, line-of-sight magnetograms from hmi.M_45 series of HMI with temporal cadence of 45 seconds are employed. The original magnetogram (panel (a) in figure 7.1) having dimensions of 4096×4096 in pixel units is CEA projected and cropped to match the pre-defined dimensions of HARP active region patch (Hoeksema et al., 2014) for AR NOAA 12253, which is 877×445 in pixel units (panel (b) in figure 7.1). Using these, it is found that over a period of 72 min., starting from 15:00 UT up to 16:12 UT, relative changes in positive and negative flux with respect to their initial values are 0.36 % and 0.42 %, respectively. The evolution of the flare is explored by using observations from 1600 Å and 304 Å

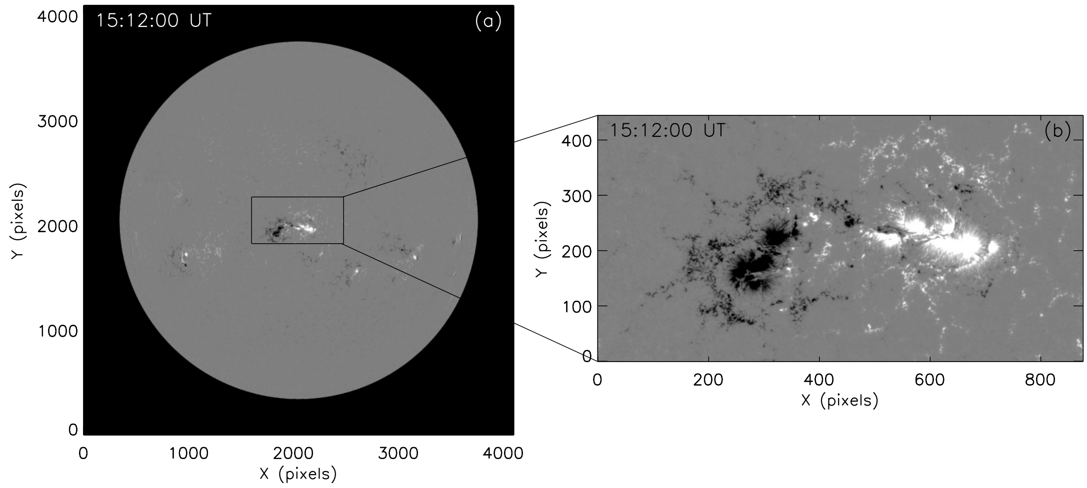

Figure 7.1: (a) The line-of-sight magnetogram at 15:12 UT on 04 January, 2015, from SDO/HMI. The corresponding dimensions in pixel units are 4096×4096 (b) CEA projected and cropped magnetogram (based on HARP active region patch) at 15:12 UT, having dimensions 877× 445 in pixel units for AR NOAA 12253. Both the figures are scaled to represent magnetic field strength within ±1000 Gauss, with *black* patches representing the negative polarity and *white* patches representing the positive polarity.

channels of AIA. In figure 7.2, panel (a) depicts the location of a brightening (labeled B_1) during the beginning of flare. The location is relevant because it might host a potential reconnection site and hence, merits attention. The subsequent evolution reveals multiple brightenings during the flare peak (labeled B_2), as shown in panel (b). Notably, in the observations of 304 Å channel, the presence of a dome-shaped structure is found, whose spatial extent is marked by the *yellow* colored box in panel (c). A zoomed in view of this boxed region with better image contrast is given in panel (e). The panel highlights the approximate edges (drawn manually) of the structure by *yellow* lines. These lines depict multiple connections between the central location C and the traced, approximately circular periphery. Further, the line toward the right of C indicates the association of dome structure with magnetic morphology in rest of the active region. The lines are in agreement with the expected two dimensional projection of a dome structure. As the flare progresses, the complete spatial extent of the brightening is revealed, where specific chromospheric flare ribbons are recognizable as marked in panel (d) by *white* arrows. Therefore, in observations, the brightenings B_1, B_2 and the dome-shaped structure are identified to be of significance and hence, merit investigation of associated magnetic field line morphologies for an understanding of their role in the flaring activity and relaxation process.

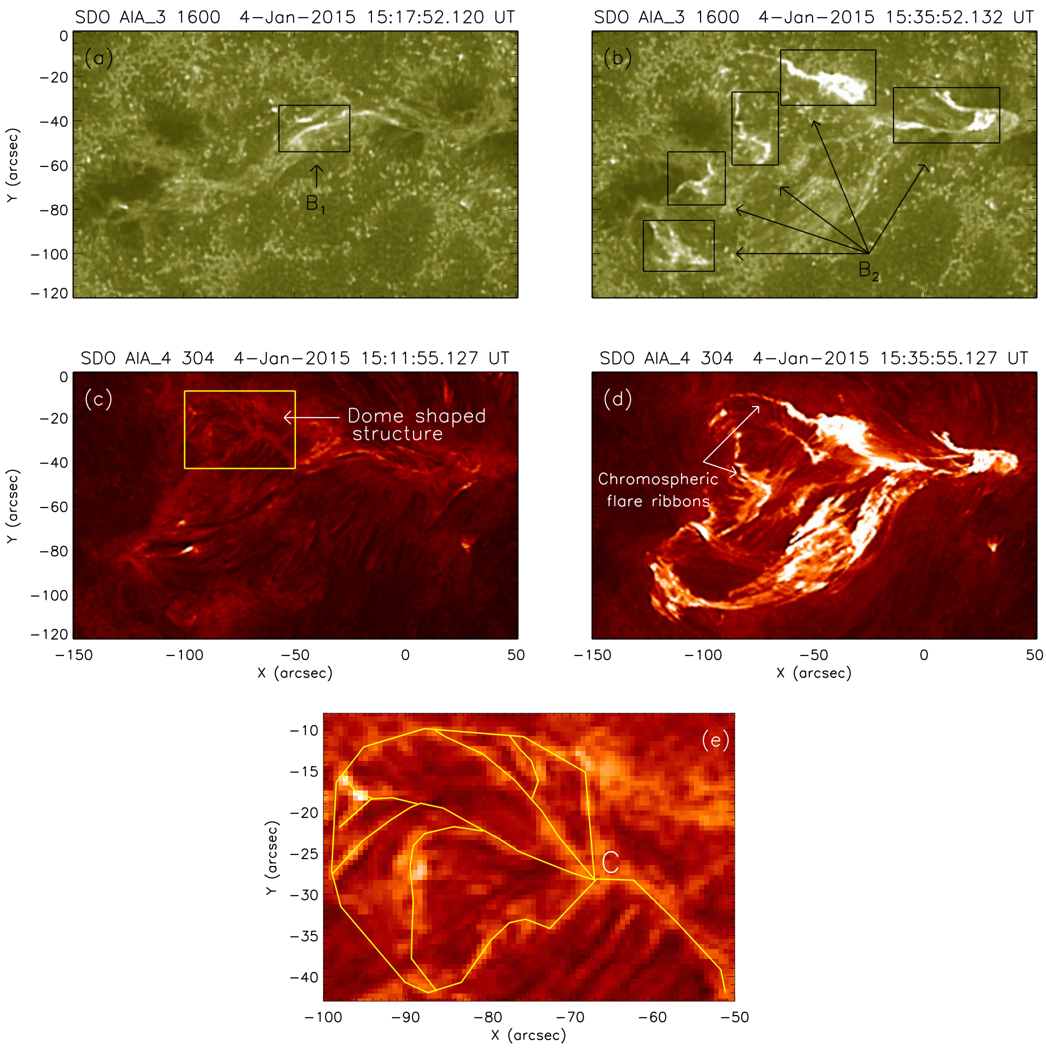

Figure 7.2: Snapshots from observations of the solar flare in 1600 Å and 304 Å channels of SDO/AIA. Panels (a) and (b) reveal the brightening locations in 1600 Å during the beginning and peak phases of flare, marked by B_1 and B_2. Panels (c) and (d) highlight the initial configuration of the identified dome-shaped structure and chromospheric flare ribbons during the peak phase of flare. A zoomed in image of the boxed region in panel (c) is presented in panel (e) with enhanced image contrast. The *yellow* color lines represent the manual tracing of the structure, while C labels the central location, where all the lines meet.

7.3 Details of Magnetic Field Extrapolation

In this study, non-force-free field (NFFF) extrapolation is carried out using the vector magnetogram at 15:12 UT from the hmi.sharp_cea_720s series of SDO/HMI as bottom boundary. The magnetogram dimensions are 877×445 pixels (≈317.91 Mm×161.31 Mm). As in the case of previous study, the magnetogram is suitably cropped and scaled to new dimensions of 216×110 pixels (≈313.2 Mm×159.5 Mm) to save the computational cost of simulation. The extrapolation is carried out in the computational box defined by 216×110×110 voxels. The cropping and scaling procedures render the relative changes in positive and negative magnetic fluxes to be 0.02 % and 0.84 %, respectively, which suggests that such processing has not altered the original magnetogram in any significant way and that the resultant magnetogram approximately satisfies the condition $\mathrm{B_z}$ = const. used in the MHD simulation. The robustness of extrapolated magnetic field is evaluated by computing the following parameters. First, the angle θ (see equation 4.7) is estimated, being equal to $\theta = 63.73°$, which is expected because the model is non-force-free. Second, a modified definition of the averaged fractional flux error (see equation 6.1) given by Gilchrist et al. (2020) is employed to quantify the solenoidality of the magnetic field. It is defined as

$$\langle |f_d| \rangle = \left\langle \frac{\int_{\partial S_i} \mathbf{B} \cdot d\mathbf{S}}{\int_{S_i} |\mathbf{B}| dV} \right\rangle, \tag{7.1}$$

where ∂S_i represents the surface area of any voxel and S_i it's volume. The value is calculated to be 3.366×10^{-9}, which is numerically small enough to justify the divergence-free property of the extrapolated magnetic field. Lastly, the ratio of total magnetic energy with respect to the total potential state energy, denoted by $E_{\mathrm{NFFF}}/E_{\mathrm{P}}$ is estimated. The ratio sheds light on the capability of model to account for energy released during the transient phenomenon and turns out to be 1.305, implying that the extrapolated magnetic field has ≈ 30.5% more energy than the potential field. Quantitatively, the amount of the available free magnetic energy is 5.6×10^{31} ergs, which is presumably enough to power a GOES M-class flare (Rempel et al., 2021).

7.4 Morphological Investigation

The extrapolated non-force-free field is explored to look for the potential sites of magnetic reconnection by focusing on brightenings B_1 and B_2, and the dome-shape structure. Cospatial with B_1, a HFT is found, as shown in figure 7.3. Panel (a) of the figure shows magnetic field line linkage of the HFT configuration, constituted by the four quasi-connectivity domains in *blue*, *yellow*, *pink*, and *red* colors. These domains comprise of two intersecting QSLs, one by *blue* and *yellow* MFLs and the other by *pink* and *red* MFLs. Notably, these configurations are preferred sites for reconnection and hence are of interest. Panel (a) shows the $\ln Q$ map in a plane perpendicular to the bottom boundary and crossing through the HFT morphology, where Q is the squashing degree. For $\ln Q \geq 8$, the characteristic X-shape along the HFT is found, which further confirms the interpretation of HFT morphology. Similarly, in panel (b), regions of high gradient at the bottom boundary are seen to be nearly cospatial with B_2, thus suggesting a plausible scenario for slipping reconnection. In particular, as evident from panels (c) and (d), the footpoints of *yellow* MFLs lie on the boundary of dome, while those at one end of *pink* MFLs partially cover the periphery of the dome. The presence of high gradients in footpoint mapping of the MFLs is indicative of slippage, which can possibly explain parts of brightening B_2 and chromospheric flare ribbons. The robustness of the extrapolated magnetic field and association of the HFT with observations suggest that the extrapolated NFFF can be reliably utilized as an input for the MHD simulation.

7.5 The MHD Simulation and its Analysis

The EULAG-MHD model is employed to execute the simulation. The boundaries are kept open, meaning that the net flux through the boundaries is constant. The simulation is initiated from a static state (initial plasma flow is zero) using the extrapolated NFFF, having dimensions 216×110×110, which is mapped on a computational grid of $x \in$ [-0.981,0.981], $y \in$ [-0.5,0.5], and $z \in$ [-0.5,0.5] in a Cartesian coordinate system. The spatial step sizes are $\Delta x = \Delta y = \Delta z \approx 0.0091$ ($\equiv 1450$ km), while the time step is $\Delta t = 2\times10^{-4}$ ($\equiv 0.2544$ sec). Using the

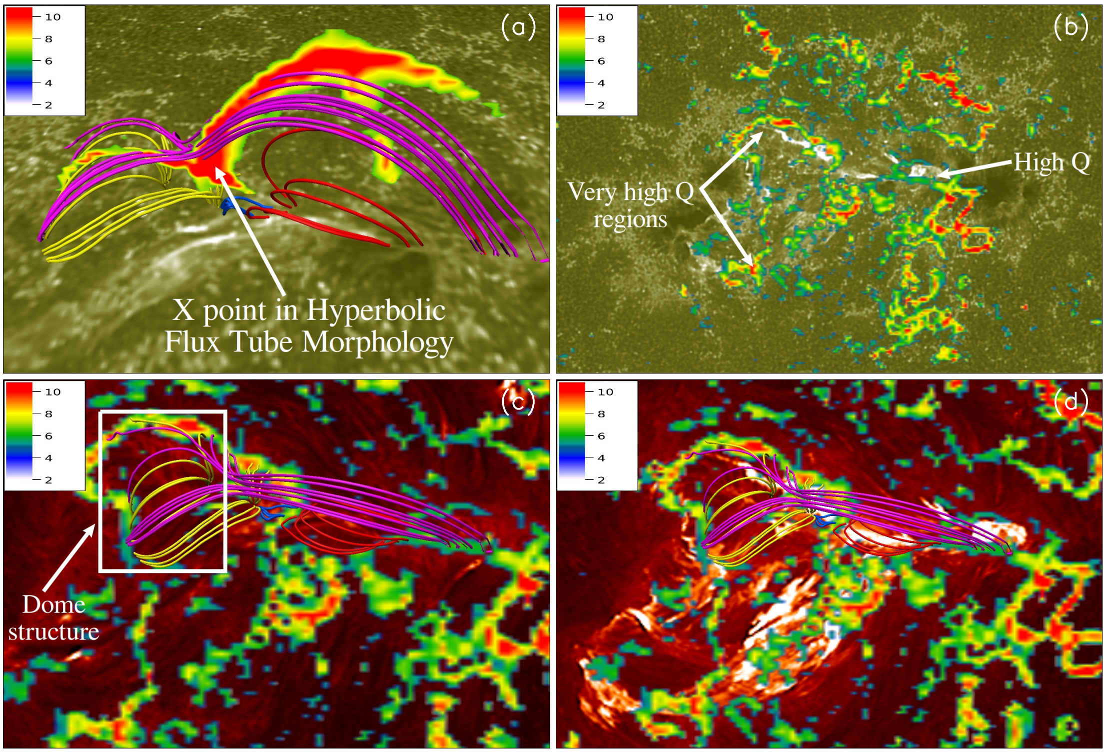

Figure 7.3: Regions of high squashing degree and morphology of the hyperbolic flux tube (HFT). Panels (a), (b) and panels (c), (d) are overlaid with observations in 1600 Å and 304 Å channel of SDO/AIA at the bottom boundary, corresponding to the same time instants as in Figure 7.2. In all the panels, the map of squashing degree $\ln Q$ is given with color table. In panel (a), the map is perpendicular to the bottom boundary, crossing through the HFT, while in panels (b), (c) and (d), the $\ln Q$ map is in the plane of the bottom boundary. Panel (a) shows HFT from a side view, while panels (c) and (d) show HFT from a top-down view. Panels (a) and (c) use a zoomed-in viewpoint while panels (b) and (d) use a zoomed-out viewpoint. In panel (c), the dome-shaped structure is marked with a *white* color box.

typical values in the solar corona, $L_{\text{cor.}} = 100$ Mm, $V_A|_{\text{cor.}} = 1000$ $\text{km}\,\text{s}^{-1}$, and kinematic viscosity $\nu_{\text{cor.}} = 4\times10^9\ \text{m}^2\,\text{s}^{-1}$, the corresponding fluid Reynolds number turns out to be $R_F^A|_{\text{cor.}} = 25{,}000$. However, in the numerical setup for simulation, $R_F^A|_{\text{sim.}} = 5000 \equiv 0.2 \times R_F^A|_{\text{cor.}}$, which can be envisaged as a smaller Alfvén speed $V_A|_{\text{sim.}} \approx 0.125\times V_A|_{\text{cor.}}$ for $L_{\text{sim.}} = 110 \times 1450\,\text{km} = 159.5$ Mm. The total time of simulation in physical units is equivalent to $nt \times \Delta t \times (L_{\text{sim.}}/V_A|_{\text{sim.}}) \approx 63.6$ min., where $nt =$ 15000. Toward understanding the implications of reconnection in the magnetofluid dynamics, attention is paid to the temporal evolution of magnetic energy, current density, twist parameter, and gradients in the magnetic field. The corresponding grid averaged values of these quantities are defined as

$$\mathrm{W}_{\mathrm{av}}^{\mathrm{V}} = \frac{1}{N} \times \sum_{i=0}^{N-1} |\mathbf{B}|_i^2 \,, \tag{7.2}$$

$$|\mathbf{J}|_{\mathrm{av}}^{\mathrm{V}} = \frac{1}{N} \times \sum_{i=0}^{N-1} |\mathbf{J}|_i^2 \,, \tag{7.3}$$

$$|\Gamma|_{\mathrm{av}}^{\mathrm{V}} = \frac{1}{N} \times \sum_{i=0}^{N-1} \left| (\mathbf{J}\cdot\mathbf{B})_i \Big/ |\mathbf{B}|_i^2 \right| \,, \tag{7.4}$$

$$(|\mathbf{J}|/|\mathbf{B}|)_{\mathrm{av}}^{\mathrm{V}} = \frac{1}{N} \times \sum_{i=0}^{N-1} \sqrt{\frac{|\mathbf{J}|_i^2}{|\mathbf{B}|_i^2}} \,, \tag{7.5}$$

where, i denotes the voxel index and the volume V encloses the volume of interest. $\mathrm{W}_{\mathrm{av}}^{\mathrm{V}}$, $|\mathbf{J}|_{\mathrm{av}}^{\mathrm{V}}$, and $|\Gamma|_{\mathrm{av}}^{\mathrm{V}}$ measure the grid averaged magnetic energy, current density, and twist, whereas $(|\mathbf{J}|/|\mathbf{B}|)_{\mathrm{av}}^{\mathrm{V}}$ quantifies the gradient of magnetic field. Toward exploring the magnetofluid dynamics at the global scale, where global refers to the full computational box, panel (a) of figure 7.4 plots the temporal evolution of $\mathrm{W}_{\mathrm{av}}^{\mathrm{V}}$. The continuous decrease of magnetic energy is in alignment with the possibility of magnetic relaxation through reconnection. To support this idea

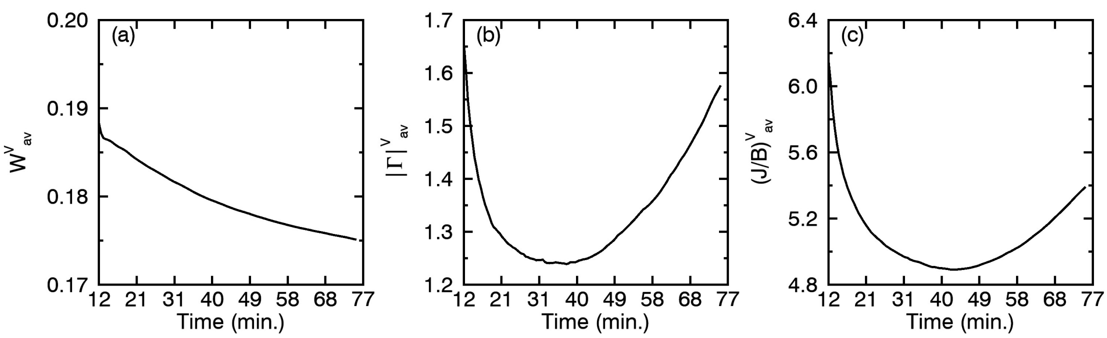

Figure 7.4: Temporal evolution of grid averaged parameters (a) Magnetic energy ($\mathrm{W}_{\mathrm{av}}^{\mathrm{V}}$) (b) Twist ($|\Gamma|_{\mathrm{av}}^{\mathrm{V}}$) (c) Gradient in magnetic field ($(|\mathbf{J}|/|\mathbf{B}|)_{\mathrm{av}}^{\mathrm{V}}$). The origin of time scale maps from 15:12 UT.

further, panel (b) of the same figure plots $|\Gamma|_{\mathrm{av}}^{\mathrm{V}}$, showing that the average twist decreases up to ≈ 40 minutes, followed by a rise. The initial decay is in conformity with the scenario of magnetic reconnection being responsible for the untwisting of global field structure (Wilmot-Smith et al., 2010) and reducing the complexity of magnetic field lines. This scenario is further reinforced by a similar variation of $(|\mathbf{J}|/|\mathbf{B}|)_{\mathrm{av}}^{\mathrm{V}}$ shown in panel (c) because reconnection is expected to smooth out steep field gradients (see Appendix C). Notably, the rise in both $|\Gamma|_{\mathrm{av}}^{\mathrm{V}}$ and $(|\mathbf{J}|/|\mathbf{B}|)_{\mathrm{av}}^{\mathrm{V}}$

toward the end of simulation is due to a current enhancement localized near the top of the computational domain—addressed later in the chapter. Since, reconnection changes the connectivity of magnetic field lines, their dynamics merits attention. As mentioned earlier, defining a relaxation volume having perfectly conducting walls is not possible for an open system like the solar corona. Consequently, the computational volume is partitioned into three sub-volumes that are considered to define the volume of interest for exploring magnetic relaxation. These sub-volumes are interpreted in the context of investigating the dynamics at local scales whereas the full computational box associates with the global scale. The spatial location and extent of the sub-volumes are summarized in table 7.1.

	X_{off}	Y_{off}	Z_{off}	X_{size}	Y_{size}	Z_{size}
S_1	102	56	0	8	10	5
S_2	80	50	0	60	30	20
S_3	70	20	0	70	60	110

Table 7.1: The offset and extent (in voxels) for sub-volumes of interest (S_i, i=1,2,3) in x, y, and z directions

The selection of sub-volumes focuses on the hyperbolic flux tube (HFT) as the principal reconnection site and on the observed extent of brightenings in the active region, as depicted in figure 7.5. The two-dimensional projections of sub-volumes S_1, S_2, and S_3 are shown in *cyan*, *green*, and *yellow* color boxes. Sub-volume S_1 encloses brightening B_1 and is centered on the X-region of HFT, thus consisting of those regions where the development of strongest current layers is possible. S_2 encloses the HFT morphology that envelops B_1 and partly B_2 such that the field line connectivities of depicted MFLs (see figure 7.3) are contained within S_2. Lastly, S_3 covers the complete spatial extent of the observed brightening (see figure 7.2) and full vertical height of the computational box. The following sections analyze the magnetofluid evolution in each of the sub-volumes.

7.5.1 Sub-volume S_1

The time evolution of W_{av}^{V}, $|\mathbf{J}|_{av}^{V}$, $|\Gamma|_{av}^{V}$, and $(|\mathbf{J}|/|\mathbf{B}|)_{av}^{V}$ is depicted in panels (a), (b), (c), and (d) of figure 7.6, respectively. To understand their dynamical evolution, the time duration of numerical simulation is partitioned into five phases, denoted by $P_1^{(i)}$, where, $i = 1, 2, ..., 5$. Notably, the composition of S_1 has five layers along

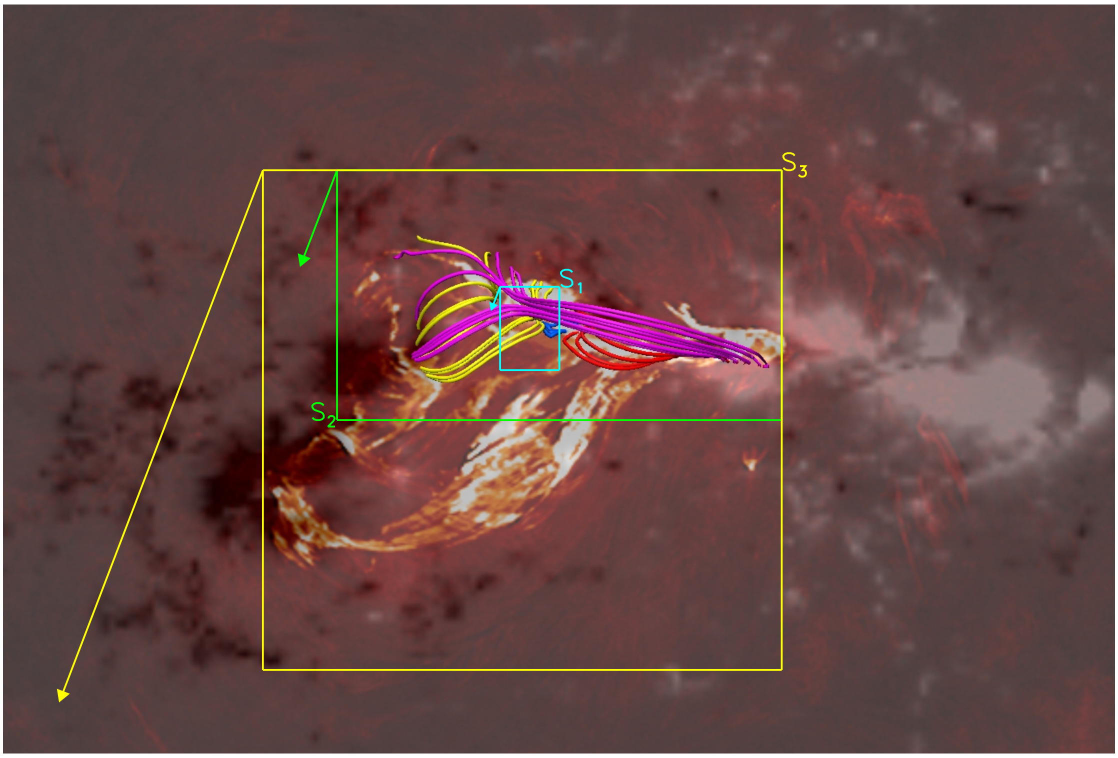

Figure 7.5: Visual representation of sub-volumes S_1, S_2, and S_3. The hyperbolic flux tube (HFT) configuration, overlaid with the vertical component of magnetic field and observation of the flaring event in 304 Å channel of SDO/AIA at 15:35:52 UT is shown. A zoomed-in viewpoint is used, corresponding to a cutout of 150×90 pixels. The extent and spatial position of sub-volumes S_1, S_2, and S_3 are marked by the *cyan*, *green*, and *yellow* colored boxes. The arrows indicate the extent of sub-volumes along the z-direction and are drawn in proportion to the actual vertical sizes of sub-volumes given in table 7.1.

the vertical direction, denoted by $z_0 = 0, 1, ..., 4$, and the contribution of each layer in the shaping of parameter profile is examined. For each layer, grid average of magnetic energy (W^H_{av}), current density ($|\mathbf{J}|^H_{av}$), and twist ($|\Gamma|^H_{av}$) is calculated over different $z = z_0$ layers, each having $N = 8 \times 10$ voxels along the x and y directions. It is found that W^V_{av} increases initially up to phase ${P_1}^{(4)}$, followed by a continuous decay during ${P_1}^{(5)}$. Notably, the profile of W^H_{av} in all the layers is qualitatively similar to W^V_{av}, as evident from panel (a) in figure 7.7. Contrarily, as may be seen from panels (b) and (c) of figure 7.7, the same is not true for $|\mathbf{J}|^V_{av}$ and $|\Gamma|^V_{av}$—an explanation for which is presented below.

Owing to $z_0 = 0, 1$, $|\mathbf{J}|^V_{av}$ decreases sharply in the beginning phase ${P_1}^{(1)}$. During the rising phase ${P_1}^{(2)}$, while all the layers exhibit similar profile, only $z_0 = 2, 3, 4$ contribute most significantly because the X-region of HFT exists at these heights, which is a prominent site for development of strong currents. Lastly, from phase

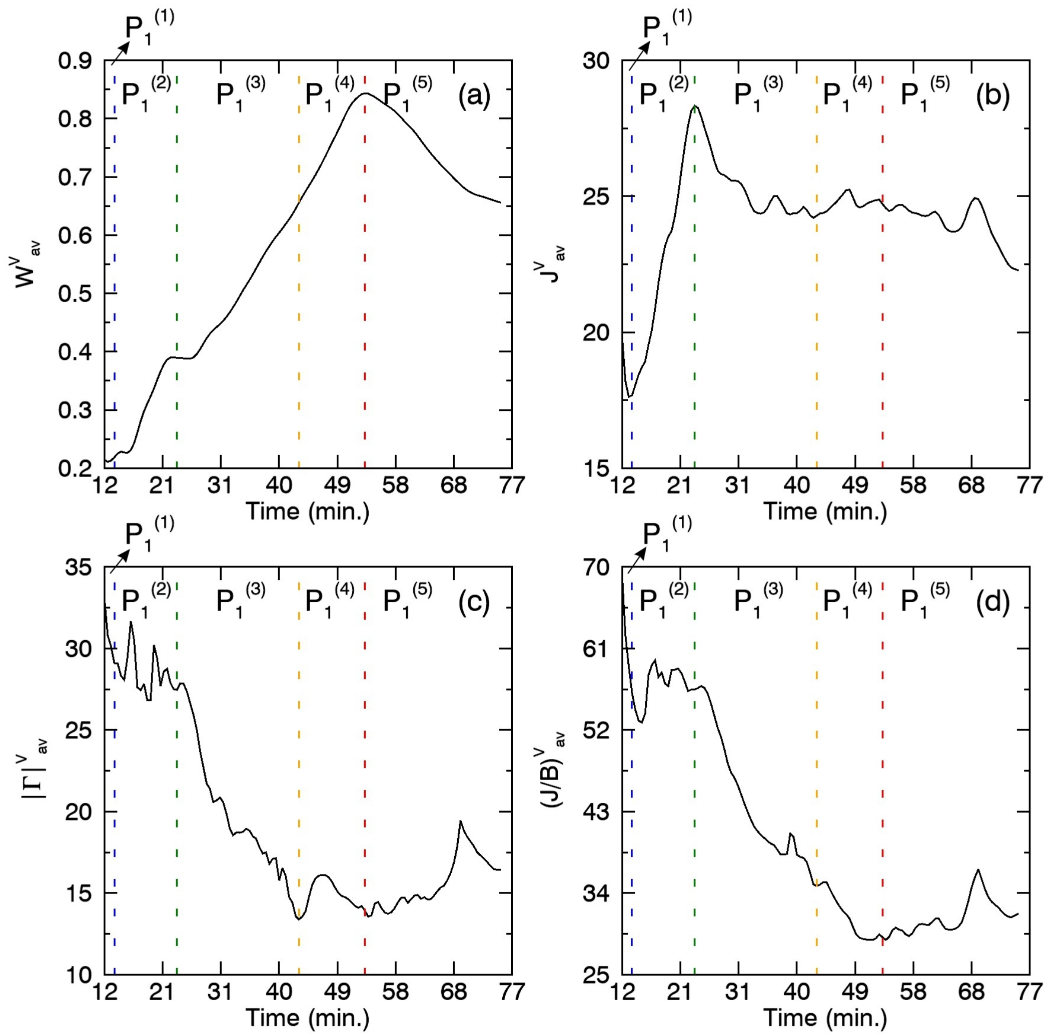

Figure 7.6: Time evolution of grid averaged (a) magnetic energy ($\mathrm{W}^{\mathrm{V}}_{\mathrm{av}}$) (b) current density ($|\mathbf{J}|^{\mathrm{V}}_{\mathrm{av}}$) (c) twist parameter($|\Gamma|^{\mathrm{V}}_{\mathrm{av}}$), and (d) $(|\mathbf{J}|/|\mathbf{B}|)^{\mathrm{V}}_{\mathrm{av}}$ in sub-volume S_1, during phases $\mathrm{P}_1^{(1)}$ (marked by the *black* arrow), $\mathrm{P}_1^{(2)}$, $\mathrm{P}_1^{(3)}$, $\mathrm{P}_1^{(4)}$, and $\mathrm{P}_1^{(5)}$, respectively. The *dashed* lines in *blue*, *green*, *orange*, and *red* colors separate the different phases in each of the profiles. The origin of the time scale maps to 15:12 UT.

${\mathrm{P}_1}^{(3)}$ to ${\mathrm{P}_1}^{(5)}$, there is an overall decrease in $|\mathbf{J}|^{\mathrm{V}}_{\mathrm{av}}$, again due to $\mathrm{z}_0 = 2, 3, 4$ along with some wiggling—predominantly due to $\mathrm{z}_0 = 0, 1, 2$. The $|\Gamma|^{\mathrm{V}}_{\mathrm{av}}$ profile during phases ${\mathrm{P}_1}^{(1)}$ and ${\mathrm{P}_1}^{(2)}$ is shaped by $\mathrm{z}_0 = 0, 1$. The decline during ${\mathrm{P}_1}^{(3)}$ is attributed to $\mathrm{z}_0 = 2, 3, 4$, while the evolution in ${\mathrm{P}_1}^{(4)}$ and ${\mathrm{P}_1}^{(5)}$ is strongly determined by the bottom two layers, i.e., $\mathrm{z}_0 = 0, 1$. The pronounced effect of the bottom two layers could be because the magnetic structures near the bottom boundary are not well resolved due to the rescaling of magnetic field during extrapolation. Consequently, the dynamics in near neighborhood of the X-region of HFT leads to fluctuations

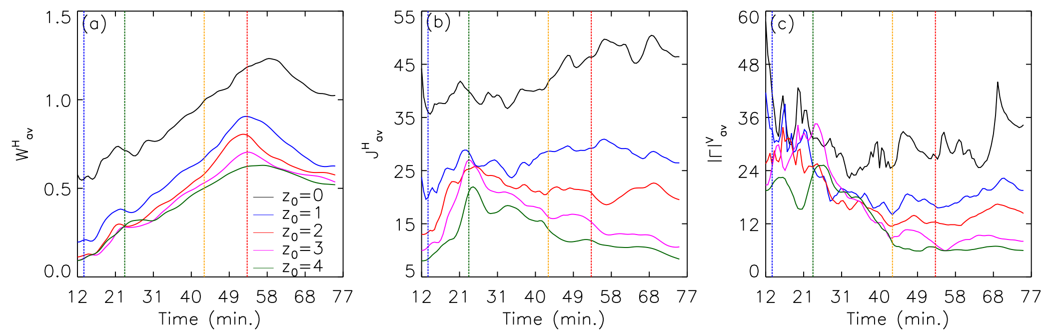

Figure 7.7: Time evolution of horizontally grid averaged (a) magnetic energy (W^H_{av}) (b) current density ($|\mathbf{J}|^H_{av}$) and (c) twist parameter($|\Gamma|^H_{av}$) in sub-volume S_1. Similar to figure 7.6, the *dashed* lines in *blue*, *green*, *orange*, and *red* colors separate the different phases. The *solid* lines plot the respective quantities for $z = z_0$ layers as labeled in panel (a). The origin of the time scale maps to 15:12 UT.

in the profile of J^V_{av} and $|\Gamma|^V_{av}$, which do not smooth out due to the small size of sub-volume S_1. Lastly, it is seen that the evolution of $(|\mathbf{J}|/|\mathbf{B}|)^V_{av}$ is qualitatively similar to $|\Gamma|^V_{av}$ profile. The quantitative changes in the grid-averaged parameters

	$P_1^{(1)}$	$P_1^{(2)}$	$P_1^{(3)}$	$P_1^{(4)}$	$P_1^{(5)}$	Net
W^V_{av}	+0.004	+0.170	+0.266	+0.188	-0.188	+0.440
$\|\mathbf{J}\|^V_{av}$	-2.123	+10.660	-4.048	+0.427	-2.430	+2.486
$\|\Gamma\|^V_{av}$	-3.914	-1.644	-14.079	+0.544	+2.514	-16.580
$(\|\mathbf{J}\|/\|\mathbf{B}\|)^V_{av}$	-12.957	+0.392	-21.705	-5.667	+2.598	-37.340

Table 7.2: Summary of the quantitative changes in grid averaged profiles of magnetic energy (W^V_{av}), current density ($|\mathbf{J}|^V_{av}$), twist parameter($|\Gamma|^V_{av}$), and magnetic field gradient ($(|\mathbf{J}|/|\mathbf{B}|)^V_{av}$) for sub-volume S_1, during phases $P_1^{(1)}$, $P_1^{(2)}$, $P_1^{(3)}$, $P_1^{(4)}$, and $P_1^{(5)}$, respectively. The positive and negative values indicate the rising and declining phases, while the net value in the rightmost column tells about the difference between terminal and initial states.

during each of the phases are summarized in table 7.2 and the rightmost column reveals that the net magnetic energy and current density have increased while the overall twist and gradients have reduced in sub-volume S_1. The evolution of magnetic field line dynamics, as shown in panels (a) and (b) of Figure 7.8, reveals that the field lines change their connectivity as soon as the simulation is initiated. The change in connectivity occurs because of reconnection at the X-region of HFT. With reconnection being known to dissipate magnetic energy, the increase of W^V_{av} demands additional analysis. In this regard, it is realized that magnetic

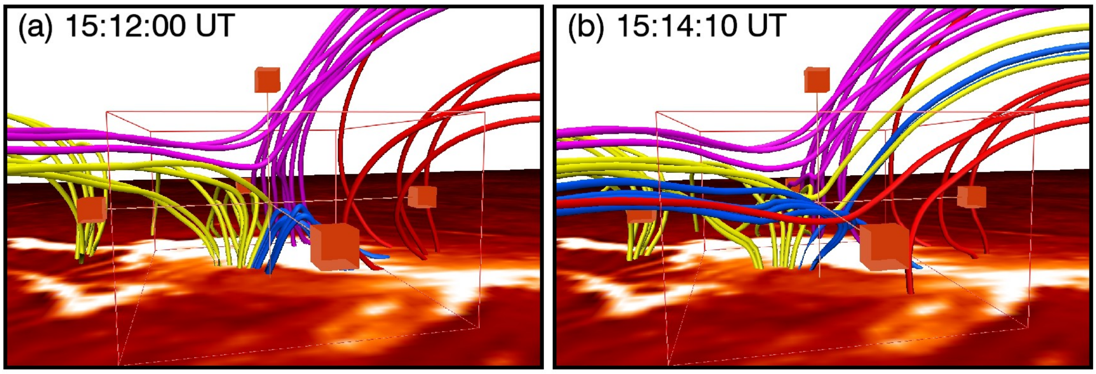

Figure 7.8: Panels (a) and (b): Illustration of changes in the field line connectivity of *yellow*, *blue*, and *red* MFLs due to reconnection at the X-region of HFT configuration. The *red* colored box marks the edges of S_1 while the bottom boundary is overlaid with an image in 304 Å channel of SDO/AIA

energy in a sub-volume can change because of an interplay between dissipation, Poynting flux, and the work done by the Lorentz force. With field line twist decreasing, the energy may increase if the net energy flux entering the sub-volume S_1 supersedes the energy dissipation at the X-region of the HFT. Such an analysis requires estimations of Poynting flux and dissipation to high accuracy, which is presently beyond the scope of the work carried out in this thesis. Nevertheless, an attempt is made toward a coarse estimation. A variable $|\mathbf{D}|$ is defined as

$$|\mathbf{D}|_i = \left|\frac{\partial \mathbf{B}_i}{\partial t} - \nabla \times (\mathbf{v}_i \times \mathbf{B}_i)\right|. \tag{7.6}$$

to approximate the $\mathbf{D_B}$ in equation (3.92), indicating when and where non-ideal effects can be important, where i denotes the voxel index. Due to the ILES nature of the computation, only the ideal contribution of electric field (see section 1.2.6) is used. Then, from equation 1.22, it can be realized that the Poynting flux across the bounding surface (B) of a sub-volume can be written as

$$\mathrm{S}^{\mathrm{B}}_{\mathrm{av}} = \frac{1}{N} \times \sum_{i=0}^{N-1} \left(|\mathbf{B}^t_i|^2 \mathbf{v}^n_i - (\mathbf{B}^t_i \cdot \mathbf{v}^t_i)\mathbf{B}^n_i\right) \cdot \Delta\mathbf{a}, \tag{7.7}$$

where N has usual meaning, n and t mark the normal and tangential components to the area element vector denoted by $\Delta\mathbf{a}$, respectively. Notably, v_z remains zero at the bottom boundary throughout the computation because of the employed boundary condition and the initial static state. Consequently, only the second term contributes to the Poynting flux through the bottom boundary. In figure 7.9, panel (a) plots the two-dimensional data planes of temporally averaged (averaged over the total computation time) $|\mathbf{D}|$ extracted from its 3D data volume, using the slice renderer function of VAPOR (see Appendix A) and $|\mathbf{D}|$ is found to line in the range $|\mathbf{D}| \in \{0.01, 0.11\}$. Notably, $|\mathbf{D}|$ is largest in the neighborhood of the X-region of HFT depicted in panel (a) of figure 7.8 and decreases away from it. The panel (b) plots $\mathrm{S}_{\mathrm{av}}^{\mathrm{B}}$. A positive value of $\mathrm{S}_{\mathrm{av}}^{\mathrm{B}}$ indicates outflow of magnetic energy whereas negative value means energy influx. Straightforwardly, the plot

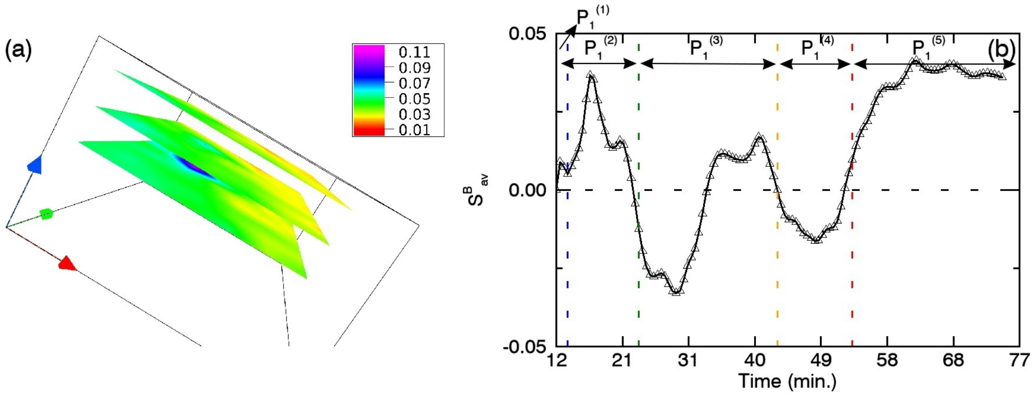

Figure 7.9: (a) Two-dimensional data planes of temporally averaged $|\mathbf{D}|$ at three different heights in sub-volume S_1. The mapping of data values is shown in the color bar. (b) Temporal evolution of $\mathrm{S}_{\mathrm{av}}^{\mathrm{B}}$ for sub-volume S_1. The *dashed* lines in *blue*, *green*, *orange*, and *red* colors separate the different phases. The origin of the time scale maps to 15:12 UT.

shows an outward energy flux up to $\mathrm{P}_1^{(2)}$, followed mostly by an inward energy flux up to $\mathrm{P}_1^{(4)}$, except for a brief time duration in $\mathrm{P}_1^{(3)}$. In the range $\mathrm{P}_1^{(5)}$, the energy flux is again outward. A comparison with magnetic energy evolution (panel (a), figure 7.6) shows the direction of energy fluxes to be overall consistent with energy variations for the phases $\mathrm{P}_1^{(3)}$, $\mathrm{P}_1^{(4)}$, and $\mathrm{P}_1^{(5)}$ but in complete disagreement for $\mathrm{P}_1^{(2)}$ and briefly for $\mathrm{P}_1^{(3)}$. An absolute reasoning for this disagreement is not viable within the employed framework of the EULAG-MHD model.

7.5.2 Sub-volume S_2

The evolution of $\mathrm{W}_{\mathrm{av}}^{\mathrm{V}}$, $|\mathbf{J}|_{\mathrm{av}}^{\mathrm{V}}$, $|\Gamma|_{\mathrm{av}}^{\mathrm{V}}$, and $(|\mathbf{J}|/|\mathbf{B}|)_{\mathrm{av}}^{\mathrm{V}}$ for S_2 are presented in panels (a), (b), (c), and (d) of figure 7.10. Again, five phases are considered, denoted by $\mathrm{P}_2^{(\mathrm{i})}$, where, $\mathrm{i} = 1, 2, ..., 5$. Notably, these phases are not the same as in sub-volume

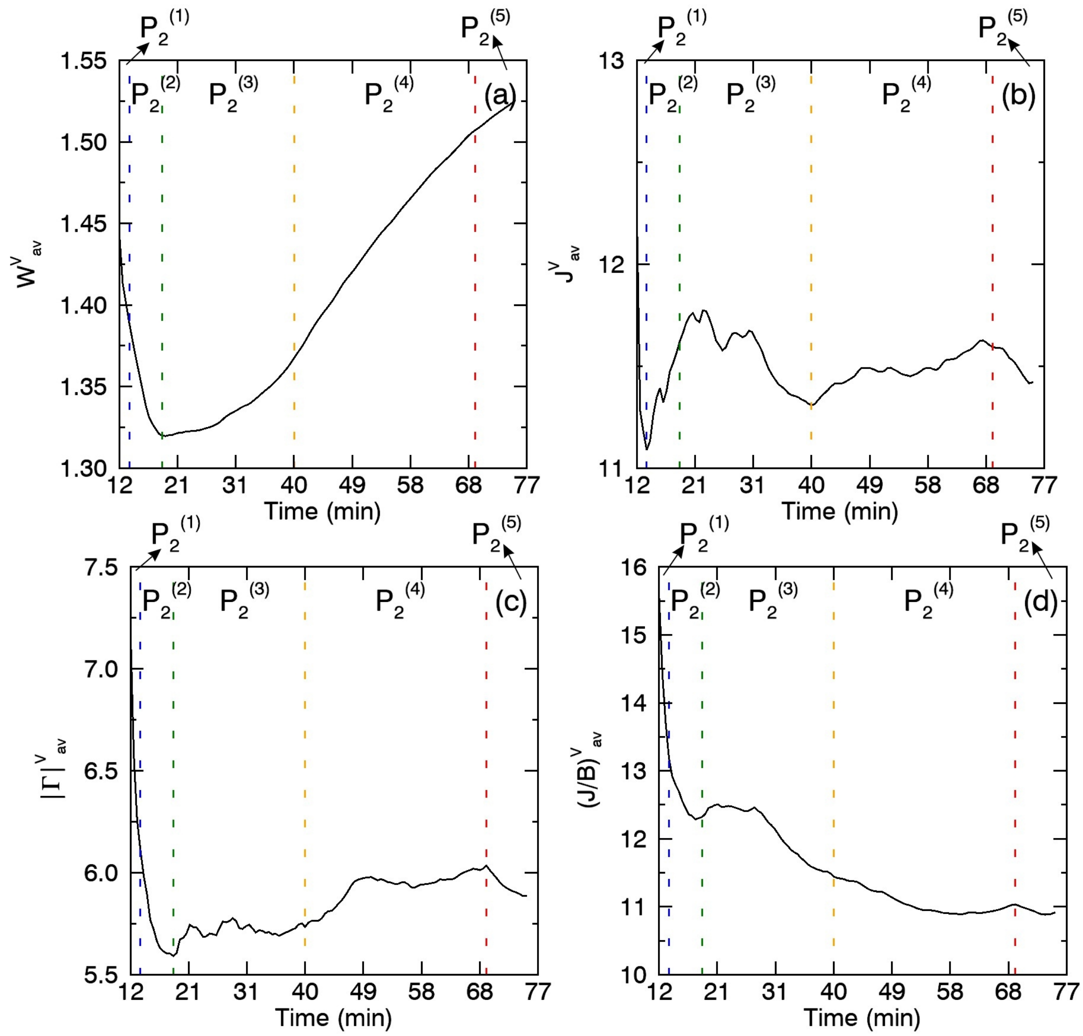

Figure 7.10: Time evolution of grid averaged (a) magnetic energy (W^V_{av}) (b) current density ($|\mathbf{J}|^V_{av}$) (c) twist parameter($|\Gamma|^V_{av}$), and (d) $(|\mathbf{J}|/|\mathbf{B}|)^V_{av}$ in sub-volume S_2, during phases $P_2^{(1)}$ (marked by the *black* arrow), $P_2^{(2)}$, $P_2^{(3)}$, $P_2^{(4)}$, and $P_2^{(5)}$ (also marked by *black arrow*), respectively. The *dashed* lines in *blue*, *green*, *orange*, and *red* colors separate the different phases in each of the profiles. The origin of the time scale maps to 15:12 UT.

S_1 and are chosen in accordance with the dynamics of S_2 itself. In phases $P_2^{(1)}$ and $P_2^{(2)}$, W^V_{av}, $|\Gamma|^V_{av}$, and $(|\mathbf{J}|/|\mathbf{B}|)^V_{av}$ exhibit a sharp decline. Similar behavior is observed during $P_2^{(1)}$ for $|\mathbf{J}|^V_{av}$. Subsequently, over the span $P_2^{(3)}$ to $P_2^{(5)}$, there is an overall increase in W^V_{av} and $|\Gamma|^V_{av}$, and similarly in $|\mathbf{J}|^V_{av}$ from $P_2^{(2)}$ to $P_2^{(5)}$. However, $(|\mathbf{J}|/|\mathbf{B}|)^V_{av}$ decreases almost continuously. The quantitative changes corresponding to different phases are summarized in table 7.3 from which, a comparison of the terminal and initial states of the simulation reveals that the net magnetic energy in S_2 increases, while the other parameters decrease. The exploration of dynamics

	$P_2^{(1)}$	$P_2^{(2)}$	$P_2^{(3)}$	$P_2^{(4)}$	$P_2^{(5)}$	Net
W_{av}^V	-0.054	-0.069	+0.048	+0.140	+0.018	+0.083
$\|\mathbf{J}\|_{av}^V$	-1.172	+0.532	-0.313	+0.286	-0.174	-0.841
$\|\Gamma\|_{av}^V$	-1.074	-0.521	+0.142	+0.300	-0.148	-1.301
$(\|\mathbf{J}\|/\|\mathbf{B}\|)_{av}^V$	-2.387	-0.866	-0.876	-0.408	-0.120	-4.657

Table 7.3: Summary of the quantitative changes in grid averaged profiles of magnetic energy (W_{av}^V), current density ($|\mathbf{J}|_{av}^V$), twist parameter($|\Gamma|_{av}^V$), and magnetic field gradient ($(|\mathbf{J}|/|\mathbf{B}|)_{av}^V$) for sub-volume S_2, during phases $P_2^{(1)}$, $P_2^{(2)}$, $P_2^{(3)}$, $P_2^{(4)}$, and $P_2^{(5)}$, respectively. The positive and negative values indicate the rising and declining phases, while the net value in the rightmost column tells about the difference between terminal and initial states.

reveals that each layer (each having $N = 60\times30$ voxels along the x and y directions) along the vertical direction of computational box (denoted by $z_0 = 0, 1, ..., 19$) has nearly similar profile for magnetic energy, while for $|\mathbf{J}|_{av}^V$ and $|\Gamma|_{av}^V$, this is not true.

The sharp decline in $|\mathbf{J}|_{av}^V$ during phase $P_2^{(1)}$ is predominantly caused by $z_0 = 0, 1$. The rising phase $P_2^{(2)}$ has contributions from the layers $z_0 = 2$ to 9, dominantly from $z_0 = 2, 3, 4$, and maximum from $z_0 = 3$. Similarly, the declining $P_2^{(3)}$ phase is shaped by layers $z_0 = 0$ to 4 but the most significant role is played by layers $z_0 = 1, 2, 3$, while the maximum contribution arises from $z_0 = 2$. In the later phase, i.e. $P_2^{(4)}$, $|\mathbf{J}|_{av}^V$ increases again because of $z_0 = 11$ to 19. Notably, during $P_2^{(4)}$, the layers $z_0 = 2$ to 10 display declining values of current density, thus suggesting that while current density decreases in lower layers, the overall phase is governed by the dynamical evolution in higher layers. Lastly, in the concluding phase $P_2^{(5)}$, layers from $z_0 = 0$ to 15 exhibit decrease of current density, thus resulting in an overall decay.

The $|\Gamma|_{av}^V$ profile reveals sharp decline during phases $P_2^{(1)}$ and $P_2^{(2)}$, primarily due to initial five to six layers ($z_0 = 0$ to 5) but as in the case of $|\mathbf{J}|_{av}^V$, the bottom two layers $z_0 = 0, 1$ determine the overall profile. The subsequent rising phases $P_2^{(3)}$ and $P_2^{(4)}$ are seen to be governed by layers $z_0 = 8$ to 19 and $z_0 = 12$ to 19, respectively. Notably, during these two phases, the lower layers, identified by $z_0 = 0$ to 7 and $z_0 = 0$ to 11 show lowering of twist over time. This behavior is reminiscent of $|\mathbf{J}|_{av}^V$ during $P_2^{(4)}$. In the end phase $P_2^{(5)}$, all except the top four layers, show lowering of twist, thus resulting in an overall decaying profile. During the early phases, i.e., up to $P_2^{(3)}$ for $|\mathbf{J}|_{av}^V$ and $P_2^{(2)}$ for $|\Gamma|_{av}^V$, the lower layers ($z_0 = 0, 1, ..., 5$) of sub-volume S_2

are seen to be playing the major role in determining the evolution of grid averaged parameters. This is due to the fact that the non-ideal region (the X-region of HFT) is within the first five layers of bottom boundary. Since S_2 contains S_1, the reconnection at X-region plays an important role during the beginning phase of W^{V}_{av}. Moreover, the energy reduction has added contribution from other sources as S_2 covers the observed brightening B_2 as well. An instance of this possibility is explored using the anticipated slipping reconnection in *yellow* and *pink* MFLs constituting the observed dome structure. Panels (a) and (b) in Figure 7.11 depict a situation where sudden flipping of three selective magnetic field lines occurs, which implies slipping reconnection. For easy identification, the footpoints of the three field lines are marked with *black*, *white*, and *red* colored circles. The increase

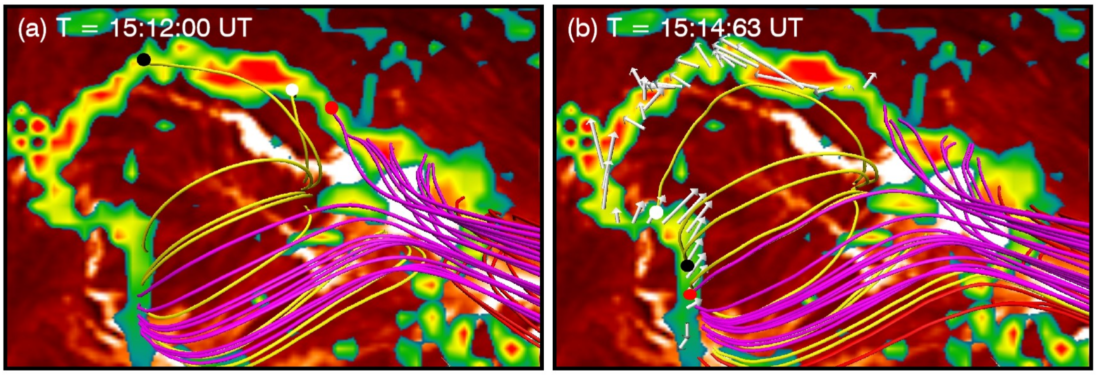

Figure 7.11: Panels (a) and (b): Illustration of sudden shift in the footpoints of *yellow* and *pink* magnetic field lines within the sub-volume S_2 due to slipping reconnection. Panel (a) highlights the initial footpoints of three selective MFLs in *black*, *white*, and *red* colored circles. Panel (b) depicts the sudden movement of these footpoints, which is not along the direction of plasma flow (shown in white arrows). The bottom boundary is overlaid with squashing degree map and an image in 304 Å channel of SDO/AIA.

in twist from $P_2^{(3)}$ to $P_2^{(5)}$ is in accordance with the magnetic energy increase. To gain further insight, figure 7.12 plots the time averaged deviation $|\mathbf{D}|$ and Poynting flux in panels (a) and (b), respectively. In S_2 $|\mathbf{D}| \in \{0.0, 0.05\}$, which is smaller compared to that in S_1 (marked by the black colored box in panel (a)), signifying larger values of $|\mathbf{D}|$ to be localized at S_1. The Poynting flux is positive for most of the $P_2^{(2)}$, which is in conformity with the energy decay. For phases $P_2^{(3)}$ to $P_2^{(5)}$, the Poynting flux is negative, which can further be visualized from figure Figure 7.13, where a portion of *green* field lines are pushed completely inside S_2 (*red* colored box). The corresponding energy influx along with the increment in twist seems to overwhelm dissipation, thus resulting in the observed energy increase.

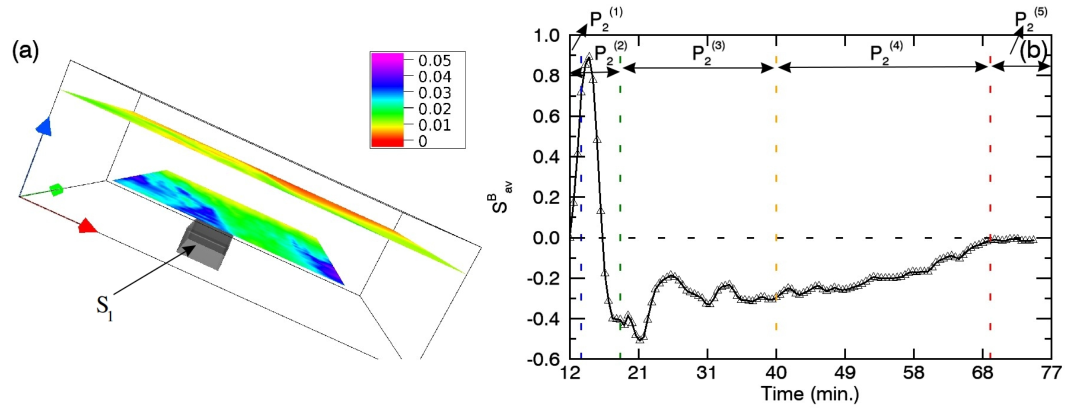

Figure 7.12: (a) Two-dimensional data planes of temporally averaged $|\mathbf{D}|$ at two different heights in sub-volume S_2. The mapping of data values is shown in the color bar. The *black* box marks the sub-volume S_1 (b) Temporal evolution of S^B_{av} for sub-volume S_2. The *dashed* lines in *blue*, *green*, *orange*, and *red* colors separate the different phases. The origin of the time scale maps to 15:12 UT.

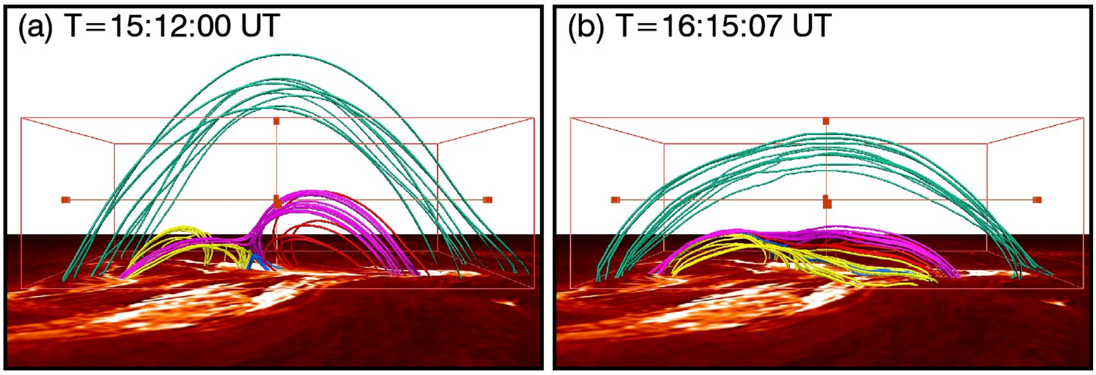

Figure 7.13: Panels (a) and (b): Illustration of magnetic flux transfer within the sub-volume S_2. The field lines comprising the HFT are shown, along with an additional set of *green* colored MFLs, which are pushed completely inside the sub-volume S_2 during simulation. The *red* colored box marks the edges of S_2 while the bottom boundary is overlaid with an image in 304 Å channel of SDO/AIA.

7.5.3 Sub-volume S_3

The sub-volume S_3 encompasses the complete extent of the observed brightening. For convenience, the evolution in S_3 is investigated in five phases, defined by $P_3^{(i)}$, where, $i = 1, 2, ..., 5$. The temporal evolution of the grid averaged parameters is shown in Figure 7.14. Panel (a) reveals that S_3 exhibits continuous decrease in W^V_{av} up to $P_3^{(4)}$, which is in close agreement with the end time of the flare. Such uninterrupted decrement is a prime signature of relaxation in the considered

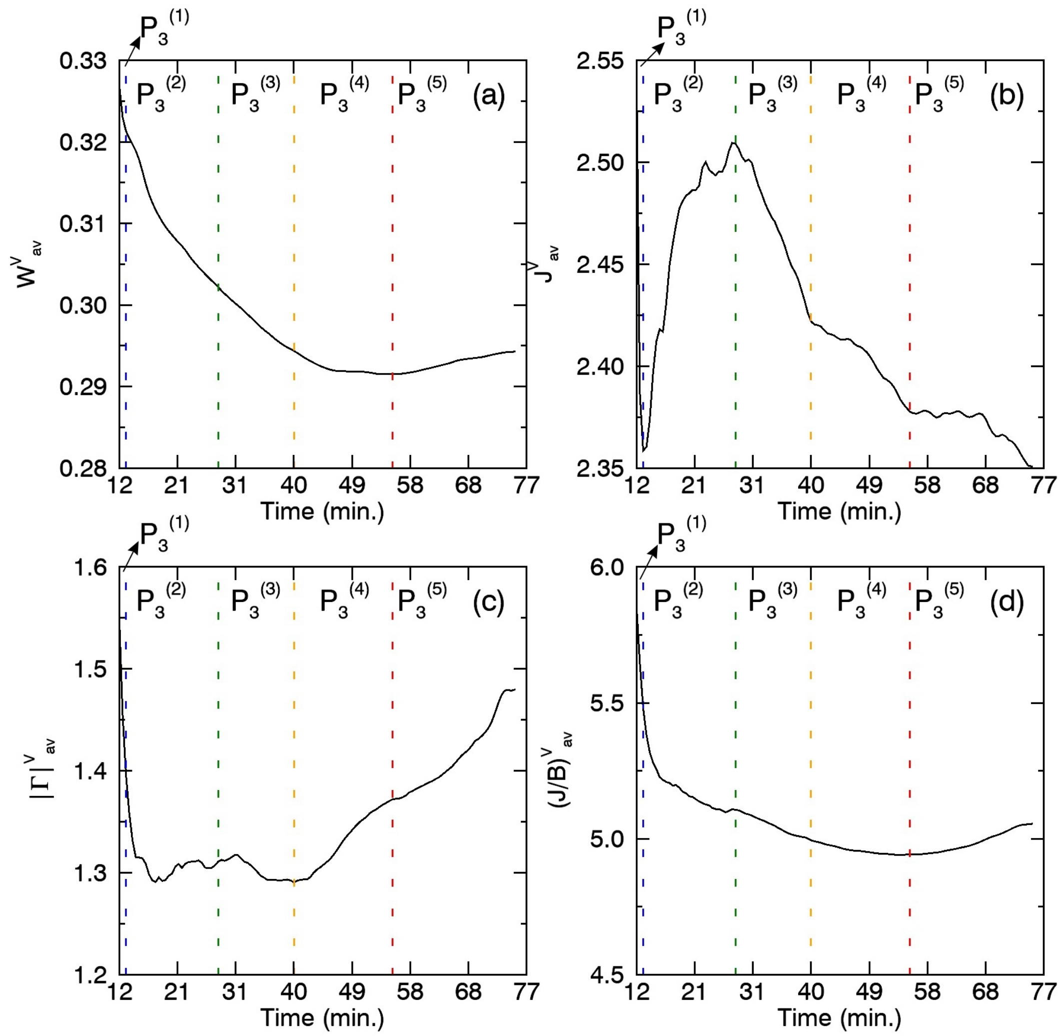

Figure 7.14: Time evolution of grid averaged (a) magnetic energy (W^V_{av}) (b) current density ($|\mathbf{J}|^V_{av}$) (c) twist parameter($|\Gamma|^V_{av}$), and (d) $(|\mathbf{J}|/|\mathbf{B}|)^V_{av}$ in sub-volume S_3 during phases $P_3^{(1)}$ (marked by the *black* arrow), $P_3^{(2)}$, $P_3^{(3)}$, $P_3^{(4)}$, and $P_3^{(5)}$, respectively. The *dashed* lines in *blue*, *green*, *orange*, and *red* colors separate the different phases in each of the profiles. The origin of the time scale maps to 15:12 UT.

volume. From panel (b), it is seen that after an initial drop, $|\mathbf{J}|^V_{av}$ peaks at 15:27 UT, subsequently followed by a declining profile. Panel (c) indicates that $|\Gamma|^V_{av}$ decays up to 15:39 UT, which nearly corresponds to the peak time of the flare. This suggests lowering of overall twist and hence a simplification of field line complexity, which further complements the interpretation of relaxation within the sub-volume. In the later phase, there is an increase in twist while the magnetic field gradient (panel (d)) is seen to be declining continuously with very small increment toward the end of simulation. Overall, the volume averaged MHD evolution in S_3 is similar to the overall simulated dynamics. The quantitative changes associated with the grid averaged profiles are summarized in table 7.4. Notably, in this sub-volume, the terminal state is characterized by a reduced value of all the parameters, i.e. magnetic energy, current density, twist, and magnetic field gradients.

	$\mathrm{P}_3^{(1)}$	$\mathrm{P}_3^{(2)}$	$\mathrm{P}_3^{(3)}$	$\mathrm{P}_3^{(4)}$	$\mathrm{P}_3^{(5)}$	Net
$\mathrm{W}_{\mathrm{av}}^{\mathrm{V}}$	-0.005	-0.019	-0.008	-0.003	+0.003	-0.033
$\lvert\mathbf{J}\rvert_{\mathrm{av}}^{\mathrm{V}}$	-0.185	+0.151	-0.087	-0.044	-0.027	-0.192
$\lvert\Gamma\rvert_{\mathrm{av}}^{\mathrm{V}}$	-0.151	-0.086	-0.020	+0.081	+0.107	-0.069
$(\lvert\mathbf{J}\rvert/\lvert\mathbf{B}\rvert)_{\mathrm{av}}^{\mathrm{V}}$	-0.373	-0.374	-0.112	-0.052	+0.113	-0.800

Table 7.4: Summary of the quantitative changes in grid averaged profiles of magnetic energy ($\mathrm{W}_{\mathrm{av}}^{\mathrm{V}}$), current density ($\lvert\mathbf{J}\rvert_{\mathrm{av}}^{\mathrm{V}}$), twist parameter($\lvert\Gamma\rvert_{\mathrm{av}}^{\mathrm{V}}$), and magnetic field gradient ($(\lvert\mathbf{J}\rvert/\lvert\mathbf{B}\rvert)_{\mathrm{av}}^{\mathrm{V}}$) for sub-volume S_3, during phases $\mathrm{P}_3^{(1)}$, $\mathrm{P}_3^{(2)}$, $\mathrm{P}_3^{(3)}$, $\mathrm{P}_3^{(4)}$, and $\mathrm{P}_3^{(5)}$, respectively. The positive and negative values indicate the rising and declining phases, while the net value in the rightmost column tells about the difference between terminal and initial states.

Notably, sub-volume S_3 spans the full extent of observed brightenings and the full vertical extent of the computational box. Therefore, toward understanding the magnetofluid dynamics in S_3 more comprehensively, $\mathrm{W}_{\mathrm{av}}^{\mathrm{H}}$, $\lvert\mathbf{J}\rvert_{\mathrm{av}}^{\mathrm{H}}$, and $\lvert\Gamma\rvert_{\mathrm{av}}^{\mathrm{H}}$ are analyzed, where the grid averages are carried out over different $\mathrm{z} = \mathrm{z}_0$ layers, each having $N = 70 \times 60$ voxels along the x and y directions, respectively.

Figure 7.15 shows the temporal profile of $\mathrm{W}_{\mathrm{av}}^{\mathrm{H}}$ for some of the selected layers. In phase $\mathrm{P}_3^{(1)}$, all the layers exhibit decreasing $\mathrm{W}_{\mathrm{av}}^{\mathrm{H}}$ with significant contribution from $\mathrm{z}_0 = 0, 1, 2$, thus leading to declining $\mathrm{W}_{\mathrm{av}}^{\mathrm{V}}$. Further, as exemplified in panels (a) and (b), the subsequent phases are characterized by an increasing $\mathrm{W}_{\mathrm{av}}^{\mathrm{H}}$ for $\mathrm{z}_0 = 0$ to 3 in $\mathrm{P}_3^{(2)}$, $\mathrm{z}_0 = 1$ to 10 in $\mathrm{P}_3^{(3)}$, $\mathrm{z}_0 = 0$ to 14 in $\mathrm{P}_3^{(4)}$, and $\mathrm{z}_0 = 0$ to 17 in $\mathrm{P}_3^{(5)}$, respectively. Notably, the evolution of $\mathrm{W}_{\mathrm{av}}^{\mathrm{H}}$ differs by an order of magnitude in the two panels. The remaining layers during these phases exhibit declining $\mathrm{W}_{\mathrm{av}}^{\mathrm{H}}$, as evident from panels (b), (c), and (d). In effect then, owing to their larger number, these remaining layers dominate the profile evolution of $\mathrm{W}_{\mathrm{av}}^{\mathrm{V}}$ during phases $\mathrm{P}_3^{(2)}$, $\mathrm{P}_3^{(3)}$, and $\mathrm{P}_3^{(4)}$. However, in the end phase, the dynamics in $\mathrm{z}_0 = 0$ to 17 takes control, thus leading to increasing $\mathrm{W}_{\mathrm{av}}^{\mathrm{V}}$ during $\mathrm{P}_3^{(5)}$. Due to larger volume of S_3, the resulting $\mathrm{W}_{\mathrm{av}}^{\mathrm{V}}$ profile is jointly governed by both larger (smaller) decrements in the lower (higher) layers. However, for S_2, whose vertical extent is restricted to $\mathrm{z}_0 = 19$, layers from panel (a) and partly from panel (b) can be envisaged to

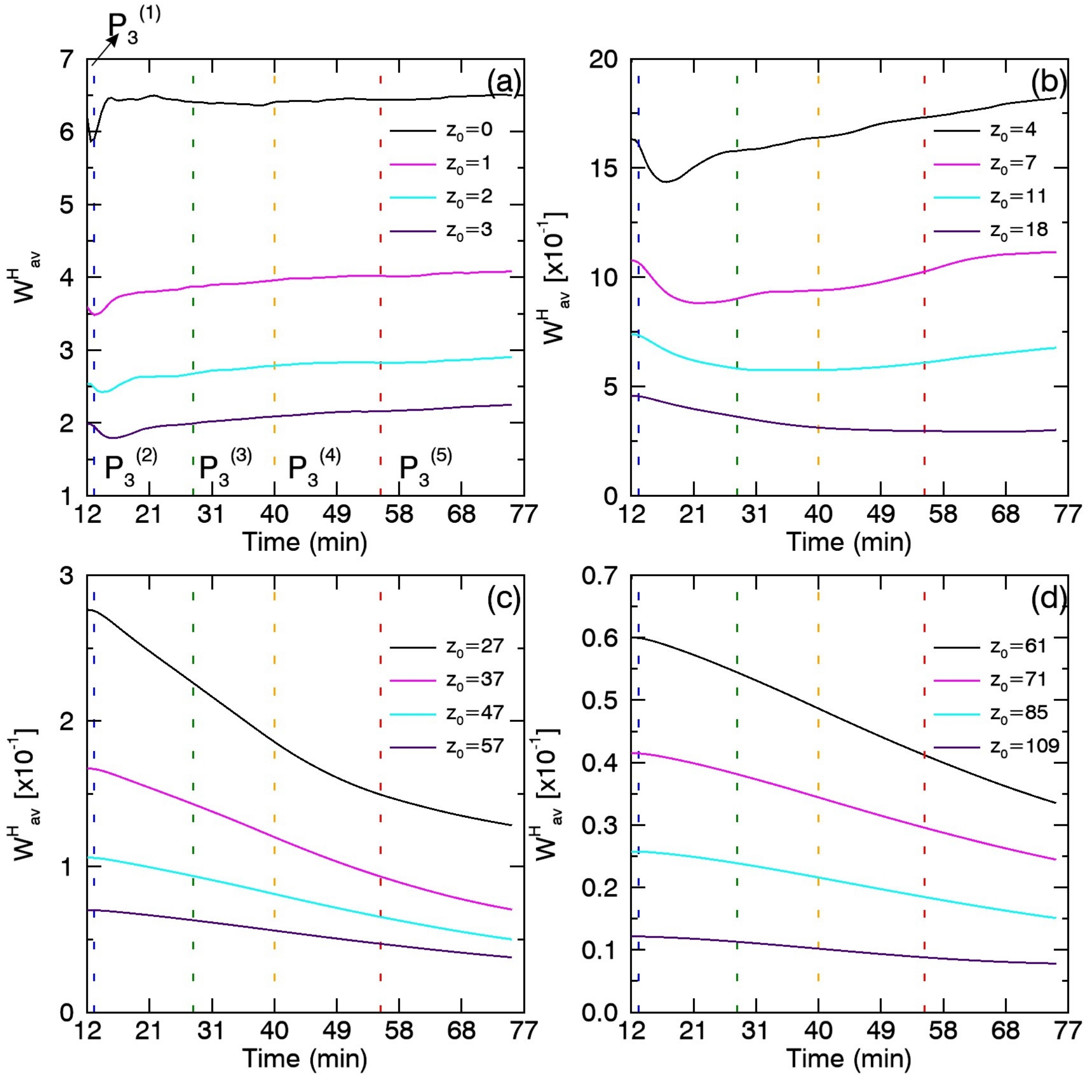

Figure 7.15: Time evolution of $\mathrm{W}_{\mathrm{av}}^{\mathrm{H}}$ for sub-volume S_3 at different $\mathrm{z} = \mathrm{z}_0$ layers, shown by the *black*, *magenta*, *cyan*, and *indigo* color *solid* lines. The labels indicate the chosen z_0 value in each panel. The different phases $\mathrm{P}_3^{(\mathrm{i})}$, where $\mathrm{i} = 0, 1, ..., 5$, are marked only in panel (a) to avoid clutter, while the *dashed* lines separating the phases are marked in each of the panels. The *y*-scale in panels (b), (c), and (d) differs by an order of magnitude (10^{-1}) than in panel (a). The origin of time on x-axis maps to 15:12 UT.

jointly reproduce an initial fall, followed by continuous rise.

Subsequently, the behavior of $|\mathbf{J}|_{\mathrm{av}}^{\mathrm{H}}$ is explored, as shown in figure 7.16. During $\mathrm{P}_3^{(1)}$, other than the top two, all layers exhibit decreasing $|\mathbf{J}|_{\mathrm{av}}^{\mathrm{H}}$, thereby causing the sharp decline of $\mathrm{J}_{\mathrm{av}}^{\mathrm{V}}$ in this phase. The dominant role is played by the bottom layers $\mathrm{z}_0 = 0, 1$, as may be seen from panel (a). In the next two phases, the process of current formation and dissipation within the HFT governs the evolution. The increase in $\mathrm{J}_{\mathrm{av}}^{\mathrm{V}}$ during $\mathrm{P}_3^{(2)}$ is essentially due to the increasing $|\mathbf{J}|_{\mathrm{av}}^{\mathrm{H}}$ in layers $\mathrm{z}_0 = 2$

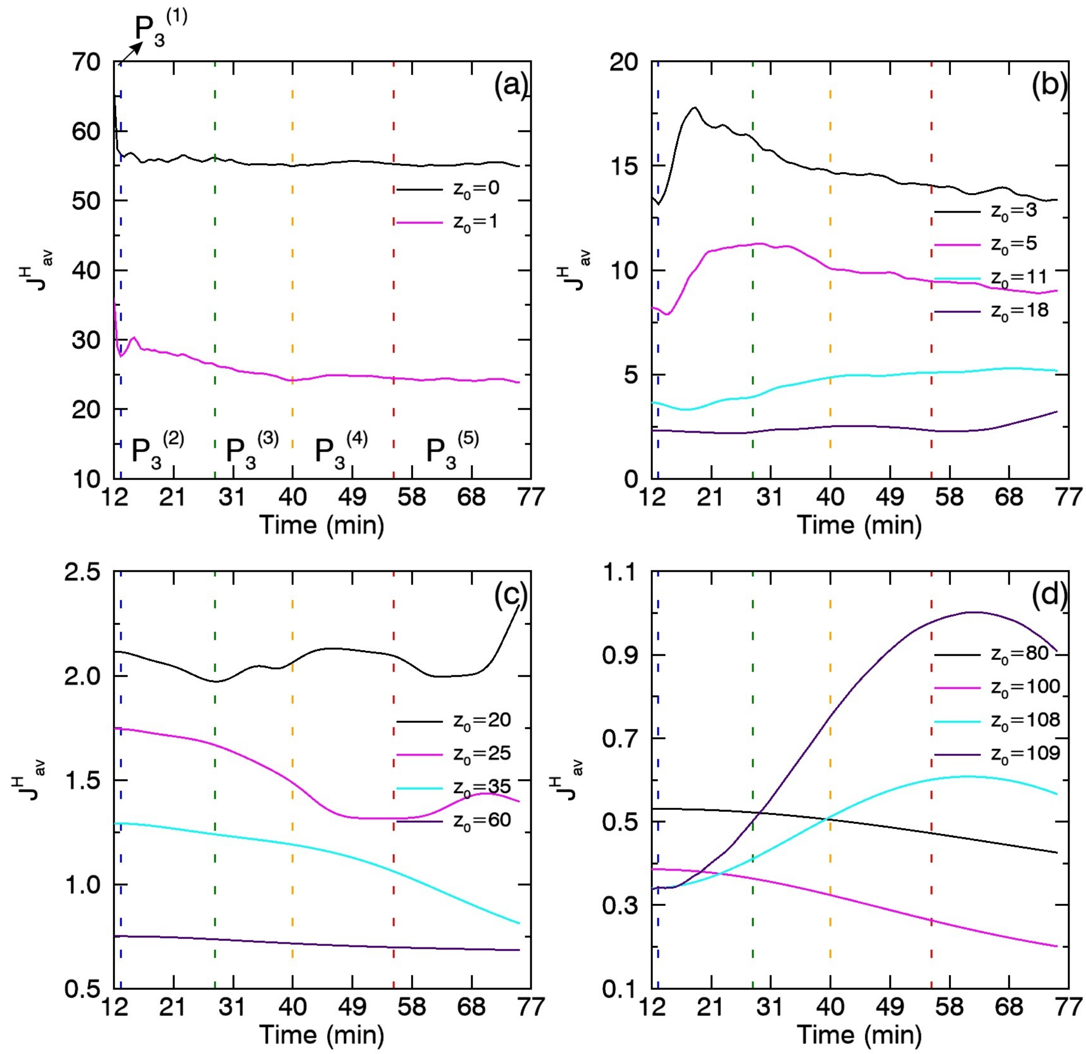

Figure 7.16: Time evolution of $|\mathbf{J}|^{\mathrm{H}}_{\mathrm{av}}$ for sub-volume S_3 at different $\mathrm{z} = \mathrm{z}_0$ layers, shown by the *black*, *magenta*, *cyan*, and *indigo* color *solid* lines. The labels indicate the chosen z_0 value in each panel. The different phases $\mathrm{P}_3^{(\mathrm{i})}$, where $\mathrm{i} = 0, 1, ..., 5$, are marked only in panel (a) to avoid clutter, while the *dashed* lines separating the phases are marked in each of the panels. The origin of time on x-axis maps to 15:12 UT.

to 11, as depicted in panels (a) and (b). Similarly, the decreasing $|\mathbf{J}|^{\mathrm{H}}_{\mathrm{av}}$ in $\mathrm{z}_0 = 0$ to 7 causes the decline of $\mathrm{J}^{\mathrm{V}}_{\mathrm{av}}$ during phase $\mathrm{P}_3^{(3)}$ despite the increasing $|\mathbf{J}|^{\mathrm{H}}_{\mathrm{av}}$ in $\mathrm{z}_0 = 8$ to 20. In the remaining two phases $\mathrm{P}_3^{(4)}$ and $\mathrm{P}_3^{(5)}$, the segregation of any dominant contribution from $\mathrm{z} = \mathrm{z}_0$ layers was found to be difficult. Nevertheless, the profile of $\mathrm{J}^{\mathrm{V}}_{\mathrm{av}}$ is understood from the finding that $|\mathbf{J}|^{\mathrm{H}}_{\mathrm{av}}$ decreases significantly in layers $\mathrm{z}_0 = 23$ to 107 and $\mathrm{z}_0 = 26$ to 109, respectively, as evident from panels (c) and (d). Interestingly, the two topmost layers reveal an abrupt increase in $|\mathbf{J}|^{\mathrm{H}}_{\mathrm{av}}$, an understanding of which requires investigation of field line dynamics.

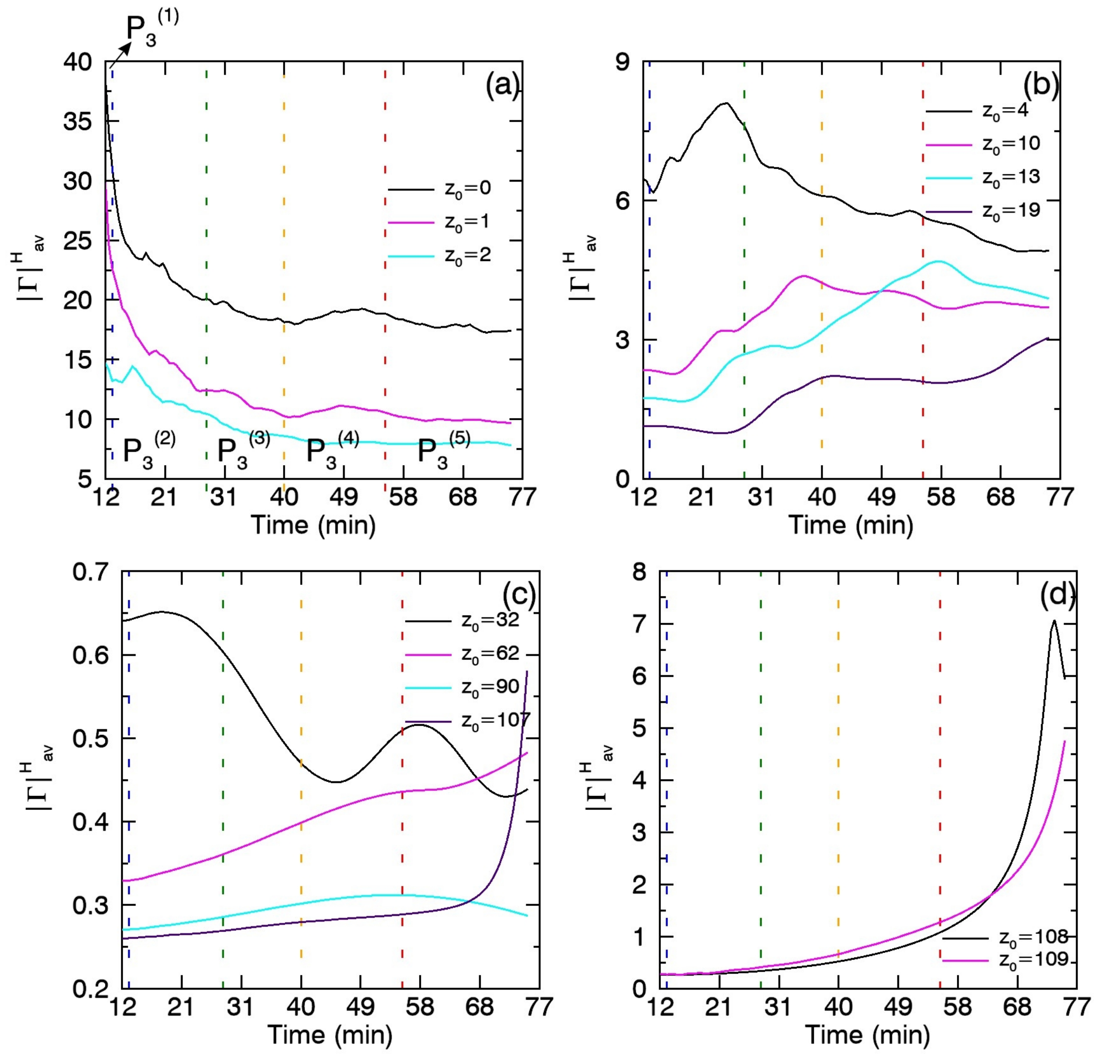

Figure 7.17: Time evolution of $|\Gamma|^{\rm H}_{\rm av}$ for sub-volume S_3 at different $z = z_0$ layers, shown by the *black*, *magenta*, *cyan*, and *indigo* color *solid* lines. The labels indicate the chosen z_0 value in each panel. The different phases $P_3^{(i)}$, where $i = 0, 1, ..., 5$, are marked only in panel (a) to avoid clutter, while the *dashed* lines separating the phases are marked in each of the panels. The origin of time on x-axis maps to 15:12 UT.

Lastly, the behavior of $|\Gamma|^{\rm H}_{\rm av}$ is explored, as depicted in figure 7.17. Panels (a) and (b) reveal that $|\Gamma|^{\rm H}_{\rm av}$ decreases for $z_0 = 0$ to 11 and increases for $z_0 = 3$ to 16 during phases $P_3^{(1)}$ and $P_3^{(2)}$, respectively. However, $|\Gamma|^{\rm V}_{\rm av}$ declines during both the phases due to the dominating decrease of $|\Gamma|^{\rm H}_{\rm av}$ in the bottom layers, i.e. $z_0 = 0, 1, 2$. A similar behavior is observed for phase $P_3^{(3)}$, where the fall of $|\Gamma|^{\rm H}_{\rm av}$ in $z_0 = 0$ to 7 dominates the rise of $|\Gamma|^{\rm H}_{\rm av}$ in $z_0 = 8$ to 23. The increase of $|\Gamma|^{\rm V}_{\rm av}$ during $P_3^{(4)}$ is seen to be consequence of dynamics in $z_0 = 11$ to 16 (panel (b)) and $z_0 = 20$ to 32 (panel (c)). In the concluding phase $P_3^{(5)}$, $|\Gamma|^{\rm V}_{\rm av}$ increases further owing to increasing $|\Gamma|^{\mathrm{H}}_{\mathrm{av}}$ in $z_0 = 14$ to 20 (panel (b)) and the abrupt increase of $|\Gamma|^{\mathrm{H}}_{\mathrm{av}}$ in the topmost layers, namely $z_0 = 107, 108, 109$ (panel (d)). The underlying reason for this abrupt rise may be understood from figure 7.18. Panel (a) depicts *blue* MFLs

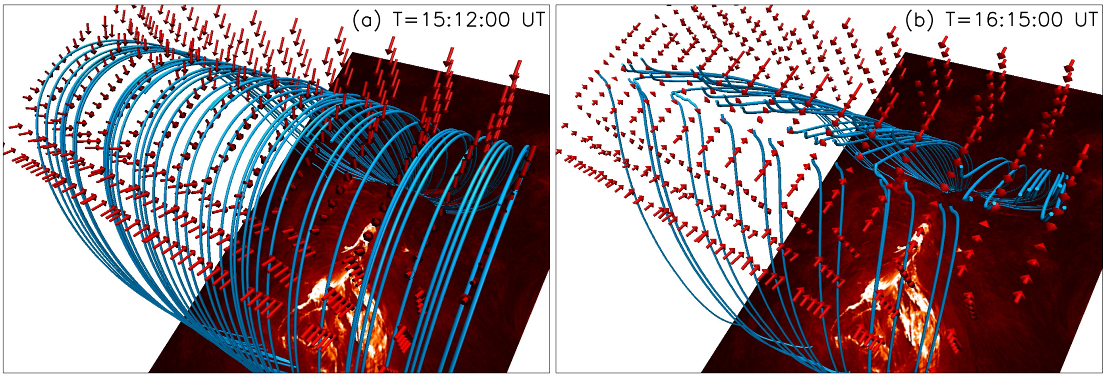

Figure 7.18: Illustration of magnetic field line dynamics responsible for abrupt rise of $\mathrm{J}^{\mathrm{H}}_{\mathrm{av}}$ and $|\Gamma|^{\mathrm{H}}_{\mathrm{av}}$ in the top two layers of the computational box. The *blue* MFLs and *red* arrows in panel (a) depict the bipolar potential field lines and direction of Lorentz force in the beginning of simulation. Panel (b) depicts the deformation in MFLs due to action of Lorentz force over the course of simulation. The bottom boundary is overlaid with image in 304 Å channel of SDO/AIA.

which constitute the bipolar loops, while the *red* arrows show direction of Lorentz force around the topmost region of computational box. As evident from panel (b), the converging force pushes magnetic field lines toward each other, which leads to stressing of the configuration. Notably, it is not clear whether the disconnected MFLs in panel (b) are a consequence of reconnection or movement of field lines outward from the box. Such a discontinuity results in a large gradient and hence sudden rise in $|\mathbf{J}|^{\mathrm{H}}_{\mathrm{av}}$ and $|\Gamma|^{\mathrm{H}}_{\mathrm{av}}$.

Figure 7.19 plots slice rendering of time averaged $|\mathbf{D}|$ along with the Poynting flux. The $|\mathbf{D}| \in \{0, 0.003\}$, which is one and two orders less than its values in S_2 and S_1 (marked in panel (a) with arrows), respectively. Comparison of $|\mathbf{D}|$ in all the three sub-volumes indicates localization of maximal $|\mathbf{D}|$ at S_1 and specifically, at the neighborhood of the X-region—the primary reconnection site. Such localization of $|\mathbf{D}|$ is compatible with the general idea of ILES. On an average the Poynting flux is $\approx 30\%$ of its value for S_2 and is predominantly negative, implying energy influx. As a consequence, the decrease in magnetic energy can be attributed to the overall decrease in twist conjointly with non-ideal effects, contributed primarily from S_1 and further augmented by slipping reconnections in

S_2.

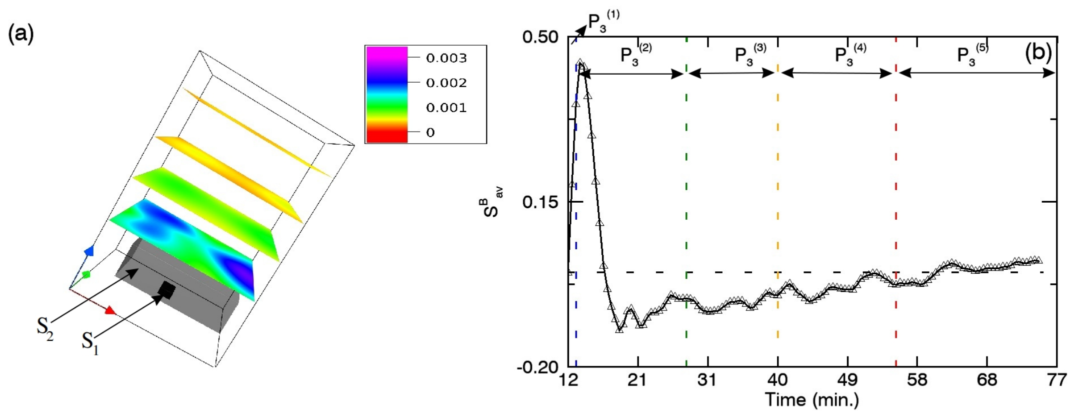

Figure 7.19: (a) Two-dimensional data planes of temporally averaged $|\mathbf{D}|$ at different heights in sub-volume S_3. The mapping of data values is shown in the color bar. The *black* boxes mark the sub-volumes S_1 and S_2 (b) Temporal evolution of S^B_{av} for sub-volume S_3. The *dashed* lines in *blue*, *green*, *orange*, and *red* colors separate the different phases. The origin of the time scale maps to 15:12 UT.

7.5.4 Extent of Magnetic Relaxation

As describe earlier, force-free states are characterized by the field aligned current density. Further, due to the unavailability of a suitable methodology for magnetic helicity estimation, the angle between **J** and **B** serves as a useful proxy to explore the extent of magnetic relaxation. Consequently, histograms of angle (θ) between **J** and **B** are compared at the beginning and end of the simulation for each of the sub-volumes. Notably, the θ plots in figure 7.20 utilize the transformation $180° - \theta$ to map $\theta \geq 90°$ in the range $0° \leq \theta \leq 90°$.

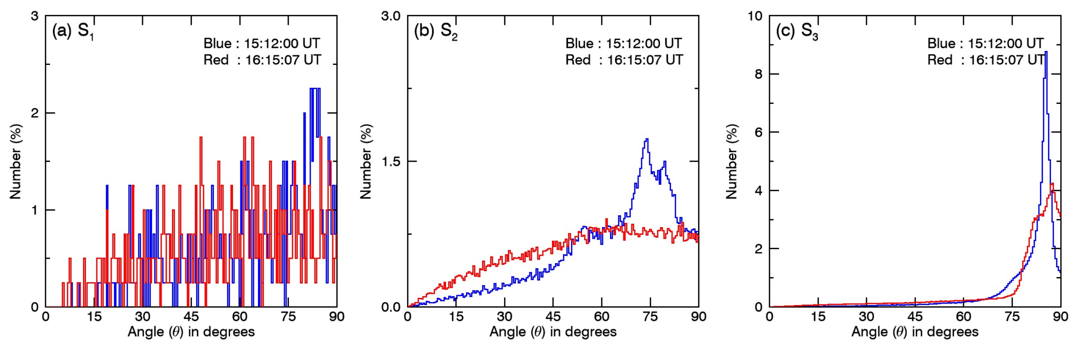

Figure 7.20: Distribution of angles between current density (**J**) and magnetic field vectors (**B**) in sub-volumes S_1, S_2, and S_3 at the beginning (*blue*) and end (*red*) of simulation.

Panels (a) and (b) for sub-volumes S_1 and S_2 reveal wide distributions of θ that extend over the entire range of angles for both the time instants. On the other hand, panel (c) for S_3 shows comparatively narrow distributions peaking around 90°. This is presumably because of the fact that S_3 spans the full vertical extent of the computational box and the variation of θ along height in non-force-free extrapolation model exhibits an increasing trend up to 90°, as exemplified in the previous chapter (see figure 6.4). Due to small size of S_1 and hence limited number of voxels, any trend in the variation of θ with time could not be identified except that the distribution is wide, which does not support the presence of field aligned current in terminal state. However, careful comparison of the *blue* and *red* profiles in panels (b) and (c) suggests that during simulation, fraction of voxels with $\theta \geq 60°$ in S_2 and S_3 decrease, which is estimated to be 20% and 24%, respectively. This suggests that the magnetic configuration tends to relax toward a force-free state. However, in the present simulation, neither the wide distribution in S_2 nor the narrow distribution centered around $\theta = 90°$ in S_3 support a strictly field aligned current density. Therefore, the terminal state of the simulation remains in non-equilibrium, suggesting that further magnetic relaxation is possible. To check this, another simulation whose time duration is twice than that of the original one is carried out. It is then found that when integrated over the whole computational domain, the grid averaged angle drops by 5.7° (64.32° to 58.62°) as compared to 4.3° (64.32° to 60.01°) in the original simulation, validating the possibility of further relaxation. Furthermore, since the distribution of the scalar function α distinguishes between the nonlinear and linear force-free states, the time evolution of the twist parameter (Γ) for each of the sub-volumes is investigated, as shown in figure 7.21. The *red* and the *blue* colors represent the negative and positive values of Γ. It is found that at the initial time instant, the distribution is dominated by positive Γ for each sub-volume, as shown in panels (a),(c), and (e). As the simulation progresses, negative Γ begins to increase and terminal state consists of both positively and negatively signed values, implying that a linear force-free state is not attained. Another noteworthy aspect is the progressively increasing intermixing of the *blue* and *red* colors, exhibiting gradual fragmentation into smaller structures, as evident from panels (d) and (f). Such fragmentation is indicative of development of turbulence (e.g. Pontin et al., 2011, also see Veltri et al., 2009) but since, a quantitative investigation regarding the extent of developed turbulence is presently beyond the scope of this work, it is difficult to comment on this aspect further.

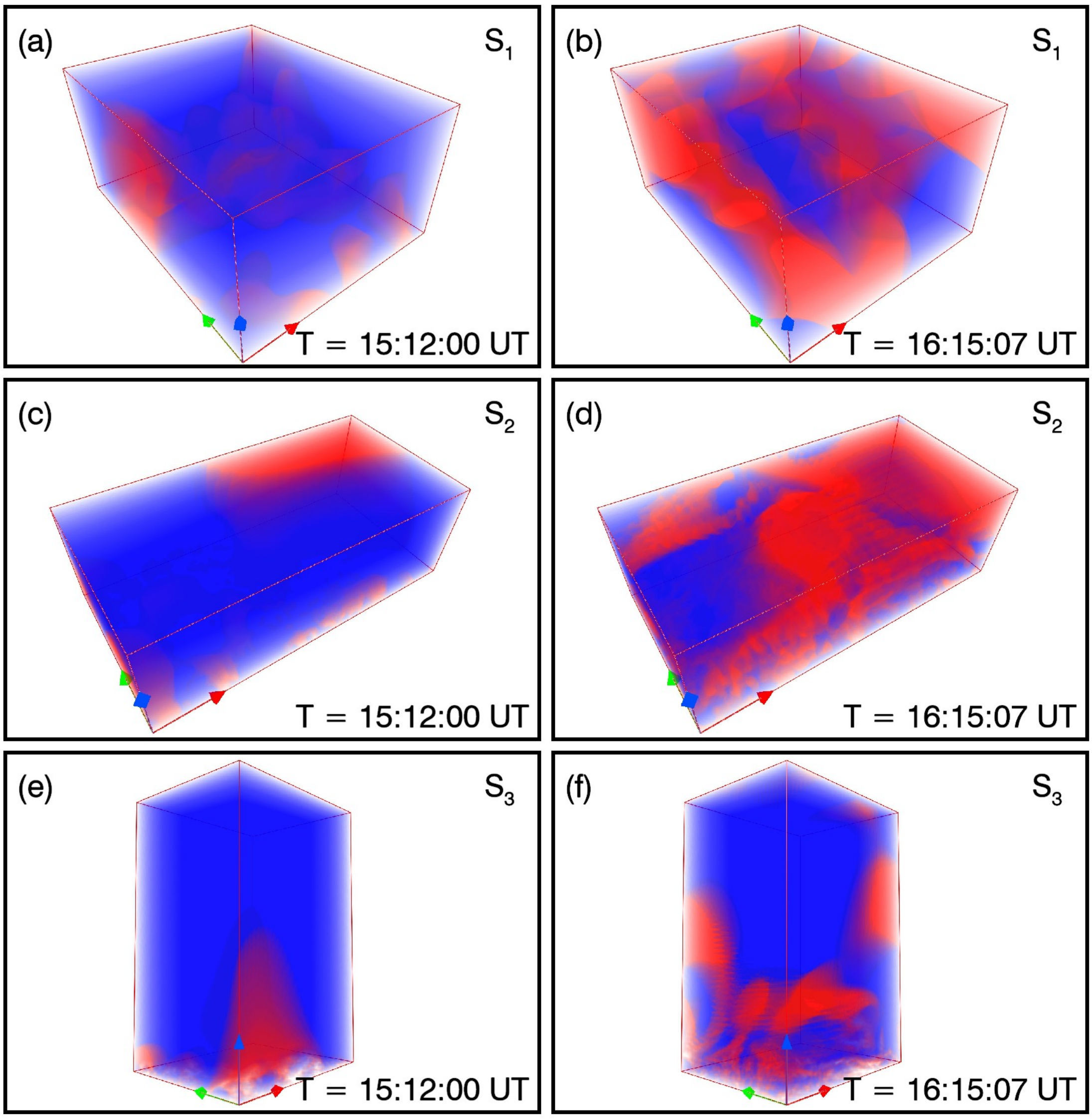

Figure 7.21: Direct Volume Rendering (DVR) of the twist parameter (Γ) for sub-volumes S_1, S_2, and S_3 at the initial and terminal state of numerical simulation. The *blue* and *red* colors represent positive and negative values of Γ.

7.6 Summary

The chapter explores magnetofluid dynamics, energetics at local and global scales, and extent of magnetic relaxation in data-based MHD simulation of a solar flare. In particular, the study investigates changes in connectivity of field lines, evolution of magnetic energy, and angular alignment between $\mathbf{J}$ and $\mathbf{B}$. The observations of flare reveal the associated brightening (marked $\mathrm{B_1}$ and $\mathrm{B_2}$), chromospheric flare ribbons, and a dome-shaped structure. The extrapolated non-force-free field at 15:12 UT identifies a HFT, which is envisaged to be the primary reconnection site because of its spatial correlation with the brightenings. Toward understanding the implications of reconnection on the magnetofluid dynamics, temporal evolution of the grid-averaged magnetic energy ($\mathrm{W_{av}^V}$), current density ($|\mathbf{J}|_{\mathrm{av}}^{\mathrm{V}}$), twist parameter ($|\Gamma|_{\mathrm{av}}^{\mathrm{V}}$), and gradients in the magnetic field ($(|\mathbf{J}|/|\mathbf{B}|)_{\mathrm{av}}^{\mathrm{V}}$) is considered.

At the global scale (referring to the full computational domain), $\mathrm{W_{av}^V}$, $|\Gamma|_{\mathrm{av}}^{\mathrm{V}}$, and $(|\mathbf{J}|/|\mathbf{B}|)_{\mathrm{av}}^{\mathrm{V}}$ decrease with time, indicating simplification of the field line complexity and occurrence of magnetic relaxation. For a detailed analysis, three sub-volumes of interest are identified within the computational domain, namely $\mathrm{S_1}$, $\mathrm{S_2}$, and $\mathrm{S_3}$. These sub-volumes are interpreted in the context of local scales because their size is relatively smaller as compared to the computational box. $\mathrm{S_1}$ is centered on the X-region of the HFT, $\mathrm{S_2}$ encloses the HFT configuration, and $\mathrm{S_3}$ covers the full spatial extent of observed flaring region. To investigate the dynamics, the simulation time is partitioned into five phases, labeled by $\mathrm{P_1^{(i)}}$, $\mathrm{P_2^{(i)}}$, and $\mathrm{P_3^{(i)}}$ (where $\mathrm{i} = 1, 2, ..., 5$) for each sub-volumes.

In all the sub-volumes, final values of $|\Gamma|_{\mathrm{av}}^{\mathrm{V}}$ and $(|\mathbf{J}|/|\mathbf{B}|)_{\mathrm{av}}^{\mathrm{V}}$ are smaller than their initial values, indicating a reduction in both twist and field gradient, which is consistent with the scenario of relaxation. Further, common to all sub-volumes, a sudden drop in $|\mathbf{J}|_{\mathrm{av}}^{\mathrm{V}}$ during the initial phase is governed prominently by layers adjacent to the bottom boundary, indicating a possible boundary condition effect. Importantly, while the magnetic energy decreases monotonically at global scale, the same is not true for sub-volumes. Since, lowering of magnetic energy is a prime signature of relaxation, investigation of energetics at the local scales is necessary. For this purpose, numerical dissipation is approximated by $|\mathbf{D}|$ (equation 7.6) and the Poynting flux is estimated using the ideal contribution of electric field (equation 7.7). Subsequently, their properties are explored in each sub-volume.

The largest values of $|\mathbf{D}|$ are found to be localized at $\mathrm{S_1}$, particularly coinciding with the X-region of HFT, which is harmonious with the spirit of ILES. Further, the magnetic energy evolution in $\mathrm{S_1}$ is in conformity with physical expectations, apart from the phase $P_1^{(2)}$ and briefly in $P_1^{(3)}$. The disagreement could be due to a failure of idealized Ohm's law, implying that the induction equation in its ideal limit is not satisfied. Similar analyses have been carried out to explore energy variations in S_2 and S_3 also. In S_2, the energy influx along with increase in twist from phase $P_2^{(3)}$ onward overwhelms dissipation, thus resulting in the observed energy increase from $P_2^{(3)}$ to $P_2^{(5)}$. The decrease in magnetic energy in S_3 is found to be due to non-ideal effects primarily localized in S_1. Therefore, to numerically realize the observed release of magnetic energy during transients and hence magnetic relaxation, the size of the chosen relaxation volume needs to be large enough such that the energy transfer due to Poynting flux is small.

In order to estimate the extent of relaxation, the angle (θ) between $\mathbf{J}$ and $\mathbf{B}$ at every voxel is calculated. When integrated over the whole computational domain, the grid averaged angle drops by 4.3°, implying that the magnetic configuration tends to relax toward a force-free state. Furthermore, the changes in θ distribution over the course of simulation are not very clear for S_1 due to its small size. In S_2 and S_3, the peak of θ distribution becomes smaller, as realized from the decrease in fraction of voxels having $\theta \geq 60°$. The decrease in higher values of θ indicates increase in alignment between current density and magnetic field.

In tandem, the above results indicate an ongoing magnetic relaxation and also reveal the importance of understanding the magnetofluid dynamics at both the local and global scales. The temporal evolution of the θ distribution between $\mathbf{J}$ and $\mathbf{B}$ suggests that although there is magnetic relaxation, but it is not enough to reach a force-free state. The terminal state of the simulation remains in non-equilibrium, suggesting the possibility for further relaxation. To further contemplate, magnetic reconnection being localized in the flaring regions, the redistribution of helicity might be restricted only to the nearby surroundings. Under such circumstances, invariance of helicity is non-trivial and a complete field alignment of current density may not be achieved. Overall, the simulation suggests that a solar flare induced magnetic relaxation is not complete and in this regard, an exploration of magnetic relaxation in energetically different flares merits attention, which forms the subject matter of the next chapter.

Chapter 8

Study on the Extent of Magnetic Relaxation

8.1 Introduction

In the previous two chapters, the study of relaxation using data-based simulations of solar flares has revealed some interesting results. In particular, chapter 6 shows that the aspects pertaining to reconnection such as changes in the connectivity of field lines, amount of the dissipated free magnetic energy, and the spontaneous generation of complex coherent structures at small-scales (e.g. null point topology) are nearly independent of the initial conditions. Subsequently, in chapter 7, the detailed investigation of the magnetofluid dynamics at both local and global scales demonstrates that the evolution of magnetic energy and other related quantities like current density, twist, and gradients in magnetic field depend on the size of volume chosen for studying magnetic relaxation. Importantly, the increase in angular alignment between the current density and magnetic field indicates that in presence of magnetic reconnections, the magnetic configuration tends to relax toward a force-free state but the relaxation is not complete. As a result, this opens up the possibility for further research in this direction, particularly an exploration of magnetic relaxation in energetically different flares. It also homogenizes the difference in selection of flare class for studying magnetic relaxation. This chapter presents the results of such an investigation, where data-based MHD simulations of three flares are analyzed and compared. In the next section, details of the chosen solar flares are discussed.

8.2 The Selected Solar Flares

In this study, three energetically different flares are selected, identified as B6.4, C4.0, and M1.1 flares in the GOES classification scheme. The details of the flares are summarized in table 8.1. Notably, the peak soft X-ray intensities of flares differ

GOES flare class	Date	Active Region	Start Time (GOES)	Peak Time (GOES)	End Time (GOES)
B6.4	30/04/14	12047	13:36	13:39	13:41
C4.0	12/12/14	12234	14:35	14:40	14:42
M1.1	12/06/14	12089	19:56	20:03	20:05

Table 8.1: Details of the flares describing GOES class, date of the flare, active region, start, peak, and end time of flares as recorded by the GOES satellite

by an order of magnitude, making them energetically different. The observations of flares in the extreme ultraviolet (EUV: 94, 131, 304 Å) and UV (1600 Å) channels of the AIA reveal the spatio-temporal evolution of flares and intensity of emission in each of the wavelengths. Panels (a)-(c) in figure 8.1 plot the AIA light curves

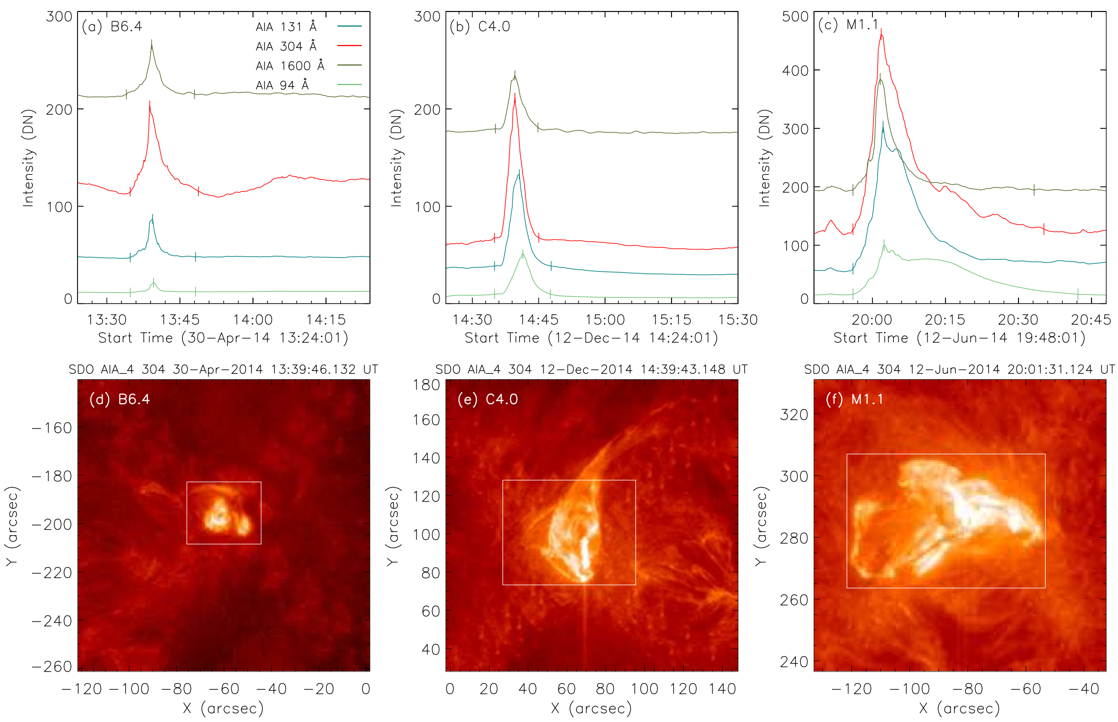

Figure 8.1: Panels (a)-(c): Light curves for each flare in 94, 131, 304 , and 1600 Å wavelength channels of SDO/AIA. The vertical bars in each panel denote the rise, peak, and end time of intensity enhancement for each of the wavelengths. Panels (d)-(f) depict the observations of flare morphology in 304 Å for the GOES B6.4, C4.0, and M1.1 flares. The *white* boxes delineate the extent of observed brightenings.

(time variation of intensity) in data number (DN) units. The rise, peak, and end time of intensity enhancement for each of the wavelengths are marked by vertical bars in each panel. In each flare, the maximum emission is found to occur in the 304 Å channel. Consequently, panels (d)-(f) show a magnified view of the flare morphologies near their peak time in 304 Å. The intensity of emission across the chosen wavelength channels are compared with respect to the B6.4 flare by defining the ratio $R = I/I_0$, where I represents intensity of emission integrated over the flare duration for the C4.0 and M1.1 flares, while I_0 corresponds to the B6.4 flare. The values of R are given in table 8.2, which indicate that the emissions are in accordance with expectation, being maximum for the M1.1 flare and minimum for the B6.4 flare.

GOES	$R = I/I_0$			
flare class	94 Å	131 Å	304 Å	1600 Å
C4.0	5.98	3.32	1.40	1.26
M1.1	49.45	23.71	9.39	6.67

Table 8.2: The values of ratio R comparing the intensity of emission in flares across the chosen wavelengths with respect to the B6.4 flare

8.3 Details of Magnetic Field Extrapolations

To identify the magnetic configurations where reconnection occurs in each of these flares, NFFF extrapolation model is used. The photospheric vector magnetograms from hmi.sharp_cea_720s data series of HMI are used as the bottom boundary. An overlay of extrapolated magnetic field lines over flare brightenings observed in the 304 Å channel identifies magnetic null points (detected using trilinear method) for the B6.4 and C4.0 flares, and a HFT for the M1.1 flare as primary reconnection morphologies. Figure 8.2 depicts this cospatiality of the magnetic field lines with the region of observed brightenings. The time and computational box size for the carried out extrapolations are summarized in table 8.3. Further, the precise spatial location of null points and approximate position of the X-region in HFT are also mentioned along with the corresponding magnetic field strength. Importantly, the energy released during flares is some fraction of the available free magnetic energy ($W_{\rm m}^{\rm free}$), estimated as $W_{\rm m}^{\rm free} = W_{\rm m}^{\rm NFFF} - W_{\rm m}^{\rm pot.}$, where $W_{\rm m}^{\rm NFFF}$ and $W_{\rm m}^{\rm pot.}$ denote

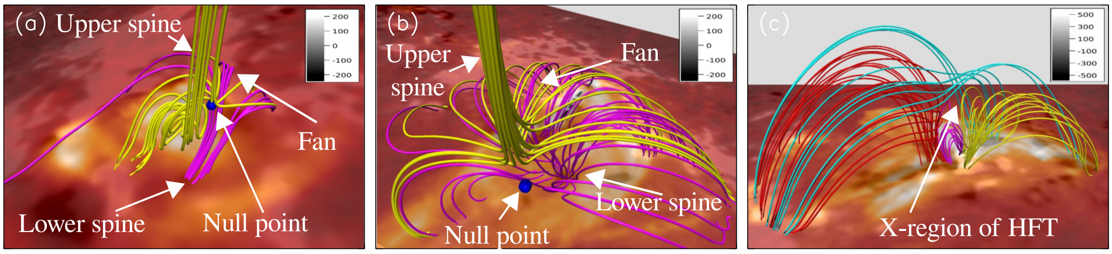

Figure 8.2: Panels (a) and (b) delineate the magnetic null point topology constituted by the fan (*pink*) surfaces and spines (*yellow*) in B6.4 and C4.0 flares. Panel (c) depicts the HFT in M1.1 flare, where the four quasi-connectivity domains are shown in *pink*, *yellow*, *red*, and *cyan* colors. The bottom boundary in each panel is overlaid with the SDO/AIA observation near peak time of flares and the vertical magnetic field along with its corresponding color bar at the time of extrapolation.

the volume integrated magnetic energies of the extrapolated NFFF and potential magnetic field, respectively. The last column of table 8.3 lists the available $W_{\mathrm{m}}^{\mathrm{free}}$ for each case, suggesting that the extrapolated magnetic fields for B6.4 and M1.1 flares correspond to maximum and minimum free magnetic energy. Notably, the amount of available $W_{\mathrm{m}}^{\mathrm{free}}$ does not correlate directly with the amount of released energy in a transient.

GOES flare	Time	Dimensions (voxel units)	x	y	z	$\lvert\mathbf{B}\rvert$ (Gauss)	$W_{\mathrm{m}}^{\mathrm{free}}$ (erg)
B6.4	13:24	$400 \times 250 \times 250$	274	185	9	0.00088	5.1×10^{31}
C4.0	14:24	$608 \times 196 \times 196$	198	183	28	0.00021	3.3×10^{31}
M1.1	19:48	$400 \times 200 \times 200$	188	118	25	20	2.0×10^{31}

Table 8.3: Set-up for magnetic field extrapolations, position (voxel units) of the detected magnetic nulls in B6.4 and C4.0 flares and of the X-region in HFT along with the corresponding magnetic field strength, and total free magnetic energy.

8.4 The MHD Simulations and their Analysis

The EULAG-MHD model is employed for the simulation, where $B_0 = 2000$ Gauss, $R_F^A = 5000$, $V_A = 0.2\,\mathrm{Mm/s}$, and simulation time step $\Delta t = 10^{-3}$ are kept same for all simulations. The total simulation time is chosen such that it encompasses the time interval between the time of extrapolated magnetic field and the end time of flare. These are approximately equal to 17 m, 18 m, and 17 m (m $\equiv$ minutes) for the B6.4, C4.0, and M1.1 flares. Consequently, the simulation times are 2.6 τ_A, 3.4 τ_A, and 3.3 τ_A, being nearly equal to 19.63 m, 20.13 m, and 19.94 m in physical units. The simulations are carried out at the resolution of HMI data and are initiated from a motionless state (zero plasma velocity), where the Lorentz force resulting from the NFFF extrapolation model drives the dynamics. In the previous two chapters, open boundary condition was used along all the directions, which is presumably standard for open systems like the solar corona. However, realizing that broadly, the solar magnetic field decays significantly along the vertical direction only and that the primary reconnection sites are usually situated away from the lateral boundaries, the use of periodic boundary conditions is considered to be a viable option. Consequently, the lateral boundaries are kept periodic while the top and bottom boundaries are treated as open in the present study. Notably, the simulation set-up (defined by $B_0, R_F^A, \Delta t$) is kept identical across all simulations to ensure that magnetic relaxation in each case is determined solely by flare energetic and is not affected by possible numerical effects such as grid resolution and the rate of simulated magnetofluid evolution.

The investigation of the magnetofluid dynamics in each simulation reveals that the magnetic field lines (MFLs) constituting the primary reconnection morphology undergo a sudden change in connectivity, and hence reconnection. As an example, the snapshots in panels (a)-(c) of figure 8.3 illustrate the MFLs undergoing slipping reconnection in the null point topology, which accounts for part of the brightening observed during the spatio-temporal evolution of the GOES B6.4 flare in 304 Å channel. For clear presentation, a magnetic field line is isolated in the fan surface of null point topology with *black* color. A comparison of its footpoint position in panels (a) and (c) reveals that the movement of the footpoint is not in the direction of plasma flow (shown by *white* arrows), implying slipping reconnection. Further, this result is augmented by estimating the squashing degree, which is standardly used to investigate slipping reconnection in QSLs. Its plot as $\ln Q$ at the bottom boundary reveals the footpoint movement to be localized within the well-defined strip having $\ln Q \leq 1.5$, which provides additional support to the interpretation. Importantly, magnetic reconnection is expected to dissipate the magnetic energy and relax the magnetofluid. Therefore, an estimation of this dissipated energy is carried out to compare the extent of relaxation across the three simulations. For this purpose, equation 3.92 is used to write the rate of change in magnetic energy (in usual notations) as,

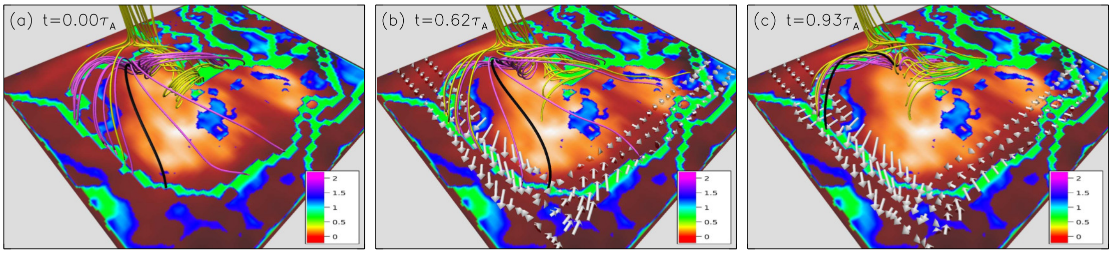

Figure 8.3: Panels (a)-(c): Snapshots from the simulated dynamics of GOES B6.4 flare at $0, 0.63\,\tau_A$, and $0.93\,\tau_A$. The *black* color field line in the fan surface of null illustrates slipping reconnection, *white* arrows depict the direction of plasma flow. The bottom boundary shows observation of flare brightening at 13:39:46 UT in 304 Å channel and map of $\ln Q$ along with its color table.

$$\frac{\mathrm{d}W_{\mathrm{m}}}{\mathrm{d}t} = -\int_V \mathbf{v}\cdot(\mathbf{j}\times\mathbf{B})\,\mathrm{d}^3x + \frac{1}{\mu_0}\int_S (\mathbf{v}\times\mathbf{B})\times\mathbf{B}\cdot\hat{\mathbf{n}}\,\mathrm{d}^2x + \frac{1}{\mu_0}\int_V \mathbf{B}\cdot\mathbf{D_B}\,\mathrm{d}^3x \ , \tag{8.1}$$

where the first term represents the work done by the Lorentz force on magnetofluid, second term denotes the ideal contribution of the Poynting flux, and the third term corresponds to the numerical dissipation. To simplify the notations, hereafter the combination of first two terms is written as $\mathrm{d}W_{\mathrm{m}}^I/\mathrm{d}t$ and the third term is written as $\mathrm{d}W_{\mathrm{m}}^D/\mathrm{d}t$, where I and D refer to "ideal" and "dissipation", respectively. The computation of W_{m}^D for each simulation is carried out in three different volumes of integration to avoid any selection bias. The volumes are denoted by $V_{i\mathrm{X}}$, where $i = 1, 2, 3$ and $\mathrm{X} = \mathrm{B}, \mathrm{C}, \mathrm{M}$ for the B6.4, C4.0, and M1.1 solar flares. The chosen volumes enclose the reconnection morphologies symmetrically along the transverse ($xy-$plane) direction as exemplified in panel (a) of figure 8.4 for the null point topology in B6.4 flare. For a meaningful comparison, the size of volumes (for any i in $V_{i\mathrm{B}}$, $V_{i\mathrm{C}}$, $V_{i\mathrm{M}}$) is kept nearly identical.

The estimation of W_{m}^D averaged over all the integration volumes reveals that the fraction of dissipated free magnetic energy is approximately $7\%, 16.8\%$, and 33% for the B6.4, C4.0, and M1.0 flares, indicating that the magnetic configuration in the end of simulations remains substantially non-potential. Contextually, panel (b) of Fig. 8.4 depicts a null point topology (*red* and *yellow* MFLs), detected at

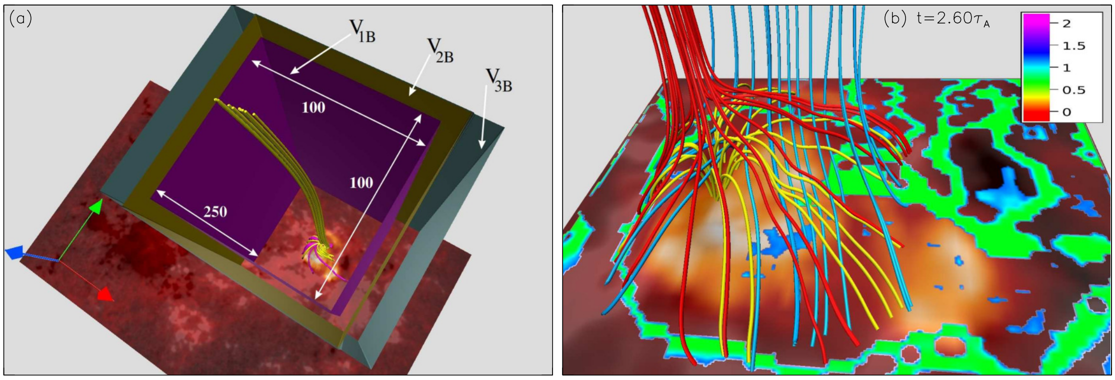

Figure 8.4: Panel (a): $V_{i\mathrm{B}}$ for $i = 1, 2, 3$, where *red*, *green*, and *blue* arrows depict x, y, and $z-$direction. Panel (b): The *red* and *yellow* MFLs constitute a null point topology at $t = 2.6\tau_A$ in simulation for B6.4 flare. The *blue* MFLs correspond to extrapolated potential field at the same time.

the end time of simulation ($t = 2.6\tau_A$) for B6.4 flare. However, in the extrapolated potential field (*blue* MFLs) at the same time, no such null point is found, implying a topological difference. Figure 8.5 plots W^I_{m} (*solid line*) and W_{m} (*dashed line*), while table 8.4 summarizes the net W^D_{m} in each simulation. Notably W_{m} is always less than W^I_{m}, which is to be expected as reconnection dissipates the magnetic energy as heat, which is lost irrecoverably from the system. Further, in all volumes,

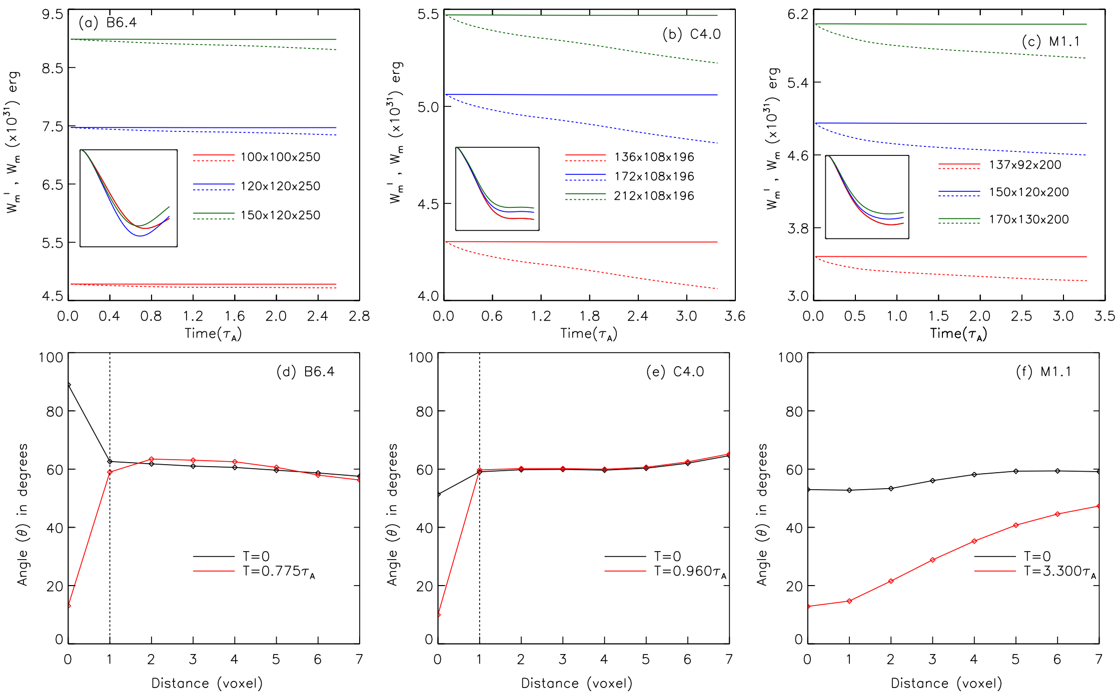

Figure 8.5: Panels (a)-(c): The temporal evolution of W^I_{m} (*solid line*) and W_{m} (*dashed line*) for different volumes of integration ($V_{i\mathrm{X}}$) in simulation of GOES B6.4, C4.0, and M1.1 flares. The sub-panels show a magnified view of W^I_{m} to illustrate the qualitative changes in its profile. Panels (d)-(f): The variation of θ as a function of distance from the location of reconnection site.

$W_{\rm m}^D$ is minimum for $V_{i\rm B}$, followed by $V_{i\rm C}$ and $V_{i\rm M}$, indicating that the results are in agreement with the expectation that GOES B6.4 flare will dissipate minimum magnetic energy, followed by the GOES C4.0 and M1.1 flares. Importantly, $W_{\rm m}^D$ is two orders less when calculated in a volume devoid of any reconnection site, adding credibility to the ILES nature of simulation.

Size	ΔW	Size	ΔW
$V_{1\rm B}: 100 \times 100 \times 250$	0.645	$V_{2\rm B}: 120 \times 120 \times 250$	1.25
$V_{3\rm B}: 150 \times 120 \times 250$	1.77		
$V_{1\rm C}: 136 \times 108 \times 196$	2.40	$V_{2\rm C}: 172 \times 108 \times 196$	2.48
$V_{3\rm C}: 212 \times 108 \times 196$	2.46		
$V_{1\rm M}: 137 \times 92 \times 200$	2.63	$V_{2\rm M}: 150 \times 120 \times 200$	3.47
$V_{3\rm M}: 170 \times 130 \times 200$	3.73		

Table 8.4: Size of the chosen volumes of integration ($V_{i\rm X}$) and the corresponding net $W_{\rm m}^D$ (in units of 10^{30} erg) in each simulation.

Further exploration of the magnetic relaxation focuses on the angular alignment between **J** and **B** at the reconnection site itself rather than the full computational box as in previous chapters. The rationale for this approach is that reconnection being localized, a global impact on the angular alignment is improbable. In this regard, the variation of θ as a function of distance from the non-ideal region (i.e. null point/X-region of HFT) is quantified. For this purpose, seven (the number is restricted by the height of null point in the B6.4 flare) symmetric cubical shells are envisaged about the reconnection sites such that the dimension of $(i+1)^{th}$ shell is larger than the i^{th} shell by exactly two voxels along each of the directions in Cartesian geometry. Subsequently, θ is averaged over each shell and with θ at the reconnection site, figure 8.5 plots the variation of θ with distance at the beginning of simulation (*black*) and at the time instant (*red*) which amounts to maximum alignment. The decrease in θ at the reconnection site is found to be 75.92°, 41.37°, and 40.13° in simulations of the B6.4, C4.0, and M1.1 flares. The decrease implies an increase in the alignment, which suggests a localized occurrence of the magnetic relaxation. Notably, except in the case of M1.1 flare, θ is approximately constant with distance, which is presumably due to the extended X-region of HFT not being as localized as a null point.

In addition to the investigation of relaxation in the MHD simulations, another interesting result is obtained from the analysis of magnetic configurations which constitute the primary reconnection morphologies With $A = \mathrm{N}_x \times \mathrm{N}_y$ being the transverse (xy-plane) extent (corresponds to the *white* boxes shown in panels (d)-(f) of figure 8.1) of the reconnection sites in voxel units, H being the height of null points/X-region of HFT in voxel units, and ($|\mathbf{B}|$) representing the magnetic field strength in near neighborhood of the reconnection site, a quantity $R_{\mathrm{X}} = A \times H \times |\mathbf{B}|$ is constructed, where X has the same connotation as in $V_{i\mathrm{X}}$. Then, the ratios $R_{\mathrm{C}}/R_{\mathrm{B}} = 5.28$ and $R_{\mathrm{M}}/R_{\mathrm{B}} = 20.26$ are found to be in close agreement with the ratio of measured GOES soft X-ray intensities at peak time of flares, denoted and given by $I_{\mathrm{C}}/I_{\mathrm{B}} = 6.25$ and $I_{\mathrm{M}}/I_{\mathrm{B}} = 17.18$. The calculations pertaining to this analysis are summarized in table 8.5. While this agreement could be coincidental

	N_x	N_y	A	H	$\lvert\mathbf{B}\rvert$	R_{X}
B6.4	64	54	3456	9	10	311040
C4.0	136	108	14688	28	4	1645056
M1.1	137	92	12604	25	20	6302000

Table 8.5: Details of $R_{\mathrm{X}} = A \times H \times |\mathbf{B}|$ estimation

and the exact values of $R_{\mathrm{C}}/R_{\mathrm{B}}$ or $R_{\mathrm{M}}/R_{\mathrm{B}}$ may depend on a precise estimation of A and $|\mathbf{B}|$, it nevertheless suggests that R_{X} may have the utility of being an indicator in predicting the GOES class of solar flares.

8.5 Summary

The chapter explores magnetic relaxation using data-based MHD simulations of three energetically different flares, identified as B6.4, C4.0, and M1.1 in the GOES scheme. An observational analysis of the solar flares in $94, 131, 304$, and $1600\,\text{Å}$ channels of SDO/AIA reveals the spatio-temporal evolution of flares. The intensity of emission in each wavelength agrees with the expectation that the total amount of released energy should be maximum for the M1.1 flare and minimum for the B6.4 flare. A non-force-free field extrapolation of the photospheric magnetic field identifies magnetic null point topologies as the primary reconnection sites overlying the observed brightenings in B6.4 and C4.0 flares. Similarly, a hyperbolic flux tube (HFT) is found for M1.1 flare. The magnetofluid dynamics exhibits reconnection in the spirit of ILES at the identified reconnection sites. Toward investigating the extent of magnetic relaxation, it is found that approximately $7\%, 16.8\%$, and 33%

of the available free magnetic energy is dissipated because of numerical dissipation in the simulation of B6.4, C4.0, and M1.1 flares. Therefore, from the perspective of decrease in the magnetic energy due to reconnection, the extent of magnetic relaxation is maximum for the M1.1 flare and minimum for the B6.4 flare. However, although the increase in angular alignment between current density and magnetic field at the reconnection site indicates a localized magnetic relaxation in each case, an interpretation of this result in the context of relaxation extent across the chosen energetically different flares is found to be non-trivial. A part of the reasoning for this is that maximum alignment occurs for the B6.4 flare and minimum for the M1.1 flare, which seems counter-intuitive. Further, since this result is based on a study of only three flares, it is not appropriate to stretch its scope for concluding anything significant regarding extent of magnetic relaxation. The preceding note winds up the works carried out in this thesis toward exploring relaxation in solar transients. The next chapter summarizes this thesis and outlines a few prospects for further investigations in the future.

Chapter 9

Thesis Summary and Future Prospects

9.1 Summary

Solar eruptive events like flares and Coronal Mass Ejections (CMEs) are believed to be the manifestations of magnetic reconnection—a fundamental process known to occur in both naturally occurring and laboratory plasmas. Broadly, the importance of studying these events emerges in the context of their possible harmful impact on space-based and ground-based technologies. However, in this thesis, the scientific curiosity is motivated from the fundamental perspective of self-organization in magnetized plasmas, also known as plasma relaxation.

Relevantly, during eruptive events, a large amount of energy gets released by the process of reconnection, which converts magnetic energy into heat, bulk kinetic energy of the plasma, and particle acceleration. The decrease in magnetic energy is expected to relax the overall magnetic field configuration to a state having lesser magnetic energy. Consequently, it is realized that this state of lesser energy can be viewed in association with the relaxed states obtained theoretically using principles of self-organization. In particular, the thesis focuses on magnetically relaxed states that are obtained by a constrained minimization of magnetic energy while keeping magnetic helicity as an invariant. Specifically, the relevant relaxed states are the Woltjer and Taylor states, which are also known as force-free states because of the field aligned current density giving zero Lorentz force.

Importantly, previous studies exploring relaxation for the case of solar plasma have been based on either observations or numerical experiments employing simple analytical magnetic fields as an initial condition. In this context, examples of MHD simulations exploring the formation and evolution of magnetic flux ropes in a 3D bipolar sheared arcade and a quadrupolar magnetic geometry are presented. The simulations exemplify the changes in connectivity of magnetic field lines because of reconnection, which leads to the flux rope formation. Further, the simulations exhibit decreasing magnetic energy and the magnetic configurations tend to evolve toward a force-free state, both of which are are realized to be the signatures of a magnetic relaxation process. However, to account for the field complexity of an actual active region, data-based simulations in combination with an analysis of observations are required to explore the implications of reconnection in eruptive events and its consequences on relaxation of the magnetofluid.

The thesis work focuses on MHD simulations of flares in which, an extrapolated magnetic field is employed as an initial condition. The photospheric magnetogram data from SDO/HMI are used for magnetic field extrapolations. The extrapolated magnetic field is analyzed in combination with the observations from SDO/AIA to identify the magnetic configurations where reconnection might occur, such as magnetic null point, quasi-separatrix layer (QSL), and hyperbolic flux tube (HFT). Further, the simulated dynamics is compared with the observed spatio-temporal evolution of flares to add further credibility. Such data-based MHD simulations are carried out in this thesis using the EULAG-MHD numerical model.

Noticeably, the need to model the solar magnetic field accurately has led to the development of various extrapolation models. Consequently, it is important to investigate their effect on the simulated dynamics of a solar transient. Since, the reconnection process is dissipative, it is expected that the changes in connectivity of field lines and the dissipated magnetic energy might be relatively insensitive to the initial conditions. Further, such an expectation also aligns with the fact that relaxed states are nearly independent of the system's initial configuration. Toward such an exploration, data-based MHD simulations of a GOES C6.6 flare in active region NOAA 11977 are carried out using three different conditions, where an initial condition is constituted by a pair of initial magnetic and velocity fields. The initial magnetic fields are generated using the non-force-free field (NFFF) and nonlinear force-free field (NLFFF) extrapolations. The NFFF initiates simulation S_1, NLFFF is used for S_2, and in S_3, an external flow is provided to the initial

NLFFF, keeping the strength of the perturbation small. The crucial findings of this study are listed below.

1. A quantitative and morphological comparison of the two extrapolated fields reveals that they are nearly similar. Both the models reproduce similar field line structures, although the extent of agreement between the two varies. In particular, a lasso shaped magnetic configuration is identified on the global scale while a magnetic null point configuration and a hyperbolic flux tube (HFT) are found to be cospatial with the observed flare brightening.

2. The analysis of the simulated dynamics reveals that the order of dissipated free magnetic energy is nearly similar (5.5%) across the simulations. Further, the changes in field line connectivity corresponding to the null point and HFT configurations are nearly similar.

3. The study finds spontaneous appearance and disappearance of a 3D magnetic null (referred to as the transient null) near the HFT in all the simulations. Importantly, the field line constituting the fan plane of this null are found to exhibit slipping reconnection, thus contributing to the observed brightening.

4. The study also finds that the evolution of kinetic energy, time instants at which reconnection occurs in the null point and HFT configurations, and the timing of transient null appearance and disappearance vary across the three simulations. This is presumably due to a dependence on the strength of the initial Lorentz force and plasma flow that drive the dynamics.

Overall, the near similarity of changes in the dissipated magnetic energy, changes in the field line connectivity, and spontaneous appearance and disappearance of the transient null across the simulations suggest near independence with respect to the initial conditions. Therefore, both NFFF and NLFFF extrapolations can be used as valid initial conditions for data-based simulations. Further, it is concluded that the simulations exhibit signatures of a self-organization process, which further motivates an investigation of the magnetofluid dynamics and magnetic relaxation in eruptive events. For this purpose, a data-based simulation of a GOES M1.3 flare in active region NOAA 12253 is carried out. The NFFF extrapolation identifies a

HFT overlying the observed flare brightening. Toward understanding the dynamics of magnetofluid, attention is focused on the spatio-temporal evolution of magnetic energy, current density, twist, and magnetic field gradients in the full simulation box as well as in three different sub-volumes inside the box. The sub-volume S_1 is centered on the X-region of HFT, S_2 encloses the HFT morphology, and S_3 covers the complete spatial extent of the observed brightening and full vertical height of the computational box. Notably, the size of S_3 is largest and that of S_1 is smallest. Notably, an approximate estimation of the Poynting flux and numerical diffusion inherent to EULAG-MHD is also carried out to understand their role in governing the dynamics within the sub-volumes. Importantly, due to the unavailability of a suitable methodology for magnetic helicity estimation, its decay rate with that of the magnetic energy could not be compared. Therefore, the consequence of helicity conservation, namely the force-free aspect of the magnetic field is investigated by analyzing the temporal evolution of angular alignment between the magnetic field and current density. The important results of this study are summarized below.

1. The grid-averaged magnetic energy for the full computational box decreases monotonically, which suggests an ongoing magnetic relaxation. In addition, the initial decrease of twist and magnetic field gradient further reinforces the scenario of reconnection assisted relaxation.

2. Similar analysis reveals that the twist and magnetic field gradients exhibit an overall decrement in each sub-volume, which is consistent with the scenario of relaxation. The magnetic energy profile in S_1 and S_2 is primarily governed by the Poynting flux. In regard with S_3, it is found that the largest values of numerical diffusion are localized in S_1, particularly at the X-region of HFT, which is in harmony with the spirit of ILES. Additionally, since the Poynting flux through S_3 is small, it is concluded that the magnetic energy profile in S_3 is governed by non-ideal effects, contributed primarily from S_1 and further augmented by slipping reconnections in S_2.

3. The grid-averaged angle between current density and magnetic field decreases by 4.3° (from 64.32° to 60.01°), which implies an increase in the alignment.

Overall, the simulation exhibits signatures of magnetic relaxation but the relaxation is not enough to reach a force-free state. The terminal state of the simulation remains in non-equilibrium, suggesting the possibility for further relaxation, which also indicates that the extent of a solar flare induced magnetic relaxation may have a dependency on the flare energetics and its duration. Consequently, data-based simulations of three energetically different flares, namely GOES B6.4, C4.0, and M1.1 are explored. The NFFF extrapolation identifies magnetic null points for the B6.4 and C4.0 flares, and a HFT for the M1.1 flare as primary reconnection morphologies. The analysis of these sites and of the simulated dynamics leads to the following important results

1. An estimation of the magnetic energy dissipated due to the non-ideal effects (numerical diffusion in the simulation) amounts to approximately 7%, 16.8%, and 33% of the available free magnetic energy for the B6.4, C4.0, and M1.1 flares. In physical units, it is equivalent to 1.18, 2.45, and 3.33 ($\times 10^{30}$) erg, respectively. Therefore, the result is in concurrence with the general energy relation between the classes of chosen flares.

2. The maximum decrease in the angle between current density and magnetic field at the reconnection site in each case is found to be 75.92°, 41.37°, and 40.13° in simulations of the B6.4, C4.0, and M1.1 flares, implying an increase in alignment, indicating magnetic relaxation. However, this result could not be understood from the perspective of extent of relaxation.

3. An interesting finding of the work is a parameter based on the analysis of reconnection morphologies that may have applications in predicting the strength of solar flares.

The inference of the thesis may be summarized as follows. Solar transients exhibit signatures of a self-organization process and consequently of magnetic relaxation. From the perspective of magnetic energy decrease, the extent of such relaxation is directly proportional to the amount of energy release during transients. However, from the evolution of angular alignment with time, it is inferred that in general, a force-free state is not achieved. The thesis work suggests that in order to further understand the relaxation process in transients, it is imperative to investigate the interconnection between the small-scale and large-scale magnetofluid dynamics.

9.2 Future Prospects

The works carried out in this thesis investigate solar transients from the perspective of self-organization and magnetic relaxation using data-based MHD simulations. For further exploration in this direction, future works will focus on

1. Calculating the relative magnetic helicity (H_R) and its rate of decay, where H_R represents the gauge invariant definition of helicity for open systems (e.g. solar corona) that are open to magnetic flux penetration. Consequently, the dissipation of helicity due to reconnection and the changes due to Poynting flux can be estimated separately. From these calculations, a comparison of the magnetic energy and helicity decay rates can be made, which will help to gain further insights into the dynamics of sub-volumes and to understand magnetic relaxation in solar transients.

2. Exploring the effects of increasing the number of reconnection regions on the extent of magnetic relaxation. For this purpose, MHD simulations using both analytical and extrapolated magnetic fields will be carried out. For the data-based simulations, the focus will be on small-scale reconnection events, such as the recently discovered campfires. The rationale for focusing on such events is their expected ubiquity, which will presumably increase the number of reconnection regions within the simulation box.

The analysis of reconnection morphologies in extrapolated non-force-free fields has identified a quantity (denoted by R_X) in the thesis work that may have application in predicting the strength of solar flares. Since, the parameter may have potential space-weather applications, the work will be extended to

1. Perform a statistical investigation where non-force-free field extrapolations will be carried out for a large sample of flares. The target will be to identify the relevant reconnection morphologies in each case, calculate R_X, and check its validity. If found true, it will be tantalizing to look for the physical cause that explains the qualitative association between the quantity R_X and the amount of energy released during a flare.

Appendix A

The Visualization Tool - VAPOR

A visualization tool plays an important role in extracting meaningful information from the extrapolated magnetic field data. For this purpose, the Visualization and Analysis Platform for Ocean, Atmosphere, and Solar Researchers (VAPOR), has been used in this thesis. It was developed and is maintained by the National Center for Atmospheric Research's (NCAR) Computational and Information Systems Lab. Li et al. (2019) provides a detailed description of the VAPOR package. Here, only those functionalities are discussed that are relevant for the interpretation of results presented in this thesis. There are six different kinds of data visualization methods, also known as renderers in VAPOR. These are the Barb, Direct Volume Rendering (DVR), Flow, Isosurface, Image, and Slice renderers, respectively.

The Barb feature plots arrows, which indicate the direction of vector fields at any given point. The DVR control allows an inspection of three-dimensional scalar variables by a color mapping of its values (Kaufman & Mueller, 2005). An opacity option can be adjusted for transparency, thus revealing the distribution at varying depths inside the volume. The Flow renderer employs a fourth order Runge-Kutta scheme (Press et al., 2007) to integrate equation $d\mathbf{l} \times \mathbf{B} = 0$ for obtaining the magnetic field lines. The field lines can be colored, which helps to distinguish between the different topological domains. The Isosurface option renders a surface of constant value within a region of space. Using Image renderer, it is possible to import the multi-wavelength observations of transients as 2D images, which is very helpful in identifying the spatial association of magnetic structures with the transients. Lastly, the Slice control allows an extraction of 2D data plane from a 3D variable. This is very useful in depicting the distribution of magnetic polarities at the bottom boundary by using the extrapolated vertical magnetic field.

Appendix B

Trilinear Method of Magnetic Null Point Detection

The magnetic field extrapolation procedure in Cartesian geometry produces a 3D data cube for each of the components. In other words, $\mathbf{B}_i = \mathbf{B}_i(\mathrm{N}_1, \mathrm{N}_2, \mathrm{N}_3)$, where $i = x, y$, and z, while $\mathrm{N}_1, \mathrm{N}_2$, and N_3 are the number of voxels along the respective directions. A voxel represents a value on a regular grid in 3D space. In order to trace magnetic field lines, it is crucial to have information about the magnetic field at sub-grid scales, i.e. the scales below that of the voxel. For the purpose, often trilinear interpolation is used. The described null detection algorithm (Haynes & Parnell, 2007) utilizes such interpolation to locate magnetic null points at sub-grid scales.

The first step of the method is reduction, where voxels which cannot have a null point are eliminated. This is accomplished by using the fact that $\mathbf{B}_i = 0$ at a null point for each i and that trilinear interpolation forces the sub-grid scale values to lie within the minimum and maximum of $\mathbf{B}_i$ at corners of cell. Consequently, if any $\mathbf{B}_i$ has same sign at every corner, the voxel is removed from further analysis.

The second step is referred to as analysis, which identifies the intersection of curves represented by $\mathbf{B}_i = \mathbf{B}_j = 0$ and $\mathbf{B}_k \neq 0$ with the boundaries of voxel. The resulting end points on the boundary for each curve must have opposite signs in the third component to ensure the presence of a null point.

In the last step, null points are located precisely by using a 3D Newton-Raphson scheme (Press et al., 2007), as follows

$$\mathbf{r}_{n+1} = \mathbf{r}_n - \frac{\mathbf{B}(\mathbf{r}_n)}{\nabla \mathbf{B}\big|_{\mathbf{r}_n}} \ , \tag{B.1}$$

where $\mathbf{r}_n$ refers to the initial guess, which is taken either at the center or corner of voxel.

Appendix C

Effect of Magnetic Reconnection on the Magnetic Field Gradient

The magnetic field gradient is quantified by $|\mathbf{J}|/|\mathbf{B}|$. Consequently, the temporal evolution of $|\mathbf{J}|/|\mathbf{B}|$ in the presence of magnetic reconnection can be explored using a straightforward time derivative, given by

$$\frac{\partial}{\partial t}\left(\frac{|\mathbf{J}|}{|\mathbf{B}|}\right) = \frac{1}{2}\left[\frac{1}{|\mathbf{J}|^2}\frac{\partial|\mathbf{J}|^2}{\partial t} - \frac{1}{|\mathbf{B}|^2}\frac{\partial|\mathbf{B}|^2}{\partial t}\right] \times \left(\frac{|\mathbf{J}|}{|\mathbf{B}|}\right) \ . \tag{C.1}$$

Since, the interest lies in exploring the effect of reconnection, an isolated system is considered to exclude contributions from the Poynting flux. As a result, equation 1.21 suggests that

$$\frac{\partial|\mathbf{B}|^2}{\partial t} \propto -\eta|\mathbf{J}|^2 - \mathbf{v}\cdot(\mathbf{J}\times\mathbf{B}) \ , \tag{C.2}$$

which implies that equation C.1 can be written as

$$\frac{\partial}{\partial t}\left(\frac{|\mathbf{J}|}{|\mathbf{B}|}\right) \propto \frac{1}{2}\left[\frac{1}{|\mathbf{J}|^2}\frac{\partial|\mathbf{J}|^2}{\partial t} + \eta\frac{|\mathbf{J}|^2}{|\mathbf{B}|^2} + \mathcal{A}\right] \times \left(\frac{|\mathbf{J}|}{|\mathbf{B}|}\right) \ , \tag{C.3}$$

where $\mathcal{A}$ denotes the term arising from $\mathbf{v}\cdot(\mathbf{J}\times\mathbf{B})$. Subsequently, Ampere's law and magnetic induction equation can be used to write

$$\frac{\partial|\mathbf{J}|^2}{\partial t} \propto 2\mathbf{J}\cdot\left(\nabla\times\frac{\partial\mathbf{B}}{\partial t}\right) = -2\eta\mathbf{J}\cdot(\nabla\times\nabla\times\mathbf{J}) + 2\mathbf{J}\cdot\left[\nabla\times\nabla\times(\mathbf{v}\times\mathbf{B})\right] \ , \tag{C.4}$$

which leads to the following equation

$$\frac{\partial}{\partial t}\left(\frac{|\mathbf{J}|}{|\mathbf{B}|}\right) \propto \frac{1}{2}\left[-2\eta\frac{\mathbf{J}\cdot(\nabla\times\nabla\times\mathbf{J})}{|\mathbf{J}|^2} + \eta\frac{|\mathbf{J}|^2}{|\mathbf{B}|^2} + \mathcal{A}\right] \times \left(\frac{|\mathbf{J}|}{|\mathbf{B}|}\right) \ , \tag{C.5}$$

where the second term of equation C.4 is subsumed into $\mathcal{A}$ because the focus is on reconnection, which is due to the resistive term only. Using an order of estimate for the first term, the final equation is

$$\frac{\partial}{\partial t}\left(\frac{|\mathbf{J}|}{|\mathbf{B}|}\right) \propto \frac{1}{2}\left[-2\eta\frac{|\mathbf{J}|^2}{|\mathbf{B}|^2} + \eta\frac{|\mathbf{J}|^2}{|\mathbf{B}|^2} + \mathcal{A}\right] \times \left(\frac{|\mathbf{J}|}{|\mathbf{B}|}\right) , \tag{C.6}$$

which gives the result

$$\frac{\partial}{\partial t}\left(\frac{|\mathbf{J}|}{|\mathbf{B}|}\right) \propto \frac{1}{2}\left[-\eta\frac{|\mathbf{J}|^2}{|\mathbf{B}|^2} + \mathcal{A}\right] \times \left(\frac{|\mathbf{J}|}{|\mathbf{B}|}\right) . \tag{C.7}$$

The negative sign in the first term inside the square brackets serves to show that reconnection leads to decrease in the magnetic field gradient over time.

Bibliography

Alfvén, H., Existence of Electromagnetic-Hydrodynamic Waves, 1942, *Nature*, 150, 405

Alissandrakis, C. E., On the computation of constant alpha force-free magnetic field, 1981, *Astron. Astrophys.*, 100, 197

Altschuler, M. D., & Newkirk, G., Magnetic Fields and the Structure of the Solar Corona. I: Methods of Calculating Coronal Fields, 1969, *Solar Phys.*, 9, 131

Aly, J. J., On some properties of force-free magnetic fields in infinite regions of space, 1984, *Astrophys. J.*, 283, 349

Aly, J. J., On the Reconstruction of the Nonlinear Force-Free Coronal Magnetic Field from Boundary Data, 1989, *Solar Phys.*, 120, 19

Amari, T., Boulmezaoud, T. Z., & Aly, J. J., Well posed reconstruction of the solar coronal magnetic field, 2006, *Astron. Astrophys.*, 446, 691

Amari, T., Canou, A., & Aly, J.-J., Characterizing and predicting the magnetic environment leading to solar eruptions, 2014, *Nature*, 514, 465

Amari, T., & Luciani, J. F., Helicity Redistribution during Relaxation of Astrophysical Plasmas, 2000, *Phys. Rev. Lett.*, 84, 1196

Amari, T., Luciani, J. F., Aly, J. J., Mikic, Z., & Linker, J., Coronal Mass Ejection: Initiation, Magnetic Helicity, and Flux Ropes. I. Boundary Motion-driven Evolution, 2003, *Astrophys. J.*, 585, 1073

Aschwanden, M. J., 2005, Physics of the Solar Corona. An Introduction with Problems and Solutions (2nd edition) (Springer)

Aschwanden, M. J., 2019, New Millennium Solar Physics, Vol. 458

Aulanier, G., 2011, in Physics of Sun and Star Spots, ed. D. Prasad Choudhary & K. G. Strassmeier, Vol. 273, 233

Aulanier, G., Pariat, E., Démoulin, P., & DeVore, C. R., Slip-Running Reconnection in Quasi-Separatrix Layers, 2006, *Solar Phys.*, 238, 347

Aulanier, G., Török, T., Démoulin, P., & DeLuca, E. E., Formation of Torus-Unstable Flux Ropes and Electric Currents in Erupting Sigmoids, 2010, *Astrophys. J.*, 708, 314

Beaudoin, P., Strugarek, A., & Charbonneau, P., Differential Rotation in Solar-like Convective Envelopes: Influence of Overshoot and Magnetism, 2018, *Astrophys. J.*, 859, 61

Benz, A. O., Flare Observations, 2017, Living Reviews in Solar Physics, 14, 2

Berger, M. A., & Field, G. B., The topological properties of magnetic helicity, 1984, Journal of Fluid Mechanics, 147, 133

Berger, M. A., & Prior, C., The writhe of open and closed curves, 2006, Journal of Physics A Mathematical General, 39, 8321

Berghmans, D., et al., Extreme-UV quiet Sun brightenings observed by the Solar Orbiter/EUI, 2021, *Astron. Astrophys.*, 656, L4

Bhattacharjee, A., Ma, Z. W., & Wang, X., 2003, in Turbulence and Magnetic Fields in Astrophysics, ed. E. Falgarone & T. Passot, Vol. 614 351

Bhattacharyya, R., & Janaki, M. S., Dissipative relaxed states in two-fluid plasma with external drive, 2004, Physics of Plasmas, 11, 5615

Bhattacharyya, R., Janaki, M. S., Dasgupta, B., & Zank, G. P., Solar Arcades as Possible Minimum Dissipative Relaxed States, 2007, *Solar Phys.*, 240, 63

Bhattacharyya, R., Low, B. C., & Smolarkiewicz, P. K., On spontaneous formation of current sheets: Untwisted magnetic fields, 2010, Physics of Plasmas, 17, 112901

Bineau, M., On the existence of force-free magnetic fields, 1972, Communications on Pure and Applied Mathematics, 25, 77

Birn, J., Hesse, M., & Schindler, K., Theory of magnetic reconnection in three dimensions, 1997, Advances in Space Research, 19, 1763

Birn, J., & Priest, E. R., 2007, Reconnection of magnetic fields : magnetohydrodynamics and collisionless theory and observations

Bobra, M. G., Sun, X., Hoeksema, J. T., Turmon, M., Liu, Y., Hayashi, K., Barnes, G., & Leka, K. D., The Helioseismic and Magnetic Imager (HMI) Vector Magnetic Field Pipeline: SHARPs - Space-Weather HMI Active Region Patches, 2014, *Solar Phys.*, 289, 3549

Book, D. L., Boris, J. P., & Hain, K., Flux-Corrected Transport. II - Generalizations of the method, 1975, Journal of Computational Physics, 18, 248

Bora, K., Agarwal, S., Kumar, S., & Bhattacharyya, R., Hall effect on the magnetic reconnections during the evolution of a three-dimensional magnetic flux rope, 2023, Physica Scripta, 98, 065016

Bora, K., Bhattacharyya, R., Prasad, A., Joshi, B., & Hu, Q., Comparison of the Hall Magnetohydrodynamics and Magnetohydrodynamics Evolution of a Flaring Solar Active Region, 2022, *Astrophys. J.*, 925, 197

Bora, K., Bhattacharyya, R., & Smolarkiewicz, P. K., Evolution of Three-dimensional Coherent Structures in Hall Magnetohydrodynamics, 2021, *Astrophys. J.*, 906, 102

Boris, J. P., & Book, D. L., Flux-Corrected Transport. I. SHASTA, A Fluid Transport Algorithm That Works, 1973, Journal of Computational Physics, 11, 38

Boris, J. P., & Book, D. L., Flux-Corrected Transport. III. Minimal-Error FCT Algorithms, 1976, Journal of Computational Physics, 20, 397

Borrero, J. M., Tomczyk, S., Kubo, M., Socas-Navarro, H., Schou, J., Couvidat, S., & Bogart, R., VFISV: Very Fast Inversion of the Stokes Vector for the Helioseismic and Magnetic Imager, 2011, *Solar Phys.*, 273, 267

Boulmezaoud, T. Z., & Amari, T., On the existence of non-linear force-free fields in three-dimensional domains, 2000, Zeitschrift Angewandte Mathematik und Physik, 51, 942

Brown, J. C., The Deduction of Energy Spectra of Non-Thermal Electrons in Flares from the Observed Dynamic Spectra of Hard X-Ray Bursts, 1971, *Solar Phys.*, 18, 489

Browning, P., & Lazarian, A., Notes on Magnetohydrodynamics of Magnetic Reconnection in Turbulent Media, 2013, *Space Sci. Rev.*, 178, 325

Browning, P. K., Helicity injection and relaxation in a solar-coronal magnetic loop with a free surface, 1988, Journal of Plasma Physics, 40, 263

Browning, P. K., Gerrard, C., Hood, A. W., Kevis, R., & van der Linden, R. A. M., Heating the corona by nanoflares: simulations of energy release triggered by a kink instability, 2008, *Astron. Astrophys.*, 485, 837

Büchner, J., Three-Dimensional Magnetic Reconnection in Astrophysical Plasmas - Kinetic Approach, 1999, *Astrophys. Space Sci.*, 264, 25

Calabretta, M. R., & Greisen, E. W., Representations of celestial coordinates in FITS, 2002, *Astron. Astrophys.*, 395, 1077

Carcedo, L., Brown, D. S., Hood, A. W., Neukirch, T., & Wiegelmann, T., A Quantitative Method to Optimise Magnetic Field Line Fitting of Observed Coronal Loops, 2003, *Solar Phys.*, 218, 29

Cargill, P. J., Coronal magnetism: Difficulties and prospects, 2009, Space Science Reviews, 144, 413

Carmichael, H., A Process for Flares, 1964, NASA Special Publication, 50, 451

Chamberlin, P. C., Woods, T. N., Eparvier, F. G., & Jones, A. R., 2009, in Society of Photo-Optical Instrumentation Engineers (SPIE) Conference Series, Vol. 7438, Solar Physics and Space Weather Instrumentation III, ed. S. Fineschi & J. A. Fennelly, 743802

Chandrasekhar, S., & Kendall, P. C., On Force-Free Magnetic Fields., 1957, *Astrophys. J.*, 126, 457

Charbonneau, P., & Smolarkiewicz, P. K., Modeling the Solar Dynamo, 2013, Science, 340, 42

Chen, P. F., Coronal Mass Ejections: Models and Their Observational Basis, 2011, Living Reviews in Solar Physics, 8, 1

Chintzoglou, G., Vourlidas, A., Savcheva, A., Tassev, S., Tun Beltran, S., & Stenborg, G., Magnetic Flux Rope Shredding By a Hyperbolic Flux Tube: The Detrimental Effects of Magnetic Topology on Solar Eruptions, 2017, *Astrophys. J.*, 843, 93

Chiu, Y. T., & Hilton, H. H., Exact Green's function method of solar force-free magnetic-field computations with constant alpha . I. Theory and basic test cases., 1977, *Astrophys. J.*, 212, 873

Choudhuri, A. R., 1998, The physics of fluids and plasmas : an introduction for astrophysicists

Couvidat, S., et al., Observables Processing for the Helioseismic and Magnetic Imager Instrument on the Solar Dynamics Observatory, 2016, *Solar Phys.*, 291, 1887

De Rosa, M. L., et al., A Critical Assessment of Nonlinear Force-Free Field Modeling of the Solar Corona for Active Region 10953, 2009, *Astrophys. J.*, 696, 1780

Démoulin, P., Extending the concept of separatrices to QSLs for magnetic reconnection, 2006, Advances in Space Research, 37, 1269

Demoulin, P., Henoux, J. C., Priest, E. R., & Mandrini, C. H., Quasi-Separatrix layers in solar flares. I. Method., 1996, *Astron. Astrophys.*, 308, 643

DeRosa, M. L., et al., The Influence of Spatial resolution on Nonlinear Force-free Modeling, 2015, *Astrophys. J.*, 811, 107

Domaradzki, J. A., Xiao, Z., & Smolarkiewicz, P. K., Effective eddy viscosities in implicit large eddy simulations of turbulent flows, 2003, Physics of Fluids, 15, 3890

Donnelly, R. F., Grubb, R. N., & Cowley, F. C., 1977, Solar x-ray measurements from sms-1, sms-2, and goes-1 : information for data users, Technical Memorandum

Duan, A., Jiang, C., Hu, Q., Zhang, H., Gary, G. A., Wu, S. T., & Cao, J., Comparison of Two Coronal Magnetic Field Models to Reconstruct a Sigmoidal Solar Active Region with Coronal Loops, 2017, *Astrophys. J.*, 842, 119

Dudík, J., et al., Slipping Magnetic Reconnection, Chromospheric Evaporation, Implosion, and Precursors in the 2014 September 10 X1.6-Class Solar Flare, 2016, *Astrophys. J.*, 823, 41

Dungey, J., Lxxvi. conditions for the occurrence of electrical discharges in astrophysical systems, 1953, The London, Edinburgh, and Dublin Philosophical Magazine and Journal of Science, 44, 725

Dungey, J. W., Interplanetary magnetic field and the auroral zones, 1961, Phys. Rev. Lett., 6, 47

Eisenstat, S. C., A Note on the Generalized Conjugate Gradient Method, 1983, SIAM Journal on Numerical Analysis, 20, 358

Eisenstat, S. C., Elman, H. C., & Martin, H. S., Variational Iterative Methods for Nonsymmetric Systems of Linear Equations, 1983, SIAM Journal on Numerical Analysis, 20, 345–357

Fan, Y., The emergence of a twisted Ω-tube into the solar atmosphere, 2001, The Astrophysical Journal, 554, L111

Fan, Y., On the Eruption of Coronal Flux Ropes, 2010, *Astrophys. J.*, 719, 728

Fan, Y., Magnetic fields in the solar convection zone, 2021, Living Reviews in Solar Physics, 18, 5

Fan, Y., & Gibson, S. E., The Emergence of a Twisted Magnetic Flux Tube into a Preexisting Coronal Arcade, 2003, *Astrophys. J. Lett.*, 589, L105

Fang, F., & Fan, Y., δ-Sunspot Formation in Simulation of Active-region-scale Flux Emergence, 2015, *Astrophys. J.*, 806, 79

Faraco, D., & Lindberg, S., Proof of taylor's conjecture on magnetic helicity conservation, 2020, Communications in Mathematical Physics, 373, 707

Faraco, D., Lindberg, S., MacTaggart, D., & Valli, A., On the proof of taylor's conjecture in multiply connected domains, 2022, Applied Mathematics Letters, 124, 107654

Gary, G. A., Linear Force-free Magnetic Fields for Solar Extrapolation and Interpretation, 1989, *Astrophys. J. Suppl.*, 69, 323

Gary, G. A., Plasma Beta above a Solar Active Region: Rethinking the Paradigm, 2001, *Solar Phys.*, 203, 71

Gibson, S. E., Solar prominences: theory and models, 2018, Living Reviews in Solar Physics, 15, 7

Gilchrist, S. A., Leka, K. D., Barnes, G., Wheatland, M. S., & DeRosa, M. L., On Measuring Divergence for Magnetic Field Modeling, 2020, *Astrophys. J.*, 900, 136

Giovanelli, R. G., A Theory of Chromospheric Flares, 1946, *Nature*, 158, 81

Goedbloed, J. P. H., & Poedts, S., 2004, Principles of Magnetohydrodynamics

Gosain, S., Démoulin, P., & Fuentes, M. L., Distribution of electric currents in sunspots from photosphere to corona, 2014, The Astrophysical Journal, 793, 15

Grinstein, F., Margolin, L., & Rider, W., Implicit large eddy simulation: Computing turbulent fluid dynamics, 2007, Implicit Large Eddy Simulation: Computing Turbulent Fluid Dynamics, Cambridge University Press

Grinstein, F. F., & Drikakis, D., Computing Turbulent Flow Dynamics With Implicit Large Eddy Simulation, 2007, Journal of Fluids Engineering, 129, 1481

Hagyard, M. J., & Teuber, D., Comparisons of measured and calculated potential magnetic fields., 1978, *Solar Phys.*, 57, 267

Hasegawa, A., Self-organization processes in continuous media, 1985, Advances in Physics, 34, 1

Haynes, A. L., & Parnell, C. E., A trilinear method for finding null points in a three-dimensional vector space, 2007, Physics of Plasmas, 14, 082107

Hesse, M., & Cassak, P. A., Magnetic Reconnection in the Space Sciences: Past, Present, and Future, 2020, Journal of Geophysical Research (Space Physics), 125, e25935

Hesse, M., & Schindler, K., A theoretical foundation of general magnetic reconnection, 1988, *J. Geophys. Res.*, 93, 5559

Heyvaerts, J., & Priest, E. R., Coronal heating by reconnection in DC current systems - A theory based on Taylor's hypothesis, 1984, *Astron. Astrophys.*, 137, 63

Hirayama, T., Theoretical Model of Flares and Prominences. I: Evaporating Flare Model, 1974, *Solar Phys.*, 34, 323

Hoeksema, J. T., et al., The Helioseismic and Magnetic Imager (HMI) Vector Magnetic Field Pipeline: Overview and Performance, 2014, *Solar Phys.*, 289, 3483

Hood, A. W., Browning, P. K., & van der Linden, R. A. M., Coronal heating by magnetic reconnection in loops with zero net current, 2009, *Astron. Astrophys.*, 506, 913

Howard, T., 2011, Coronal Mass Ejections: An Introduction, Vol. 376

Hoyle, F., 1949, Some recent researches in solar physics.

Hu, Q., & Dasgupta, B., An Improved Approach to Non-Force-Free Coronal Magnetic Field Extrapolation, 2008, *Solar Phys.*, 247, 87

Hu, Q., Dasgupta, B., Derosa, M. L., Büchner, J., & Gary, G. A., Non-force-free extrapolation of solar coronal magnetic field using vector magnetograms, 2010, Journal of Atmospheric and Solar-Terrestrial Physics, 72, 219

Hudson, H. S., Thick-Target Processes and White-Light Flares, 1972, *Solar Phys.*, 24, 414

Hudson, T. S., & Wheatland, M. S., Topological Differences Between Force-Free Field Models, 1999, *Solar Phys.*, 186, 301

Inoue, S., Magnetohydrodynamics modeling of coronal magnetic field and solar eruptions based on the photospheric magnetic field, 2016, Progress in Earth and Planetary Science, 3, 19

Inoue, S., Hayashi, K., & Kusano, K., Structure and stability of magnetic fields in solar active region 12192 based on nonlinear force-free modeling, 2016, The Astrophysical Journal, 818, 168

Jiang, C., et al., A fundamental mechanism of solar eruption initiation, 2021, Nature Astronomy, 5, 1126

Jiang, C., Wu, S. T., Feng, X., & Hu, Q., Data-driven magnetohydrodynamic modelling of a flux-emerging active region leading to solar eruption, 2016, Nature Communications, 7, 11522

Joshi, N. C., Joshi, B., & Mitra, P. K., Evolutionary stages and triggering process of a complex eruptive flare with circular and parallel ribbons, 2021, *Mon. Not. Roy. Astron. Soc.*, 501, 4703

Kaufman, A., & Mueller, K., 2005, in Visualization Handbook, ed. C. D. Hansen & C. R. Johnson (Burlington: Butterworth-Heinemann), 127

Kawabata, Y., Inoue, S., & Shimizu, T., Non-potential Field Formation in the X-shaped Quadrupole Magnetic Field Configuration, 2017, The Astrophysical Journal, 842, 106

Khlystova, A., & Toriumi, S., Photospheric Velocity Structures during the Emergence of Small Active Regions on the Sun, 2017, *Astrophys. J.*, 839, 63

Khomenko, E., 2020, Multi-Fluid Extensions of MHD and Their Implications on Waves and Instabilities, ed. D. MacTaggart & A. Hillier (Cham: Springer International Publishing), 69

Kopp, R. A., & Pneuman, G. W., Magnetic reconnection in the corona and the loop prominence phenomenon, 1976, *Solar Phys.*, 50, 85

Koumtzis, A., & Wiegelmann, T., A New Global Nonlinear Force-Free Coronal Magnetic-Field Extrapolation Code Implemented on a Yin-Yang Grid, 2023, *Solar Phys.*, 298, 20

Kumar, S., & Bhattacharyya, R., Continuous development of current sheets near and away from magnetic nulls, 2016, Physics of Plasmas, 23, 044501

Kumar, S., Bhattacharyya, R., Dasgupta, B., & Janaki, M. S., Chaotic magnetic field lines and spontaneous development of current sheets, 2017, Physics of Plasmas, 24, 082902

Kumar, S., Bhattacharyya, R., & Smolarkiewicz, P. K., On the role of topological complexity in spontaneous development of current sheets, 2015, Physics of Plasmas, 22, 082903

Kumar, S., Nayak, S. S., Prasad, A., & Bhattacharyya, R., Magnetic Reconnections in the Presence of Three-Dimensional Magnetic Nulls and Quasi-Separatrix Layers, 2021, *Solar Phys.*, 296, 26

Kumar, S., Prasad, A., Sarkar, R., & Bhattacharyya, R., Magnetohydrodynamics evolution of three-dimensional magnetic null in NOAA active region 11515 initiated using non-force-free field extrapolation, 2022, Frontiers in Astronomy and Space Sciences, 9, 1039061

Kusano, K., Maeshiro, T., Yokoyama, T., & Sakurai, T., Measurement of Magnetic Helicity Injection and Free Energy Loading into the Solar Corona, 2002, *Astrophys. J.*, 577, 501

Kusano, K., Suzuki, Y., Kubo, H., Miyoshi, T., & Nishikawa, K., Three-dimensional simulation study of the magnetohydrodynamic relaxation process in the solar corona. 1: Spontaneous generation of Taylor-Heyvaerts-Priest state, 1994, *Astrophys. J.*, 433, 361

Lantz, S. R., & Fan, Y., Anelastic Magnetohydrodynamic Equations for Modeling Solar and Stellar Convection Zones, 1999, *Astrophys. J. Suppl.*, 121, 247

Lapenta, G., Markidis, S., Divin, A., Newman, D., & Goldman, M., Separatrices: The crux of reconnection, 2015, Journal of Plasma Physics, 81, 325810109

Lazarian, A., Vlahos, L., Kowal, G., Yan, H., Beresnyak, A., & de Gouveia Dal Pino, E. M., Turbulence, Magnetic Reconnection in Turbulent Fluids and Energetic Particle Acceleration, 2012, *Space Sci. Rev.*, 173, 557

Lemen, J. R., et al., The Atmospheric Imaging Assembly (AIA) on the Solar Dynamics Observatory (SDO), 2012, *Solar Phys.*, 275, 17

Li, H., Feng, X., & Wei, F., Comparison of Synoptic Maps and PFSS Solutions for The Declining Phase of Solar Cycle 24, 2021, Journal of Geophysical Research (Space Physics), 126, e28870

Li, S., Jaroszynski, S., Pearse, S., Orf, L., & Clyne, J., VAPOR: A Visualization Package Tailored to Analyze Simulation Data in Earth System Science, 2019, Atmosphere, 10, 488

Li, T., Priest, E., & Guo, R., Three-dimensional magnetic reconnection in astrophysical plasmas, 2021, Proceedings of the Royal Society of London Series A, 477, 20200949

Liu, R., Chen, J., Wang, Y., & Liu, K., Investigating Energetic X-Shaped Flares on the Outskirts of A Solar Active Region, 2016a, Scientific Reports, 6, 34021

Liu, R., et al., Structure, Stability, and Evolution of Magnetic Flux Ropes from the Perspective of Magnetic Twist, 2016b, *Astrophys. J.*, 818, 148

Liu, Y., Welsch, B. T., Valori, G., Georgoulis, M. K., Guo, Y., Pariat, E., Park, S.-H., & Thalmann, J. K., Changes of Magnetic Energy and Helicity in Solar Active Regions from Major Flares, 2023, *Astrophys. J.*, 942, 27

Low, B. C., Solar Activity and the Corona, 1996, *Solar Phys.*, 167, 217

Mackay, D. H., & Yeates, A. R., The Sun's Global Photospheric and Coronal Magnetic Fields: Observations and Models, 2012, Living Reviews in Solar Physics, 9, 6

Manchester, I., W., Gombosi, T., DeZeeuw, D., & Fan, Y., Eruption of a Buoyantly Emerging Magnetic Flux Rope, 2004, *Astrophys. J.*, 610, 588

Margolin, L. G., & Rider, W. J., A rationale for implicit turbulence modelling, 2002, International Journal for Numerical Methods in Fluids, 39, 821

Margolin, L. G., Rider, W. J., & Grinstein, F. F., Modeling turbulent flow with implicit LES, 2006, Journal of Turbulence, 7, 15

Margolin, L. G., Smolarkiewicz, P. K., & Wyszogradzki, A. A., Dissipation in Implicit Turbulence Models: A Computational Study, 2006, Journal of Applied Mechanics, 73, 469

Margolin, L. G., Smolarkiewicz, P. K., & Wyszogrodzki, A. A., Implicit Turbulence Modeling for High Reynolds Number Flows , 2002, Journal of Fluids Engineering, 124, 862

Marsh, G. E., 1996, Force-Free Magnetic Fields: Solutions, Topology and Applications

Mason, E. I., Antiochos, S. K., & Viall, N. M., Observations of Solar Coronal Rain in Null Point Topologies, 2019, *Astrophys. J. Lett.*, 874, L33

Masuda, S., Kosugi, T., Hara, H., Tsuneta, S., & Ogawara, Y., A loop-top hard X-ray source in a compact solar flare as evidence for magnetic reconnection, 1994, *Nature*, 371, 495

Matthaeus, W. H., & Montgomery, D., Selective decay hypothesis at high mechanical and magnetic reynolds numbers, 1980, Annals of the New York Academy of Sciences, 357, 203

Maurya, Y. K. K., Bhattacharyya, R., & Pontin, D., Generation and annihilation of three dimensional magnetic nulls in extrapolated solar coronal magnetic field: Data-based implicit large eddy simulation, 2024, Physica Scripta

Metcalf, T. R., Resolving the 180-degree ambiguity in vector magnetic field measurements: The minimum energy solution, 1994, *Solar Phys.*, 155, 235

Mierla, M., et al., Prominence eruption observed in He II 304 Å up to ¿6 $R_\odot$ by EUI/FSI aboard Solar Orbiter, 2022, *Astron. Astrophys.*, 662, L5

Mitra, P. K., Joshi, B., Veronig, A. M., Chandra, R., Dissauer, K., & Wiegelmann, T., Eruptive-Impulsive Homologous M-class Flares Associated with Double-decker Flux Rope Configuration in Minisigmoid of NOAA 12673, 2020, *Astrophys. J.*, 900, 23

Mitra, P. K., Joshi, B., Veronig, A. M., & Wiegelmann, T., Multiwavelength Signatures of Episodic Nullpoint Reconnection in a Quadrupolar Magnetic Configuration and the Cause of Failed Flux Rope Eruption, 2022, The Astrophysical Journal, 926, 143

Miyoshi, T., Kusano, K., & Inoue, S., A Magnetohydrodynamic Relaxation Method for Non-force-free Magnetic Field in Magnetohydrostatic Equilibrium, 2020, *Astrophys. J. Suppl.*, 247, 6

Molodenskii, M. M., Integral Properties of Force-Free Fields., 1969, *Soviet Astron.*, 12, 585

Molodensky, M. M., Equilibrium and Stability of Force-Free Magnetic Field, 1974, *Solar Phys.*, 39, 393

Monteiro, G., Guerrero, G., Del Sordo, F., Bonanno, A., & Smolarkiewicz, P. K., Global simulations of Tayler instability in stellar interiors: a long-time multistage evolution of the magnetic field, 2023, *Mon. Not. Roy. Astron. Soc.*, 521, 1415

Moore, R. L., Sterling, A. C., Hudson, H. S., & Lemen, J. R., Onset of the Magnetic Explosion in Solar Flares and Coronal Mass Ejections, 2001, *Astrophys. J.*, 552, 833

Murray, S. A., Bloomfield, D. S., & Gallagher, P. T., Evidence for partial Taylor relaxation from changes in magnetic geometry and energy during a solar flare, 2013, *Astron. Astrophys.*, 550, A119

Nakagawa, Y., & Raadu, M. A., On Practical Representation of Magnetic Field, 1972, *Solar Phys.*, 25, 127

Nandy, D., Hahn, M., Canfield, R. C., & Longcope, D. W., Detection of a Taylor-like Plasma Relaxation Process in the Sun, 2003, *Astrophys. J. Lett.*, 597, L73

Nayak, S. S., Bhattacharyya, R., & Kumar, S., Magnetohydrodynamics model of an X-class flare in NOAA active region 12017 initiated with non-force-free extrapolation, 2021, Phys. Plasmas, 28, 024502

Nayak, S. S., Bhattacharyya, R., Prasad, A., Hu, Q., Kumar, S., & Joshi, B., A Data-constrained Magnetohydrodynamic Simulation of Successive Events of Blowout Jet and C-class Flare in NOAA AR 12615, 2019, *Astrophys. J.*, 875, 10

Neukirch, T., 2005, in ESA Special Publication, Vol. 596, Chromospheric and Coronal Magnetic Fields, ed. D. E. Innes, A. Lagg, & S. A. Solanki, 12.1

Nikolić, L., On Solutions of the PFSS Model With GONG Synoptic Maps for 2006-2018, 2019, Space Weather, 17, 1293

Nishio, M., Yaji, K., Kosugi, T., Nakajima, H., & Sakurai, T., Magnetic Field Configuration in Impulsive Solar Flares Inferred from Coaligned Microwave/X-Ray Images, 1997, *Astrophys. J.*, 489, 976

Norman, C. A., & Heyvaerts, J., The final state of a solar flare., 1983, *Astron. Astrophys.*, 124, L1

Ohtaka, K., 2003, Green's Functions (John Wiley & Sons, Ltd)

Ortolani, S., & Schnack, D. D., 1993, Magnetohydrodynamics of Plasma Relaxation (World Scientific Publishing Co. Pte. Ltd.)

Pariat, É., 2020, Using Magnetic Helicity, Topology, and Geometry to Investigate Complex Magnetic Fields, ed. D. MacTaggart & A. Hillier (Cham: Springer International Publishing), 145

Pariat, E., Aulanier, G., & Démoulin, P., 2006, in SF2A-2006: Semaine de l'Astrophysique Francaise, ed. D. Barret, F. Casoli, G. Lagache, A. Lecavelier, & L. Pagani, 559

Pariat, E., Valori, G., Démoulin, P., & Dalmasse, K., Testing magnetic helicity conservation in a solar-like active event, 2015, *Astron. Astrophys.*, 580, A128

Parker, E. N., Sweet's Mechanism for Merging Magnetic Fields in Conducting Fluids, 1957, *J. Geophys. Res.*, 62, 509

Parker, E. N., Spontaneous current sheets in magnetic fields:with applications to stellar x-rays, 1994, Spontaneous current sheets in magnetic fields:with applications to stellar x-rays. International Series in Astronomy and Astrophysics, 1

Parker, E. N., Singular magnetic equilibria in the solar x-ray corona, 2012, Plasma Physics and Controlled Fusion, 54, 124028

Parnell, C. E., Smith, J. M., Neukirch, T., & Priest, E. R., The structure of three-dimensional magnetic neutral points, 1996, Physics of Plasmas, 3, 759

Passos, D., & Charbonneau, P., Characteristics of magnetic solar-like cycles in a 3D MHD simulation of solar convection, 2014, *Astron. Astrophys.*, 568, A113

Pesnell, W. D., Thompson, B. J., & Chamberlin, P. C., The Solar Dynamics Observatory (SDO), 2012, *Solar Phys.*, 275, 3

Petschek, H. E., Magnetic Field Annihilation, 1964, NASA Special Publication, 50, 425

Pontin, D. I., & Hornig, G., The Parker problem: existence of smooth force-free fields and coronal heating, 2020, Living Reviews in Solar Physics, 17, 5

Pontin, D. I., & Priest, E. R., Magnetic reconnection: MHD theory and modelling, 2022, Living Reviews in Solar Physics, 19, 1

Pontin, D. I., Priest, E. R., & Galsgaard, K., On the Nature of Reconnection at a Solar Coronal Null Point above a Separatrix Dome, 2013, *Astrophys. J.*, 774, 154

Pontin, D. I., Wilmot-Smith, A. L., Hornig, G., & Galsgaard, K., Dynamics of braided coronal loops. II. Cascade to multiple small-scale reconnection events, 2011, *Astron. Astrophys.*, 525, A57

Prasad, A., Bhattacharyya, R., Hu, Q., Kumar, S., & Nayak, S. S., A Magnetohydrodynamic Simulation of Magnetic Null-point Reconnections in NOAA AR 12192, Initiated with an Extrapolated Non-force-free Field, 2018, *Astrophys. J.*, 860, 96

Prasad, A., Bhattacharyya, R., & Kumar, S., Magnetohydrodynamic Modeling of Solar Coronal Dynamics with an Initial Non-force-free Magnetic Field, 2017, *Astrophys. J.*, 840, 37

Prasad, A., Kumar, S., Sterling, A. C., Moore, R. L., Aulanier, G., Bhattacharyya, R., & Hu, Q., Formation of an observed eruptive flux rope above the torus instability threshold through tether-cutting magnetic reconnection, 2023, *Astron. Astrophys.*, 677, A43

Press, W. H., Teukolsky, S. A., Vetterling, W. T., & Flannery, B. P., 2007, Numerical Recipes 3rd Edition: The Art of Scientific Computing (3 ed.) (USA: Cambridge University Press)

Priest, E., 2014, Magnetohydrodynamics of the Sun

Priest, E., 2016, MHD Structures in Three-Dimensional Reconnection, ed. W. Gonzalez & E. Parker (Cham: Springer International Publishing), 101

Priest, E., & Forbes, T., 2000, Magnetic Reconnection

Priest, E. R., & Forbes, T. G., Magnetic Flipping: Reconnection in Three Dimensions Without Null Points, 1992, *J. Geophys. Res.*, 97, 1521

Priest, E. R., & Forbes, T. G., The magnetic nature of solar flares, 2002, *Astron. Astrophys. Rev.*, 10, 313

Priest, E. R., Hornig, G., & Pontin, D. I., On the nature of three-dimensional magnetic reconnection, 2003, Journal of Geophysical Research (Space Physics), 108, 1285

Prusa, J. M., & Smolarkiewicz, P. K., An all-scale anelastic model for geophysical flows: dynamic grid deformation, 2003, Journal of Computational Physics, 190, 601

Prusa, J. M., Smolarkiewicz, P. K., & Wyszogrodzki, A. A., EULAG, a computational model for multiscale flows, 2008, Computers Fluids, 37, 1193–1207

Reep, J. W., & Knizhnik, K. J., What Determines the X-Ray Intensity and Duration of a Solar Flare?, 2019, *Astrophys. J.*, 874, 157

Régnier, S., Magnetic Energy Storage and Current Density Distributions for Different Force-Free Models, 2012, *Solar Phys.*, 277, 131

Rempel, M., Cheung, M., & Chintzoglou, G., 2021, in 43rd COSPAR Scientific Assembly. Held 28 January - 4 February, Vol. 43, 1772

Riley, K. F., Hobson, M. P., & Bence, S. J., 2002, Fourier series (2 ed.) (Cambridge University Press), 421–438

Robinson, R. A., Aulanier, G., & Carlsson, M., Quiet Sun flux rope formation via incomplete Taylor relaxation, 2023, *Astron. Astrophys.*, 673, A79

Sakurai, T., Green's Function Methods for Potential Magnetic Fields, 1982, *Solar Phys.*, 76, 301

Sakurai, T., Computational Modeling of Magnetic Fields in Solar Active Regions, 1989, *Space Sci. Rev.*, 51, 11

Schatten, K. H., Prediction of the Coronal Structure for the Solar Eclipse of September 22, 1968, 1968, *Nature*, 220, 1211

Schatten, K. H., Wilcox, J. M., & Ness, N. F., A model of interplanetary and coronal magnetic fields, 1969, *Solar Phys.*, 6, 442

Scherrer, P. H., et al., The Helioseismic and Magnetic Imager (HMI) Investigation for the Solar Dynamics Observatory (SDO), 2012, *Solar Phys.*, 275, 207

Schindler, K., Hesse, M., & Birn, J., General magnetic reconnection, parallel electric fields, and helicity, 1988, *J. Geophys. Res.*, 93, 5547

Schmidt, H. U., 1964, On the Observable Effects of Magnetic Energy Storage and Release Connected with Solar Flares, ed. W. N. Hess (Washington, D. C.: Scientific and Technical Information Division, National Aeronautics and Space Administration), 107

Schmieder, B., Aulanier, G., Démoulin, P., & Pariat, E., Coronal loops, flare ribbons and aurora during slip-running, 2009, Earth, Planets and Space, 61, 565

Schou, J., et al., Design and Ground Calibration of the Helioseismic and Magnetic Imager (HMI) Instrument on the Solar Dynamics Observatory (SDO), 2012, *Solar Phys.*, 275, 229

Schrijver, C. J., et al., Nonlinear Force-Free Modeling of Coronal Magnetic Fields Part I: A Quantitative Comparison of Methods, 2006, *Solar Phys.*, 235, 161

Schrijver, C. J., et al., Nonlinear Force-free Field Modeling of a Solar Active Region around the Time of a Major Flare and Coronal Mass Ejection, 2008, *Astrophys. J.*, 675, 1637

Seehafer, N., Determination of constant α force-free solar magnetic fields from magnetograph data, 1978, *Solar Phys.*, 58, 215

Semel, M., Contribution à létude des champs magnétiques dans les régions actives solaires, 1967, Annales d'Astrophysique, 30, 513

Smolarkiewicz, P., & Szmelter, J., A nonhydrostatic unstructured-mesh soundproof model for simulation of internal gravity waves, 2011, Acta Geophysica, 59, 1109

Smolarkiewicz, P. K., A Simple Positive Definite Advection Scheme with Small Implicit Diffusion, 1983, Monthly Weather Review, 111, 479

Smolarkiewicz, P. K., A Fully Multidimensional Positive Definite Advection Transport Algorithm with Small Implicit Diffusion, 1984, Journal of Computational Physics, 54, 325

Smolarkiewicz, P. K., On forward-in-time differencing for fluids, 1991, Monthly Weather Review, 119, 2505

Smolarkiewicz, P. K., Multidimensional positive definite advection transport algorithm: an overview, 2006, International Journal for Numerical Methods in Fluids, 50, 1123

Smolarkiewicz, P. K., & Charbonneau, P., EULAG, a computational model for multiscale flows: An MHD extension, 2013, Journal of Computational Physics, 236, 608

Smolarkiewicz, P. K., & Clark, T. L., The multidimensional positive definite advection transport algorithm - Further development and applications, 1986, Journal of Computational Physics, 67, 396

Smolarkiewicz, P. K., & Grabowski, W. W., The Multidimensional Positive Definite Advection Transport Algorithm: Nonoscillatory Option, 1990, Journal of Computational Physics, 86, 355

Smolarkiewicz, P. K., Grubišić, V., & Margolin, L. G., On Forward-in-Time Differencing for Fluids: Stopping Criteria for Iterative Solutions of Anelastic Pressure Equations, 1997, Monthly Weather Review, 125, 647

Smolarkiewicz, P. K., & Margolin, L. G., On forward-in-time differencing for fluids - Extension to a curvilinear framework, 1993, Monthly Weather Review, 121, 1847

Smolarkiewicz, P. K., & Margolin, L. G., 1994, Variational elliptic solver for atmospheric applications

Smolarkiewicz, P. K., & Margolin, L. G., On forward-in-time differencing for fluids: an eulerian/semi-lagrangian non-hydrostatic model for stratified flows, 1997, Atmosphere-Ocean, 35, 127

Smolarkiewicz, P. K., & Margolin, L. G., MPDATA: A Finite-Difference Solver for Geophysical Flows,, 1998, Journal of Computational Physics, 140, 459

Smolarkiewicz, P. K., & Margolin, L. G., 2001, MPDATA-A Multipass Donor Cell Solver for Geophysical Flows, ed. E. F. Toro (New York, NY: Springer US), 833

Smolarkiewicz, P. K., Margolin, L. G., & Wyszogrodzki, A. A., Implicit Large-Eddy Simulation in Meteorology: From Boundary Layers to Climate, 2007, Journal of Fluids Engineering, 129, 1533

Smolarkiewicz, P. K., & Pudykiewicz, J. A., A class of semi-Lagrangian approximations for fluids, 1992, Journal of Atmospheric Sciences, 49, 2082

Smolarkiewicz, P. K., & Szmelter, J., Iterated upwind schemes for gas dynamics, 2009, Journal of Computational Physics, 228, 33

Solanki, S. K., Inhester, B., & Schüssler, M., The solar magnetic field, 2006, Reports on Progress in Physics, 69, 563

Sonnerup, B. U. Ö., et al., Reconnection of magnetic fields., 1984, NASA Reference Publication, 1120, 1

Steinhauer, L. C., & Ishida, A., Relaxation of a Two-Specie Magnetofluid, 1997, *Phys. Rev. Lett.*, 79, 3423

Stenflo, J. O., Solar magnetic fields as revealed by Stokes polarimetry, 2013, *Astron. Astrophys. Rev.*, 21, 66

Stix, M., 2002, Tools for Solar Observation (Berlin, Heidelberg: Springer Berlin Heidelberg), 67

Strugarek, A., Beaudoin, P., Brun, A. S., Charbonneau, P., Mathis, S., & Smolarkiewicz, P. K., Modeling turbulent stellar convection zones: Sub-grid scales effects, 2016, Advances in Space Research, 58, 1538

Sturrock, P. A., Model of the High-Energy Phase of Solar Flares, 1966, *Nature*, 211, 695

Sun, X., Hoeksema, J. T., Liu, Y., Aulanier, G., Su, Y., Hannah, I. G., & Hock, R. A., Hot spine loops and the nature of a late-phase solar flare, 2013, The Astrophysical Journal, 778, 139

Sun, X., Hoeksema, J. T., Liu, Y., Chen, Q., & Hayashi, K., A Non-radial Eruption in a Quadrupolar Magnetic Configuration with a Coronal Null, 2012, *Astrophys. J.*, 757, 149

Sweet, P. A., 1958, in Electromagnetic Phenomena in Cosmical Physics, ed. B. Lehnert, Vol. 6, 123

Syntelis, P., Lee, E. J., Fairbairn, C. W., Archontis, V., & Hood, A. W., Eruptions and flaring activity in emerging quadrupolar regions, 2019, *Astron. Astrophys.*, 630, A134

Tadesse, T., Wiegelmann, T., Gosain, S., MacNeice, P., & Pevtsov, A. A., First use of synoptic vector magnetograms for global nonlinear, force-free coronal magnetic field models, 2014, *Astron. Astrophys.*, 562, A105

Tadesse, T., Wiegelmann, T., & Inhester, B., Nonlinear force-free coronal magnetic field modelling and preprocessing of vector magnetograms in spherical geometry, 2009, *Astron. Astrophys.*, 508, 421

Tadesse, T., Wiegelmann, T., Inhester, B., & Pevtsov, A., Nonlinear force-free field extrapolation in spherical geometry: improved boundary data treatment applied to a SOLIS/VSM vector magnetogram, 2011, *Astron. Astrophys.*, 527, A30

Taylor, J. B., Relaxation of Toroidal Plasma and Generation of Reverse Magnetic Fields, 1974, Physical Review Letters, 33, 1139

Taylor, J. B., Relaxation and magnetic reconnection in plasmas, 1986, Reviews of Modern Physics, 58, 741

Taylor, J. B., Relaxation revisited, 2000, Physics of Plasmas, 7, 1623

Titov, V. S., Generalized Squashing Factors for Covariant Description of Magnetic Connectivity in the Solar Corona, 2007, *Astrophys. J.*, 660, 863

Titov, V. S., Hornig, G., & Démoulin, P., Theory of magnetic connectivity in the solar corona, 2002, Journal of Geophysical Research (Space Physics), 107, 1164

Van Ballegooijen, A. A., & Martens, P. C. H., Formation and Eruption of Solar Prominences, 1989, *Astrophys. J.*, 343, 971

Vasyliunas, V. M., Theoretical models of magnetic field line merging, 1., 1975, Reviews of Geophysics and Space Physics, 13, 303

Vekstein, G., Storing free magnetic energy in the solar corona, 2016, Journal of Plasma Physics, 82, 925820401

Veltri, P., Carbone, V., Lepreti, F., & Nigro, G., 2009, Self-Organization in Magnetohydrodynamic Turbulence, ed. R. A. Meyers (New York, NY: Springer New York), 8009

Venkatakrishnan, P., & Gary, G. A., Off Disk Center Potential Field Calculations Using Vector Magnetograms, 1989, *Solar Phys.*, 120, 235

Venkatakrishnan, P., Hagyard, M. J., & Hathaway, D. H., Elimination of Projection Effects from Vector Magnetograms - the Pre-Flare Configuration of Active Region AR:4474, 1988, *Solar Phys.*, 115, 125

Vourlidas, A., The flux rope nature of coronal mass ejections, 2014, Plasma Physics and Controlled Fusion, 56, 064001

Waite, M. L., & Smolarkiewicz, P. K., Instability and breakdown of a vertical vortex pair in a strongly stratified fluid, 2008, Journal of Fluid Mechanics, 606, 239

Warren, H. P., Crump, N. A., Ugarte-Urra, I., Sun, X., Aschwanden, M. J., & Wiegelmann, T., Toward a Quantitative Comparison of Magnetic Field Extrapolations and Observed Coronal Loops, 2018, *Astrophys. J.*, 860, 46

Wendt, J. F., 1992, Computational fluid dynamics - An introduction

Wheatland, M. S., Sturrock, P. A., & Roumeliotis, G., An optimization approach to reconstructing force-free fields, 2000, The Astrophysical Journal, 540, 1150

Wiegelmann, T., Optimization code with weighting function for the reconstruction of coronal magnetic fields, 2004, *Solar Phys.*, 219, 87

Wiegelmann, T., Computing Nonlinear Force-Free Coronal Magnetic Fields in Spherical Geometry, 2007, *Solar Phys.*, 240, 227

Wiegelmann, T., & Inhester, B., How to deal with measurement errors and lacking data in nonlinear force-free coronal magnetic field modelling?, 2010, *Astron. Astrophys.*, 516, A107

Wiegelmann, T., Inhester, B., & Sakurai, T., Preprocessing of Vector Magnetograph Data for a Nonlinear Force-Free Magnetic Field Reconstruction, 2006, *Solar Phys.*, 233, 215

Wiegelmann, T., & Neukirch, T., 2002, in EGS General Assembly Conference Abstracts, EGS General Assembly Conference Abstracts, 872

Wiegelmann, T., et al., Magneto-static Modeling from Sunrise/IMaX: Application to an Active Region Observed with Sunrise II, 2017, *Astrophys. J. Suppl.*, 229, 18

Wiegelmann, T., Petrie, G. J. D., & Riley, P., Coronal Magnetic Field Models, 2017, *Space Sci. Rev.*, 210, 249

Wiegelmann, T., & Sakurai, T., Solar force-free magnetic fields, 2021, Living Reviews in Solar Physics, 18, 1

Wiegelmann, T., Thalmann, J. K., Inhester, B., Tadesse, T., Sun, X., & Hoeksema, J. T., How Should One Optimize Nonlinear Force-Free Coronal Magnetic Field Extrapolations from SDO/HMI Vector Magnetograms?, 2012, *Solar Phys.*, 281, 37

Wilmot-Smith, A. L., Pontin, D. I., & Hornig, G., Dynamics of braided coronal loops. I. Onset of magnetic reconnection, 2010, *Astron. Astrophys.*, 516, A5

Woltjer, L., A Theorem on Force-Free Magnetic Fields, 1958, Proceedings of the National Academy of Science, 44, 489

Yamada, M., Kulsrud, R., & Ji, H., Magnetic reconnection, 2010, Rev. Mod. Phys., 82, 603

Yan, X. L., Yang, L. H., Xue, Z. K., Mei, Z. X., Kong, D. F., Wang, J. C., & Li, Q. L., Simultaneous Observation of a Flux Rope Eruption and Magnetic Reconnection during an X-class Solar Flare, 2018, *Astrophys. J. Lett.*, 853, L18

Yeates, A. R., 2020, Magnetohydrodynamic Relaxation Theory, ed. D. MacTaggart & A. Hillier (Cham: Springer International Publishing), 117

Yeates, A. R., Hornig, G., & Wilmot-Smith, A. L., Topological Constraints on Magnetic Relaxation, 2010, *Phys. Rev. Lett.*, 105, 085002

Yeates, A. R., Russell, A. J. B., & Hornig, G., Physical role of topological constraints in localized magnetic relaxation, 2015, Proceedings of the Royal Society of London Series A, 471, 50012

Yeates, A. R., Russell, A. J. B., & Hornig, G., Evolution of field line helicity in magnetic relaxation, 2021, Physics of Plasmas, 28, 082904

Yoshida, Z., & Giga, Y., Remarks on spectra of operator rot, 1990, Mathematische Zeitschrift, 204, 235

Yoshida, Z., & Mahajan, S. M., Variational principles and self-organization in two-fluid plasmas, 2002, Phys. Rev. Lett., 88, 095001

Yu, F., Zhao, J., Su, Y., Zhu, X., Guo, Y., Shen, J., & Li, H., Magnetic Field Extrapolation in Active Region Well Comparable to Observations in Multiple Layers, 2023, *Astrophys. J.*, 951, 54

Zeeman, P., The effect of magnetisation on the nature of light emitted by a substance, 1897, Nature, 55, 347

Zhao, J., Li, H., Pariat, E., Schmieder, B., Guo, Y., & Wiegelmann, T., Temporal Evolution of the Magnetic Topology of the NOAA Active Region 11158, 2014, *Astrophys. J.*, 787, 88

Zhu, X., Neukrich, T., & Wiegelmann, T., Magnetohydrostatic modeling of the solar atmosphere, 2022, Science in China E: Technological Sciences, 65, 1710

Zweibel, E. G., & Yamada, M., Perspectives on magnetic reconnection, 2016, Proceedings of the Royal Society of London Series A, 472, 20160479